Universitat Autònoma de Barcelona

Doping and interface effects on the ferroelectric properties of epitaxial HfO2-based thin films

Tingfeng Song

Universitat Autònoma de Barcelona

Doping and interface effects on the ferroelectric properties of epitaxial HfO_2-based thin films

Tingfeng Song

Doctoral Thesis

SUPERVISORS

Dr. Florencio Sánchez Barrera

Dr. Ignasi Fina Martínez

Institut de Ciència de Materials de Barcelona (ICMAB-CSIC)

TUTOR

Dr. Eva Maria Pellicer Vilà

Universitat Autònoma de Barcelona

Department of Physics, Faculty of Science

Doctoral Program: Materials Science

ICMAB INSTITUT DE CIÈNCIA DE MATERIALS DE BARCELONA EXCELENCIA SEVERO OCHOA

CSIC CONSEJO SUPERIOR DE INVESTIGACIONES CIENTÍFICAS

Dr. Florencio Sánchez Barrera, research scientist **and Dr. Ignasi Fina Martínez**, tenured scientist, at the Institut de Ciència de Materials de Barcelona - Consejo Superior de Investigaciones Científicas, and **Dr. Eva Maria Pellicer Vilà**, associate professor at Universitat Autònoma de Barcelona

CERTIFY

that **Tingfeng Song** carried out under their direction the research work entitled "Doping and interface effects on the ferroelectric properties of epitaxial HfO_2-based thin films". This work has been developed within a PhD program in Materials Science at the department of physics of Universitat Autònoma de Barcelona.
For that record they sign the certificate.

Bellaterra, July 2022

Dr. Florencio Sánchez Barrera Dr. Ignasi Fina Martínez

Dr. Eva Maria Pellicer Vilà

Acknowledgments

First of all, I would like to express my great gratitude to my research supervisors, Dr. Florencio Sánchez Barrera and Dr. Ignasi Fina Martínez for giving me the opportunity working in ICMAB and Mulfox group to develop my Ph.D. I acknowledge the time, patience, encouragement and guidance from them during my doctoral study. Their deep knowledge about the preparation, characterization, and theory mechanism of functional oxide device is the fundamental for the achievements in my thesis. I also appreciate the great support from them during the writing of the thesis.

I'm deeply thankful for the kind help, patience and guidance from Dr. Nico Dix about the sample preparation and the XRD characterization of thin films. Special thanks to Raul Solanas and Dr. Mengdi Qian for the growth of thin films and sample fabrication in pulsed laser deposition lab. Special thanks to Dr. Saúl Estandía and Dr. Jaume Gazquez for their time and effort to obtain great STEM images and analysis of the results. Special thanks to the guidance of the electrical measurements from Dr. Jike Lyu at the first year. Special thanks to Huan Tan for the piezoelectric force microscopy measurement for the better understanding of ferroelectric property. Special thanks to Dr. Romain Bachelet and Dr. Guillaume Saint-Girons for providing the $SrTiO_3$ buffered Si wafers, and also thanks the measurement and data collection of high temperature XRD by Dr. Rahma Moalla from Institut des Nanotechnologies de Lyon (INL-CNRS).

I also acknowledge the support and help of the technicians from the scientific service in ICMAB, especially Anna Crespi, Javier Campos and Joan Esquius for the XRD measurements and knowledge sharing, and Maite Simón and Andrés Gómez for AFM measurements.

I would like to thank Prof. Josep Fontcuberta, Dr. Gervasi Herranz, Dr. Can Onur, Dr. Yu Chen, Dr. Mikko Kataja, Dr. Milena Cervo Sulzbach, Xiao Long, Yunwei Sheng, Jiahui Jia, Dr. Alberto Quintana, for valuable comments and discussions of my research results in group meetings during last four years. Thanks Dr. Gervasi Herranz for organizing these group meetings. I also very thanks the supplement of lab from Dr. José Caicedo for target

preparation. And I want to extend my gratitude to the friendly and comfortable academic environment from all group members during the study at ICMAB.
Apart from the support from the academic aspect, I would like to extend my gratitude to my family and my friends. Thanks the constant and unconditional support, encourage and understanding from my family. And thanks the company from my friends to make each day cheerful.

I am also very grateful to China Scholarship Council (CSC) for financial support with grant number 201807000104 during my doctoral study.

Abstract

Ferroelectric HfO_2-based thin films have aroused great interest in the research field of memory devices, because it is a complementary metal oxide semiconductor compatible material with excellent scalability. However, it is needed to further clarify the nature of ferroelectricity and enhance the ferroelectric properties. Epitaxial thin films, with more controlled microstructure than polycrystalline films, can help to this objective. This thesis is focused on epitaxial HfO_2-based films, investigating new deposition conditions, the use of different substrates and doping and their impact on basic functional properties. Switching and fatigue mechanisms are also investigated.

In order to tailor the epitaxial growth of HfO_2-based thin films, first, we grown $Hf_{0.5}Zr_{0.5}O_2$ (HZO) films under lower oxidizing condition with inert Ar gas to decrease the pulsed laser deposition (PLD) plasma energy when reducing the oxygen pressure in the deposition process. Optimized mixing Ar and O_2 atmosphere allows increase of polarization around 50% respect films grown by conventional pulsed laser deposition. Second, we have investigated the effect of seed layers. Ultrathin HZO seed layer was grown on the bottom electrode to obtain crystallization of HZO film at lower deposition temperature. Third, we have found that orthorhombic phase can also be epitaxially stabilized on LSMO/STO(110) and LSMO/STO(111), having the films different in-plane epitaxial relationship than films on LSMO/STO(001)

Doping effect of Zr and La on the ferroelectricity of HfO_2 epitaxial films has been systematically studied. First, $Hf_{1-x}Zr_xO_2$ films in all the explored compositions are ferroelectric without wake-up effects. Endurance is better in HZO film than that of HfO_2 and ZrO_2 films. Second, we investigated the influence of La content, film thickness, and substrate induced epitaxial stress on the ferroelectricity of La:HfO_2 films. The optimized La content is 2-5 at%. 2 at% La:HfO_2 films with thickness less than 7 nm show a high P_r of about 30 $\mu C/cm^2$, slight wake-up, an endurance of at least 10^{10} cycles and a retention of more than 10 years. 2 at% La:HfO_2 films show the highest P_r for films grown on scandate substrates when compared with other perovskite substrates. Third, the Zr and La co-doping on HfO_2-based films is explored. In 1% La doped HZO films, it is found that, as for other compositions, there is a reduction of polarization with thickness increase in the explored range; however, for the studied composition the reduction is less than for

films without La doping. Endurance in epitaxial La-doped HZO films is more than 10^{10} cycles, and it is accompanied by excellent retention of more than 10 years at same voltage. This proves that there is no endurance-retention dilemma in La-doped HZO films as stated in previous literature. Furthermore, phases and polarization of the HfO_2-ZrO_2-La_2O_3 ternary system has been mapped observing that indeed 1%La doped HZO show the best performance

Impact of crystal phases on ferroelectric properties, such as endurance and switching dynamics, is also investigated. Epitaxial HZO films almost free of parasitic monoclinic phase suffer severe fatigue. In contrast, fatigue is mitigated in films with greater amount of paraelectric phase. On the other hand, switching analysis reveals that pure orthorhombic phase films follow the Kolmogorov-Avrami-Ishibashi switching model. Instead, the mixed orthorhombic/monoclinic phase films show nucleation limited switching. Films having larger fraction of non-ferroelectric phase with concomitant larger number of incoherent grain boundaries show 2 orders of magnitude faster switching time. Both studies allow to conclude that the films showing the largest amount of ferroelectric orthorhombic phase do not show the best functional properties.

Resumen

Las capas finas ferroeléctricas basadas en HfO_2, debido a su alta escalabilidad y a la compatibilidad con los procesos *complementary metal oxide semiconductor* - CMOS, han centrado un gran interés en el campo de los dispositivos de memoria. Sin embargo, es necesario entender mejor la naturaleza de la ferroelectricidad en este material con el fin de mejorar sus propiedades ferroeléctricas. Las capas finas epitaxiales, con microestructura más controlada que la de las capas policristalinas, pueden ayudar a realizar dicho objetivo. Esta tesis se focaliza en capas epitaxiales basadas en HfO_2, investigando nuevas condiciones de depósito, usando distintos substratos, e investigando efectos de dopaje. Los mecanismos de conmutación y fatiga también se han investigado.

Con el objetivo de lograr un mayor control en el crecimiento epitaxial de HfO_2 dopado, hemos crecido en primer lugar capas finas de $Hf_{0.5}Zr_{0.5}O_2$ (HZO) bajo condiciones de baja oxidación. Para ello hemos usado una baja presión de oxígeno, introduciendo simultáneamente Ar gas en la cámara de depósito de láser pulsado (PLD) controlando la energía del plasma generado por ablación laser a la vez que las condiciones de oxidación. La optimización de la mezcla de gases de O_2 y Ar ha permitido aumentar la polarización de las capas en un 50% respecto a capas equivalentes crecidas mediante condiciones PLD convencionales. En segundo lugar, hemos investigado los efectos de capas semilla, creciendo capas ultrafinas de HZO sobre el electrodo inferior para poder crecer encima HZO a menor temperatura. En tercer lugar, hemos demostrado que la fase ortorrómbica también puede estabilizarse epitaxialmente sobre LSMO/STO(110) y LSMO/STO(111), presentando las capas una relación epitaxial diferente a la de las capas sobre LSMO/STO(001).

Se ha realizado un estudio sistemático de los efectos de dopaje con La y Zr sobre la ferroelectricidad de capas epitaxiales de HfO_2. En primer lugar, demostramos que las capas de $Hf_{1-x}Zr_xO_2$ son ferroeléctricas en todo el rango de composición (desde x = 0 a x = 1), sin presentar además efecto de wake-up. La resistencia al ciclado es mejor en HZO que en capas de HfO_2 o ZrO_2. En segundo lugar, hemos investigado la influencia del contenido de La, espesor, y tensión epitaxial inducida por el substrato en la ferroelectricidad de capas de La:HfO_2. El contenido óptimo de La es 2-5 at%. Capas de 2

at% La:HfO_2 de espesor inferior a 7 nm presentan una alta P_r de unos 30 $\mu C/cm^2$, efectos de wake-up mínimos, resistencia al ciclado de al menos 10^{10} ciclos y retención de más de 10 años. Creciendo 2 at% La:HfO_2 sobre diversos substratos tipo perovskita hemos demostrado que la mayor polarización se obtiene sobre escandatos. En tercer lugar, hemos explorado el efecto sinérgico de co-dopar con La y Zr. En capas de HZO dopadas con 1% La se observa que la disminución de la polarización con el espesor es menor que en capas sin La. La resistencia al ciclado de capas de HZO dopadas con La es superior a 10^{10} ciclos, y además la retención es de más de 10 años cuando se ha usado el mismo voltaje, lo que demuestra que no existe un dilema entre retención y resistencia al ciclado en HZO dopado con La. Finalmente, hemos determinado el mapa de fases y polarización en el sistema ternario HfO_2-ZrO_2-La_2O_3.

Hemos investigado el impacto de las fases presentes sobre las propiedades ferroeléctricas, en particular sobre la resistencia al ciclado y la dinámica de conmutación ferroeléctrica.

La capas epitaxiales de HZO casi libres de fase parásita monoclínica sufren fatiga de manera severa, mientras que ésta es mucho menor en capas con cantidad alta de fase monoclínica. Por otra parte, hemos confirmado que en las capas básicamente ortorrómbicas puras (sin fase monoclínica) la conmutación ferroeléctrica se produce según el modelo Kolmogorov-Avrami-Ishibashi. Sin embargo, el proceso de conmutación está limitado por nucleación en capas con mezcla de fases ortorrómbica y monoclínica. En estas capas con mayor fracción de fase no ferroeléctrica y con ello mayor número de fronteras de grano no coherentes, el tiempo de conmutación es dos órdenes de magnitud más rápido.

Resum

Les capas fines ferroeléctricas basades en HfO_2, a causa de la seva alta escalabilidad i a la seva compatibilitat amb processos *complementary metal oxide semiconductor* - CMOS, han centrat un gran interès en el camp dels dispositius de memòria. Tanmateix, és necessari entendre millor la naturalesa de la ferroelectricitat en aquest material per tal de millorar les seves propietats ferroelèctriques. Las capes fines epitaxials, amb microestructura més controlada que las capes policristal·lines, poden ajudar a realitzar aquest objectiu. Aquesta tesi es focalitza en capes epitaxials basades en HfO_2, investigant noves condicions de dipòsit, utilitzant diferents substrats i investigant efectes de dopatge. Els mecanismes de commutació ferroelèctrica i fatiga també s'han investigat.

Amb l'objectiu d'aconseguir millor control en el creixement epitaxial de HfO_2 dopat, hem crescut en primer lloc capes fines de $Hf_{0.5}Zr_{0.5}O_2$ (HZO) sota condicions de baixa oxidació. Hem usat baixa pressió de l'oxigen, introduint simultàniament Ar gas a la càmera de dipòsit de làser polsat (PLD) controlant l'energia del plasma generat per l'ablació làser a la vegada que les condicions d'oxidació. L'optimització de la mescla de gasos d'O_2 i Ar ha permès augmentar la polarització de les capes en un 50% respecte a capes equivalents crescudes mitjançant condicions PLD convencionals. En segon lloc, hem investigat els efectes de capes llavor, creixent capes ultrafines de HZO sobre l'elèctrode inferior per poder créixer sobre HZO a menor temperatura. En tercer lloc, hem demostrat que la fase ortoròmbica també pot estabilitzar-se epitaxialment sobre LSMO/STO(110) i LSMO/STO(111), presentant les capes una relació epitaxial diferent a la de les capes sobre LSMO/STO(001).

S'ha realitzat un estudi sistemàtic dels efectes de dopatge amb La y Zr sobre la ferroelectricidad de capes epitaxiales de HfO_2. En primer lloc, demostrem que les capes de $Hf_{1-x}Zr_xO_2$ son ferroelèctriques en tot el rang de composició (des de x = 0 a x = 1), sense presentar a més efecte de wake-up. La resistència al ciclat continu és millor en HZO que en capes de HfO_2 o ZrO_2. En segon lloc, hem investigat la influència del contingut de La, gruix, i tensió epitaxial induïda pel substrat en la ferroelectricitat de capes de La:HfO_2. El contingut òptim de La és 2-5 at%. Capes de 2 at% La:HfO_2 de gruix inferior a 7 nm presenten una alta P_r d'uns 30 $\mu C/cm^2$, efectes de wake-up mínims, resistència al cicle d'almenys 10^{10} cicles i retenció de més de 10 anys. Creixent 2 at% La:HfO_2 sobre diversos substrats tipus perovskita hem demostrat que la major polarització s'obté sobre escandats. En tercer lloc, hem explorat l'efecte sinèrgic de co-dopar amb La y Zr. En capes

de HZO dopades amb 1% La se observa que la disminució de la polarització con el gruix es menor que en capes sense La. La resistència al ciclat de capes de HZO dopades con La és superior a 10^{10} cicles, y a més la retenció de més de 10 anys quan s'ha utilitzat el mateix voltatge, el que demostra que no existeix un dilema entre retenció i resistència al ciclatge en HZO dopat amb La. Finalment, hem determinat el mapa de fases i polarització en el sistema ternari HfO_2-ZrO_2-La_2O_3.

Hem investigat l'impacte que la presencia de diferents fases presenta sobre les propietats ferroeléctricas, en particular sobre la resistència al ciclat i la dinàmica de la commutació ferroeléctrica.

La capes epitaxials de HZO quasi lliures fase paràsita monoclínica mostren fatiga de manera severa, mentre que és molt menor en capes amb una quantitat més alta de fase monoclínica. Per altra part, hem confirmat que en les capes purament ortoròmbiques (sense fase monoclínica) la commutació ferroeléctrica es produeix segons el model Kolmogorov-Avrami-Ishibashi. Tanmateix, el procés de commutació està limitat per la nucleació en capes amb barreja de fases ortoròmbica i monoclínica. En aquestes capes amb major fracció de fase no ferroeléctrica i amb el major nombre de fronteres de gra no coherents, el temps de commutació és dos ordres de magnitud més ràpid.

Contents

Chapter 1. Motivation, Objectives and Outline of the thesis

1.1 Motivation

The discovery of ferroelectricity in HfO_2-based thin films have aroused great interest in the research field of memory devices, because HfO_2 is a complementary metal oxide semiconductor (CMOS) compatible material with excellent scalability.[1–8] The generally accepted origin for the ferroelectricity in hafnium is the formation of metastable non-centrosymmetric orthorhombic phase (o-phase) with space group $Pca2_1$.[1,2,9,10] However, HfO_2 is monoclinic (paraelectric) in bulk at ambient conditions, although it has various polymorphs depending on the temperature and pressure. The transition from tetragonal phase (t-phase, $P4_2/nmc$) to cubic phase (c-phase, Fm3m) and to monoclinic phase (m-phase, $P2_1/c$) occurs at 2773K and 1973K, respectively, whereas they are all centrosymmetric phase with non-polar property.[2,11,12] The first report of ferroelectricity in HfO_2-based thin films indicated that a very low thickness (around 10 nm) and introducing a capping layer (TiN top electrode) upon the thin film before annealing process was essential to stabilize ferroelectric phase (o-phase, $Pca2_1$) and supress non polar m-phase, suggesting an effect from surface energy and stress/strain.[1,13,14] Other factors, such as doping concentration, defect concentration and spatial distribution, and kinetic mechanism during the preparation process were also reported as critical on the stabilization of the metastable polar phase.[1,15–20]

Detailed investigations have been done to optimize ferroelectric phase ratio, explore the mechanism between structure and ferroelectricity, and fabricate devices focusing on HfO_2-based thin films.[2,9,12,21–24] Most reported works invole ALD-grown films, which are polycrystalline with multiple phases (m-,t-,c-,o-phases). In addition, the low thickness and small size of grains make a thorough structure characterization more challenging. Therefore, epitaxial films with well-oriented crystallinity and more uniform microstructure are convenient to better understand the intrinsic ferroelectricity of HfO_2-based film, as well as for prototyping devices. Epitaxial Y-doped HfO_2 films was first reported in 2015 and deposited on (001)-oriented yttria-stabilized zirconia (YSZ) by pulsed laser deposition (PLD).[25] The influence of Y doping concentration on the stabilized phases and temperature dependent orthorhombic-to-tetragonal structural phase transition were investigated in the next years. After that, ferroelectric epitaxial HfO_2-

based films have been grown on perovskite substrates and buffered Si substrate with $La_{0.67}Sr_{0.33}MnO_3$ (LSMO) as bottom electrode, and high remanent polarization (>30 $\mu C/cm^2$) and long endurance (up to 10^{11} cycles) have been achieved.[14,26–32] To further clarify the nature of ferroelectricity and enhance the ferroelectricity in HfO_2-based ferroelectric materials, more research has to be done in the fabrication and functional characterization of epitaxial HfO_2-based films. The deposition conditions and doping concentration have been investigated in detail. Meanwhile, mechanisms related to ferroelectricity (remanent polarization, endurance, retention, switching dynamics, etc) are still unclear and need to be clarified.

1.2 Objectives

The thesis aims to make progress in the following three directions.

(i) Tailoring epitaxial of $Hf_{0.5}Zr_{0.5}O_2$ thin film.

Epitaxial $Hf_{0.5}Zr_{0.5}O_2$ (HZO) thin films are grown under various oxygen and argon pressure to optimize the stabilized ferroelectric orthorhombic phase and FE polarization. The effect of a seed layer is also investigated. HZO or ZrO_2 is deposited on the bottom electrode to favour crystallization under lower deposition temperature. In addition, $Hf_{0.5}Zr_{0.5}O_2$ thin films are grown on LSMO/STO(110) and LSMO/STO(111) to explore the possible stabilization of the o phase and evaluate the influence of crystal orientation on the ferroelectricity.

(ii) Stabilization of polar phase in epitaxial HfO_2-based thin films by La and Zr doping.

A series of epitaxial films of $Hf_{1-x}Zr_xO_2$ (x from 0 to 1) are deposited to explore the impact of Hf and Zr content on ferroelectric and insulating properties. La is another widely used atom to stabilize the ferroelectric phase in HfO_2-based thin films. Epitaxial La doped HfO_2 thin films (with La content in the 0-10 at%) are grown on $SrTiO_3$(001) and Si(001), and the impact of the La concentration on the stabilization of the ferroelectric phase is determined. Based on the optimized concentration, La doped HfO_2 thin films with different thickness are prepared to determine the effect on the ferroelectricity. Furthermore, the combined effect from epitaxial stress and La doping is explored. Finally, the combined doping effect by La and Zr is systematically investigated.

(iii) Exploring the endurance and switching mechanisms in HfO_2-based ferroelectric thin films.

Epitaxial HZO thin films deposited on monocrystalline substrates of varied lattice parameter influence the strain of the LSMO electrodes and strain determines the relative amount of paraelectric and ferroelectric phase in the thin films. We explore the impact of the present phases on the endurance, to determine the fatigue mechanisms. We also determine the impact of the phases on the switching speed, and the switching mechnisms are determined.

1.3 Outline of the thesis

Chapter 2 introduces the basics of ferroelectric materials and related applications. The research progress in the field of polycrystalline hafnia films and epitaxial hafnia films is reviewed.

Chapter 3 contains a description of the experimental methods involved in the samples preparation, and structural and electrical characterization of the epitaxial HfO_2-based thin films.

Chapter 4 includes the result of the optimized deposition condition by introducing argon gas. By controlling the oxidizing conditions (through O_2 partial pressure) and the energy of the pulsed laser deposition plasma (through the total pressure of O_2 and Ar), a large increase in ferroelectric polarization can be achieved. In addition, the function of inserting a seed layer to decrease the deposition temperature for stabilizing ferroelectric phase is studied. Finally, the modulation of ferroelectricity by tailoring HZO epitaxial with LSMO/STO(110) and LSMO/STO(111) is demonstrated.

Chapter 5 presents how the concentration of Zr and La determines the ferroelectricity of HfO_2-based thin films. Then, the thickness effect on the ferroelectricity of La doped HfO_2 thin films is investigated on STO(001) and Si(001) substrates. The synergic effect from epitaxial stress and La doping on the remanent polarization is explored. Apart from the single atom doping, the synergic doping of Zr and La to HfO_2-based thin films is systematically discussed focusing on the structure and polarization.

Chapter 6 discusses the endurance and switching mechanism in epitaxial HfO_2-based thin films. Films deposited on different monocrystalline substrates buffered with LSMO electrodes are used to investigate the influence of non-polar phase on the fatigue and retention. On the other hand, the role of non-polar phase on the switching dynamics of

HfO_2-based thin films is identified. The potentiation/depression and spike-timing-dependent plasticity neuromorphic-like behavior is also demonstrated.

Chapter 7 presents the general conclusions of the thesis.

Chapter 2. Introduction

2.1 Ferroelectric materials

2.1.1 Ferroelectricity

The first observation of ferroelectric phenomenon was reported in 1921 by J. Valasek.[33] Ferroelectric materials are materials that show spontaneous electric polarization switchable under external electric field. Ferroelectric materials belong to dielectric materials group (as shown in Figure 2.1.1a) with good insulating property. When applying external electric field to dielectrics, the space symmetric is broken, which creates a transient electric polarization. Within dielectric materials, a subset structure are piezoelectric materials. Piezoelectrics show deformation under electric field, or, surface charges under external stress. Pyroelectrics have a polar crystal symmetry and have polarization change with temperature increase or decrease. Ferroelectrics are a subgroup of pyroelectrics. The ferroelectric response is typically characterized by measuring the hysteresis loop (Figure 2.1.1b). In multidomain state, the domains in the ferroelectrics are random distributed. When applying an external electric field larger than coercive field (E_c), the domains will be oriented along electric field direction. After removing the electric field, a stable remanent net polarization (P_r) remains. Applying opposite electric field (larger than E_c), the domains will switch to opposite direction, and opposite stable state stays after removing electric field. The two stable states (positive and negative P_r) in ferroelectrics are taken as the two logic states ("1" and "0") in memory devices.

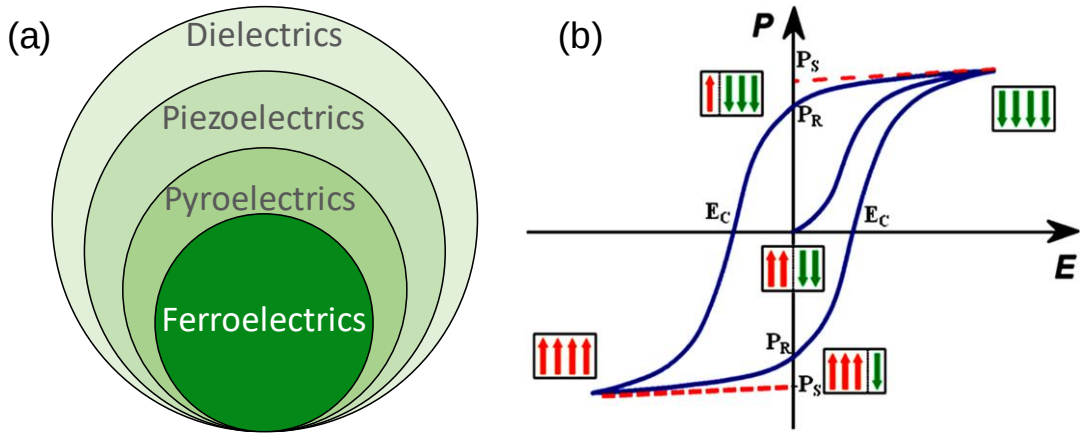

Figure 2.1.1 *(a) Hierarchy of the dielectric materials according to the piezoelectric, pyroelectric and ferroelectricity. (b) Hysteresis polarization-electric (P-E) curve in ferroelectric materials.*

2.1.2 Materials

The mostly investigated ferroelectric materials are perovskite oxides with general formula of ABO_3, such as $BaTiO_3$, $BiFeO_3$, $Pb(Zr,Ti)O_3$ (PZT). However, these conventional ferroelectrics confront various problems, including poor CMOS compatibility, Pd and Bi related environmental issue, and small bandgap and thus poor insulating properties. Since the discovery of ferroelectricity in the HfO_2-based film in 2011, where robust ferroelectricity with remanent polarization above 15 $\mu C/cm^2$ is observed in approximately 10 nm-thick films, enormous interest has been focused to this material because it is compatible with CMOS processes.[1–8] Meanwhile, HfO_2 has good electrical insulating property with an energy gap of ≈5.3-5.7 eV, and its relative dielectric constant is around 17 for monoclinic phase. Those properties make it widely applied high-k material in semiconductor industries.[34]

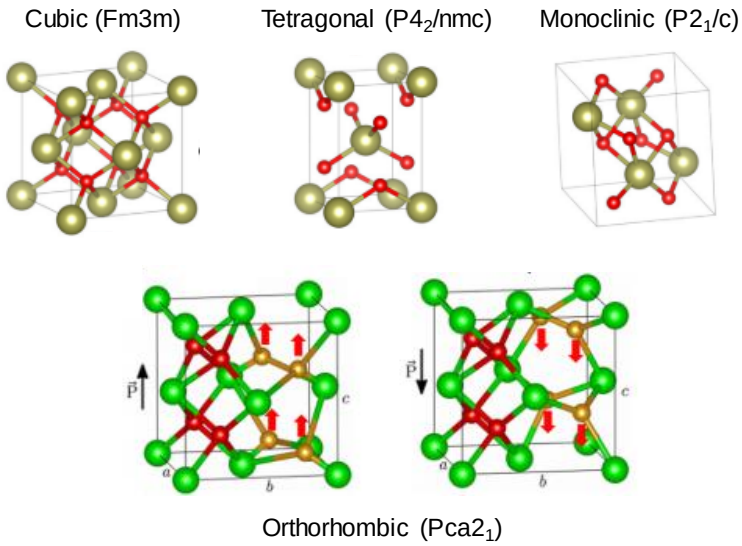

Figure 2.1.2 *Crystal structures of common HfO_2 polymorphs including cubic, tetragonal, monoclinic, and orthorhombic.*[9,24]

HfO_2 is a material with fluorite-type crystal structure. The most reported crystal structures in HfO_2-based thin films include cubic (Fm3m), tetragonal ($P4_2/nmc$), monoclinic ($P2_1/c$), and orthorhombic ($Pca2_1$), as shown in Figure 2.1.3. In bulk, transition from monoclinic to tetragonal and to cubic phase occurs at 1973, and 2773 K, respectively.[11] The process happens with temperature change without additional conditions. These three stable phases in bulk are centrosymmetric structure and non-polar. Numerous theoretical and experimental studies indicate that the polar orthorhombic phase ($Pca2_1$) exists in HfO_2-based thin films, which is responsible for the ferroelectric response.[35–41] As sketched in

Figure 2.1.2, the external electric field induced displacement of the four oxygen ions (yellow ball and marked arrows) along the c-axis is the origin of the spontaneous polarization.[1,9,35] In order to stabilize polar orthorhombic phase, some driving factors have to be introduced, such as volumetric confinement,[1,4] doping,[1,23,36,40,42–44] strain/stress,[14,45] defect concentration,[18,46–49] scale effect,[50–52] kinetics in the preparation process.[16,19]

Apart from the most reported orthorhombic phase, there is also a rhombohedral structure identified in ferroelectric HfO_2-based thin films when depositing under certain strain state and surface energy, and it can be responsible for ferroelectric response.[27,53,54] In situ electrical biasing transmission electron microscopy experiments indicate that oxygen vacancy movement is intertwined with the ferroelectric switching process in the HfO_2-based thin films.[32]

2.1.3 Devices

Ferroelectric materials, with two electrically operated spontaneous polarization states that retains without power supply, have been considered as a promising candidate for future non-volatile memory devices.[22] One type of the device is the capacitor-based ferroelectric random access memory (FeRAM), consisting of one transistor and one capacitor (1T-1C), as shown in Figure 2.1.3a. Write operation and destructive read out are performed by applying defined voltage pulses and monitoring the displacement current. The other two types ferroelectric memories are ferroelectric field effect transistor (FeFET) and ferroelectric tunnel junction (FTJ). FeFET is non-volatile memory cell consisting of one single transistor which has similar structure as the metal-oxide-semiconductor FET (MOSFET), but the gate oxide layer is replaced by a ferroelectric layer. The accumulation or depletion of carriers in semiconducting channel is controlled by the polarity of the ferroelectric layer.[55] Therefore, the threshold voltage can be modulated by ferroelectric switching, and the memory window is identified as twice the multiple of coercive field and film thickness. FTJ is based on the tunnelling current through a very thin ferroelectric thin film (nanometer level). The tunnelling current can be modulated by the polarization state with changing of the potential barrier height between two electrodes.

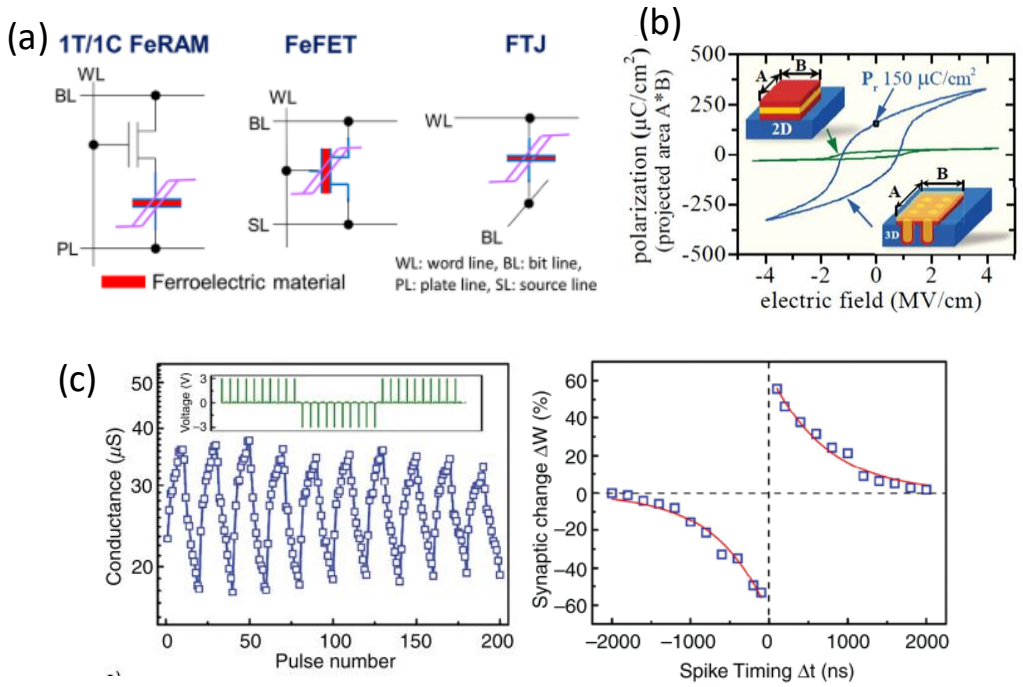

Figure 2.1.3 *(a) Device schemes for 1 transistor-1 capacitor ferroelectric random-access-memory, ferroelectric field-effect transistor, and ferroelectric tunnel junction.*[9] *(b) The polarization-electric field curves of Al-doped HfO_2 capacitors with planar and three-dimensional structures.*[7] *(c) The synaptic long term potentiation and depression characteristics (left side) of TiN/FE-HZO/Pt FTJ. And Hebbian STDP rule scheme from the synaptic array.*

For conventional perovskite-structure ferroelectrics, like PZT and $SrBi_2Ta_2O_9$ (SBT), the limited scaling and non-compatible to the CMOS process are critical issues for state-of-the-art three-dimensional stacks, because the lack of sufficient conformal deposition technologies and degradation of ferroelectricity at reduced thickness. In terms of FeFET, the decrease of the memory window has to be considered as decreasing the thickness, and a high coercive field is necessary, which is not satisfied by the conventional ferroelectrics. However, the appealing characteristics possessed by HfO_2-based ferroelectric thin films can make a breakthrough to fabricate emerging memory devices. As shown in Figure 2.1.3b, 10 nm-thick Al-doped HfO_2 films were uniformly deposited on Si trenches, and the P_r can reach up to effective 150 $\mu C/cm^2$ in three-dimensional structures which is one order of magnitude higher than that of a two-dimensional capacitor.[7] The synaptic long-term potentiation and depression characteristics and spike-timing-dependent-plasticity (STDP) behaviour in polycrystalline HfO_2 film indicates possible application for artificial neural network (Figure 2.1.3c).[56]

2.2 Ferroelectric HfO_2

Since the discovery of ferroelectricity in Si doped HfO_2 thin films in 2011,[1] a lot of researches have been done to fabricate, explore and improve the ferroelectricity of HfO_2-based thin films. Different deposition techniques have been used, such as atomic layer deposition (ALD),[8,50,57–61] chemical solution deposition,[62–64] pulsed laser deposition (PLD),[10,14,25,65] sputtering[18,66] and chemical vapour deposition.[67] Most of the research of the FE HfO_2 has involved into polycrystalline films, but since 2015,[25] epitaxial films are also intensively investigated.

2.2.1 Polycrystalline films

The majority of researches have involved in polycrystalline films, and the methods to stabilize the ferroelectric phase in those films have been explored in detail. For instance, the influence of deposition atmosphere, doping, thickness effect. Furthermore, the mechanisms related to electrical properties have also been widely investigated by using polycrystalline films.

Deposition atmosphere. During the growth of the HfO_2-based thin films, the atmosphere is critical for the stabilization of the ferroelectric phase.[18,20,48–50,68] During the deposition process, the most used oxygen source is O_2. The oxygen pressure, which greatly conditions the oxidation level of the films has been found to be crucial. As indicated in Figure 2.2.1a, the increase of oxygen percentage [O_2/(Ar + O_2)] from 0 to 3.33% results in the increase of non-polar monoclinic phase, companied with the decrease of memory window and dielectric constant. Similarly, in the deposition process using O_3, when increasing the ozone dose from 5s to 40s (Figure 2.2.1b), the intensity of monoclinic (-111) and (111) diffraction peaks increases apparently, which leads to a decrease of the switching current. First-principle calculation also proved that higher oxygen vacancy concentration is useful to lower the formation energy barrier between the m phase and other phases, which can favour the formation of polar o-phase.[18]

These results indicate that deposition HfO_2-based thin film under oxygen deficiency is beneficial to the ferroelectric polarization, but how to balance a large leakage current with high polarization under high oxygen vacancy concentration has to be concerned.

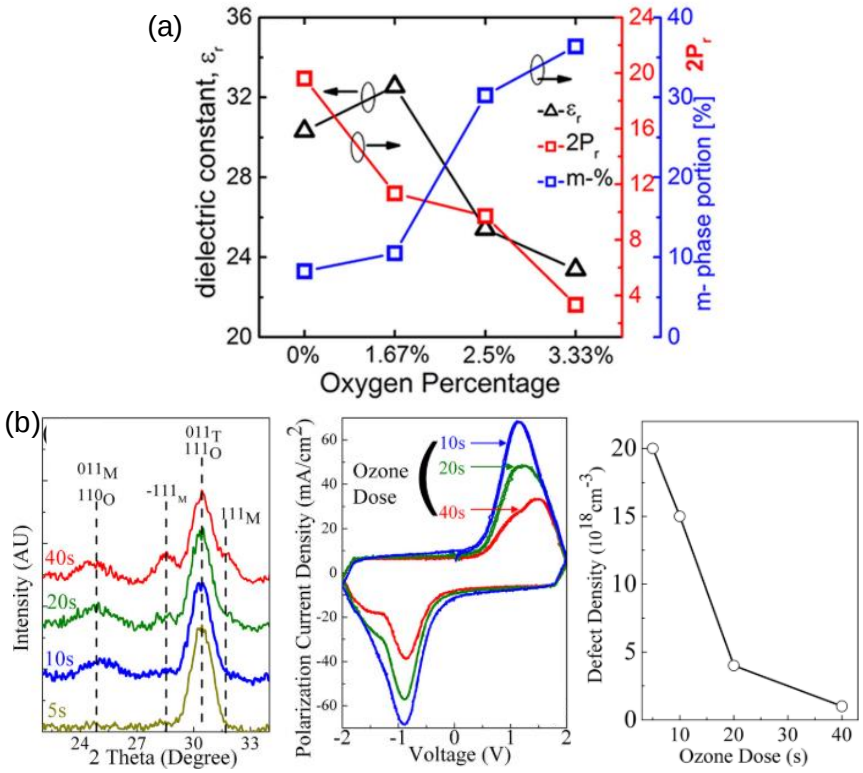

Figure 2.2.1 *(a) Influence of oxygen percentage [O_2/(Ar + O_2)] on the electric properties and microstructures of HZO films grown by sputtering.*[68] *(b) Influence of ozone dose on the microstructure, ferroelectric switching and defects density of HfO_2 films deposited by ALD.*[50]

Doping. Since 2011, various dopants, such as Gd, Tm, Y, Sr, La, Si, Zr, Al, etc have been applied to stabilize the ferroelectric phase in HfO_2-based thin films.[21,69] They can be divided into two groups, with atom radius larger (Gd, Tm, Y, Sr, La, Ba) and smaller or similar (Si, Zr, Al, Mg) than that of Hf atom (85 pm). Former researches indicate that larger dopants are helpful to increase the remanent polarization because the increased bond length of the metal-oxygen and asymmetry favors ferroelectric response.[44,70,71] In Figure 2.2.2a, compared with Mg, Sr and Ba exhibit a significantly larger polarization. For each dopant, the remanent polarization is highly dependent on the concentration. As shown in Figure 2.2.2b-c, the optimized concentration for Si, Gd, Y, Sr is around 3% and for Al is around 5%, respectively, with optimized remanent polarization around 20 μC/cm^2. However, the best concentration for high Pr is around 12% for La dopant. The different results of Sr dopant in Figure 2.2.2a and Figure 2.2.2c also indicate a dependence on the fabrication process.

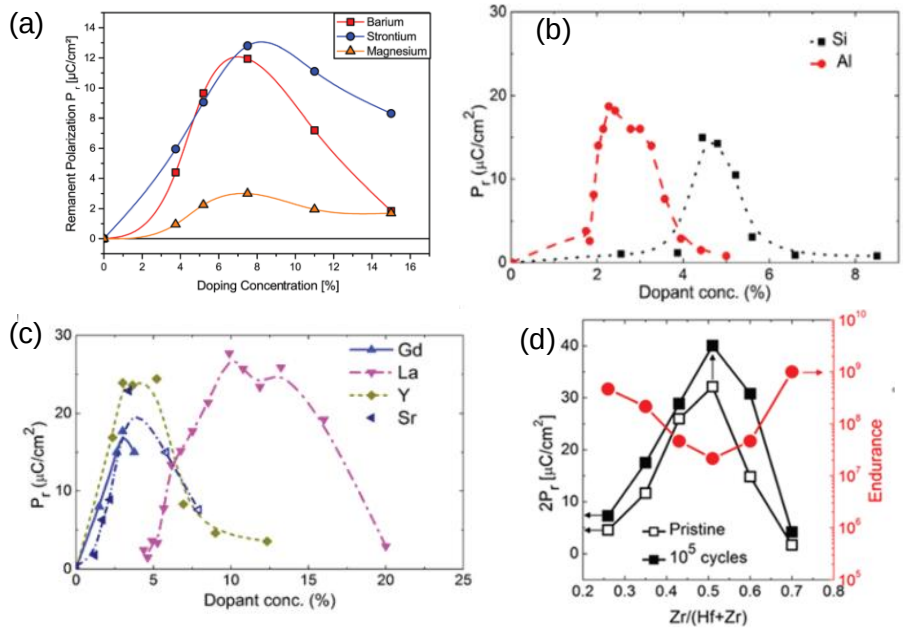

Figure 2.2.2 *(a) Remanent polarization versus the doping content of Ba, Sr and Mg using chemical vapour deposition.*[44] *Remanent polarization for ALD deposited HfO_2 layers doped with (b) Si and Al, (c) Gd, La, Y and Sr (d) Zr as a function of concentration.*[20,21]

Favoured by the similarity in physical radius and crystal structures of Zr and Hf, solid solution can be achieved in the whole range of Zr/Hf ratio, and the concentration range for the highest P_r is around 50% (Figure 2.2.2d). Undoped HfO_2 thin films are mostly formed by m-phase, presenting a dielectric behaviour and nearly-zero remanent polarization. When the content of Zr is around 50%, the polar orthorhombic phase is majority in the film, leading to a high ferroelectric polarization. Furthermore, in Zr-rich thin films, tetragonal phase induces an antiferroelectric-like behaviour.[42,72] Apart from Zr, the experimental and theoretical studies also demonstrate high P_r when using La dopant.[38,44,73] However, different respect to Zr, the phase transition with La content increase is from m-phase to o-phase, and then to c-phase.[74] This kind of difference is related to the ionic radius, which changes the symmetry of the crystal structure and the bond length between the metal and oxygen atoms.[36] In addition, ab initio simulations show that the valence difference with Hf causes oxygen vacancies which lead to structure deformation and the appearance of ferroelectricity, but vacancy-trapping capability of La dopant is useful to control the mobility of oxygen vacancies.[73]

Thickness effect. Thickness is also one of the critical factor for stabilizing ferroelectric polar phase in HfO_2-based thin films. With film thickness increase, the grain size increases and the portion of non-polar m-phase increases, leading to the degradation of ferroelectricity.[47,51,75–77] As shown in Figure 2.2.3a, with thickness increase, the

ferroelectric orthorhombic phase presenting in 6 nm pure HfO_2 film gradually transforms to m-phase and the P_r decreases from 10 μC/cm^2 to 0 in 20 nm film. Similarly, for HZO thin films (Figure 2.2.3b), the 10 nm film shows a $2P_r$ value of 30.7 μC/cm^2, but it decreases to almost negligible value in 40 nm film. Theoretical calculation (Figure 2.2.3c) also indicates a thickness effect on the phase formation and m-phase trends to form in thicker films.[37,78]

The influence of thickness is usually companied with grain size effect. In the films with small grains radius (r), the surface energy (σ) of the nanoscale grains can induce internal pressure (P=2 σ/r) to the order of gigapascals,[79,80] which is a key point for the stabilization of the ferroelectric o-phase in HfO_2-based thin films. Nowadays, ferroelectricity has been identified in the ultra-thin films with thickness around 1-2 nm.[4,81] On the other hand, the fined grain is also believed to favour the formation of polar o-phase in 1 μm HfO_2-based films.[82]

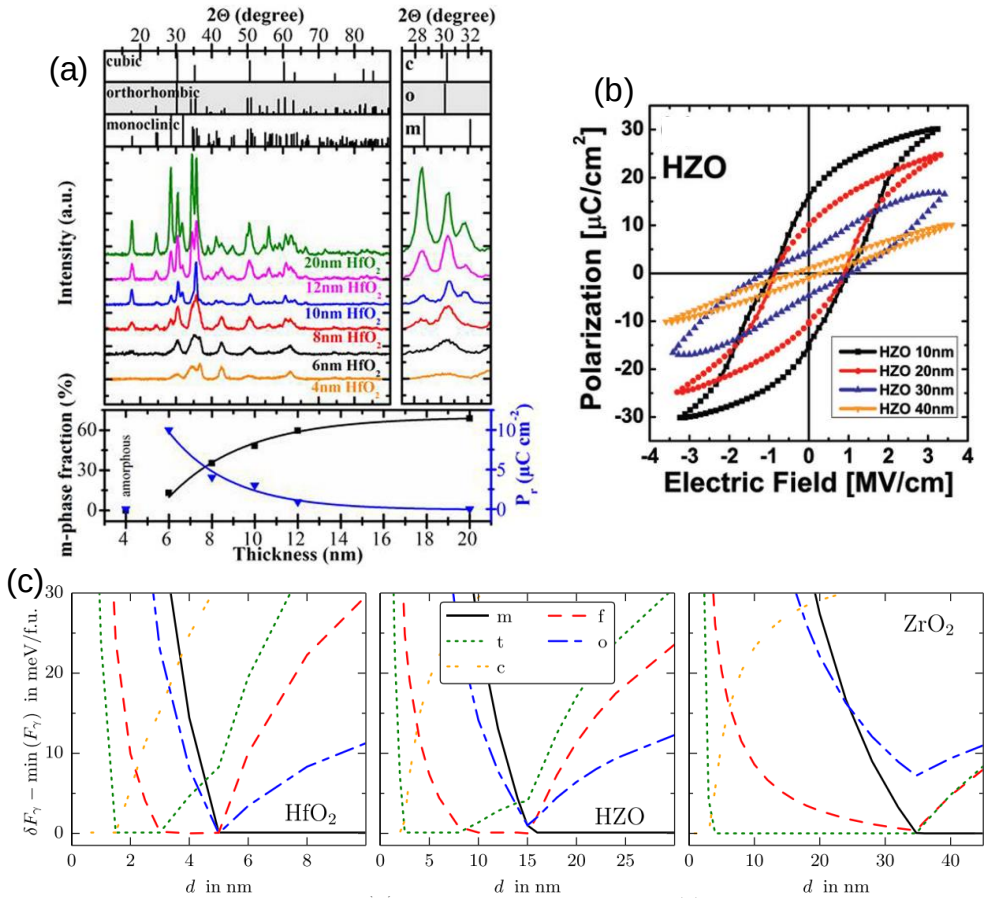

Figure 2.2.3 *(a) Grazing incident x-ray diffraction (GIXRD) data of the pure HfO_2 thin films with different thicknesses. Right side is the enlarged range around 2θ= 30°. The bottom is the calculated m-phase fraction from the XRD data and the corresponding P_r value as a function of the film thickness.*[83] *(b) Polarization loops of HZO films with various thicknesses.*[77] *(c) Calculated*

free energy difference relative to the phase with minimal Helmholtz free energy at 300K as a function of film thickness for HfO_2, HZO and ZrO_2.[37]

Apart from the detailed mentioned deposition atmosphere, doping and thickness factors, there are many other factors that also have a great effect on the phase formation in HfO_2-based thin films, such as stress, insertion of seed layer or capping layer, interfacial energy, thermal kinetics, and grain size, etc.[21] Up to now, the mechanism for the stabilization of polar phase in HfO_2-based thin films is apparently caused by a combination of various factors.

Challenges. The structures and the factors for improving the ferroelectricity in HfO_2-based thin films have been systematically investigated. However, for practical applications, there are still some challenges about this material for memory applications, such as wake-up effect and fatigue, and imprint and retention. As shown in Figure 2.2.4a-b, the wake-up effect is often related to the merge of multiple current peaks during cycling process. Since the polarization loop is an integration of the current curve, this process is accompanied with a transition of the pinched hysteresis loop to a de-pinched loop with an increase of P_r and coercive field (E_c). The possible mechanisms for wake-up effect are: (1) field-induced phase transition, the widely reported transition from t-phase to o-phase,[84–87] and also some report about the transition from m-phase or antipolar phase to polar o-phase,[88,89] (2) the redistribution of the charged defects.[74,90] External electric filed can activate the oxygen vacancies and relax the locale dipoles that are pinned by charged oxygen vacancies.[91] During cycling process, the gradually decreasing of the memory window is also one of the critical issue, called as fatigue. Possible explanations are the increase of the defect concentration leading to domain pinning effect, and the phase transition from polar phase to non-polar phase.[86,92,93] With further cycling, the increase of defects and the formation of conducting path result in an increase of leakage current and finally, suffering hard breakdown.

The existence of imprint is also detrimental to the retention and endurance, because the sacrifice of the one side polarization. The reason for the formation of imprint is related to the difference of the work function between the top and bottom electrodes, or the uneven distribution of the defects in the film.[94–96] As shown in Figure 2.2.4c, the imprint increases with baking time, which is attributed to the internal bias field formed by trapping and/or detrapping near the electrodes. By La doping, the oxygen vacancy concentration declines, thus the imprint is reduced.[96] Figure 2.2.4d summarizes P_r and the endurance of

ferroelectric HfO_2-based films. In general, a smaller endurance presents when cycling uses a higher P_r. The highest endurance is around 10^{11} cycles with P_r around 12 μC/cm^2. However, an endurance up to 10^{15} cycles is convenient for application of RAM device, thus further improvement of the endurance of doped HfO_2 films is needed.[22]

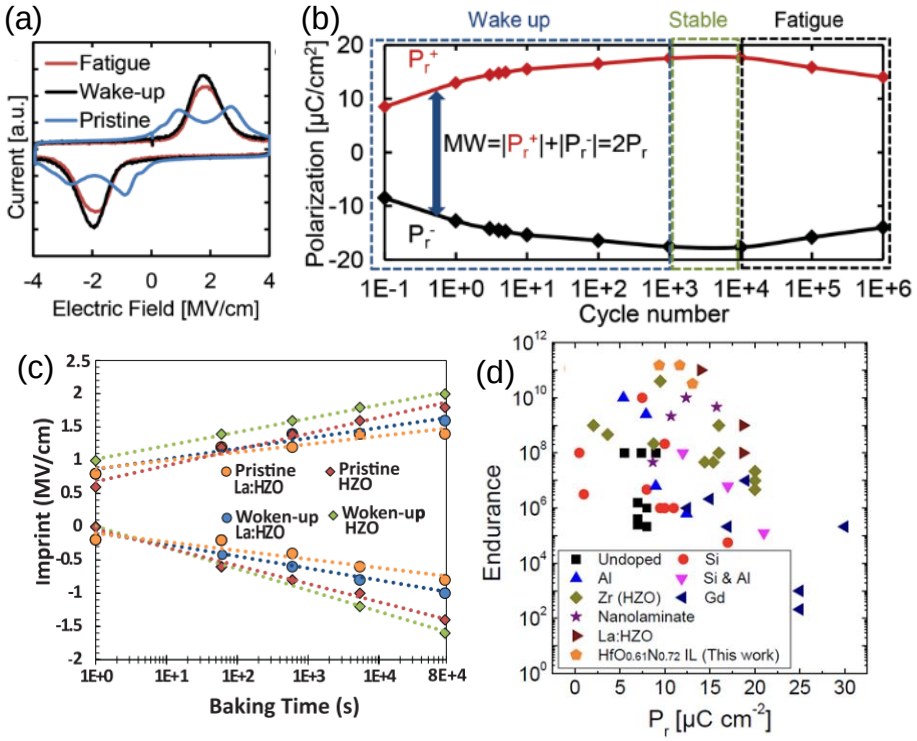

Figure 2.2.4 *(a) Current-voltage curves of Sr:HfO_2 films under pristine, wake-up, and fatigue states. (b) Evolution of the ferroelectric P_r during bipolar cycling. The difference between positive and negative P_r is defined as memory window (MW).*[86] *(c) Imprint variation of the pristine and woken-up La:HZO film and HZO film as a function of bake time.*[96] *(d) Summary of the reported endurance of films with different P_r.*[97]

2.2.2 Epitaxial films

Epitaxial films with fewer defects and more controlled microstructure than that of polycrystalline films are convenient to understand and control ferroelectricity of HfO_2-based thin films. Epitaxial HfO_2-based thin film was first reported in 2015 from Funakubo group and they reported polarization loops in 2016.[25,98] Up to now, the reported results are mainly epitaxial films grown on yttria-stabilized zirconia (YSZ), perovskite substrates and Si substrate.[23,24] The most employed method for epitaxial growth is pulsed laser deposition.

Epitaxial growth on YSZ. Shimizu et al.[25] deposited Y-doped HfO_2 (YHO) directly on YSZ substrate, and 7% Y doped films indicated polar o-phase with Curie temperature (T_c)

around 450 °C. T_c was found to depend on the thickness and orientation of the YHO film, likely due to the mediation of surface energy and epitaxial strain.[99] Inserting of oriented indium tin oxide (ITO) allowed to modulate the orientation of YHO film by controlling the mismatch between the film and the YSZ substrate, and further tailoring the phase formation and ferroelectricity.[98,100,101] The thickness influence on epitaxial YHO film was investigated in the thickness ranging from 10 nm to 1 μm.[102] Unlike conventional ferroelectric film (PZT), there was very small dependent of P_r and E_c on film thickness, and a possible reason could be the small grain size in all explored thickness range.[103–105] Interestingly, after poling the YHO film grown on (001)ITO/YSZ, a ferroelastic domain switching from the nonpolar b-axis to the polar c-axis oriented domain was observed, which resulted in large saturated polarization around 30 $\mu C/cm^2$.[106]

YHO has also been deposited on ITO buffered YSZ substrate by sputtering, and the results reveal that during deposition and following annealing process, oxygen atmosphere is detrimental to the ferroelectricity and insulation property of YHO film.[107] Mimura et al.[108] reported that decreasing the sputtering power and oxygen pressure, ferroelectricity was observed in the YHO film without subsequent annealing. Apart from ITO, TiN has also been used as bottom electrode. TiO_2 interfacial layer formed by interface reaction and the interface strain was found to be favourable to stabilize the ferroelectric phase.[109] Theoretical calculations also proves the function of growth orientation and epitaxial strain on the stabilization of ferroelectric phase.[110]

Films with other composition have also been investigated. Kiguchi et al.[111] deposited HZO films on 100-oriented YSZ substrate by solid state epitaxy, and indicated that the stability of o-phase was also attributed to doping effect and thermal mismatch between the film and the substrate. Lower Ar-ion beam energy for the sputtering and higher crystallization temperature in the post-annealing process was beneficial to obtain higher quality film.[112] Interestingly, 001 oriented HZO film has been also deposited by PLD on YSZ buffered by lattice matched $Pb_2Ir_2O_7$ electrode.[113] Electric-field-induced phase transition from t-phase to o-phase has been demonstrated in 5%Y doped HZO film.[114] Apart from the dopants mentioned above, Fe also presents as one of effective dopant for achieving ferroelectricity in epitaxial HfO_2-based thin film with optimized concentration around 5%.[115,116]

Epitaxial growth on perovskite substrates. Epitaxial ferroelectric HZO films have been deposited on STO substrate with LSMO as bottom electrode. The growth window for the

epitaxial HZO film by PLD was systematically investigated.[65] Temperature and oxygen pressure increase is positive for the stabilization of o-phase and thus increasing the P_r, and with optimized film thickness at 7 nm, a P_r up to 24 $\mu C/cm^2$ can be obtained. However, the increase of deposition temperature and oxygen pressure induce pronounced fatigue, and low deposition temperature degrades retention.[117] The reliability performance of 9 nm film shows no wake-up effect and endurance up to 10^8 cycles with long retention.[28] The epitaxial growth of HZO film on LSMO occurs by domain matching epitaxy mechanism, with arrays of dislocations with short periodicities.[118] Estandia et al.[119] reported that HZO films grown on conducting perovskite electrodes presented low (on Nb:$SrTiO_3$ and $Ba_{0.95}La_{0.05}SnO_3$)or null (on $LaNiO_3$ and $SrRuO_3$) o-phase and P_r, but manganite electrodes ($La_{1-x}Ca_xMnO_3$, A=Sr or Ca, x=0.33 or 0.5) allowed the stabilization of the ferroelectric o-phase. The interface between the o-HZO and LSMO occurs by substitution of the Mn cations in the MnO_2 expected renucleation of the manganite by a mixture of Hf/Zr atoms, with Hf/Zr occupying the sites of the Mn in the LSMO perovskite, which may play a role in the stabilization of ferroelectric phase in HZO film.[120] Although o-phase is widely reported ferroelectric phase in HfO_2-based thin film, Wei et al.[10] observed that the HZO films deposited on STO with LSMO electrode was rhombohedral. Density-functional-theory calculations and further experimental results suggested that compressive strain and thinner film (size effect) is critical for the stability of a metastable rhombohedral phase.[53,121]

To understand the influence of epitaxial stress on the stabilization of the ferroelectric o-phase, epitaxial HZO films and LSMO electrode were grown on a set of single crystalline oxide substrates, as shown in Figure 2.2.5a-b. The lattice parameter of LSMO can be controlled by the substrate. Tensilely strained LSMO promote the formation of o-phase, whereas the relaxed or compressively strained LSMO favour the m-phase.[14]

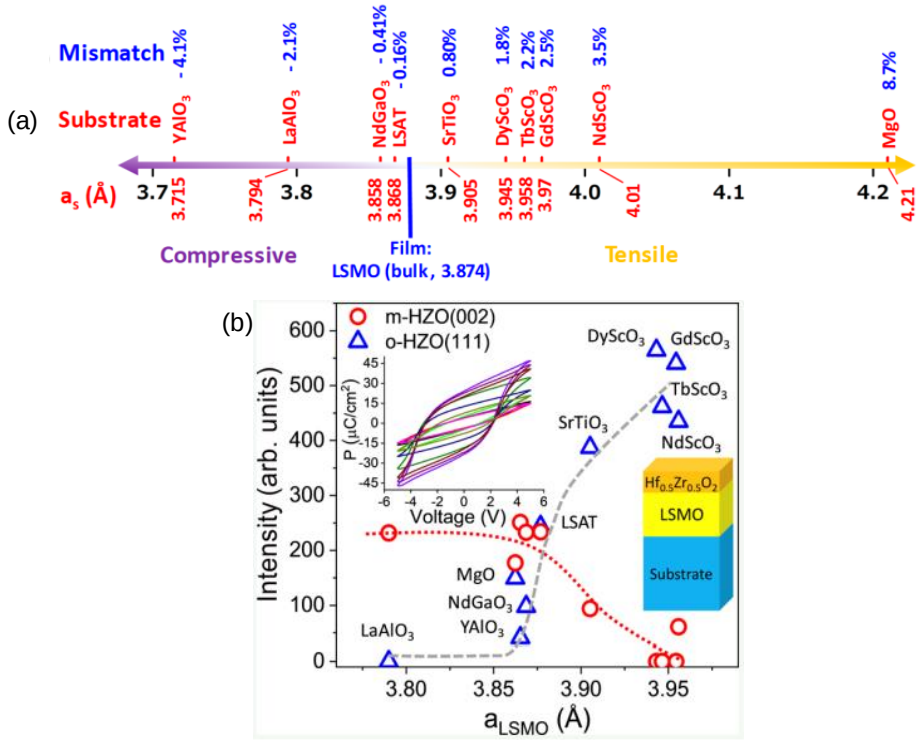

Figure 2.2.5 *(a) Sketch showing the lattice mismatch between the LSMO electrode and different oxide substrates. (b) Relationship between the intensity of XRD peaks of m and o phases as a function of HZO film and the LSMO in-plane lattice parameter on each substrate. The inset (left top) is polarization-voltage loops of films on different substrates. The right side is the sketch of the sample structure.*[14]

Epitaxial growth on Si. Lee et al.[122] reported the first epitaxial YHO film on Si substrate buffered by YSZ. Ferroelectricity was proved by hysteresis loop and the film also presented good retention. 100-oriented epitaxial YHO films, as thick as 900 nm, were also obtained on (100)YSZ//(001)Si substrates buffered by (100)-oriented epitaxial ITO layers.[102] Remarkably, epitaxial HZO thin film has been integrated on Si using STO as template, a remnant polarization as high as 34 μC/cm^2 is achieved.[29] HZO/LSMO bilayers were grown epitaxially on $LaNiO_3$/ CeO_2/YSZ/Si(001), and ferroelectricity o-phase exhibited in HZO film when growing on LSMO but not directly on $LaNiO_3$.[31] After optimizing the ferroelectricity by thickness effect, the film, with sub-5 nm, can combine high polarization, endurance and long retention under same electric field.[30] Thermal evolution indicates that with higher thermal energy, the mobility of oxygen vacancies and charge trapping is supported, thus wake-up and fatigue effect are accelerated.[123] Epitaxial HZO film has also been deposited on Si directly, the interfacial SiO_2 offers the initial compressive strain condition and polar o-phase can be stabilized by inhomogeneous strains from the surrounding m-phase.[124]

In this thesis, first, we will tailor the epitaxy of hafnium films by using lower oxidizing condition (combining low oxygen pressure with inert Ar gas to decrease the PLD plasma energy), inserting a seed layer (HZO or ZrO_2) on the bottom electrode to crystalize under lower temperature and epitaxially stabilized o-phase on LSMO/STO(110) and LSMO/STO(111). Second, we explore the influence of Zr and La dopant concentration on the ferroelectricity (polarization, leakage, retention and endurance) of HfO_2-based thin film. Third, to better understand the endurance and switching mechanism and further improve the capacitor properties, the HfO_2-based thin films on different substrates with different ratio of m- and o-phases are systematically investigated.

Chapter 3. Experimental methods

3.1 Thin films

3.1.1 Targets

The targets used in this thesis are prepared by solid state reaction. The process includes following steps: weighing the commercial oxide powders (above 99 % purity) based on the required element ratio, mixing the powder uniformly by mortar, compacting the powder into a pellet with pressure, and finally sintering in the furnace. After sintering, the targets will be checked by XRD to examine the composition. The list of the targets used in this thesis is shown in the Table 3.1.

Table 3.1 *Ceramic targets used in this thesis*

Targets	Chemicals	Composition
HfO_2	*HfO_2 powder/ Alfa Aesar/ 99.95 %* *ZrO_2 powder/ Alfa Aesar/ 99.978 %* *La_2O_3 powder/ Alfa Aesar/ 99.99 %*	*100 mol % HfO_2*
$Hf_{0.75}Zr_{0.25}O_2$*		*75 mol % HfO_2, 25 mol % ZrO_2*
$Hf_{0.5}Zr_{0.5}O_2$*		*50 mol % HfO_2, 50 mol % ZrO_2*
$Hf_{0.25}Zr_{0.75}O_2$		*25 mol % HfO_2, 75 mol % ZrO_2*
ZrO_2		*25 mol % ZrO_2*
$Hf_{0.99}La_{0.01}O_{2-x}$		*99 mol % HfO_2, 1 mol % $LaO_{1.5}$*
$Hf_{0.98}La_{0.02}O_{2-x}$		*98 mol % HfO_2, 2 mol % $LaO_{1.5}$*
$Hf_{0.95}La_{0.05}O_{2-x}$		*95 mol % HfO_2, 5 mol % $LaO_{1.5}$*
$Hf_{0.925}La_{0.075}O_{2-x}$		*92.5 mol % HfO_2, 7.5 mol % $LaO_{1.5}$*
$Hf_{0.9}La_{0.1}O_{2-x}$		*90 mol % HfO_2, 10 mol % $LaO_{1.5}$*
$Hf_{0.5}Zr_{0.49}La_{0.01}O_{2-x}$		*50 mol % HfO_2, 49 mol % ZrO_2, 1 mol % $LaO_{1.5}$*
$Hf_{0.5}Zr_{0.48}La_{0.02}O_{2-x}$		*50 mol % HfO_2, 48 mol % ZrO_2, 2 mol % $LaO_{1.5}$*
$Hf_{0.5}Zr_{0.45}La_{0.05}O_{2-x}$		*50 mol % HfO_2, 45 mol % ZrO_2, 5 mol % $LaO_{1.5}$*
$Hf_{0.5}Zr_{0.4}La_{0.1}O_{2-x}$		*50 mol % HfO_2, 40 mol % ZrO_2, 10 mol %$LaO_{1.5}$*
$Zr_{0.99}La_{0.01}O_{2-x}$		*99 mol % ZrO_2, 1 mol % $LaO_{1.5}$*
$Zr_{0.98}La_{0.02}O_{2-x}$		*98 mol % ZrO_2, 2 mol % $LaO_{1.5}$*
$Zr_{0.95}La_{0.05}O_{2-x}$		*95 mol % ZrO_2, 5 mol % $LaO_{1.5}$*
$Zr_{0.9}La_{0.1}O_{2-x}$		*90 mol % ZrO_2, 10 mol % $LaO_{1.5}$*

*targets prepared by Dr. Jike Lyu

For example, when preparing the $Hf_{0.5}Zr_{0.49}La_{0.01}O_{2-x}$ target, La_2O_3 powder needs to be dried at 1100°C with duration of 15h and then weighing the required powder at 300°C to avoid the absorption of water in the air. After mixing the powder uniformly and compacting the powder into a pellet under 7 tons with a duration of 20 min, finally the prepared pellet was sintered in the furnace, following the sintering process shown in Figure 3.1.1a. After cooling down to room temperature, the composition of the targets was checked by XRD, as shown in Figure 3.1.1b.

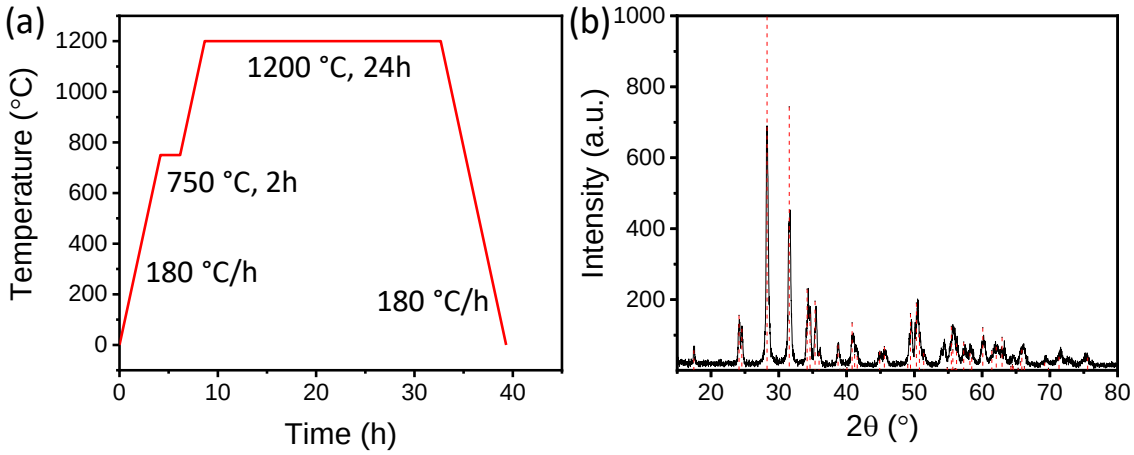

Figure 3.1.1 *(a) Temperature-time curves for sintering the targets. (b) XRD data of the target ($Hf_{0.5}Zr_{0.49}La_{0.01}O_{2-x}$) after sintering, the red dash line is the reference position from the PDF card of monoclinic HZO (04-002-5428).*

3.1.2 PLD

The PLD setup used in this thesis is at the Institut de Ciencia de Materials de Barcelona (ICMAB). A photo and sketch of the PLD system is shown in Figure 3.1.2. The process to grow thin films using PLD system can be divided into three steps. First, a pulsed KrF excimer laser with wavelength $\lambda = 248$ nm and pulse width of 10-40 ns is focused on the target fixed on the platform in the vacuum chamber. The high energy generated from the laser will ablate the target surface and form plasma plume along the direction to the substrate. The plasma plume contains the stoichiometric composition of target material. The energy and energy density of the laser can be controlled by the masks and lens in the road of the laser. Second, plasma plume expands from the target to the substrate and through the gas atmosphere in between. The process needs less than 10 μs and can be affected by the background pressure. The third step is the thin film growth. After the plasma arrives the substrate, the nucleation, diffusion and growth processes happen. The

LSMO electrodes are deposited at a substrate temperature of 700 °C under 0.1 mbar of oxygen, a laser frequency of 5 Hz, and the temperature is controlled using a thermocouple inserted in the middle of the heater block.

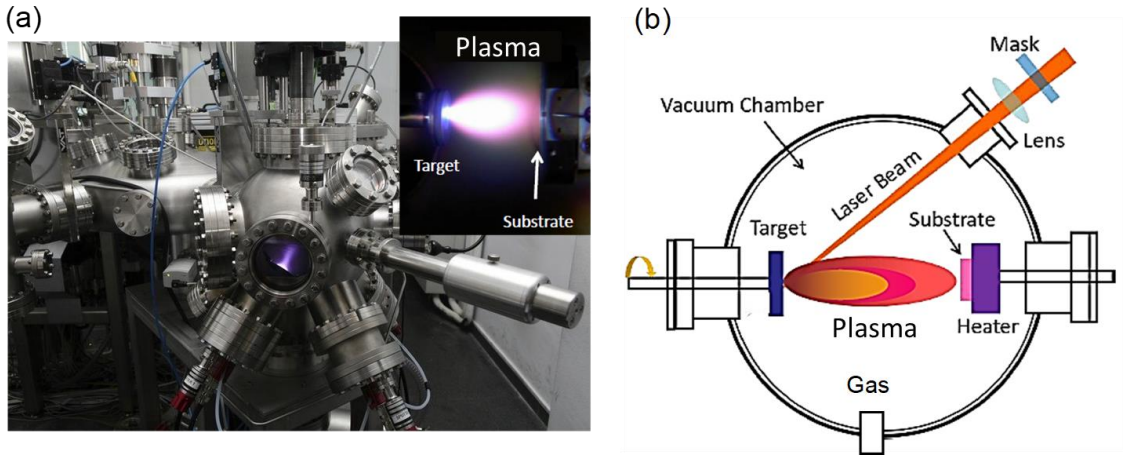

Figure 3.1.2 *(a) PLD and sputtering systems at ICMAB, the insert image is the zoomed part of the PLD plasma. (b) Sketch of a PLD system.*

3.1.3 Sputtering

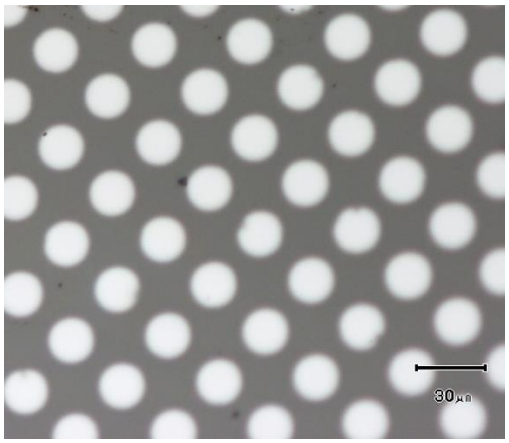

Figure 3.1.3 *Pt top contacts under optical microscopy for 20 μm diameter in circle on thin films.*

Direct current magnetron sputtering was used to fabricate top Pt electrode on the surface of the thin films, as shown in Figure 3.1.3. In the sputtering process, the Pt target is bombarded by the ionized Ar gas with pressure of 5×10^{-3} mbar, power of 10 W. A bias voltage accelerates the speed of ionized Ar, when it reaches the target surface, the target material is ejected and create plasma. The Pt plasma will be attracted towards the thin film at room temperature and condensate on the surface to form contacts for the electric measurement. The reason for the choosing of platinum is that it is a noble metal with chemical stability and high electrical conductivity.[125] Arrays of Pt electrodes, typically of

circular shape around 20 μm in diameter, were prepared by using transmission electronic microscopy (TEM) grids as stencil masks. The Pt thickness, determined by sputtering time, is 20 nm.

3.2 Structural characterization

3.2.1 XRD

X-ray diffraction (XRD) has been used to investigate the lattice parameter, phase composition, film thickness and epitaxial relationships of HfO_2-based thin films. Diffraction follows the Bragg's law, $2d\sin\theta = n\lambda$, where d is the lattice distance, θ is the diffraction angle, λ is the wavelength of x-ray, n is the integer related to the plane index. Diffraction occurs at certain angles, for which there is constructive interference, when the path difference of two x-rays is equal to an integer number of the x-ray wavelength as shown in Figure 3.2.1a. Figure 3.2.1b shows the sketch of the angle system in the x-ray diffractometers. Three rotation angles (omega ω, phi ϕ, chi χ) are necessary to define the orientation of a sample in the diffractometer, which allows the detection of the planes that are not parallel to the substrate surface. In a typical four-circle diffractometer system, there is also a 2θ circle for the point detectors.

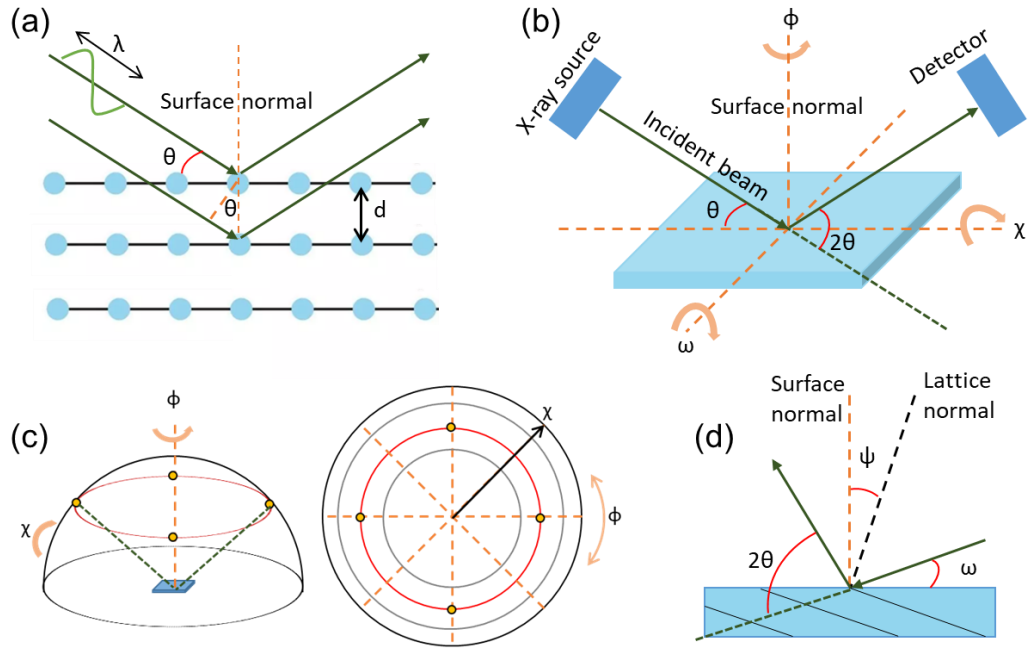

Figure 3.2.1 *(a) The schematic of Bragg's law. (b) The sketch of geometry for a diffraction setup with three axes rotation and x-ray source and detector. (c) Sphere of the pole figure defined by spherical coordinates ϕ and χ and projection of the pole sphere. (d) Sketch of an asymmetric scan.*

θ-2θ scan. The symmetric θ-2θ scan (also called ω-2θ scan) is the measurements with the x-ray source and detector rotating simultaneously along the sample surface. It is a direct measurement of the lattice planes parallel to the sample surface, namely, the out of plane crystal orientation of the thin films. Especially, high temperature XRD was performed for $Hf_{1-x}Zr_xO_2$ series samples. Temperature-dependent diffraction was done in air using an Anton Paar heater with a graphite dome on a high-brilliance (9 kW) X-ray diffractometer with high resolution (Rigaku SmartLab) equipped with a copper rotating anode and a Ge(220) monochromator with $\lambda_{CuK\alpha1}$ = 1.54056 Å.

Two-dimensional x-ray diffraction (2θ-χ frame). 2θ-χ frame is performed by two-dimensional detector, which collects the information simultaneously from the θ-2θ and the χ direction. Different reflections are simultaneously detected, which allows multiple measurements in a short time, although the resolution is less than using a point detector.

Pole figures. Sketches of the pole figure defined by spherical coordinates φ and χ and the projection of the pole sphere are shown in Figure 3.2.1c. When measuring the pole figures of the samples, the symmetric θ-2θ is fixed, and the tilt angle χ changes from 0 to 90 degree, but for time-saving, only a specified region is measured, the sample is rotated along ϕ. φ scans can be extracted at certain χ angle.

Reciprocal space mapping (RSM). As indicated in Figure 3.2.1d, the RSM is an asymmetric measurement, where the ω ≠ θ with offset angle ψ (the angle between the surface normal and the measured plane normal). It was used to determine the in-plane lattice parameters and strain states of the epitaxial films. This scan is usually around a certain range of the selected reflections. The area of reciprocal space can be mapped using the relationships: $q_{/\!/} = 1/d*\sin(\theta-\omega)$ and $q_{\perp} = 1/d*\cos(\theta-\omega)$. Where d is the lattice parameter of detected reflection. 2D contour map is usually used to show the measured intensity including diffraction peaks from the selected reflections and the area in the vicinity. It should be noted that the selected Bragg reflections should be asymmetric with respect to the surface normal to provide the in-plane and out-of-plane information of epitaxial films.

In this thesis, Cu Kα radiation is used to study the crystal structure. The θ-2θ scan is performed by Siemens D5000 diffractometer and Bruker D8-Discover equipped with point detector. The 2θ-χ frame, pole figure and RSM mapping are measured by Bruker D8-Advance equipped with a 2D detector diffractometer.

3.2.2 AFM

Atomic force microscopy (AFM) has been used to obtain topographic information of the thin films. A sketch of the AFM device is shown in Figure 3.2.2a. The nanometric tip connected with the AFM cantilever is used to sense the interaction with the sample surface. Because the interaction forces between the tip and the surface atoms (Figure 3.2.2b), bending occurs in the AFM cantilever, which results in the shift of the reflected laser point on the 4 quadrant photodetector. With the collected information from the detector, the surface topography can be determined. The topographic information can be tested by contact or non-contact model. In this thesis, the non-contact model (dynamic mode) is utilized, and the tip oscillates in resonance frequency. The resolution along vertical and lateral direction is ~1Å and nanometer range, respectively. The measurements in this thesis were performed at ICMAB using Agilent 5100 AFM system equipped with silicon tips.

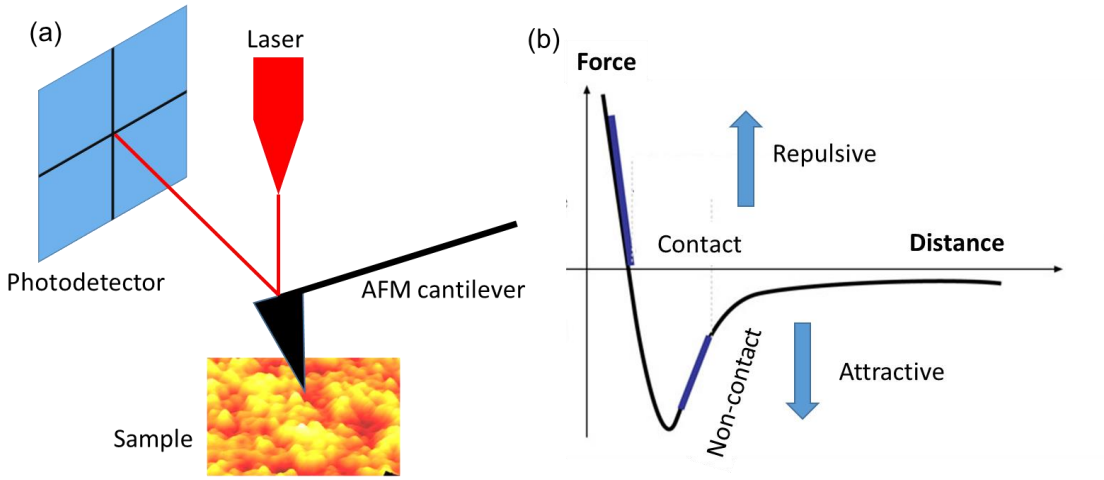

Figure 3.2.2 *(a) Schematics of an AFM device. (b) Interaction forces (Van del Waals) between the tips and surface atoms.*

3.2.3 STEM

Microstructural characterization was done by scanning transmission electron microscopy (STEM) using a Nion UltraSTEM 200, operated at 200 kV and equipped with a 5th order Nion aberration corrector. JEOL ARM 200CF STEM with a cold field emission source, equipped with a CEOS aberration corrector was also used to character microstructure.

3.3 Electrical characterization

Electrical characterizations including polarization loops, leakage current, endurance, retention, switching dynamics and neuromorphic behaviour are conducted by aixACCT TFAnalyser 2000 system. Dielectric properties are measured by impedance analyser (HP4192LF, Agilent Co.).

3.3.1 Ferroelectric characterization

The ferroelectric polarization-electric field (P-E) loops and the following electric characterizations are all done in top-bottom configuration, as indicated in Figure 3.3.1a. The voltage is applied to the top Pt electrode and the bottom electrode is grounded. There are two methods utilized in this thesis to measure ferroelectric P-E loops and remove the leakage current contribution.[126] The first one is dynamic leakage current compensation (DLCC) model. In Figure 3.3.1b, the DLCC process includes two dynamic hysteresis measurement (DHM) with two different frequencies, f and f/2. The current responses are tested from the dark blue pulses. In DLCC, the leakage current is assumed to be independent of frequency and the displacement current is linearly dependent on the frequency. Then, the leakage contribution can be subtracted by fitting the current measured at the two indicated frequencies and subtracting the constant part. The second one is positive up negative down (PUND). After the write pulse, the first opposite positive pulse includes ferroelectric switching and the leakage current contribution. But the second pulse only includes the non-switching response, and then substrate the current from the pulse P by U, the ferroelectric response can be extracted.

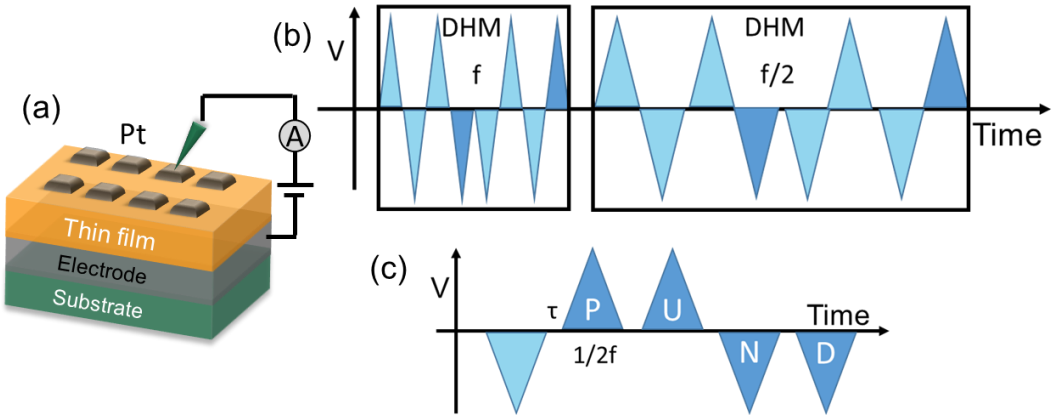

Figure 3.3.1 *(a) Top-bottom configuration for the electric properties measurements. Voltage pulse train for the (b) DLCC and (c) PUND measurement. f is the applied pulse frequency and τ is the setting delay time between the pulses.*

3.3.2 Leakage current

The leakage current is the flowing current through the capacitor under external electric field and it is an important parameter to determine device reliability. To measure the leakage current, a step shaped voltage waveform is applied to the capacitor and each step with a duration of 2s. The leakage current is read from the 70%-90% of the step time to avoid the influence from other effects, such as capacitor charging and ferroelectric switching.

3.3.3 Dielectric permittivity

The dielectric permittivity accounts for the ability of the material to be polarized under electric field. In the present work, the value of the dielectric permittivity has been used to evaluate the presence of distinct phases in HfO_2 films can not be disclosed by structural characterization. An excitation voltage of 0.3V at 50 kHz with top-bottom configuration is used to extract it. The dielectric permittivity (ε_r) can be extracted from capacitance (C) value using the $C = \varepsilon_0\varepsilon_r A/t$ relation, where ε_0 is the vacuum dielectric constant, A is the electrode area, and t is the film thickness. ε_r-V loops have been measured by varying the applied voltage in a triangular way.

3.3.4 Endurance and retention characterization

Endurance is a critical feature for ferroelectric-based devices and it describes the ability of the material to preserve ferroelectricity under cycling. The measurement process is illustrated in Figure 3.3.2a. First, the pristine state is tested by DLCC with frequency of 1 kHz. Second, bipolar pulses with frequency of 100 kHz are applied to the capacitor. After certain cycling numbers, the process stops and the capacitor is measured by DLCC model to monitor the remanent polarization. The above mentioned processes will be repeated until the memory window is less than the detection threshold due to fatigue or hard breakdown happens to the capacitor. In the context of the present thesis, fatigue refers to the reduction of switchable polarization down to the detection limit and device breakdown by the sudden increase of the device conductivity.

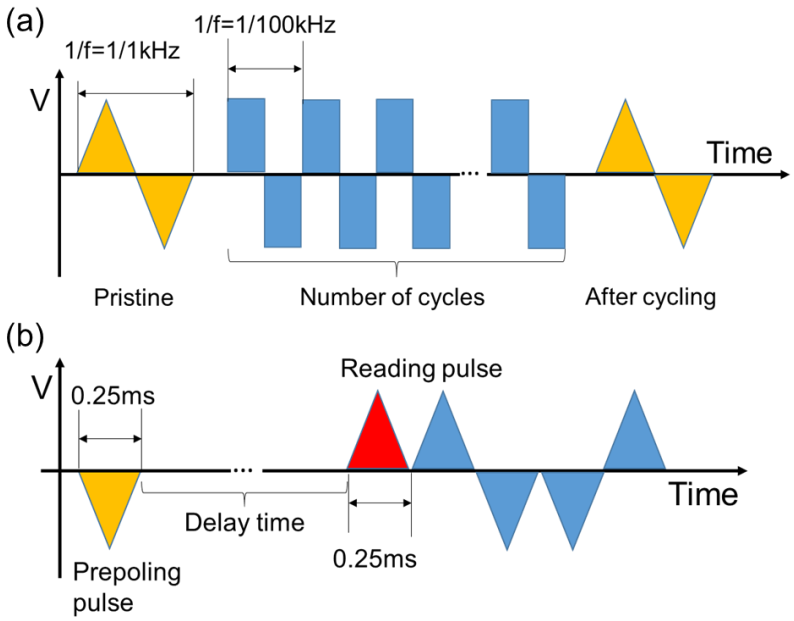

Figure 3.3.2 *Voltage pulses used for (a) endurance and (b) retention measurements.*

Retention measurement is performed to describe the decay of polarization with time. A memory device with short retention will suffer failure because the polarization drops to the minimum value that can not be detected. The measurement pulses used in this thesis are shown in Figure 3.3.2b. First, a prepoling pulse with duration of 0.25ms is applied to the capacitor, and then leave the capacitor after the setting retention time or delay time. After that defined periods, the polarization is measured by the first red pulse. The following four pulses determine the absolute polarization value. The variation can be extracted which stands for the polarization loss of the prepoling state. The retention behaviour after different delay times can be tested by repeating the procedure.

3.3.5 Switching dynamics and neuromorphic behavior characterization

Switching dynamics. The pulse train used for switching dynamics is shown in Figure 3.3.3a. Firstly, a pre-switching pulse is applied. This is long enough and its amplitude is well above coercive field to ensure polarization saturation. After, a 1st reading pulse is applied and the current is measured. The measured current only contains the non-switchable contributions as the previous pre-switching pulse has already switched the polarization. Afterwards, a switching pulse is applied. During the application of this pulse, the current is not measured to reduce the time constant of the experimental set-up. The switching pulse duration τ_w and write voltage (V_w) are varying among the experiments. Finally, during a 2nd reading pulse the current is measured which contains the switchable

and non-switchable contributions. From the subtraction of the measured current during 1st reading pulse to the 2nd reading pulse, we obtain the switched polarization by the switching pulse polarization (ΔP). Besides, the direct measurement of the switching current was performed by the application of the pulse train shown in Figure 3.3.3b using negative V_w. After prepoling, the pulse 1 results in ferroelectric switching current plus other contributions, and during the pulse 2 current only resulting from the other contributions is measured. Ferroelectric switching current is obtained from the subtraction of the current measured during pulse 2 to pulse 1. From the integration of the current through time, polarization is obtained. This latter method is more direct than the former one but with the disadvantage of having a larger set-up time constant due to current is being measured.

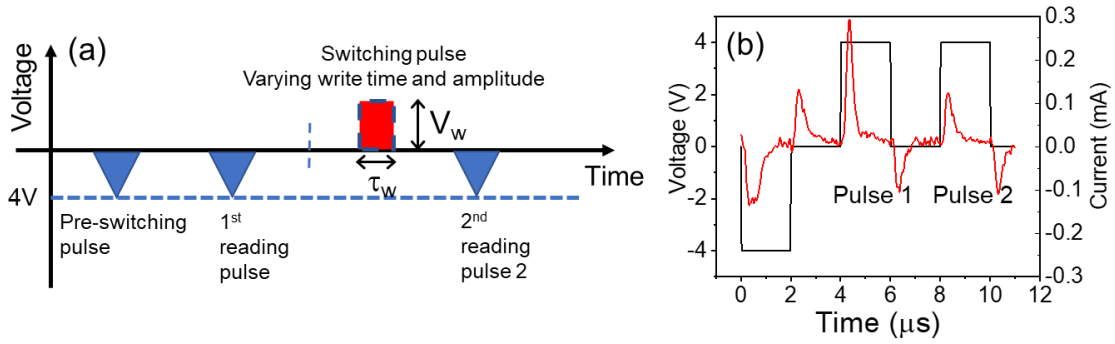

Figure 3.3.3 *(a) Sketch of the pulse train used to characterize the switching dynamics. (b) Direct measurement of the switching current, including the applied voltage and the measured current.*

Potentiation and depression. Ferroelectric-based devices with memristive characteristics allow mimicking the brain synapse for neuromorphic application.[26,127] A principle behaviour is the potentiation and depression ability after short electric stimulation. Potentiation is related to the increase of conductance, and depression corresponds to the decrease of conductance. In this thesis, potentiation and depression characteristics of the polarization state[128] of HfO_2-base thin film are investigated using the pulse scheme indicated in Figure 3.3.4a. The applied pulses are 3V and -4V for potentiation and depression, respectively, with pulse duration of 50 ns. The method to check the change of polarization (ΔP) is similar to the pulse train used to characterize the switching dynamics (Figure 3.3.3a). For example, to measure the potentiation effect, first, a negative pulse has to be applied to ensure polarization saturation, and then apply reading pulse 1. Second, modulate the capacitor by potentiation pulses. After that, another reading pulse 2 is applied. The difference between the two reading pulses is the change of the

polarization after potentiation stimulation. It has to be noted that the process to read the ΔP will change the polar state of the capacitor, which is different with the reading of resistance change.

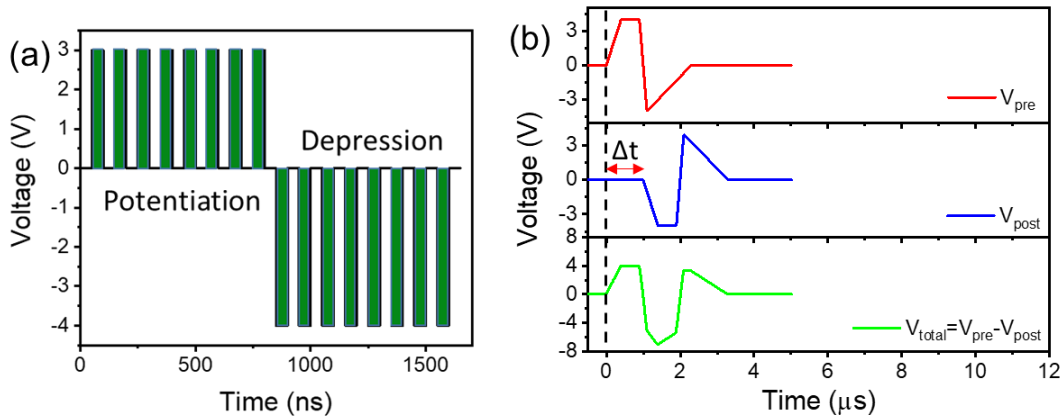

Figure 3.3.4 *(a) Sketch of the pulse train for potentiation and depression. (b) The pulses (V_{total}) for the Spike-Timing-Dependent Plasticity applied on the top electrode by overlapping the pre and post-neurons. The Δt is 1 μs.*

Spike-Timing-Dependent Plasticity. Biological synapses connect different neurons and their conductivity can be modulated through their plasticity, which is associated with their learning and adaptation abilities. Spike-Timing-Dependent Plasticity (STDP) is the model that correlates the modulation of the synapse conductance (state) with the time difference between the firing of the pre- and post-neurons ($\Delta t=t_{pre}-t_{post}$).[129] Based on this concept, generally, the transmission of the spikes should be independently on two electrodes of our capacitor, with pre-neuron on Pt electrode and post-neuron on bottom LSMO electrode. And it is necessary to control the pulses applied to the thin film with exact time difference Δt. To simplify the operation process in our set-up, an overlapped pulse from the pre- and post-neurons is directly applied to the top Pt electrode, and keeping the bottom electrode grounded.[130] As shown in Figure 3.3.4b, the post-synaptic pulse is a reversed shape compared to the pre-synaptic pulse because it is applied to the top electrode. By overlapping the V_{pre} and V_{post}, the V_{total} waveform is the final pulse applied to the top electrode with a certain time difference which determines the shape of the final spikes. The method to evaluate the spikes induced polarization change is the same as the pulse train used to characterize the switching dynamics (Figure 3.3.3a), replacing the switching pulse by the overlapped spike pulses.

Chapter 4. Tailored epitaxy of $Hf_{0.5}Zr_{0.5}O_2$

Exploration in the preparation, structure characterization and ferroelectricity of hafnium based film is enormous in polycrystalline films, while the progress in epitaxial films is limited. In order to tailor the epitaxy of hafnium film, we have applied three strategies. First, $Hf_{0.5}Zr_{0.5}O_2$ films have been grown under lower oxidizing condition with inert Ar gas to decrease the PLD plasma energy when reducing the oxygen pressure in the deposition process. Optimized mixing Ar and O_2 atmosphere allows increase of polarization around 50% respect films grown by conventional pulsed laser deposition. Second, we have investigated the effect of seed layer. Ultrathin HZO seed layer was grown on the bottom electrode to crystalize HZO film at lower deposition temperature. Third, we have found that orthorhombic phase can also be epitaxially stabilized on LSMO/STO(110) and LSMO/STO(111). The most relevant is the different orientations, and a high remanent polarization as high as 33 $\mu C/cm^2$ with high endurance and good retention can be achieved on LSMO/STO(110).

4.1 Growth under low oxidizing conditions

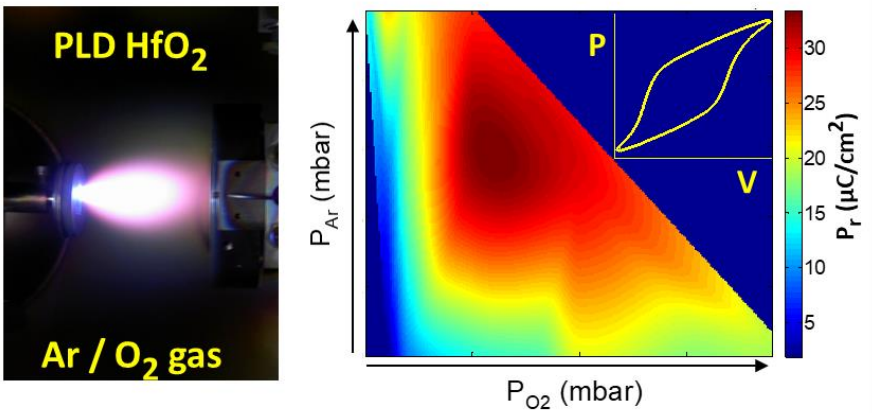

Abstract

The ferroelectric phase of HfO_2 is generally stabilized in polycrystalline films, which typically exhibit the highest polarization when deposited using low oxidizing conditions. In contrast, epitaxial film grown by pulsed laser deposition show low or suppressed polarization if low oxygen pressure is used. This degradation could be caused by the high energy of the PLD plasma when it expands towards the substrate under low pressure. We have carried out a systematic study of the epitaxial growth of $Hf_{0.5}Zr_{0.5}O_2$ combining inert Ar gas with oxidizing O_2 gas. This allows us controlling the oxidizing conditions (through O_2 partial pressure) and the energy of the pulsed laser deposition plasma (through the total pressure of O_2 and Ar). A pressure of Ar high enough to significantly reduce plasma energy and low enough O_2 to reduce oxidation conditions is found to allow a large increase in ferroelectric polarization up to about 30 $\mu C/cm^2$, representing an increase of around 50% respect films grown by conventional pulsed laser deposition. This simple growth process, with high impact in the development of ferroelectric HfO_2, can be also beneficial in the growth of thin films of other materials by pulsed laser deposition.

Introduction

It is essential to optimize the deposition conditions for stabilization of ferroelectric orthorhombic phase in doped HfO_2 films. Oxidizing condition is one of the key factors to stabilize the ferroelectric phase. It has been investigated that, when applying lower oxygen pressure condition to grow polycrystalline films, an increase of ferroelectric polarization happens in both chemical (atomic layer deposition) and physical (radio frequency magnetron sputtering) deposition techniques because of the higher concentration of oxygen vacancies.[131,132] However, in epitaxial HZO films deposited by pulsed laser deposition, a lower oxidizing atmosphere suppresses the formation of orthorhombic phase,[65] which could be caused by the high-energy plasma that is formed under low background pressure in the PLD chamber.[133,134] The high-energy plasma can reduce the crystallization[134,135] and even cause self-sputtering in the film.[133,136,137] On the other hand, if the pressure is high enough to thermalize the PLD plasma, the crystallinity of the films also degrades.[134] A method to reduce the plasma energy when using low oxygen pressure is introducing inert gas.[138] In this work, we combined O_2 and Ar as ambient gas to grow HZO films by PLD under low oxidation conditions and reduced plasma energy. This allows extending the growth window of epitaxial orthorhombic HZO to lower oxygen pressure. These films have higher amount of orthorhombic phase and larger polarization.

4.1.1 Growth conditions

HZO films were grown on $SrTiO_3$(001) substrates buffered with a $La_{0.67}Sr_{0.33}MnO_3$ electrode of thickness ~25 nm. HZO films were deposited at 800 °C under Ar/O_2 atmosphere. As indicated in Figure 4.1.1, three series of films were grown by varying the Ar pressure (P_{Ar}) with fixed O_2 pressure (P_{O2}) of 0.01 mbar, 0.05 mbar and 0.1 mbar, and four series varying P_{O2} with fixed P_{Ar} of 0 mbar, 0.05 mbar, 0.1 mbar and 0.2 mbar. HZO films were deposited with 800 laser pulses, and immediately after growth, the samples were cooled under 0.2 mbar of oxygen.

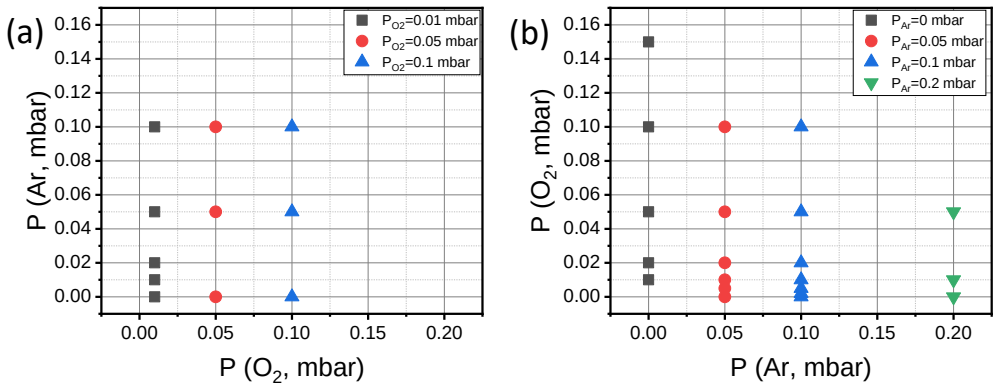

Figure 4.1.1 *In (a) the three series of films deposited at fixed P_{O2} are plotted using black squares (P_{O2} = 0.01 mbar), red circles (P_{O2} = 0.05 mbar), and blue up triangles (P_{O2} = 0.1 mbar). In (b) the four series of films deposited at fixed P_{Ar} are plotted using black squares (P_{Ar} = 0 mbar), red circles (P_{Ar} = 0.05 mbar), blue up triangles (P_{Ar} = 0.1 mbar), and green down triangles (P_{Ar} = 0.2 mbar).*

XRD θ-2θ symmetric scans shows the reflections corresponding to the P_{O2} = 0.05 mbar, P_{Ar} = 0.05 mbar sample in Figure 4.1.2a. The peaks at 2θ around 23° and 47° correspond to (001) and (002) reflections of STO substrate overlapped to LSMO electrode reflection. The peak at 2θ around 30°, accompanied with Laue reflections, is the position of o(111) reflection. Pole figures confirm the epitaxial ordering of the orthorhombic phase (Figure 4.1.2b-c). There are twelve poles from o-HZO(-111) reflection around 71° tilt angle, signaling the presence of four families of crystal variants, as reported for equivalent films grown under pure O_2 atmosphere.[28,65]

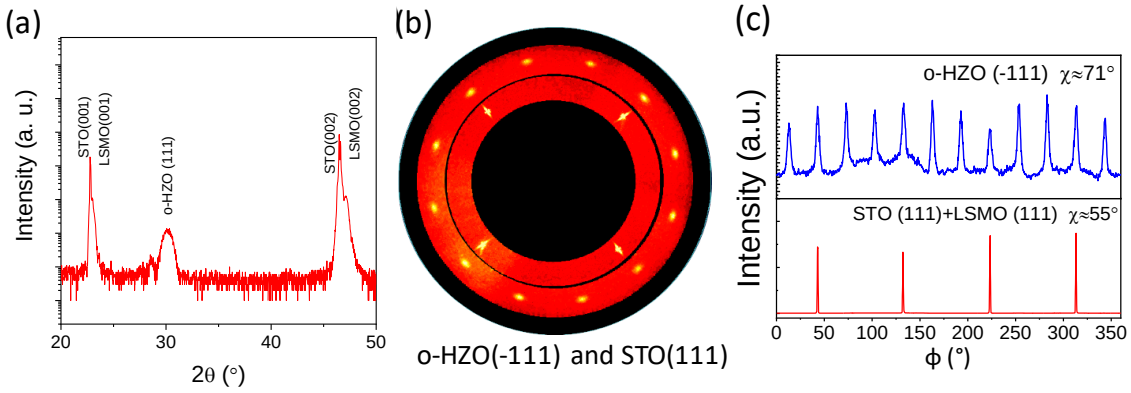

Figure 4.1.2 *(a) XRD θ-2θ scans around the o-HZO(111) reflection of film deposited under P_{O2} = 0.05 mbar and P_{Ar} = 0.05 mbar. (b) XRD pole figures of the same sample, around o-HZO(-111) and STO(111) reflections. (c) Corresponding ϕ-scans around o-HZO(-111) and STO(111).*

Longer acquisition time has been applied to do XRD θ-2θ scans around the o-HZO(111) reflection to obtain clear Laue oscillation. Film thickness is estimated by Laue oscillation simulation according to the following equation.[28]

$$I(Q) = \left(\frac{\sin\left(\frac{QNc}{2}\right)}{\sin\left(\frac{Qc}{2}\right)} \right)^2$$

where Q = 4πsin(θ)/λ is the reciprocal space vector, N the number of unit cells along the out-of-plane direction and c the corresponding lattice parameter. Figure 4.1.3a shows the scans corresponding to films deposited under P_{O2} = 0.05 mbar and P_{Ar} = 0 mbar (left) and P_{Ar} = 0.2 mbar (right). Laue fringes are less evident in the film deposited with very high pressure (P_{O2} = 0.05 mbar and P_{Ar} = 0.2 mbar), and the o-HZO(111) peak is broaden, signaling that the film is thinner, which is a consequence of the scattering of Hf and Zr atoms by the higher pressure. Films deposited under fixed P_{O2} = 0.05 mbar present varying monotonic decrease of thickness with increasing Ar pressure, and similar dependence is observed in the other series. In summary, the thickness and growth rate are decreasing with increasing of the pressure in the PLD chamber, as shown in Figure 4.1.3b.

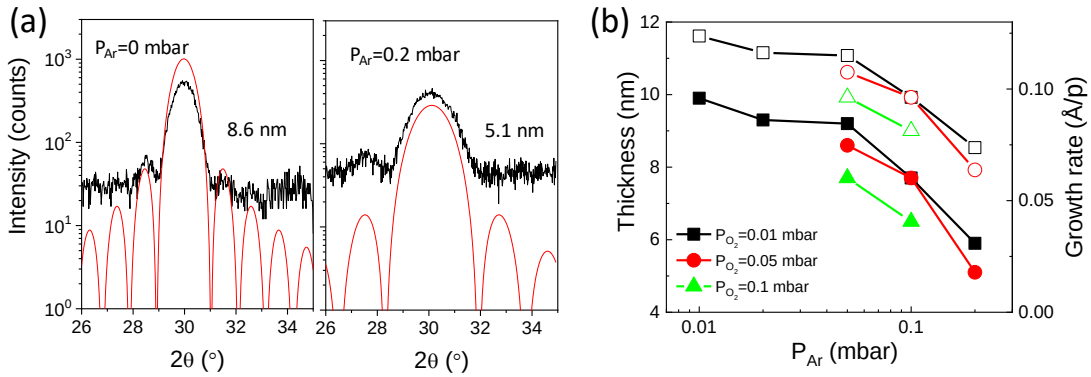

Figure 4.1.3 *(a) XRD θ-2θ scans around the o-HZO(111) reflection of films deposited under P_{O2} = 0.05 mbar and the P_{Ar} pressure indicated in each panel.(b) Thickness (solid symbols, left axis) and growth rate (empty symbols, right axis) as a function of P_{Ar} for fixed P_{O2} = 0.01 mbar (squares), P_{O2} = 0.05 mbar (circles) and P_{O2} = 0.1 mbar (triangles). Thickness of the films was estimated by simulation of Laue oscillations.*

4.1.2 Structural characterization

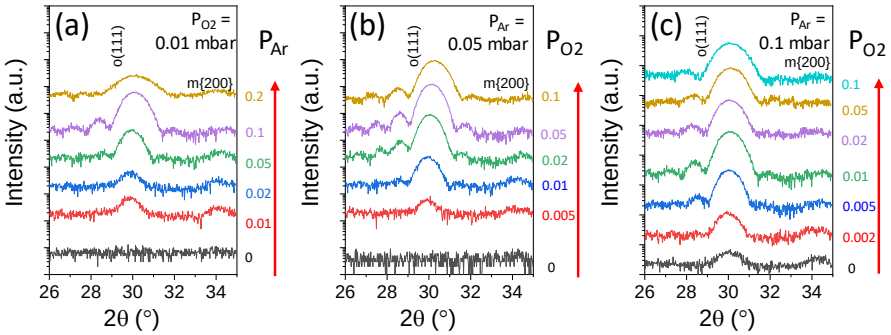

Figure. 4.1.4 *XRD θ-2θ scans of films deposited under mixed Ar/O_2 ambient. (a) Fixed P_{O2} = 0.01 mbar and varied P_{Ar}. (b) Fixed P_{Ar} = 0.05 mbar and varied P_{O2}. (c) Fixed P_{Ar} = 0.1 mbar and varied P_{O2}.*

Figure 4.1.4a shows XRD θ-2θ scans, measured around the o-HZO(111) reflection, of films deposited under fixed P_{O2} = 0.01 mbar and varied P_{Ar}. The film deposited without Ar, i.e. under pure P_{O2} = 0 mbar (black line), is not crystallized, in agreement with the reported growth window for conventional PLD.[65] In contrast, the films deposited under mixed Ar/O_2 ambient exhibit a diffraction peak at the position of the o-HZO(111) reflection (2θ ~ 30°) and a less intense peak at 2θ ~ 34° that can correspond to a {200} reflection of the monoclinic (m) phase. The intensity of the o-HZO(111) peak is low in the P_{Ar} = 0.01 mbar and 0.02 mbar samples (red and blue lines, respectively), and high in the P_{Ar} = 0.05 mbar and 0.1 mbar samples (green and purple lines, respectively). Laue oscillations around the o-HZO(111) peak are evident in the P_{Ar} = 0.1 mbar film. Higher Ar pressure (0.2 mbar, gold line) results in a less intense and broader o-HZO(111) peak. The width of the peak signals that the film is thinner, which is a consequence of the scattering of Hf and Zr atoms by the higher pressure (the dependence of the growth rate with the P_{Ar} is shown in Figure 4.1.3). In summary, Figure 4.1.4a shows that P_{Ar} = 0.05 - 0.1 mbar is optimal to stabilize the orthorhombic phase with very low P_{O2} of 0.01 mbar. Next, we show in Figure 4.1.4b and Figure 4.1.4c the effect of P_{O2} when P_{Ar} is fixed to 0.05 mbar and 0.1 mbar, respectively. In the P_{Ar} = 0.05 mbar series (Figure 4.1.4b), the oxygen pressure threshold for crystallization is around $P_{O2} = 5\times10^{-3}$ mbar (red line). The film grown under this P_{O2} partial pressure shows low intensity o-(111) and m-{200} peaks. The intensity of the o-(111) peak increases notably in films deposited under higher P_{O2}, and Laue oscillations are evident in the P_{O2} = 0.02 and 0.05 mbar films. The P_{O2} = 0.1 mbar film (gold line), which is thinner due to the reduced growth rate caused by plasma

scattering, also shows evident Laue fringes. In the P_{Ar} = 0.1 mbar series (Figure 4.1.4c), there is crystallization even in the film deposited without oxygen partial pressure. The XRD scan of the P_{O2} = 0 mbar film (black line) presents o-(111) and m-{200} diffraction peaks. The intensity of the o-(111) peak increases significantly in the film grown under $P_{O2} = 2\times10^{-3}$ mbar (red line), and it is very intense and accompanied of Laue fringes in the $P_{O2} = 5\times10^{-3}$ mbar (blue line) and 0.01 mbar (green line) films. The films deposited under higher P_{O2} are also orthorhombic, and a significant thickness decrease is observed in the P_{O2} = 0.1 mbar film (turquoise line).

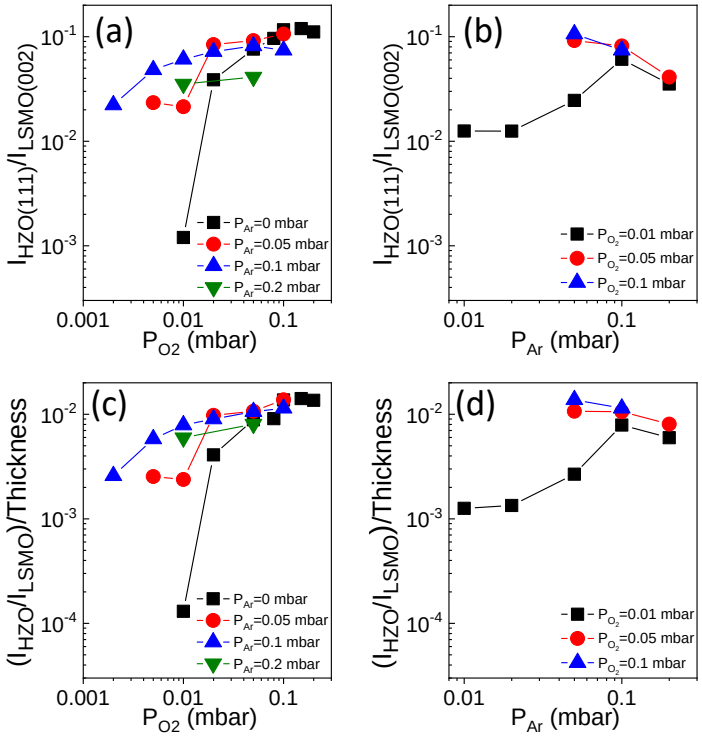

Figure 4.1.5 *Intensity of the o-(111) reflection, normalized to that of the LSMO(002) peak, $I_{HZO(111)}/I_{LSMO(002)}$, as a function of P_{O2} (a) and P_{Ar} (b). In (a) P_{Ar} is: 0 mbar (black squares), 0.05 mbar (red circles), 0.1 mbar (blue up triangles), and 0.2 mbar (green down triangles). In (b) P_{O2} is: 0.01 mbar (black squares), 0.05 mbar (red circles), and 0.1 mbar (blue up triangles). In (c) and (d), the normalized intensity of $I_{HZO(111)}/I_{LSMO(002)}$,is normalized to the film thickness.*

The intensity of the o-(111) reflection allows to quantify the dependence of the amount of orthorhombic phase on the O_2 and Ar partial pressure (Figure 4.1.5). $I_{HZO(111)}/I_{LSMO(002)}$ increases with P_{O2} (Figure 4.1.5a), with little additional effect of the Ar pressure when P_{O2} is high. The crystallization is very low in films grown under a pressure of pure oxygen lower than 0.05 mbar, but in presence of additional Ar the stabilization of the orthorhombic phase is greatly enhanced. The dependence of $I_{HZO(111)}/I_{LSMO(002)}$ on P_{Ar}

(Figure 4.1.5b) evidences that under high P_{Ar} pressure (0.1 or 0.2 mbar), the amount of orthorhombic phase only depends slightly on P_{O2}. In brief, the Ar presence notably enhances the stabilization of the o-phase for low P_{O2} (up to about 0.05 mbar) and does not produce a great effect for higher P_{O2}. The amount of orthorhombic phase is slightly underestimated in the films deposited under higher pressure due to their lower thickness, but the equivalent graphs normalized to the film thickness exhibit the same relation (Figure 4.1.5c-d).

The out-of-plane lattice parameter associated with the HZO(111) reflection, $d_{HZO(111)}$, was determined from the XRD peak position. The dependences of $d_{HZO(111)}$ on P_{O2} and P_{Ar} are shown in Figure 4.1.6a and Figure 4.1.6b, respectively. The $d_{HZO(111)}$ value expands by decreasing P_{O2} (Figure 4.1.6a). On the other hand, $d_{HZO(111)}$ of films deposited at P_{O2} below around 0.05 mbar depends on P_{Ar}, with $d_{HZO(111)}$ less expanded for higher Ar pressure. The effect of P_{Ar} is directly visualized in Figure 4.1.6b. The lattice parameter of the films deposited under P_{O2} = 0.01 mbar (black squares) decrease with increasing P_{Ar} up to P_{Ar} = 0.1 mbar. The plasma is thermalized for higher P_{Ar} and $d_{HZO(111)}$ does not change with P_{Ar} or P_{O2}. To rationalize the intriguing dependence of $d_{HZO(111)}$ on P_{Ar} and P_{O2} shown in Figure 4.1.6, two causes of cell expansion have to be considered. On one hand, when P_{O2} is lower, a higher number of oxygen vacancies is expected to form in the film. On the other hand, other point defects can be formed if the PLD plasma has high energy, which happens when the total pressure, $P_{Ar} + P_{O2}$, is low. Indeed, deposition under high-energy PLD plasma (low P_{Ar} and low P_{O2}) reduces strongly the film crystallization (Figure 4.1.4 and Figure 4.1.5). Thus, high oxygen pressure is required to avoid film degradation if P_{Ar} is low. This implies that low oxidation conditions cannot be used to grow HfO_2 films when HfO_2 films are grown using pure O_2 atmosphere. Thus, conventional PLD does not permit growth conditions closer to those that result in largest ferroelectric polarization when ALD or sputtering is used (low oxidizing conditions).[139] However, as demonstrated here, the use of inert Ar gas to reduce the PLD plasma energy allows the stabilization of the orthorhombic phase with P_{O2} around one order of magnitude lower (0.01 mbar) than the optimal pressure (0.1 mbar) in conventional PLD (Figure 4.1.5) and importantly reduce the number of defects (signaled by the d(111) expansion, Figure 4.1.6).

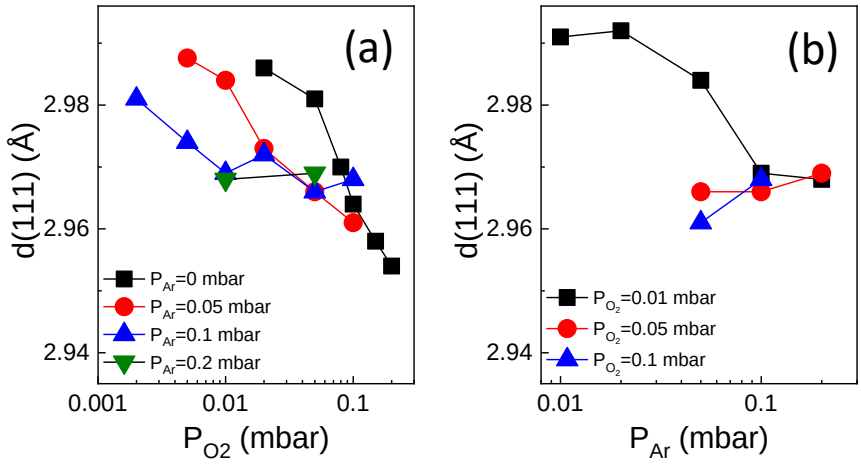

Figure 4.1.6 *Out-of-plane lattice parameter, $d_{HZO(111)}$, as a function of P_{O2} (a) and P_{Ar} (b). In (a) P_{Ar} is: 0 mbar, 0.05 mbar (red circles), 0.1 mbar (blue up triangles), and 0.2 mbar (green down triangles). In (b) P_{O2} is: 0.01 mbar (black squares), 0.05 mbar (red circles), and 0.1 mbar (blue up triangles).*

4.1.3 Electrical characterization

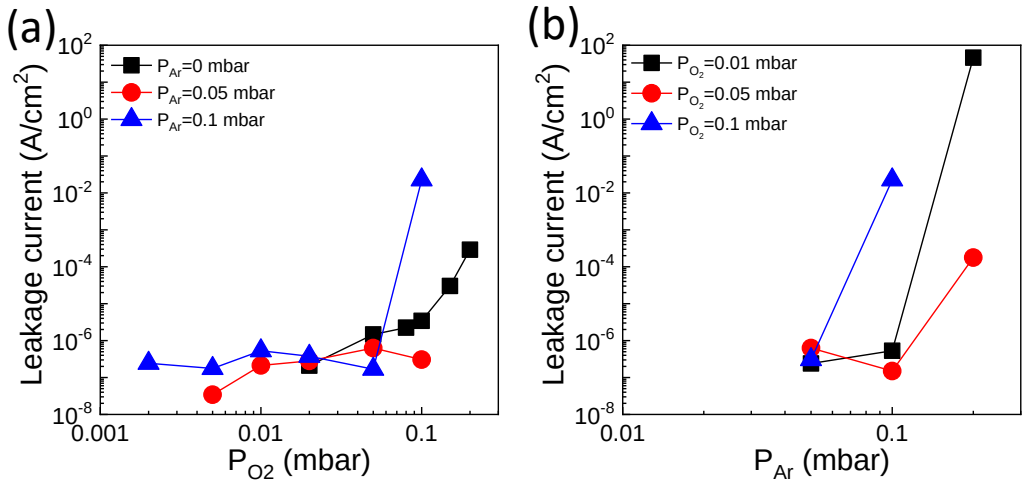

Figure 4.1.7 *(a) Leakage current at 1 V as a function of P_{O2} for P_{Ar} = 0 mbar (black squares, data reported in ref. [65]), P_{Ar} = 0.05 mbar (red circles) and P_{Ar} = 0.1 mbar (blue triangles). In (b) Leakage current at 1 V as a function of P_{Ar} for P_{O2} = 0.01 mbar (black squares), 0.05 mbar (red circles), and 0.1 mbar (blue up triangles).*

Figure 4.1.7a shows the dependence of the leakage current at 1 V on P_{O2}, for fixed P_{Ar} = 0 mbar (black squares), P_{Ar} = 0.05 mbar (red circles) and P_{Ar} = 0.1 mbar (blue triangles). The leakage of the films deposited without Ar gas (P_{Ar} = 0 mbar) increases with P_{O2}, from around 2×10^{-7} A/cm^2 (P_{O2} = 0.01 mbar) to 3×10^{-4} A/cm^2 (P_{O2} = 0.2 mbar).[65] The films

deposited under mixed O_2/Ar atmosphere and very low P_{O2} in the 2×10^{-3} - 0.01 mbar range are very insulating too, with leakage current about 2×10^{-7} A/cm^2. In contrast, the film grown under high total pressure (P_{Ar} = 0.1 mbar and P_{O2} = 0.1 mbar) is much more conducting. The effect of the total pressure is evident in Fig. 4b, which shows the leakage current at 1V as a function of P_{Ar} for fixed P_{O2} = 0.01 mbar (black squares), P_{O2} = 0.05 mbar (red circles) and P_{O2} = 0.1 mbar (blue triangles). The leakage current of the three P_{Ar} = 0.05 mbar samples is about 3×10^{-7} A/cm^2, without significant effect of P_{O2}. However, in the case of the samples grown under higher P_{Ar}, the leakage is very high when the total pressure (P_{Ar} + P_{O2}) is about 0.2 mbar. Overall, Figure 4.1.7 indicates that a PLD plasma thermalized by high ambient pressure causes strong increase in the film conductivity, whereas oxygen vacancies are not the main cause of leakage.

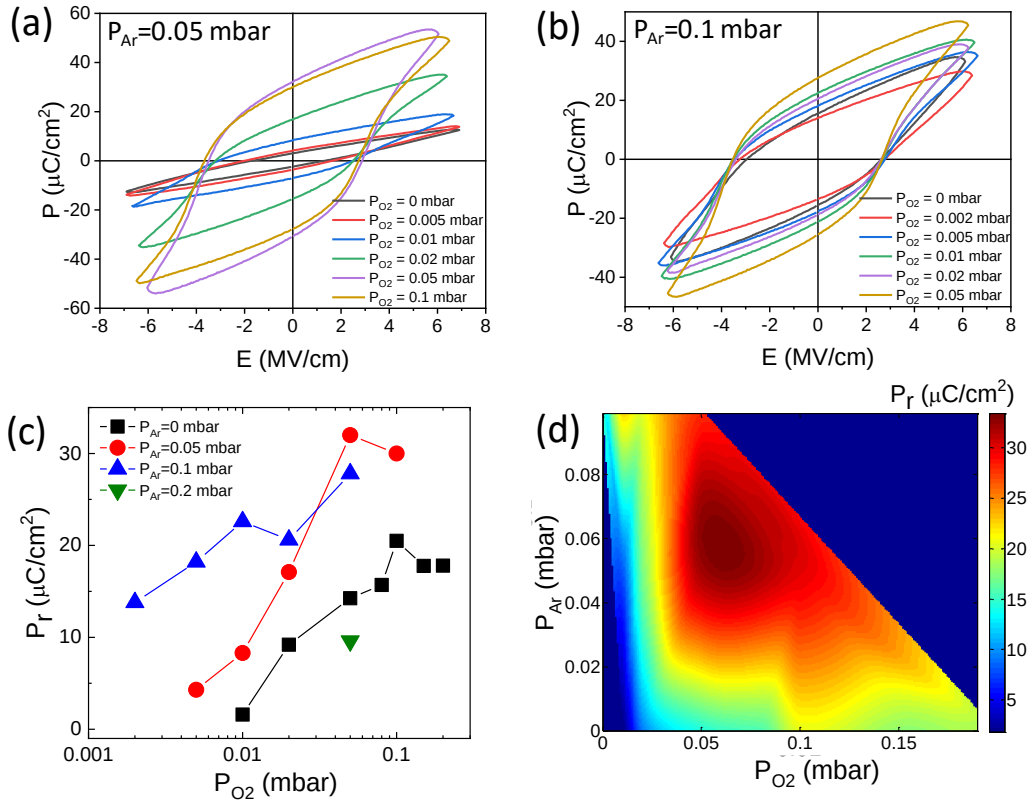

Figure 4.1.8 *Ferroelectric polarization loops of the films grown (a) under fixed P_{Ar} = 0.05 mbar and varied P_{O2} and (b) under fixed P_{Ar} = 0.1 mbar and varied P_{O2}. (c) Remanent polarization as a function of P_{O2}, for fixed P_{Ar} = 0 mbar (black squares), P_{Ar} = 0.05 mbar (red circles), P_{Ar} = 0.1 mbar (blue up triangles), and 0.2 mbar (green down triangle). (d) Color map of P_r as a function of P_{Ar} and P_{O2}. The color map has been constructed after interpolating the data of panel (c) along the P_{Ar} and P_{O2} axis using cubic splines.*

The ferroelectric polarization loops of the films grown under fixed P_{Ar} = 0.05 mbar and varied P_{O2} are shown in Figure 4.1.8a. The P_{O2} = 0.01 mbar and 0.02 mbar films have low remanant polarization of 8.3 and 17.1 μC/cm^2, respectively. A slightly higher P_{O2}, 0.05 mbar, results in a high increase of polarization, with P_r = 32 μC/cm^2. Further increase of P_{O2} does not influence greatly the polarization loops, and P_r of the P_{O2} = 0.1 mbar film is slightly lower, 30 μC/cm^2. The loops of the series of films grown under fixed P_{Ar} = 0.1 mbar are shown in Figure 4.1.8b. In agreement with the presence of the XRD o-HZO(111) reflection in the P_{O2} = 2×10^{-3} and P_{O2} = 5×10^{-3} mbar, these films exhibit hysteretic polarization loops, with P_r = 13.8 and 18.2 μC/cm^2, respectively. P_r of films grown with higher P_{O2}, being 27.8 μC/cm^2 in the P_{O2} = 0.05 mbar film. The high leakage of the P_{O2} =0.1 mbar film did not allow the measurement of a loop. The dependence of P_r on P_{O2} is summarized in Fig. 4.1.8c, for the fixed P_{Ar} = 0 mbar (black squares), P_{Ar} = 0.05 mbar (red circles), P_{Ar} = 0.1 mbar (blue up triangles) and P_{Ar} = 0.2 mbar (green down triangle). As described above, P_r in the P_{Ar} = 0.05 mbar and P_{Ar} = 0.1 mbar increases with P_{O2}. The same P_{O2} dependence is observed in films grown using conventional PLD (P_{Ar} = 0 mbar).[65] Figure 4.1.8c evidences a huge increase in P_r in the films deposited under mixed Ar/O_2 atmospheres. The highest P_r in the P_{Ar} = 0 mbar series is 20.5 μC/cm^2 (P_{O2} = 0.1 mbar film), while it is 32 μC/cm^2 and 27.8 μC/cm^2 in the P_{Ar} = 0.05 mbar and P_{Ar} = 0.1 mbar series, in both cases in films grown under P_{O2} = 0.05 mbar. Deposition under higher P_{Ar}, 0.2 mbar, results in P_r reduction. A second benefit of using mixed Ar/O_2 atmosphere is that films grown under very low P_{O2} (5×10^{-3} mbar in the P_{Ar} = 0.1 mbar series) show high ferroelectric polarization and, as shown in Fig. 4.1.7, low leakage, while P_{O2} above 0.02 mbar is needed in conventional PLD. The color map of P_r as a function of P_{Ar} and P_{O2} (Figure 4.1.8d) evidences graphically that the optimal conditions to maximize P_r are P_{Ar} = 0.05 - 0.1 mbar and P_{O2} around 0.05 mbar. It has to be noted that the measured polarization corresponds to a projection of the ferroelectric dipoles, since the films are (111)-oriented. The highest measured P_r = 32 μC/cm^2 corresponds to a polarization of about 55 μC/cm^2, matching well with the value of spontaneous polarization calculated for ferroelectric HfO_2.[140,141]

Conclusions

In summary, in pulsed laser deposition of ferroelectric HfO_2 films, a mixed atmosphere of Ar and O_2 during growth is critical. Appropriate values of Ar and O_2 pressures allow independent control of plasma energy and oxidation conditions during growth. In our

study, epitaxial $Hf_{0.5}Zr_{0.5}O_2$(111) films deposited under mixed Ar/O_2 ambient show low leakage current and have remanent polarization of about 30 μC/cm^2, which represents a 50% increase with respect to equivalent films grown by conventional pulsed laser deposition. Therefore, the simple addition of Ar gas during the growth of the film allows a large increase in ferroelectric polarization, the films probably having the intrinsic polarization of the orthorhombic phase. The new growth process will facilitate the development of epitaxial ferroelectric HfO_2, and may be potentially useful in enhancing the properties of polycrystalline HfO_2 and other functional oxide and nitride thin films grown by pulsed laser deposition.

4.2 Growth at low temperature using seed layer

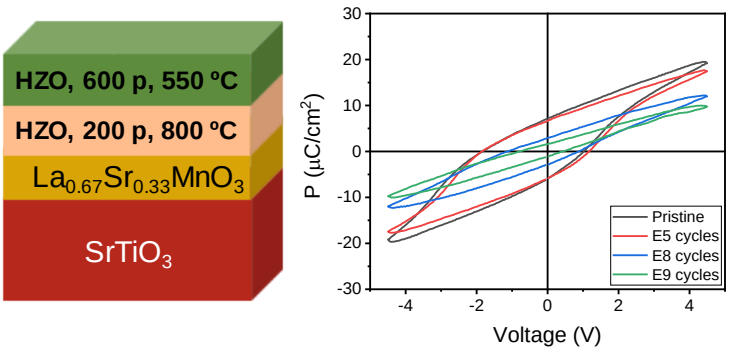

Abstract

In polycrystalline HZO films, the choosing of suitable seed layer can control the microstructure and enhancing ferroelectricity. Here, we investigated the effect of seed layer in epitaxial films. Ultrathin HZO seed layer was grown on the bottom electrode to crystalize HZO film at lower deposition temperature. With seed layer, ferroelectric o-phase can be stabilized as low as 550 °C, with ferroelectric polarization of 14 μC/cm^2. Compared with the samples without seed layer, P_r value depends only moderately on the deposition temperature in the 650-750 ℃ range, and P_r is improved more than 30% respect films grown at the sample temperature without the seed layer. Films grown on seed layer exhibit less fatigue and improved endurance.

Introduction

The optimized deposition temperature for obtaining high remanent polarization in epitaxial HZO films is around 800 °C.[65] However, to get better endurance and retention, a lower deposition temperature is preferred.[117] In polycrystalline HZO films, the choosing of suitable seed layer can control the crystalline quality and suppress the formation of non-polar phase, thus improving ferroelectricity.[142–144] Therefore, we investigated the effect of seed layer on epitaxial films when growth the HZO films under lower temperature. The results indicate that inserting ultrathin HZO seed layer on the LSMO bottom electrode, HZO film can be crystalized at lower deposition temperature, and less fatigue and improved endurance can be achieved.

4.2.1 Growth conditions

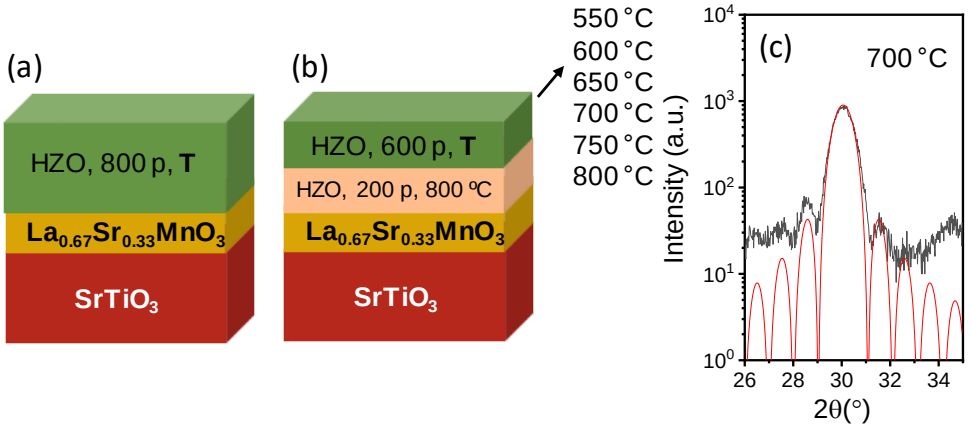

Figure 4.2.1 *(a) Sketch of the HZO films with 800 laser pulses deposited on LSMO under different temperature. (b) Sketch of the HZO films with 600 laser pulses deposited on seed layer (HZO film, 200 pulses, 800 °C) under different temperature. (c) XRD θ-2θ scans around the o-HZO(111) reflection of films with seed layer deposited under 700 °C. Red line is the simulation of Laue oscillations.*

The effect of the substrate temperature was investigated in the thesis of Dr. Jike Lyu.[65] Figure 4.2.1a sketches the samples, HZO films deposited with 800 laser pulses at substrate temperature T in the 650-825 °C range. In Figure 4.2.1b, the films with seed layer, HZO film with 200 laser pulses at 800 °C, are sketched. HZO films with 600 laser pulses are grown on the seed layer with deposition temperature changing from 550 °C to 800 °C. The total thickness of the HZO films, including the seed layer, confirmed by Laue simulation (Figure 4.2.1c) is around 8.9 nm.

4.2.2 Structural characterization

XRD θ-2θ scans of the samples with seed layer are shown in Figure 4.2.2. It can be seen that the reflections around 23° and 47° are related to (001) and (002) peaks of LSMO/STO, and the peaks at 2θ around 30° are corresponding to the position of orthorhombic (111) reflection in epitaxial HZO film. A zoomed region around o(111) reflections, with longer acquisition time, are indicated in the right panel. From bottom to top, the deposition temperature of the film on the seed layer increases from 550 to 800 °C with step of 50 °C. Low intensity peaks at 2θ around 28.5° and 34.5°, corresponding to m(-111) and m(002), respectively, can be observed in some samples. The m(-111) reflection is present in the samples deposited at 550 °C and 600 °C, and with deposition temperature increase, the peak disappears and Laue oscillations are more evident. Meanwhile, the position of the o(111) peak gradually shifts to higher 2θ angle.

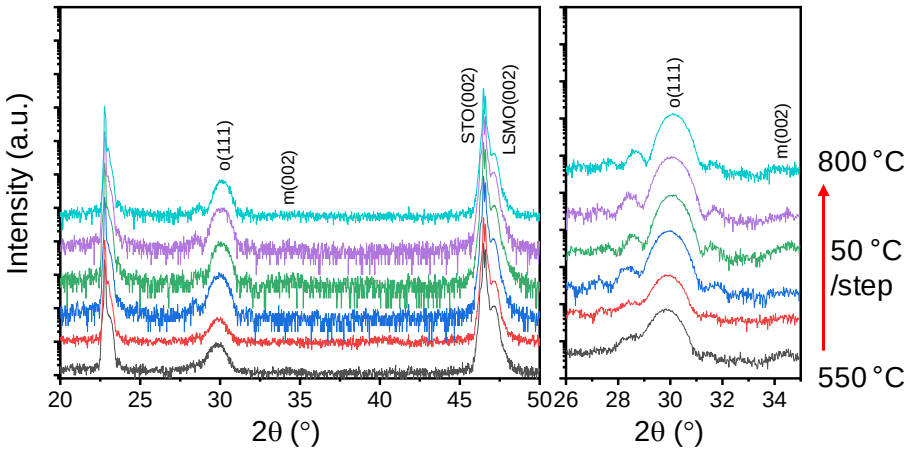

Figure. 4.2.2 *XRD θ-2θ scans of films deposited under different temperature on seed layers. The right panel shows zoomed scans around the HZO (111) reflection acquired with a longer time.*

The intensity of the o-(111) reflection allows to quantify the dependence of the amount of o-phase on the deposition temperature (Figure 4.2.3a). In the samples with seed layer (red triangles), $I_{HZO(111)}/I_{LSMO(002)}$ is nearly constant in the lower temperature range of 550 to 700 °C, but increases under higher deposition temperature (700-800 °C). Compared with the samples without seed layer,[65] the intensity of o-(111) reflection is significantly enhanced in the lower deposition temperature range, indicating the promotion of stabilizing o-phase using seed layer. While in the higher temperature range, the intensity is similar under both conditions. The out-of-plane (oop) lattice parameter of o-HZO(111), $d_{o\text{-}HZO(111)}$, is plotted in Figure 4.2.3b as a function of the deposition temperature. It can

be seen that no matter the samples with or without seed layer, the oop parameter decreases monotonously with temperature increase. It is also noted that the difference of the $d_{o\text{-}HZO(111)}$ value is small under both conditions.

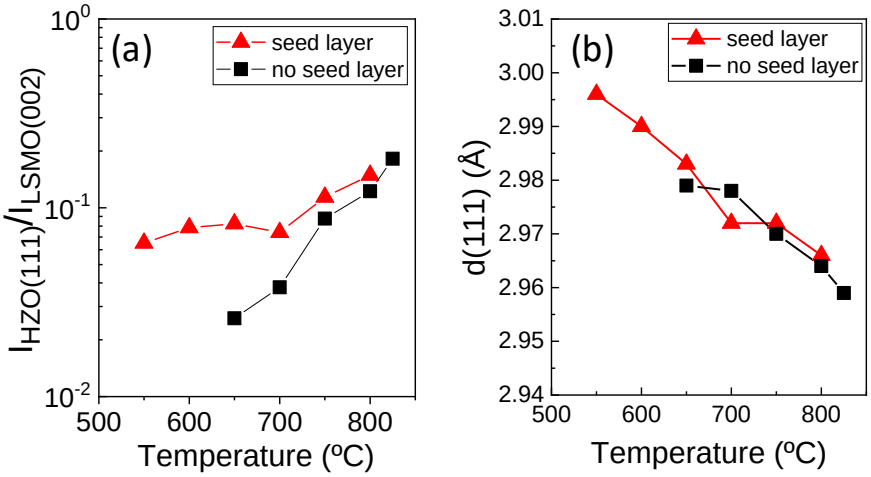

Figure 4.2.3 *(a) Intensity of the o-(111) reflection, normalized to that of the LSMO(002) peak, $I_{HZO(111)}/I_{LSMO(002)}$, as a function of deposition temperature. (b) Out-of-plane lattice parameter, $d_{HZO(111)}$, as a function of deposition temperature. In the figures, the red triangles are the films with seed layer, and the black squares are the films without seed layer.*

4.2.3 Electrical characterization

Ferroelectric hysteresis loops are evident in all of the samples prepared at different deposition temperature (Figure 4.2.4a). From the ferroelectric polarization loops, the P_r and V_c values are extracted and plotted as a function of temperature in Figures 4.2.4b-c, respectively. It can be seen that in the samples with seed layer P_r increases with deposition temperature from around 14 μC/cm^2 at 550 °C to 21 μC/cm^2 at 800 °C. Similar tendency can be observed in the sample without seed layer, although with reduced polarization for the same deposition temperature.[65] The P_r value is greatly improved in the films deposited at lower temperature range of 650-750 °C, when using seed layer. The improvement of P_r value is more than 30%. Moreover, the P_r of samples deposited at 550 °C and 600 °C with seed layer is comparable with that of the samples deposited at 650 °C without seed layer. In contrast, the variation of coercive field depending on the growth temperature is moderate in the samples with seed layer (Figure 4.2.4c). The coercive field is 2.22 V at 550 °C and slightly increases to 2.4 V at 750 °C, and reaches up to 2.7 V at 800 °C.

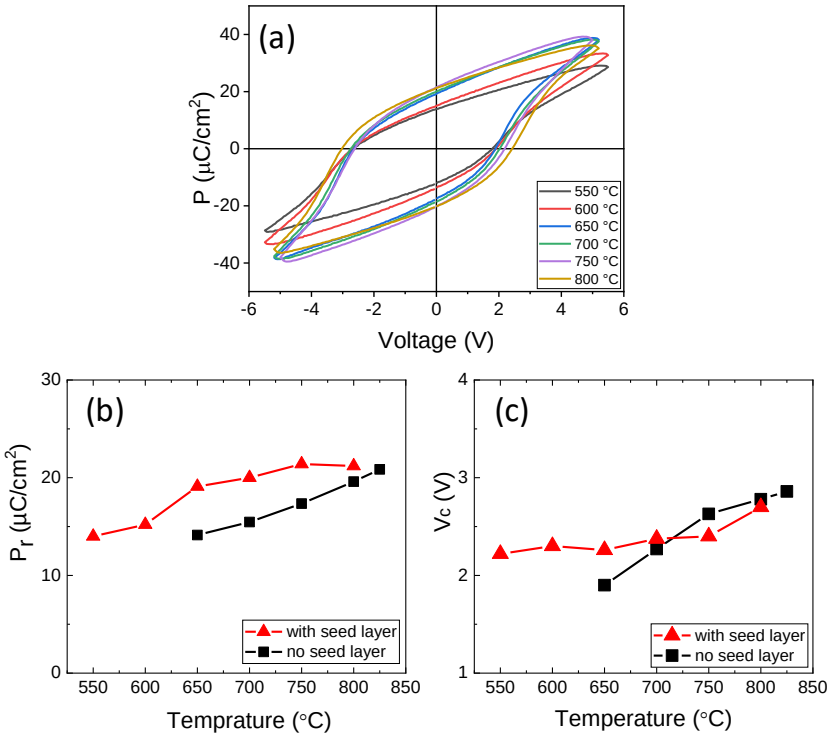

Figure 4.2.4 *(a) Ferroelectric polarization loops of the films deposited at different temperature on the seed layer. (b) Remanent polarization versus deposition temperature of films with and without seed layer. (c) Coercive field versus deposition temperature of films with and without seed layer. In the figures, the red triangles are the films with seed layer, and the black squares are the films without seed layer.*

Figure 4.2.5a shows representative polarization loops during the endurance measurement with poling voltage of 4.5 V of the film deposited at 550 °C. Memory window is $2P_r = 13.1$ μC/cm^2 in the pristine state, and remarkably, it is 12.5 μC/cm^2 after 10^5 cycles with nearly no degradation. Further cycling induces fatigue, and $2P_r$ reduces to 2.7 μC/cm^2 after 10^9 cycles. Fatigue is more evident in film deposited at 800 °C, in which $2P_r$ decreases from 31 μC/cm^2 to 20 μC/cm^2 after 10^3 cycles, and drops to 7.2 μC/cm^2 after 10^7 cycles (Figure 4.2.5b). The effect of deposition temperature on fatigue is summarized in Figure 4.2.5c, where the dependence of the normalized P_r with the number of cycles is plotted for all samples (solid lines are collected from the samples with seed layer, and dashed lines correspond to data reported in reference [117] for samples without seed layer). It can be observed that in the samples with seed layer, P_r reduces more with cycling as deposition temperature increases from 550 °C (72% after 10^7 cycles) to 800 °C (23% after 10^7 cycles), which is consistent with the tendency reported for samples without seed layer.[117] However, the samples with seed layer have significantly

lower fatigue when deposited at lower temperature. Endurance increases from 10^7 cycles (750 °C and 800 °C) to 5 10^7 cycles (650 °C and 700 °C) to 10^9 cycles (550 °C and 600 °C) with deposition temperature decrease. Endurance was limited by hard breakdown (marked by open symbols in Figure 4.2.5c).

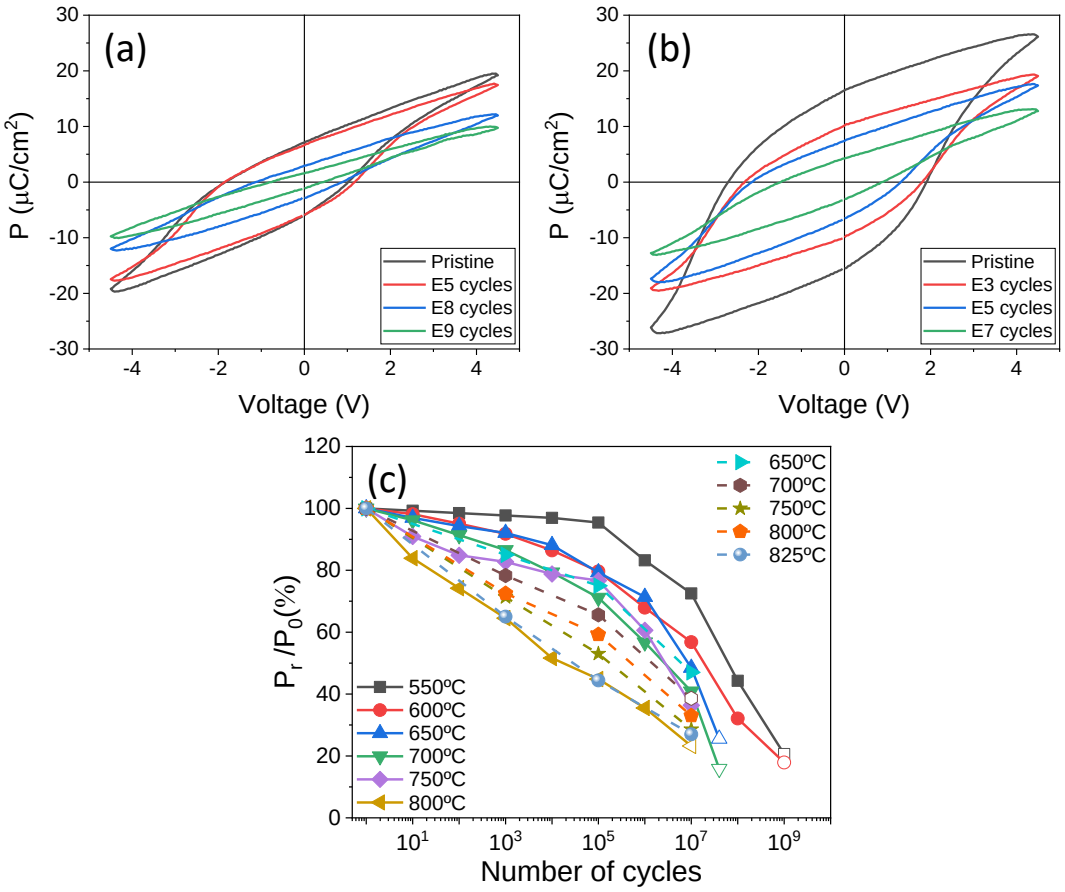

Figure 4.2.5 *Ferroelectric hysteresis loops, measured in the pristine state and after the indicated number of cycles, for films deposited at (a) 550 °C and (b) 800 °C on the seed layer. Variation with the number of cycles of P_r normalized to its pristine value, of films deposited at variable temperature. The solid lines correspond to the samples with seed layer. The dashed lines correspond to samples without seed layer [117]. Open symbols indicate hard breakdown.*

Conclusions

In summary, the use of a seed layer allows the stabilization of the ferroelectric phase in HZO films at low deposition temperature, even at the lower temperature used in this staudy, 550 °C. Compared with the samples without seed layer, P_r value is improved more than 30% in films deposited in the temperature range of 650-750 °C. Ferroelectric polarization of 14 μC/cm^2 can be obtained at low deposition temperature of 550 °C, and

films deposited at low temperature exhibit less fatigue and enhanced endurance respect to films grown at high temperature.

4.3 Growth on $SrTiO_3$(110)

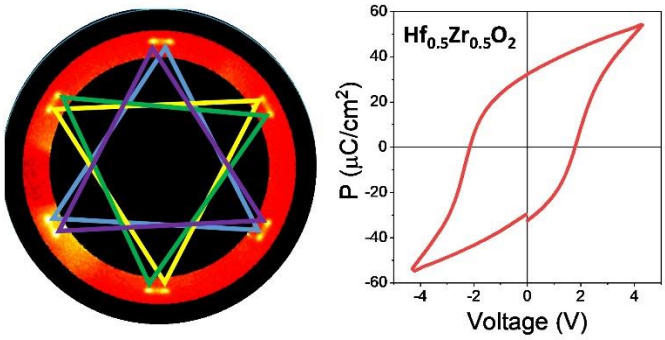

Abstract

The growth of epitaxial $Hf_{0.5}Zr_{0.5}O_2$ (HZO) thin films on $La_{0.67}Sr_{0.33}MnO_3$ (LSMO) buffered (001)-oriented $SrTiO_3$ (STO) has achieved robust ferroelectricity by stabilizing (111)-oriented orthorhombic phase. Here, we demonstrate that orthorhombic phase can also be epitaxially stabilized on LSMO/STO(110), presenting the same out-of-plane (111) orientation but a different distribution of in-plane crystalline domains. The remanent polarization of 7nm HZO film on LSMO/STO(110) is 33 μC/cm^2, which improves 50% compared to equivalent films on LSMO/STO(001). Comparatively, HZO on LSMO/STO(110) shows higher endurance up to 4 × 10^{10} cycles with retention more than 10 years. These results demonstrate that tuning epitaxial growth of ferroelectric HfO_2, here by using STO(110) substrates, allows improving functional properties of relevance for memory applications.

Introduction

It was demonstrated, by using different substrates, that epitaxial stress is critical for the stabilization of ferroelectric o-phase in HfO_2-based thin film.[14] Because of the fluorite structural difference between HfO_2 and perovskite substrates, epitaxy occurs by domain matching epitaxy mechanism.[118] This impedes using lattice mismatch to engineer lattice strain. On the other hand, o-phase can be grown on LSMO and other La-doped manganites, but not on other popular oxide electrodes such as $SrRuO_3$, $LaNiO_3$ or La:$BaSnO_3$.[119] These facts limit the possibilities of controlling the ferroelectricity of epitaxial HfO_2 films. Aiming to open new ways of tailoring, we have investigated the growth of HZO films on STO(110) substrates buffered with (110)-oriented LSMO electrodes, as an alternative to the used STO(001) substrates. The films are epitaxial and (111)-oriented like equivalent films on STO (001), but they present a different set of in-plane crystal variants. A high remanent polarization as high as 33 μC/cm^2 with high endurance and good retention.

4.3.1 Growth conditions

HZO films were grown simultaneously on LSMO buffered STO(001) and STO(110) substrates. Growth conditions were Ts=800 °C, 0.1 mbar of pure O_2, and 600 laser pulses. After deposition, XRD θ-2θ scans around the o-HZO(111) reflection were measured, as indicated in Figure 4.3.1a. The peaks at 2θ around 23°, 33° and 47° correspond to (001), (110) and (002) reflections of STO substrates with the corresponding LSMO reflections at the right of the substrate peaks. The peaks at 2θ around 30° is the place where o(111) reflection is located. A longer time scan around this peak is shown in Figure 4.3.1b. By comparing the two films, it can be observed that the out-of-plane interplanar spacing of film on STO(110) is $d_{o(111)}$ = 2.946 Å, which is slightly lower than that of the film on STO(001) with $d_{o(111)}$ value of 2.972 Å. The low intensity peaks around o(111) reflections are Laue oscillations. By fitting the Laue fringes, the film thickness is identified around 6.5 nm (Figure 4.3.1c-d). Atomic force microscopy measurement confirms that the film of STO(110) is very flat, with root mean square roughness of 0.25 nm (Figure 4.3.1e), which is comparable to the films on STO(001).[65]

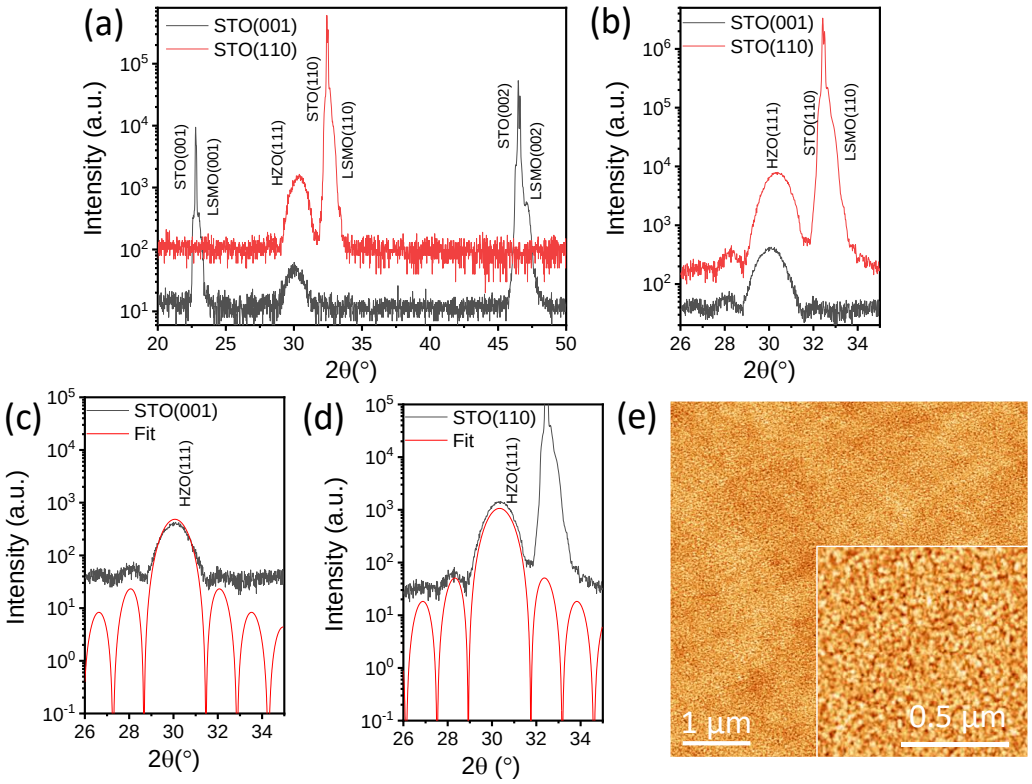

Figure 4.3.1 *(a) XRD θ-2θ scan of the HZO/LSMO/STO(001) (black line) and HZO/LSMO/STO(110) (red line) samples. (b) Zoomed scans, recorded with longer time, around the o-HZO(111) reflection. (c) and (d) are the simulations of Laue oscillations (red curves). (e) Topographic AFM image of a 5 µm × 5 µm region of the HZO/LSMO/STO(110) sample. The inset at the bottom left shows the image of a 1 µm × 1 µm region.*

4.3.2 Structural characterization

Epitaxy has been studied by XRD using a 2D detector. Figure 4.3.2a shows the reciprocal space map (RSM) around the asymmetric STO{111} reflections for the HZO/LSMO/STO(001) sample. The map was obtained from ϕ-scans with a 2D detector, recorded at ϕ angles ranging from 0° to 360°, with a step Δϕ = 1°. Apart from the STO{111} spot, the integrated frame shows the presence of a spot that corresponds to o-{11-1} reflections (Q_x = 0.316 Å^{-1}, Q_z = 0.109 Å^{-1}) and a lower intensity spot of o-{200} reflections (Q_x = 0.316 Å^{-1}, Q_z = 0.224 Å^{-1}). The presence of both spots at the same ϕ is due to 180° twinning. The diffraction spots of o-phase (dashed rectangle in Figure 4.3.2a) can be observed at specific ϕ angles (Figure 4.3.2b). The 12 spots, 30° apart, are corresponding to both o-{11-1} and o-{200} reflections. The pole figure of o-{11-1} reflections is shown in Figure 4.3.2c. It can be seen that the presence of four families (colored triangles) of in-plane crystal variant consequences of the epitaxy of o-HZO(111)

(3-fold symmetry surface) on LSMO/STO(001) (4-fold symmetry surface).[118] Similar measurements has been done for HZO/LSMO/STO(110) sample, in Figure 4.3.2d-f. Around the asymmetric STO{011} reflections, there are o-{11-1} (Q_x = 0.313 Å^{-1}, Q_z = 0.115 Å^{-1}) and o-HZO{200} reflections (Q_x = 0.313 Å^{-1}, Q_z = 0.225 Å^{-1}). In the Q_z - ϕ map, the 12 spots are distributed in 6 sets of 2 spots, each set is about 60° apart and the two spots in each set are 8.5° apart. The pole figure indicates that there are four HZO crystal domains, corresponding to the following epitaxial relationships: [-211]HZO(111)//[-112]STO(110), [-211]HZO (111)//[1-12]STO(110), [2-1-1]HZO(111)//[-112]STO(110), and [2-1-1]HZO(111)//[1-12]STO(110).

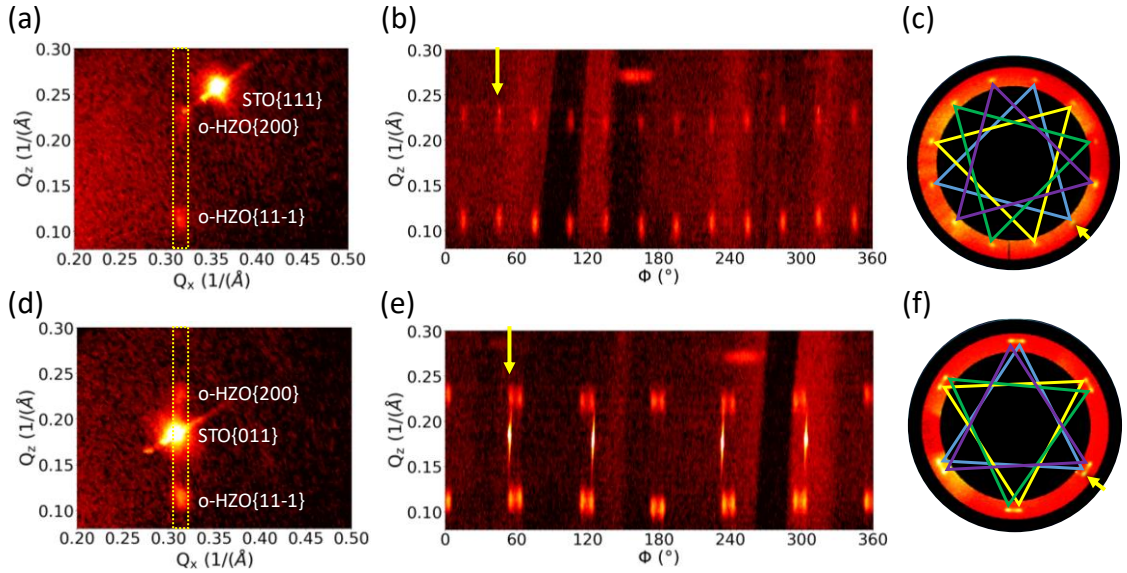

Figure 4.3.2 *(a,d) RSM obtained from processing 2D pole figure frames. Q_z is the perpendicular component and Q_x is parallel to the in-plane direction at a specific ϕ angle. The vertical dotted line indicates the position in Q_x (0.314 ± 0.005 Å^{-1}) that was used to plot in (b,e) the integrated intensity versus ϕ. The yellow arrows indicate the ϕ position of the RSM in (a,d). (c,f) Pole figures corresponding to the o-{11-1} planes integrated χ = 71 ± 7° and 2θ = 27-33°. The triangles are guides to the eye to indicate the four crystallographic o-{111} domains. Panels (a-c) and (d-f) correspond to measurements of HZO/LSMO/STO(001) and HZO/LSMO/STO(110), respectively.*

Figure 4.3.3 indicates the STEM characterization of film on STO(110) substrate. It can be observed that orthorhombic phase with different crystal variants is stabilized on LSMO(110). The vertical yellow arrows mark the position of boundaries between different grains. And the HZO film on LSMO/STO(110) is almost purely o-phase, which is remarkable because the coexisting of o and m-phase in film on LSMO/ STO(001).[14] The dashed yellow line marked area is enlarged in Figure 4.3.3b. High crystalline quality

of HZO and a well-defined (semi) coherent HZO/LSMO interface are present. At the interface, the LSMO(110) and HZO(111) unit cells does not directly matches with each other, following domain matching epitaxy.[118] Finally, we note that HZO is (111) oriented on both LSMO(001) and LSMO(110) surfaces. This suggests the relevance of the surface energy contribution in addition to the interface energy.

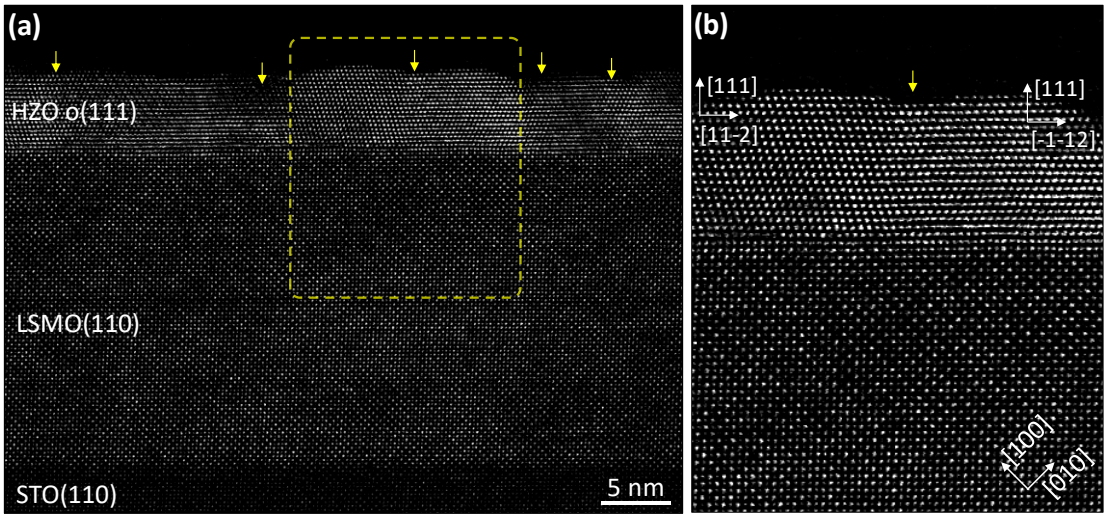

Figure 4.3.3 *(a) Cross-sectional contrast inverted annular bright field image showing, from bottom to top, the STO(110) substrate, the LSMO(110) electrode and the HZO(111) film. The location of the (coherent) boundaries between mirror-like in-plane crystallographic variants are indicated by yellow arrows at the top of the image. (b) Zoomed region showing two orthorhombic HZO grains and part of the LSMO electrode. (b) has been extracted from the area marked with yellow dashed line in (a).*

4.1.3 Electrical characterization

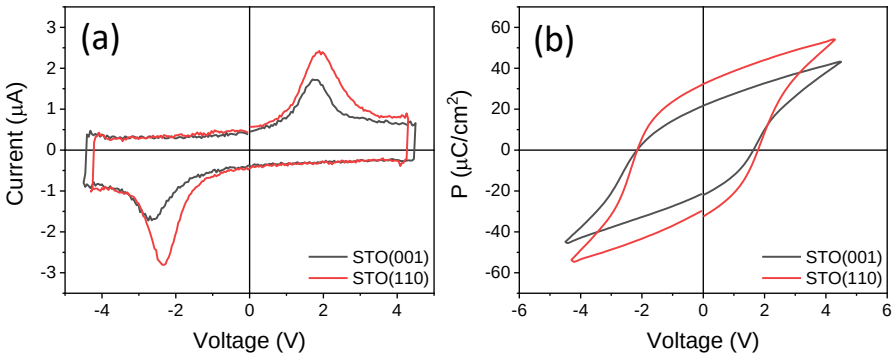

Figure 4.3.4 *(a) Current-voltage curves of HZO/LSMO/STO(001) (black line) and HZO/LSMO/STO(110) (red line) samples, measured in the pristine state. (b) Corresponding polarization loops.*

Figure 4.3.4 shows the current - voltage curves and corresponding polarization loops of HZO films on LSMO/STO(001) and LSMO/STO(110). The switching peaks confirms the ferroelectricity in both films. In the film on STO (001) (black line in Figure 4.3.4a-b), the position of two current peaks is -2.7 and 1.8 V, indicating average coercive field of 3.4 MV/cm and internal field (1.3 MV/cm) pointing down to LSMO electrode. The corresponding polarization loop is well saturated and the remanent polarization is 22 $\mu C/cm^2$. In the film on STO (110) (red line in Figure 4.3.4a-b), the position of two current peaks is -2.3 and 1.9 V, indicating average coercive field of 3.2 MV/cm and similarly, internal field (0.6 MV/cm) pointing down to LSMO electrode. Remarkably, the remanent polarization is 33 $\mu C/cm^2$, which is 50% higher than the equivalent epitaxial film grown simultaneously on STO(001). The larger Pr value is likely related to the higher amount of o-phase in the film. STEM characterization has shown that it is almost pure orthorhombic (Figure 4.3.3), while films on LSMO/STO(001) present an important amount of parasitic monoclinic phase.[14] In theory, the predicted P_r value of [001]-oriented o-phase is 52-55 $\mu C/cm^2$,[140,141] from which the projected polarization along the [111] direction of a pure o-phase film would be around 31 $\mu C/cm^2$, which is similar to the measured P_r in film on STO(110).

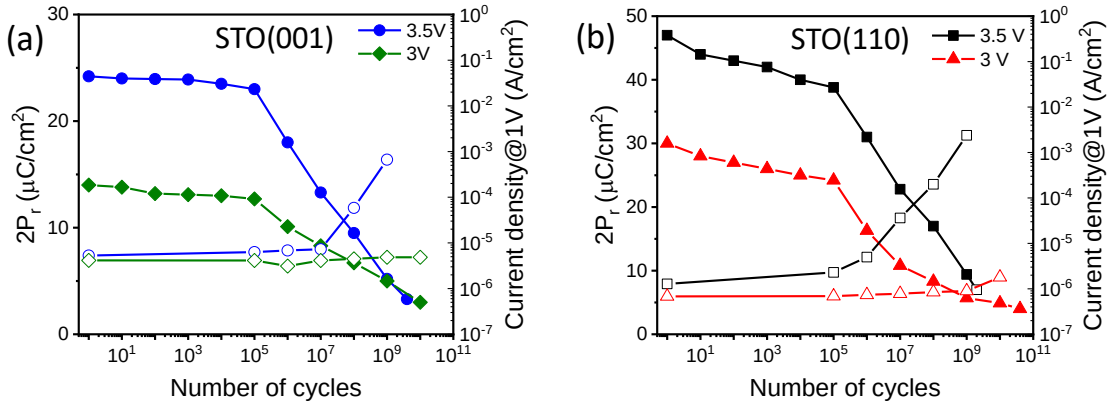

Figure 4.3.5 *(a) Endurance (solid symbols) and current leakage as a function of the number of cycles (empty symbols) of the HZO/LSMO/STO(001) sample cycled by 3.5 V (blue symbols) and 3 V (green symbols). (b) Endurance (solid symbols) and current leakage as a function of the number of cycles (empty symbols) of the HZO/LSMO/STO(110) sample cycled by 3.5 V (black symbols) and 3 V (red symbols).*

Figure 4.3.5 shows the endurance measurements of the films. The film on STO(001) (Figure 4.3.5a), cycled with voltage pulses of 3.5 V (solid blue circles), indicates initial memory window of 24.2 $\mu C/cm^2$ and without observable wake-up effect. After 10^5 cycles,

polarization value does not change significantly, but further cycling causes severe fatigue. The measurement was stopped when the polarization was as low as $2P_r$ = 3.3 μC/cm^2 after 4×10^9 cycles. The corresponding leakage current (empty blue circles) during cycling is constant up to 10^7 cycles, but increasing dramatically with additional cycles. The endurance test at lower voltage, 3V, presents a similar dependence. With a smaller initial memory window, the fatigue after 10^5 cycles is less pronounced and the capacitor can be cycled up to 10^{10} cycles (the test was stopped due to the low $2P_r$ of 3 μC/cm^2) without breakdown. The leakage current (open green diamonds) is constant during the test. The parallel measurement of film on STO(110) is shown in Figure 4.3.5b. At 3.5 V, the initial memory window is 47 μC/cm^2, and it decreases slightly from the first cycle, being more severe after 10^5 cycles. The hard breakdown happens after 2×10^9 cycles, which is likely due to the high leakage current after cycling (open black squares). To avoid breakdown, lower voltage of 3V is applied to cycling the sample. The $2P_r$ is 30 μC/cm^2 in the pristine state which is even greater than that of the film on STO(001) at 3.5V. Similar evolution of polarization after cycling can be observed, but in this case, the endurance is up to 4×10^{10} cycles without breakdown and the measurement is stopped when $2P_r$ decreases to 4 μC/cm^2. The robustness against breakdown is probably because the leakage current (open red triangles), contrary to what is observed for 3.5 V cycling voltage, does not increase significantly while cycling.

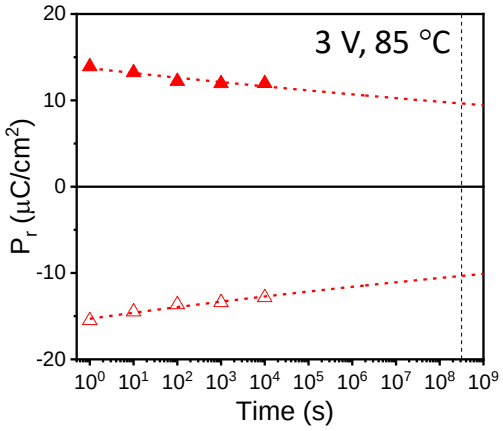

Figure 4.3.6 *Polarization retention measurements at 85 ℃ of the HZO/LSMO/STO(110) for positive and negative poling of 3 V. Lines are fits $P_r = P_0 \cdot \tau_d^n$.*

Figure 4.3.6 indicates the retention of the film on STO(110) at 85°C with poling voltage of 3V, the same voltage used for getting high endurance in Figure 4.3.5b. Dashed red lines are fits to $P_r = P_0 \cdot \tau_d^n$, where τ_d is the delay time and n a fitting parameter.[145] The

vertical black dashed line indicates a 10 years' time. It can be seen that the extrapolated remanent polarization is still high after 10 years for both positive (solid triangles) and negative poling (empty triangles) at 3 V. Therefore, the film shows high polarization ($2P_r$= 30 μC/cm^2), endurance (4×10^{10} cycles) and retention (more than 10 years) under the same poling voltage.

Conclusions

In summary, the stabilization of epitaxial HZO film on LSMO/STO(001) can also be achieved on LSMO/STO(110). o-HZO films are (111) oriented and have in-plane crystal variants on both substrates, but the variants have different angular distribution. The application of STO(110) substrate increases the ferroelectric polarization up to 30 μC/cm^2, which is 50% higher than that of the film on STO(001). Meanwhile, the high polarization is accompanied by a long endurance (4×10^{10} cycles) and good retention extrapolated to more than 10 years under the same poling voltage.

4.4 Growth on $SrTiO_3$(111)

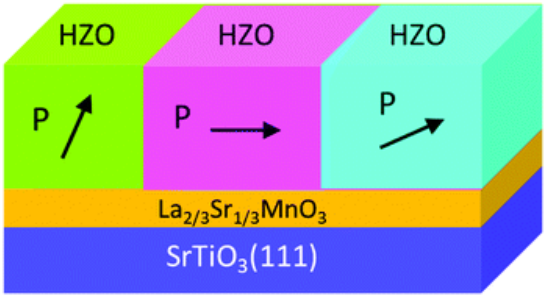

Abstract

The growth of epitaxial $Hf_{0.5}Zr_{0.5}O_2$ (HZO) thin films on $La_{0.67}Sr_{0.33}MnO_3$ (LSMO) buffered (001) and (110)-oriented $SrTiO_3$ (STO) has achieved robust ferroelectricity by stabilizing (111)-oriented orthorhombic phase. Here, we explored the deposition of HZO film on LSMO/STO(111). The results show that o-phase is stabilized by tilted epitaxy, and the orientation of orthorhombic crystallites is different from that of equivalent films on STO(001) and STO(110). Remanent polarization around 14 $\mu C/cm^2$ agrees well with the expected value considering the crystal orientation, the fraction of the o-phase in the film, and the predicted polarization of ferroelectric HfO_2. Endurance and retention are also measured.

Introduction

As shown in chapter 4.3, the HZO films can be epitaxially stabilized on (001) and (110) oriented LSMO by tailoring with (001) and (110) oriented STO substrates. The formed o-phase is (111) oriented on both substrates, but with different in-plane orientations. Different with STO(001) and STO(110) substrates, STO(111) substrate with 3-fold in-plane symmetry could result in different orientation of o-phase and pave the way towards the epitaxial integration of ferroelectric HfO_2-based thin films on other substrates. In this section, we have deposited HZO film on LSMO(111)/$SrTiO_3$(111) to determine if ferroelectric o-phase can be epitaxially stabilized on (111) oriented LSMO. The results reveal the existence of three families of orthorhombic crystal variants with an orthorhombic HZO[001] axis tilted by about 24°, 66° and 90° with respect to the plane-normal direction of the film. P_r of about 14 μC/cm^2, an endurance of up to 10^8 cycles and a retention of more than 10 years can be obtained.

4.4.1 Growth conditions

HZO and LSMO films were grown in a single process on (111)-oriented STO substrates by PLD. The thicknesses of the HZO and LSMO films were around 6 and 22 nm, respectively. The corresponding deposition parameters of HZO were 2 Hz, 800 °C and 0.1 mbar. At the end of the deposition, the oxygen pressure was increased to 0.2 mbar and the heater was switched off. More details of sample preparation can be found in chapter 3.

4.4.2 Structural characterization

Figure 4.4.1a shows the XRD θ-2θ scan. LSMO(111) and STO(111) diffraction peaks are observed at 2θ around 40°, but no HZO reflections. Wider regions of the reciprocal space were explored using a 2D detector. Figure 4.4.1b shows the ψ-2θ map obtained by summing single ψ–2θ maps recorded at $\phi = 90 \pm 4°$, with an interval of $\Delta\phi = 1°$. Besides the STO(011) peak at $2\theta = 32.3°$ and $\psi = 35.3°$, two weaker spots belonging to orthorhombic HZO can be identified. They correspond to HZO(111) ($2\theta \sim 30.0°$, $\psi \sim 40.0°$) and HZO(002) ($2\theta \sim 34.8°$, $\psi \sim 24.8°$) reflections. Reflections corresponding to the monoclinic phase of HZO are not detected due to the limited sensitivity of the laboratory diffractometer.

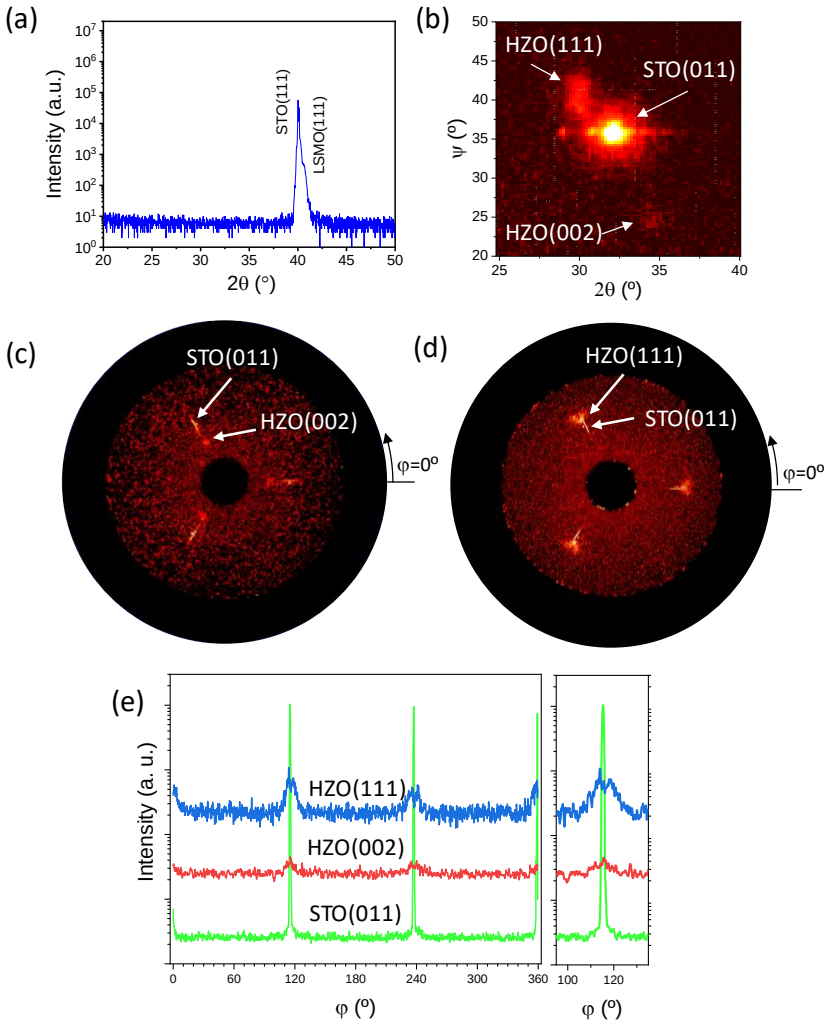

Figure 4.4.1 *(a) XRD symmetric θ-2θ scan measured using a 1D detector. (b) 2θ-ψ map around the asymmetric STO(011), orthorhombic HZO(111) and orthorhombic HZO(002) reflections. The map is a summing intensity of a set of maps measured using a 2D detector and recorded in a range of ϕ = ± 4°, with $\Delta\phi$ = 1°. (c and d) Pole figures around the HZO(002) and (d) HZO(111) diffraction spots. The corresponding phi scans are plotted in (e) with the region around ϕ = 115° magnified. The intensity scale is logarithmic.*

The pole figures from orthorhombic HZO(111) and HZO(002) reflections and the corresponding integrated ϕ scans are shown in Figure 4.4.1c-e. There are three STO(011) substrate reflections, 120° apart with each other. HZO(002) reflections are found at the same ϕ position as the substrate peaks, while each HZO(111) reflection is split in two peaks at about 5° apart. Analysis of the pole figures points to the orientation of the HZO film close to (012). Considering a cell (for simplicity cubic) with the out-of-plane HZO(012) orientation, the corresponding HZO(002) planes are at ψ = 26° and ϕ = 0°, while HZO(111) planes are at ψ = 39° and ϕ = ± 114°, leading to a ϕ splitting of HZO(111)

of around ± 6°. The broad peaks observed for HZO(111) and HZO(002) point to a certain mosaicity both the in-plane and out-of-plane. Nevertheless, the observed peaks are compatible with the existence of 3 distinct crystal domains with an epitaxial relationship [0$\bar{2}$1]HZO(012)//[$\bar{2}$11]STO(111). Due to the very low intensity of HZO(012) reflections and the nanometric thickness of the HZO film (6 nm), no HZO diffraction peaks are detected in the symmetric XRD scan.

The topographic AFM image of a 5 μm × 5 μm region (Figure 4.4.2) shows that the surface of the film is very flat, with a root mean square roughness of 0.17 nm. The maximum height variation in the profile across the marked dashed blue line is less than 1 nm. The detailed view of Figure 4.4.2a reveals the morphology of terraces and steps, which can also be appreciated in the zoomed 1 μm × 1 μm region (Figure 4.4.2b).

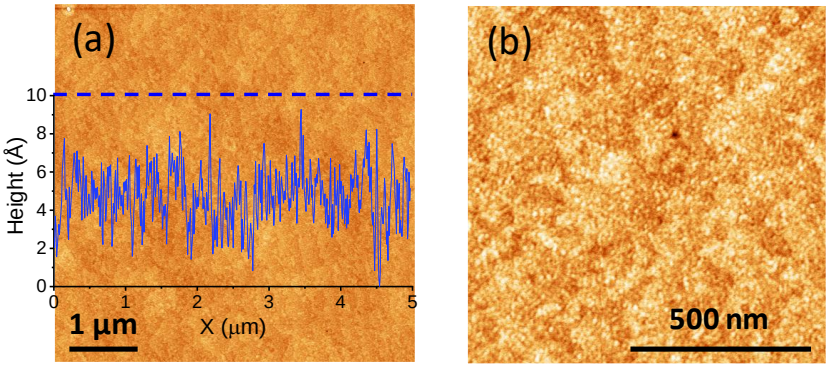

Figure 4.4.2 *(a) Topographic AFM image of the 5 μm × 5 μm scanned region, with a height profile along the horizontal dashed line. (b) Topographic AFM image of the 1 μm × 1 μm scanned region.*

To further identify the phase formed in the HZO film and epitaxy orientation, the sample was characterized by STEM. Figure 4.2.3 shows cross-sectional HAADF images, observed along the [01$\bar{1}$] zone axis (corresponding to the [111]/[$\bar{2}$11] observation plane). Given the 3-fold symmetry of the LSMO/STO(111) surface planes, HZO epitaxial crystallites have the same probability of growing along the three equivalent in-plane directions (120° apart). The latter, given the epitaxial relationship between HZO and LSMO/STO(111), entails that only 1/3 of the crystallites can be observed simultaneously by STEM, while the other 2/3 of grains will be off-axis. This is compatible with the observations shown in Figure 4.4.3: those crystallites belonging to the 1/3 group are appropriately oriented for the STEM observation and show well-defined cation atomic columns, which allows the epitaxial relationship between the orthorhombic HZO crystallites and LSMO/STO(111) to be identified. On the other hand, those crystallites

belonging to the other crystal variants are not appropriately oriented for the STEM observation and the atomic column resolution is lost; instead, atomic planes are resolved. Three different atomic-column cation patterns can be discerned in the well-oriented orthorhombic HZO crystallites, with projection onto planes *b*-*c*, *a*-*c* and *a*-*b*, as shown in Figure 4.4.3b-d. In every case, the orthorhombic HZO unit cell is found oriented with one <001> direction tilted by about 24° with respect to the out-of-plane direction, while the other directions have angles of about 66° and 90°. Note that these three variants are equivalent in a cubic, non-polar cell, but for an orthorhombic cell, the polar axis *c* has a different orientation in each of them. The similarity of the three orthorhombic lattice parameters (a = 5.234 Å, b = 5.010 Å, and c = 5.043 Å)[146] may allow the coexistence of these three crystal variants, each associated with a specific orientation of the polar *c* axis. Specifically, *c* is observed to lay at 24° (biggest out-of-plane polarization component, Figure 4.4.3b), 66° (intermediate polarization component, Figure 4.4.3c) or in the plane (90°, null out-of-plane polarization component, Figure 4.4.3d) with respect to the plane-normal direction in three different grains. Therefore, each kind of grain is expected to contribute differently to the macroscopic polarization measured in the capacitor-like devices.

In addition to the polar tilted orthorhombic HZO(001), the non-polar monoclinic phase is also observed. Like the orthorhombic phase, the monoclinic phase presents the [001] direction tilted by about 24° away from the plane-normal direction. A zoomed monoclinic grain and comparison with model is shown in Figure 4.4.3e. Interestingly, the coexistence of the o and m crystallites with a similar epitaxial orientation allows the formation of coherent o/m grain boundaries (Figure 4.4.3f), in contrast to the incoherent o(111)/m(001) grain boundaries found in HZO films on (001) substrates. In particular, the coherent m/o boundary forms despite the nominal 5% larger m(001) lattice spacing compared to the o(001) lattice spacing. The coherent boundaries are observed between grains with equivalent in-plane epitaxial orientation, but HZO crystallites can grow along any of the three equivalent in-plane directions. Thus, the grain boundaries between differently in-plane oriented HZO crystallites may not be coherent. This possibility could not be confirmed due to the difficulties in observing the cation columns for the misoriented crystallites. Besides, the intensity of the HAADF image (which scales approximately as Z^2, Z being the atomic number) at the HZO/LSMO interface (Figure 4.4.3f) suggests a

similar interfacial reconstruction to the one found in HZO/LSMO/STO(001),[120] where Hf/Zr atoms substitute Mn atoms right at the interface.

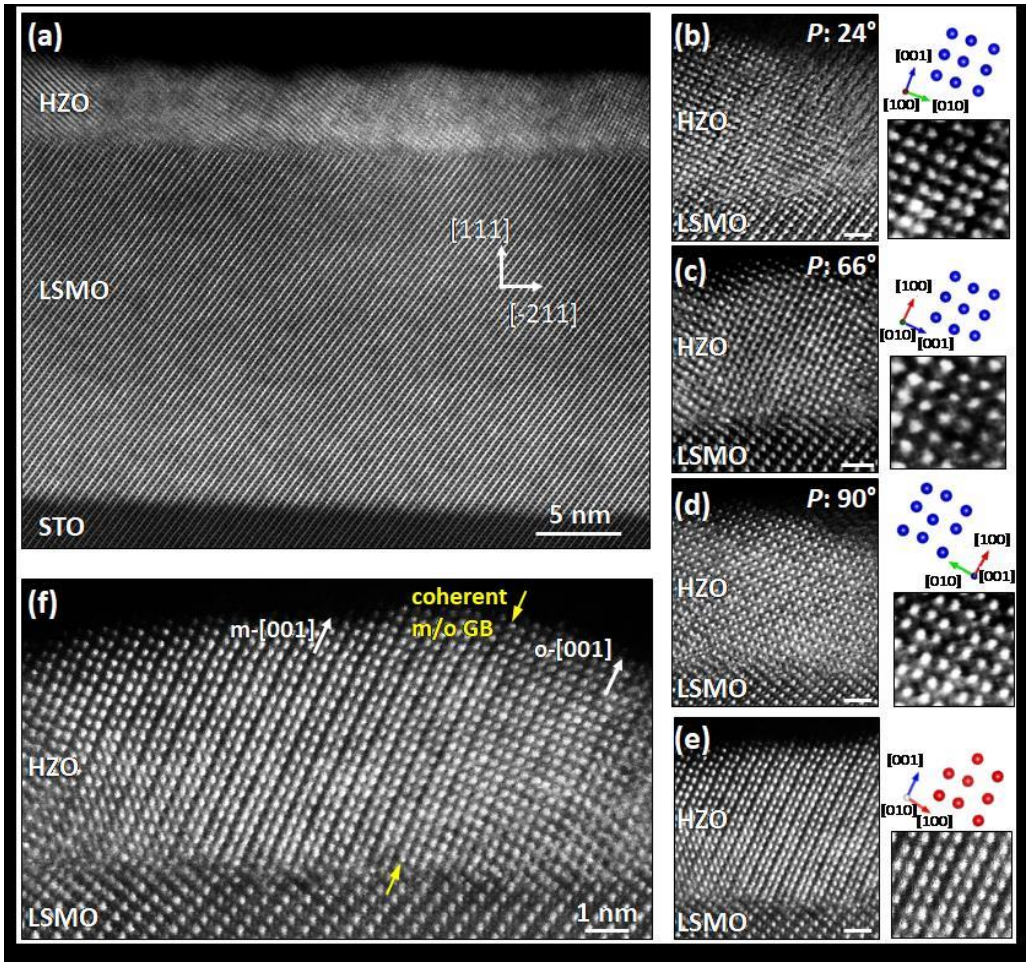

Figure 4.4.3 *(a) Large field of view HAADF image showing the STO(111) substrate, the LSMO(111) electrode and the HZO film. (b-d) Zooms of the three o-HZO crystal variants found in the HZO film, extracted from larger images collected at different locations. The [001] polar axis is tilted with respect to the plane-normal direction by 24° (b), 66° (c) and 90° (d). The $Pca2_1$ orthorhombic model shows the Hf/Zr cations (blue balls) as seen along the different directions. (e) Zoom of the m-HZO phase and comparison with the $P2_1/c$ monoclinic model showing the Hf/Zr cations (red balls). Note that the angle between the [001] and [100] directions is more than 90°, which is the characteristic of the monoclinic phase. (f) Zoom around the HZO film, showing tilted m-HZO(001) and o-HZO(001) grains and the coherent grain boundary (GB) between them, as indicated by the yellow top and bottom arrows. Scale bar in (b-e): 1 nm.*

Grains that have grown along the two other equivalent in-plane directions of STO(111) and are not in perfect on-axis in the STEM images also provide valuable information. The resolved planes can be identified as belonging to the {111} or {$\bar{1}$11} families, which is the expected view if one grain is rotated in-plane by 120° clock or anticlockwise.

Interestingly, it can be seen that these {111} or {$\bar{1}$11} planes appear fully coherent with the (110) planes of LSMO, with a one-to-one matching along the direction parallel to the interface (corresponding to the following directions: [42$\bar{1}$]HZO/[$\bar{2}$11]LSMO, see Figure 4.4.4a-b). Given the dissimilarity between the HZO polymorphs and the LSMO structure, these well-matched planes can play an important role in the epitaxial stabilization of orthorhombic HZO on LSMO(111). The expected lattice mismatch between HZO {111} or {$\bar{1}$11} and LSMO/STO (110) planes is about 6%, which is a high but still feasible value for the strained growth of the nanometric film.

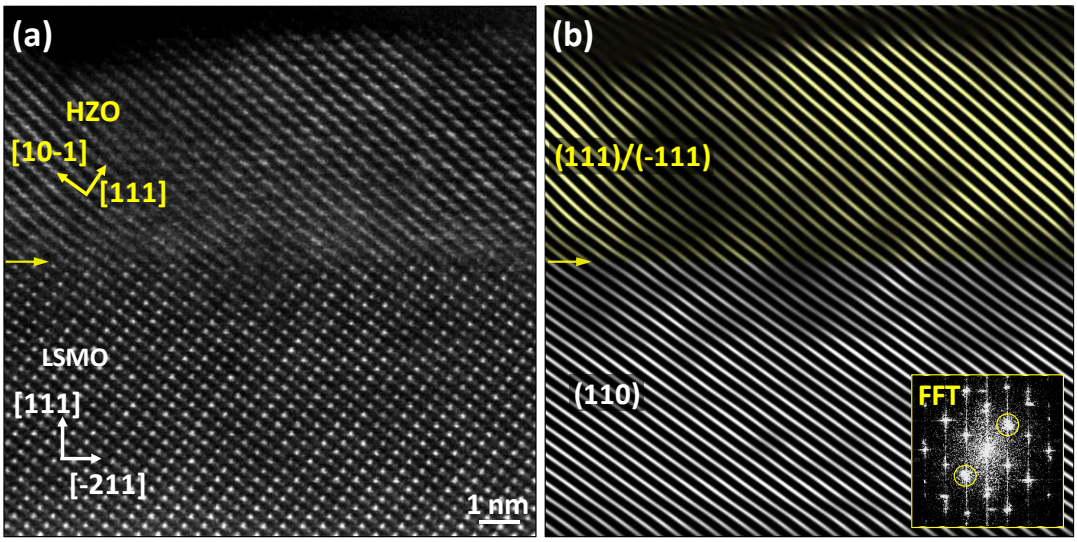

Figure 4.4.4 *(a) HAADF cross-sectional image of an orthorhombic HZO crystallite and the LSMO electrode. (b) The corresponding fast Fourier Transform (FFT) filtered image. {111}/{$\bar{1}$11} HZO planes and {110} LSMO planes are selected in the FFT (see the bottom-right inset) and used to obtain the image containing only the selected planes. Note that both HZO {111}/{$\bar{1}$11} and LSMO {110} reflections appear as one spot as they are not resolved separately. For clarity, planes in the HZO are shown in yellow while those in LSMO are shown in white. The location of the HZO/LSMO interface is indicated with a horizontal yellow arrow both in (a) and (b).*

4.4.3 Electrical characterization

Current-voltage curve (Figure 4.4.5a, red line) shows two clear ferroelectric switching current peaks, with notably shift to negative voltage side. The coercive fields of positive and negative side are 1.8 MV/cm^2 and -3.3 MV/cm^2, respectively, signalling an imprint of 750 kV/cm pointing towards the bottom LSMO electrode. The corresponding polarization loop (Figure 4.4.5a, blue line) evidences the ferroelectric behavior of the Pt/HZO/LSMO/STO(111) capacitor, with a remanent polarization P_r of around 14 μC/cm^2. As discussed in Figure 4.4.3, the three families of o-phase have the c-axis tilted

at 24°, 66° and 90° with respect to the out-of-plane direction, and thus the corresponding contributions to the polarization are $0.91P_{bulk}$, $0.41P_{bulk}$ and 0, where P_{bulk} is the polarization of HZO film, which is around 52-55 μC/cm^2 from theory calculation.[140,141] Therefore, the polarization of the film is expected to be $P=\alpha\cdot(1/3\times0.91P_{bulk} + 1/3\times0.41P_{bulk} + 1/3\times0)$, where α is the fraction of o-phase in the film. From the electrical measurement, the P value is around 14 μC/cm^2, thus, it can be estimated that α is around 0.6, which matches with the STEM observation quantitatively. The leakage current as a function of electric field is shown in Figure 4.4.5b. The leakage is low with a value around 6×10^{-8} A/cm^2 at 1 MV/cm.

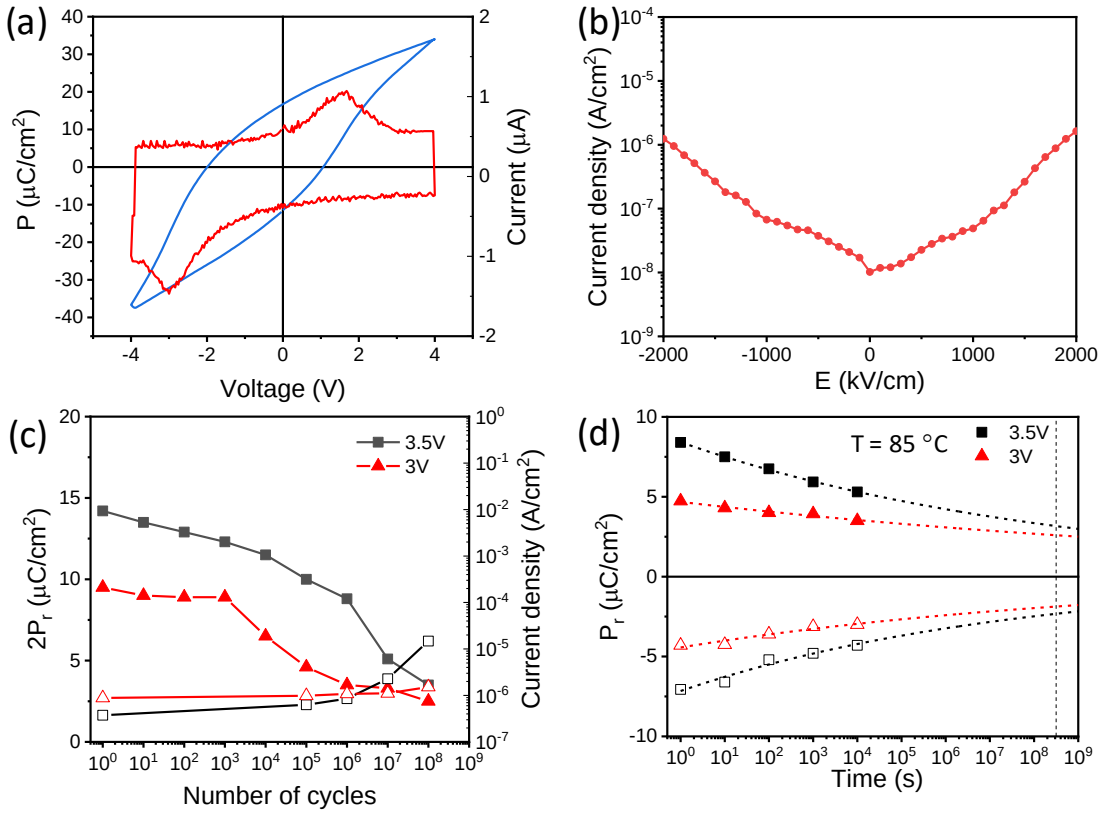

Figure 4.4.5 *(a) Current-electric field curve (red line) and the corresponding ferroelectric polarization loop (blue curve). (b) Leakage current as a function of the electric field. (c) Evolution of memory window with the number of bipolar cycles of amplitude 3V (solid triangles) and 3.5V (solid squares). Open symbols show the evolution of the leakage current (value at 1V) during the endurance measurements at 3V (triangles) and 3.5V (squares). (d) Retention at 85 °C after poling with positive (solid symbols) or negative (open symbols) voltage pulses with amplitude of 3.5V (squares) and 3V (triangles). Dashed lines correspond to the fitting of $P_r \propto t_d^{-n}$ equation, where t_d is the time after poling. The vertical dash line marks a time of 10 years.*

The endurance (solid symbol) companied with leakage current (open symbol) evolution under cycling amplitudes of 3 V (triangles) and 3.5 V (squares) is shown in Figure 4.4.5c. It can be seen that there is no wake-up effect, and at 3.5V, the memory window gradually decreases from 14 μC/cm^2 to 8.8 μC/cm^2 after 10^6 cycles, and then degrades more severe to 3.5 μC/cm^2 after 10^8 cycles. Similarly, at 3V, the initial $2P_r$ slightly drops to 8.9 μC/cm^2 after 10^3 cycles, and diminishes faster with further cycling down to 2.5 μC/cm^2 after 10^8 cycles. The leakage current is nearly constant at 3 V and increases slightly after 10^7 cycles at 3.5 V, which shows a lack of correlation with the ferroelectric fatigue. It suggests that the fatigue process is probably not dominated by the generation of new oxygen vacancies, and it is proposed that the fatigue in this film is mainly caused by the fast growth of pinned ferroelectric domains within each orthorhombic grain. The retention is measured at 85 °C, as shown in Figure 4.4.5d, using the same poling voltage for endurance measurements. The experimental data, up to 10^4 s, are fitted to the $P_r = P_0 t_d^{-k}$ equation (dashed lines), where t_d is the time after poling. The extrapolated retention can extend beyond 10 years (vertical dotted line) for both poling voltages of 3 V (triangles) and 3.5 V (squares).

Conclusions

In summary, epitaxial HZO film has been stabilized on LSMO/STO(111) with coexisting of m-phase and o-phase. The o-phase shows tilted epitaxy and has three crystal variants with a polar [001] axis at different angles (24°, 66° and 90°) with respect to the plane-normal direction. The remanent polarization around 14 μC/cm^2 matches with the estimated value considering the o-phase orientation. Good retention and endurance are also demonstrated.

Chapter 5. Epitaxial $Hf_{1-x}Zr_xO_2$ and La-doped $(Hf,Zr)O_2$ thin films

Doping allows to stabilize the ferroelectric o-phase and optimize the ferroelectricity for HfO_2-based thin film. One of extensively investigated dopants is Zr, since the wide optimized doping window and low crystallization temperature.[147] La is another promising dopant with large atomic radius to achieve high remanent polarization and good ferroelectricity (low leakage current and long endurance).[74,148] In polycrystalline films, the doping effect has been investigated, while in epitaxial HfO_2-based film, the results are seldom at the beginning of the present thesis. To gain more sights into the influence of doping on the intrinsic ferroelectricity of HfO_2-based films, we systematically studied the doping effect of Zr and La dopants. First, ferroelectricity of a series of 10 nm epitaxial films of $Hf_{1-x}Zr_xO_2$ with different compositions are explored. Films in all the explored compositions are ferroelectric without wake-up effects. Endurance is better in HZO film than that of HfO_2 and ZrO_2 films. Second, we investigated the influence of La content, film thickness, and substrate induced epitaxial stress on the ferroelectricity of La:HfO_2 films. The optimized La content is 2-5 at% with P_r higher than 20 $\mu C/cm^2$. 2 at% La:HfO_2 films with thickness less than 7 nm show a high P_r of about 30 $\mu C/cm^2$, slight wake-up, an endurance of at least 10^{10} cycles and a retention of more than 10 years, with the endurance and retention measured at the same poling voltage. 2 at% La:HfO_2 films on different perovskite substrates show P_r up to 29 $\mu C/cm^2$ in films deposited on $TbScO_3$ substrate, and chemical doping and epitaxial stress can be collaborated to tailor ferroelectricity. Third, the synergic doping effect of Zr and La on HfO_2-based films is explored. The results of epitaxial 1% La doped HZO film with different thicknesses indicate that La decreases the reduction of polarization with thickness increase compared with Zr doped films. Despite fatigue present, endurance in epitaxial La-doped films is more than 10^{10} cycles, and this good property is accompanied by excellent retention of more than 10 years, which proves that there is no endurance-retention dilemma in La-doped epitaxial HZO films. Furthermore, the HfO_2-ZrO_2-La_2O_3 ternary system has been studied. When increasing the Zr content, a lower La content is more suitable for achieving higher P_r, and the optimized P_r of about 30 $\mu C/cm^2$ can be obtained in 2% La:HZO film.

5.1 Epitaxial $Hf_{1-x}Zr_xO_2$ thin films

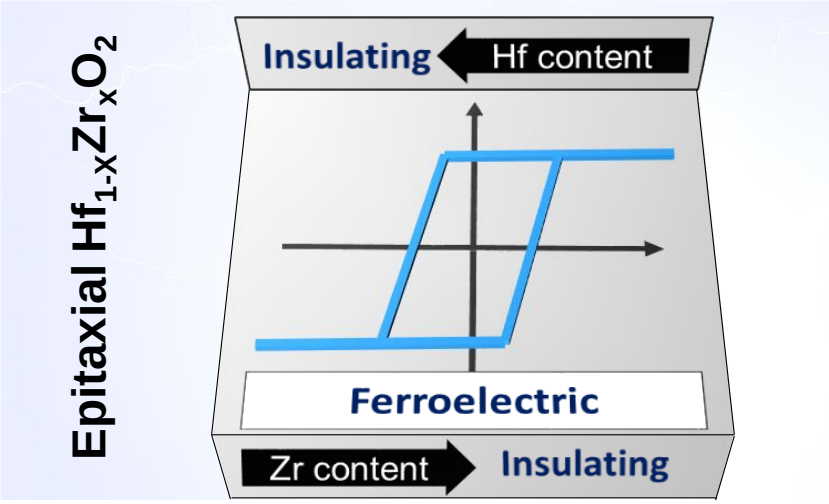

Abstract

Systematic studies on polycrystalline $Hf_{1-x}Zr_xO_2$ films with varying Zr contents show that HfO_2 films are paraelectric (monoclinic) with good insulating properties. Instead, if the Zr content is increased, films become ferroelectric (orthorhombic) and then antiferroelectric (tetragonal). In between, $Hf_{0.5}Zr_{0.5}O_2$ shows good ferroelectricity at the expense of poorer insulating properties than HfO_2 and ZrO_2 films, respectively. However, similar investigations on epitaxial $Hf_{1-x}Zr_xO_2$ films has not been addressed. In this section, we explore the ferroelectric, and insulating properties of a series of epitaxial films of $Hf_{1-x}Zr_xO_2$ with different Zr content. We show that epitaxial growth permits the stabilization of the ferroelectric phase in a whole range of Zr content (from $x = 0$ to $x = 1$). In epitaxial ZrO_2 films, ferroelectricity coexists with better insulating properties than $Hf_{0.5}Zr_{0.5}O_2$, and in HfO_2 epitaxial films, ferroelectricity coexists with better insulating properties than $Hf_{0.5}Zr_{0.5}O_2$. For the case of ZrO_2 films, large electroresistance is also observed. In both cases, the ferroelectric endurance is poorer than that for $Hf_{0.5}Zr_{0.5}O_2$ films.

Introduction

The systematic investigation of polycrystalline $Hf_{1-x}Zr_xO_2$ (x=0-1) films grown by atomic layer deposition indicates that: i) the paraelectric centrosymmetric monoclinic phase ($P2_1/c$) stabilizes in pure HfO_2 films, ii) in films with x near to 0.5, the ferroelectric orthorhombic phase ($Pca2_1$) stabilizes and iii) tetragonal phase ($P4_2/nmc$) stabilizes in Zr-rich films.[42,43,52,147,149] Investigations on epitaxial films are scarcely reported. Ferroelectric, insulating, and electroresistance properties of a series of 10 nm epitaxial films of $Hf_{1-x}Zr_xO_2$ with different compositions are explored here. Furthermore, the wake-up effect, endurance and the stability of orthorhombic phase under higher temperature are investigated in parallel. Our results reveal that epitaxial growth enhances the stabilization of the ferroelectric orthorhombic phase for a wider compositional range than polycrystalline film. Films in all the explored compositions are ferroelectric without wake-up effects, increasing the remanent polarization with the Zr content. And there are no detectable phase changes in $Hf_{0.5}Zr_{0.5}O_2$ and ZrO_2 films after heating up to 1000 K and cooling down to room temperature.

5.1.1 Growth conditions

Five $Hf_{1-x}Zr_xO_2$ ceramic bulks with composition of HfO_2, $Hf_{0.75}Zr_{0.25}O_2$, $Hf_{0.5}Zr_{0.5}O_2$, $Hf_{0.25}Zr_{0.75}O_2$ and ZrO_2 were sintered as targets. $Hf_{1-x}Zr_xO_2$ films were deposited at substrate temperature (measured using a thermocouple inserted in the heater block) of T_s=800 °C with dynamic oxygen pressure of PO_2 = 0.1 mbar and a laser frequency of 2 Hz. More details of the sample preparation can be found in Chapter 3.1. $Hf_{1-x}Zr_xO_2$ (x=0-1) films (t≈8 nm for HfO_2 film, t≈9 nm for $Hf_{0.75}Zr_{0.25}O_2$, $Hf_{0.5}Zr_{0.5}O_2$, $Hf_{0.25}Zr_{0.75}O_2$ film, and t≈12 nm for ZrO_2 film. Thickness is extracted from Laue fringes fitting as shown in Figure 5.1.1).

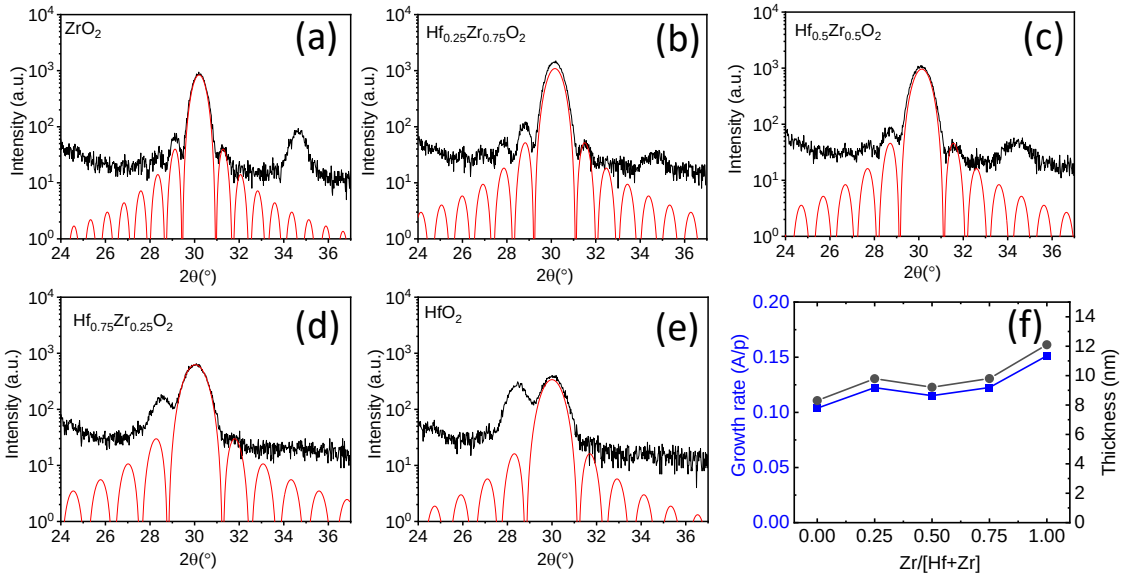

Figure 5.1.1 *(a-e) XRD θ-2θ scans and (f) the estimated thickness (black circles) and growth rate (blue squares) of $Hf_{1-x}Zr_xO_2$ films on LSMO/STO(001). Red curves are simulations of Laue oscillations.*

5.1.2 Structural characterization

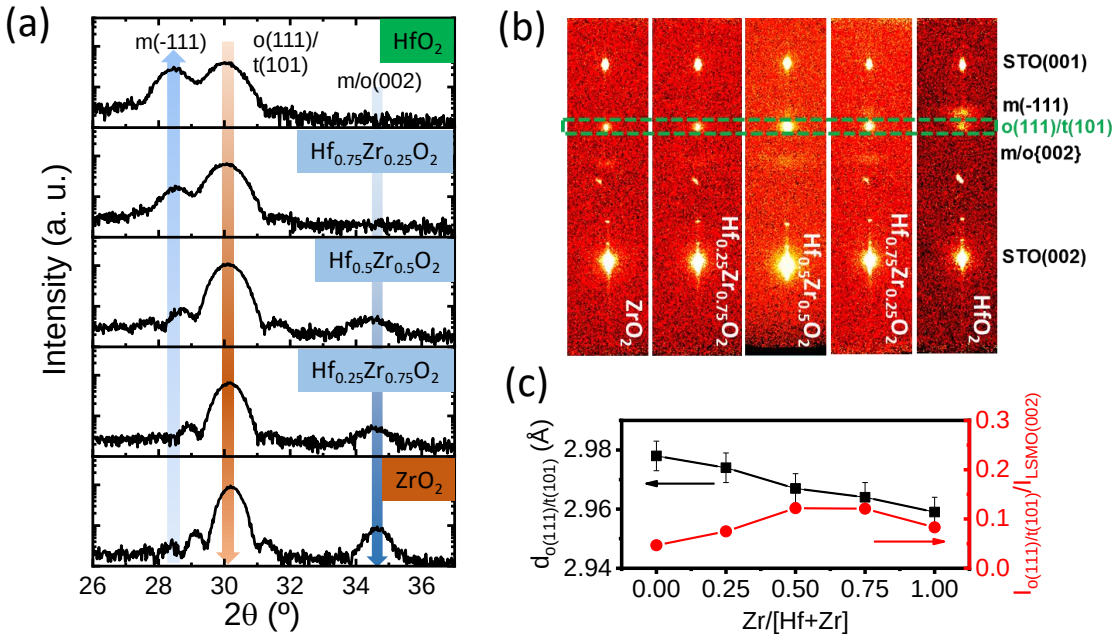

Figure 5.1.2 *(a) XRD θ-2θ scans of $Hf_{1-x}Zr_xO_2$ films (x=0, 0.25, 0.5, 0.75 and 1). (b) XRD 2θ-χ frames of $Hf_{1-x}Zr_xO_2$ films. Dashed green line rectangle mark the position of the HZO o (111)/t(101) reflection. (c) Out-of-plane o(111)/t(101) lattice distance of $Hf_{1-x}Zr_xO_2$ films (black squares) and intensity of o(111)/t(101) normalized to LSMO(002) (red cycles), plotted as a function of Zr content.*

Figure 5.1.2a shows XRD θ-2θ scans of all $Hf_{1-x}Zr_xO_2$ films (x=0, 0.25, 0.5, 0.75 and 1). It can be clearly observed that there is a peak at 2θ around 30.1° in all films which is corresponding to the position of orthorhombic (111) reflection. It needs to be noted that (101) reflection of tetragonal phase could overlap with orthorhombic (111) reflection, although transmission electronic microscopy indicates no presence of tetragonal phase in $Hf_{0.5}Zr_{0.5}O_2$ film,[14] which likely disregards its significant presence in the low Zr content films, but not on films with greater Zr content. The peak at around 28.5° signals the formation of monoclinic (-111) phase in x=0 and 0.25 films. But when increasing Zr content, this peak gradually vanishes and only Laue fringes from o(111)/t(011) peak can be observed. Diffraction peak at around 34.5° is related to the {002} reflection of m, o or t phase. In Figure 5.1.2b, XRD 2θ-χ frames indicate bright circular spots corresponding to the STO substrate, the LSMO electrode, and the o(111)/t(101) reflection as indicated. The narrow spot around χ=0° signals epitaxial ordering. The out-of-plane lattice parameter of $d_{o(111)/t(101)}$ and normalized intensity of the o(111)/t(101) peak are shown in Figure 5.1.2c. It can be seen that the $d_{o(111)/t(101)}$ value gradually decreases (square symbols) from 2.978 Å to 2.959 Å while increasing Zr content, in agreement with results found in polycrystalline films.[42] The maximum intensity of o(111)/t(101) peak ($I_{o(111)/t(101)}$, round symbols) is in $Hf_{0.5}Zr_{0.5}O_2$ film, which indicates a higher content of o(111)/t(101) phase.

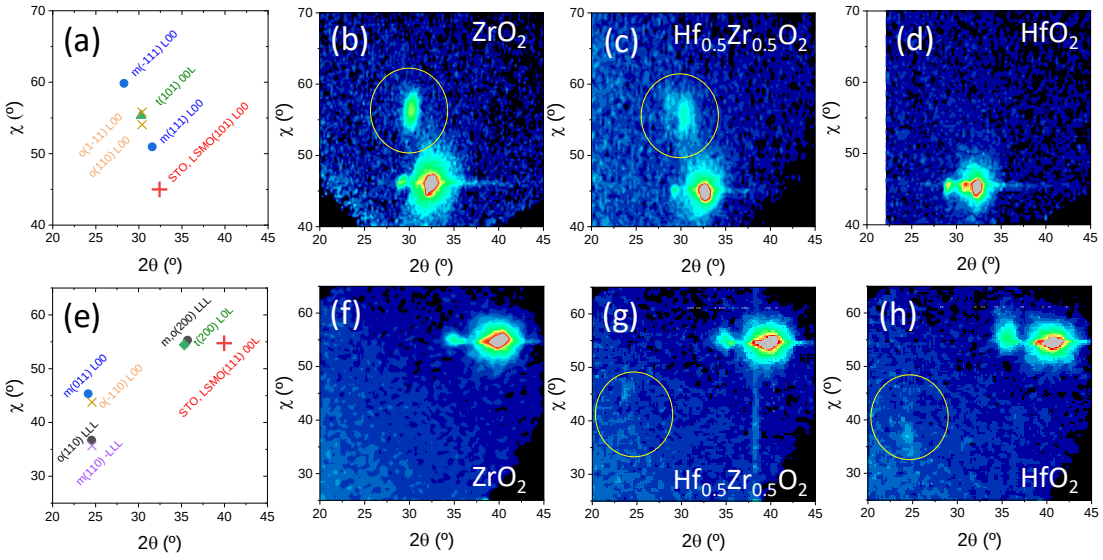

Figure 5.1.3 *XRD 2θ-χ maps of ZrO_2, $Hf_{0.5}Zr_{0.5}O_2$, and HfO_2 films around asymmetric (b-d) STO(101) and (f-h) STO(111) reflections. The corresponding sketches are in panels (a) and (e).*

To further explore the phase formed in the film, we analysed the XRD 2θ-χ maps of ZrO_2 $Hf_{0.5}Zr_{0.5}O_2$, and HfO_2 films around STO(101) and STO(111) reflections, as indicated in

Figure 5.1.3. Sketches in (a) and (e) show the position of relevant reflections in the maps around STO(101) and STO(111), respectively. In panel b, the o(111)/t(101) reflection in ZrO_2 arises from {00L} oriented crystallites without splitting, also evidenced by the peak at ~34.5° in the symmetric θ-2θ scan (shown in Figure 5.1.2a), corresponding to either {002} reflections of o and/or t phases but not to m phase. In the $Hf_{0.5}Zr_{0.5}O_2$ film (Figure 5.1.3c), the o(111)/t(101) reflection is accompanied of weak m{111} reflection, indicating that the peak at ~34.5° in the symmetric θ-2θ scan includes {002} reflections of m phase in addition of o and/or t phases. In contrast, these asymmetrical reflections are not observed in the HfO_2 film (Figure 5.1.3d), in agreement with the absence of peak at ~34.5° in the symmetric θ-2θ scan. The symmetric θ-2θ scan of the HfO_2 film showed a high intensity m(-111) peak. In the 2θ-χ map presented in Figure 5.1.3h, a very weak m(110) spot, arising from these {-111} oriented crystallites is observed. In the $Hf_{0.5}Zr_{0.5}O_2$ film (Figure 5.1.3g) this asymmetric spot is not detected, while there is a very low intensity m(011) spot arising from {00L} oriented monoclinic crystallites. None of these asymmetric spots is detected in the ZrO_2 film (Figure 5.1.3f).in summary, there is an absence of {001}-oriented monoclinic phase in ZrO_2, while m{001} and o/t{001} crystallites coexist in the $Hf_{0.5}Zr_{0.5}O_2$ film.

Figure 5.1.4a-e shows topographic AFM images of the $Hf_{1-x}Zr_xO_2$ films. The films are very flat, with a RSM roughness less than 0.42 nm (Figure 5.1.4f). Morphology of terraces and steps is appreciated with no significant variation among the film.

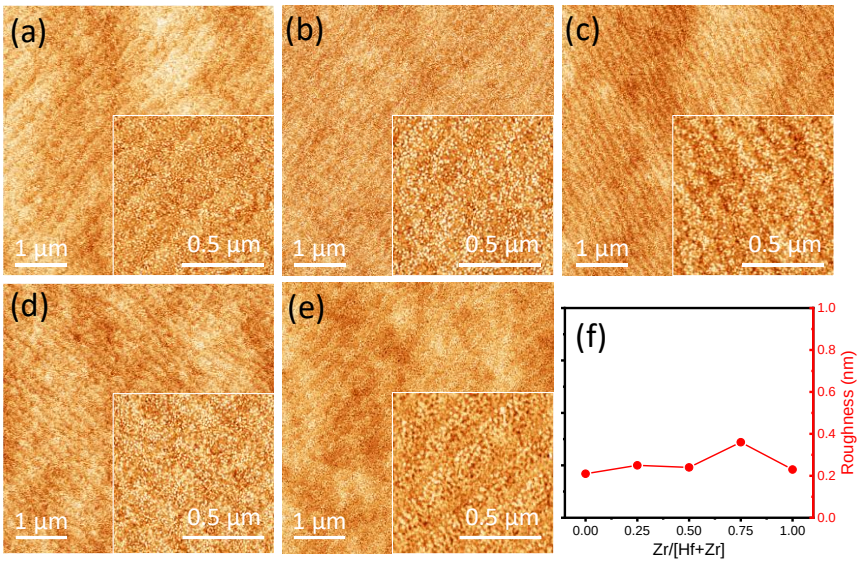

Figure 5.1.4 *(a-e) Topographic AFM images, 5 µm x 5 µm, of the $Hf_{1-x}Zr_xO_2$ films. The inset in each image is a 1 µm x 1 µm scanned area. (f) Summarized roughness (in 5 µm x 5 µm scanned areas) of films with different Zr content.*

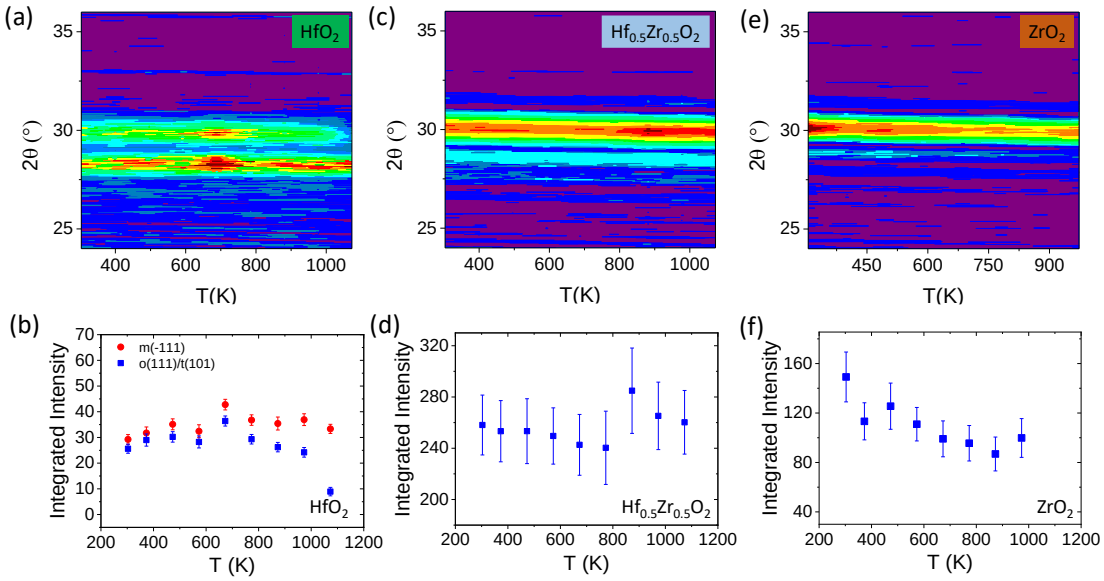

Figure 5.1.5 *2θ-temperature diffraction maps for $Hf_{1-x}Zr_xO_2$ x = (a) 0, (c) 0.5, and (e) 1 films. (b, d, f) Corresponding integrated intensity as a function of temperature for the o(111) peak. Panel (b) includes the temperature dependence of the intensity of the m(-111). Error bars correspond to the error of the fit.*

The temperature dependent XRD data of HfO_2, $Hf_{0.5}Zr_{0.5}O_2$, and ZrO_2 films are indicated in Figure 5.1.5. In HfO_2 film (Figure 5.1.5a), the peak at lower 2θ angle is ascribed to m(-111) phase which is stable up to 1100K. Instead, the o(111)/t(101) peak intensity vanishes at 1000 K. This is more clearly evidenced by the integrated peaks intensity plotted as a function of the temperature in Figure 5.1.5b. The possible reason could be the transformation of orthorhombic phase to monoclinic phase. In Figure 5.1.5c ($Hf_{0.5}Zr_{0.5}O_2$ film), only o(111)/t(101) reflections are observed in the whole explored temperature range. The small intensity peak at lower 2θ angle is caused by Laue fringes from o(111)/t(101) reflections. Furthermore, the peak intensity is nearly constant in the whole temperature range (Figure 5.1.5d), indicating a stability of orthorhombic phase up to 1100K in epitaxial $Hf_{0.5}Zr_{0.5}O_2$ film, which is above the temperature reported (650-900K) in other polycrystalline and epitaxial doped HfO_2 films.[25,40,99,115,150] The slightly jump that appeared at 900K is ascribed to an experimental artefact also observed in the reflection belonging to the substrate. From Figure 5.1.5e, it can be noted that the o(111)/t(101) reflections is well visible in the whole explored temperature range for ZrO_2 film. A gradual decrease with temperature can be observed from the integrated peak (Figure 5.1.5f) intensity of the o(111)/t(101) reflection.

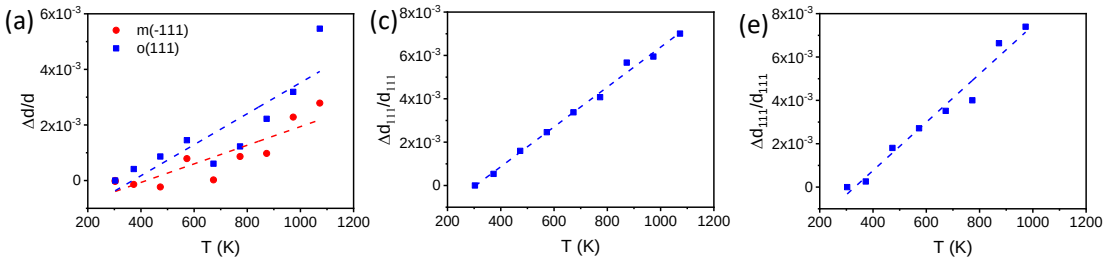

Figure 5.1.6 *The extracted relative inter-plannar spacing change with temperature of (a) m(-111) and o(111) plane in HfO_2, and o(111) plane in (b) $Hf_{0.5}Zr_{0.5}O_2$ and (c) ZrO_2 films.*

It can be observed in Figure 5.1.5 (a, c, e) that the diffraction peaks indicate a shift towards lower angles with temperature increase, which is due to thermal expansion. The extracted thermal expansion coefficients (TEC) for the o(111)/t(101) reflection are 5.5, 9.2, and 11.4 x 10^{-6} 1/K for HfO_2, $Hf_{0.5}Zr_{0.5}O_2$, and ZrO_2 films, respectively, as shown in Figure 5.1.6. The absolute TEC value can be largely affected by the substrate, but it is STO(001) substrate for all films, and thus it can be concluded that TEC increases with Zr content. Figure 5.1.7 shows the P-V loops measured increasing temperature for HfO_2, $Hf_{0.5}Zr_{0.5}O_2$, and ZrO_2 films, respectively. For HfO_2, $Hf_{0.5}Zr_{0.5}O_2$, and ZrO_2 films, polarization dependence on temperature shows a small decrease with temperature. Thus, only the HfO_2 film undergoes a possible phase transition to the high temperature stable monoclinic phase. In addition, a phase transformation between o(111) and t(101) phases in all cases cannot be excluded.

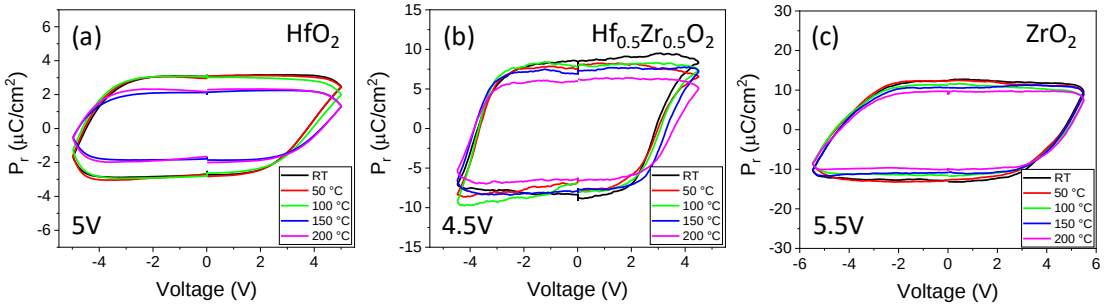

Figure 5.1.7 *PUND loops of (a) HfO_2, (b) $Hf_{0.5}Zr_{0.5}O_2$, and (c) ZrO_2 films collected at 1 kHz and indicated temperature.*

5.1.3 Electrical characterization

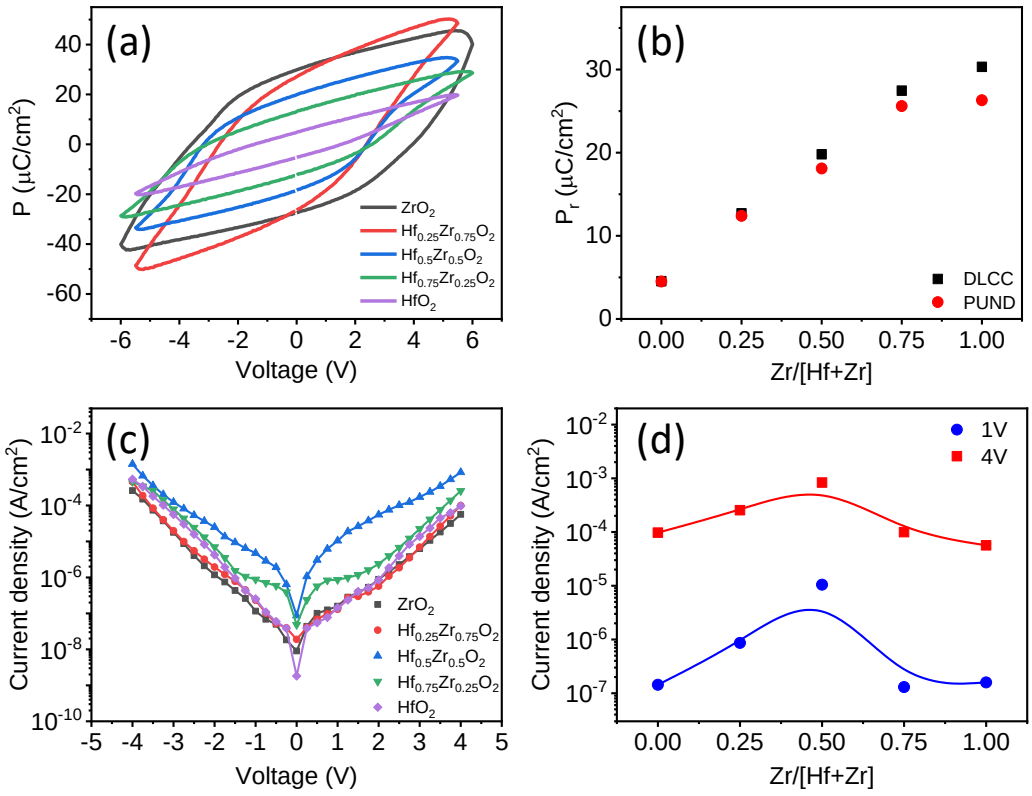

Figure 5.1.8 *(a) Hysteresis loops of $Hf_{1-x}Zr_xO_2$ films. (b) Dependence of P_r on Zr content, recorded in DLCC (black squares) and PUND (red cycles) mode. (c) Current density versus applied voltage characteristics of all $Hf_{1-x}Zr_xO_2$ films. (d) Current density versus Zr content evaluated at 1 and 4 V.*

Electrical characterization was done by grounding the LSMO bottom electrode and contacting one Pt top electrode. Figure 5.1.8a shows the polarization-voltage loops for all films, and it can be observed that all the loops indicate hysteresis with switchable remanent polarization. The remanent polarization is extracted from DLCC and PUND techniques, for subtracting contributions from leakage. The dependence of the remanent polarization with Zr content is shown in Figure 5.1.8b. With increase of Zr content, remanent polarization gradually increases. In pure HfO_2 film, the P_r is around 5 μC/cm^2. By increasing the Zr content, the P_r around 19 μC/cm^2 and 25.5 μC/cm^2 can be obtained in $Hf_{0.5}Zr_{0.5}O_2$ film and $Hf_{0.25}Zr_{0.75}O_2$ film, respectively. Interestingly, pure ZrO_2 film shows maximum $P_r \approx 27$ μC/cm^2, which is significant larger than that of the epitaxial $Hf_{0.5}Zr_{0.5}O_2$ film. In polycrystalline films, the peaky P_r is usually observed in x=0.5 of $Hf_{1-x}Zr_xO_2$ films series.[42,52,66] About the reason why there is unexpected high P_r in pure ZrO_2 film under the conditions that the orthorhombic phase in the ZrO_2 film coexists with

the paraelectric monoclinic (-111) phase and it can coexist with the tetragonal phase, as inferred from Figure 5.1.2, will be clarified in detail below. Figure 5.1.8c shows the current density versus applied voltage characteristics used to evaluate leakage current (at 1 and 4 V) shown in Figure 5.1.8d. It can be observed that the leakage is the largest for the x=0.5 film. The extreme films, x=1 and x=0, show the lowest leakage current. Thus, ferroelectricity coexists with low leakage in pure ZrO_2 and HfO_2 films.

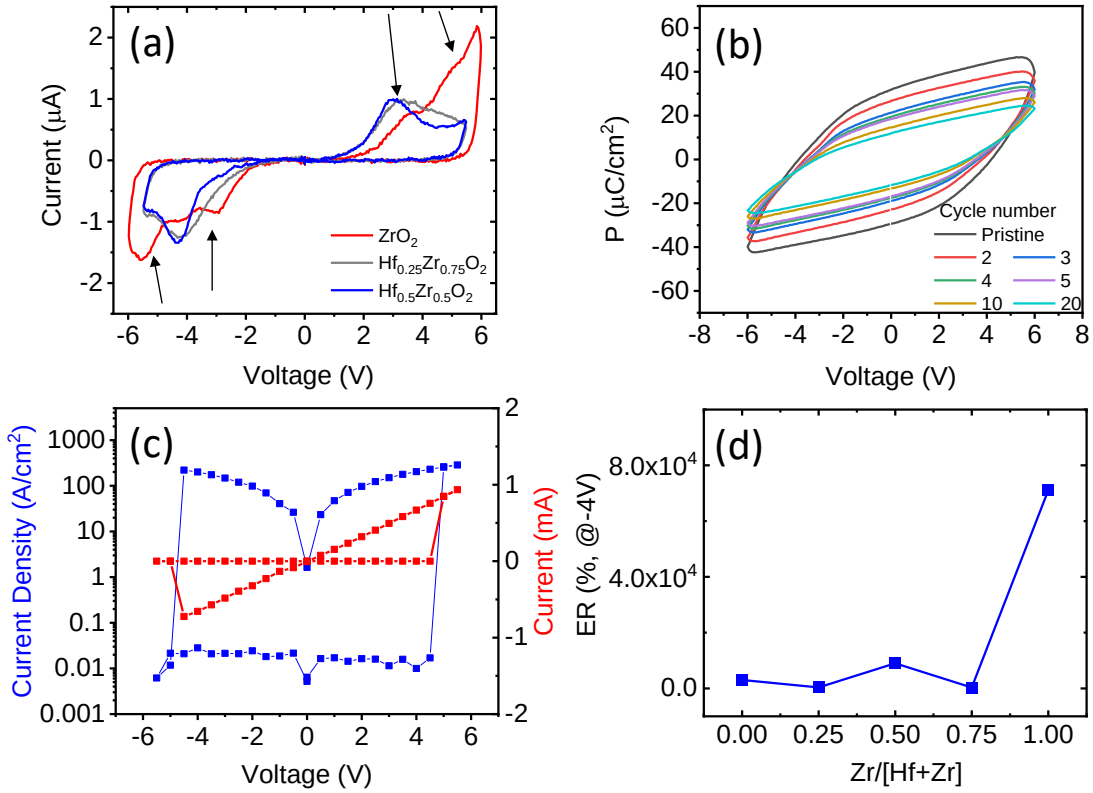

Figure 5.1.9 *(a) Current versus voltage loops using PUND measurements of ZrO_2, $Hf_{0.25}Zr_{0.75}O_2$, and $Hf_{0.5}Zr_{0.5}O_2$ films recorded at 1 kHz. (b) Consecutive polarization loops of ZrO_2 measured in pristine state and after a number of cycles in the 2 - 20 range measured at 6 V and 1 kHz. (c) Current density and corresponding current versus voltage loops of ZrO_2 epitaxial films. (d) Electroresistance of $Hf_{1-x}Zr_xO_2$ films evaluated at -4 V.*

In Figure 5.1.9a, the current versus voltage loop from PUND measurement for Zr-rich films (ZrO_2, $Hf_{0.25}Zr_{0.75}O_2$, and $Hf_{0.5}Zr_{0.5}O_2$) is plotted to further clarify the ferroelectric origin in the hysteresis loops indicated in Figure 5.1.8a. It can be observed that in pure ZrO_2 film, there are clear two switching current peaks in both positive side and negative side, which is different from the other two films with lower Zr composition. The reason for the two switching peaks can be attributed to two possible aspects. The first is electric field induced t-o phase transition, which is usually considered as the cause for the high

polarization presenting in some polycrystalline ZrO_2 and Zr-rich $Hf_{1-x}Zr_xO_2$ films.[42,43,62,151] However, this kind of field induced t-o transitions needs a large number of cycles, from 160 to thousands in polycrystalline films.[43,151] Recently, field induced t-o transitions have also been reported in epitaxial Y-doped HZO film with wake-up effect up to 100 cycles.[114] In contrast, as indicated in Figure 5.1.9b, there is not wake-up effect in our epitaxial ZrO_2 films, but is a clear decreasing of P_r. Thus, if there is field induced t-o transition in the epitaxial ZrO_2 films, it would occur completely by applying a single electric cycle. The second reason is that there is coexisting resistive switching contribution in pure ZrO_2 film. Figure 5.1.9c shows resistive switching characterization of ZrO_2 films, performed by applying a step shaped triangular voltage waveform to the films and measuring the current response at pristine state. Integration time for each data point is 2 s. Similar data have been collected in the other films. The dependent of electroresistance with Zr content is illustrated in Figure 5.1.9d, which indicates an obviously larger electroresistance in pure ZrO_2 film. It has to be noted that this kind hysteretic character cannot be completely suppressed by PUND or DLCC techniques. When measuring I-V curves of our films, four main contributions are present, ferroelectric switching, intrinsic dielectric contribution, leakage current, and series resistance from the setup. PUND allows the removal of nonswitchable contributions, like intrinsic dielectric contribution, leakage current, and series resistance. However, if the leakage current is hysteretic, as indicating in Figure 5.1.9c, it might not be fully removed. On the other hand, because this kind of probable ionic induced hysteresis is frequency-dependent, DLCC method is also not effective to remove it. Thus, the separation of the ferroelectric contribution from the I-V curve is difficult, although there is a clear ferroelectric switching peak around 3V in Figure 5.1.9a. In other compositions, this large electroresistance is not significant, which reveals that important extrinsic contributions can be disregarded in $Hf_{0.25}Zr_{0.75}O_2$ films, indicating that epitaxial $Hf_{0.25}Zr_{0.75}O_2$ shows the largest intrinsic ferroelectric polarization.

The endurance of epitaxial $Hf_{1-x}Zr_xO_2$ films is summarized in Figure 5.1.10. The decreasing of memory window after different cycling numbers indicates that there is no wake-up effect in epitaxial $Hf_{1-x}Zr_xO_2$ films, which is in contrast to polycrystalline $Hf_{1-x}Zr_xO_2$ films.[43] The high pristine $2P_r$ value in ZrO_2 film, as discussed before, consisting of ferroelectric polarization switching and resistive switching contributions or other contributions, and thus P_r is overestimated. As shown in Figure 5.1.10a, the memory window reduces from 32 to 15.2 $\mu C/cm^2$ after 10^4 cycles under an electric field of 4.5

MV/cm, and capacitor breakdown occurs for further cycling. The corresponding I-V curves are plotted in Figure 5.1.10b, it can be observed that two switching peaks (signaled by an arrow) are still present after 10^4 cycles. The fast breakdown of ZrO_2 films might result from the presence of important ionic conduction origin. In $Hf_{0.25}Zr_{0.75}O_2$ films, the hard breakdown happens after 10^6 cycles with remaining memory window of 16 $\mu C/cm^2$ under an electric field of 4.5 MV/cm. The middle $Hf_{0.5}Zr_{0.5}O_2$ film shows the best endurance up to 10^9 cycles with a cycling field of 4.4 MV/cm. $Hf_{0.75}Zr_{0.25}O_2$ films and HfO_2 films were measured at 4.9 and 6 MV/cm, and the initial polarization window dropped from 9.2 $\mu C/cm^2$ and 7.1 $\mu C/cm^2$ to about 2 $\mu C/cm^2$ after 10^6 cycles, respectively, without hard breakdown. The I-V curves of the HfO_2 films in Figure 5.1.10c indicates that the ferroelectric switching current peak is very small after 10^6 cycles and that the obtained 2 $\mu C/cm^2$ is overestimated due to residual leakage and series resistance contributions.[152] Therefore, for HfO_2 films, the device endurance is limited by the intrinsic ferroelectric fatigue instead of hard breakdown.

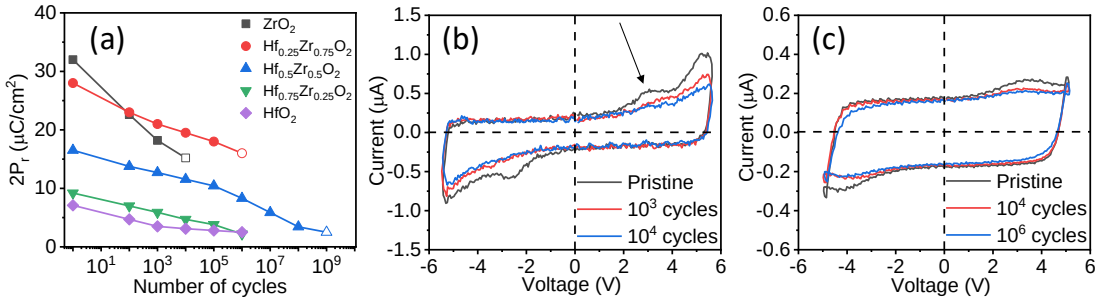

Figure 5.1.10 *(a) $2P_r$ of $Hf_{1-x}Zr_xO_2$ films after different number of cycles. Current-voltage loops of (b) ZrO_2 and (c) HfO_2 films after indicated number of cycles.*

Conclusions

In summary, ferroelectric orthorhombic phase can be epitaxially stabilized in the all $Hf_{1-x}Zr_xO_2$ (x=0, 0.25, 0.5, 0.75, 1) films. The o(111)/t(101) phase can be stabilized up to 1100K without transition to non-polar phase in $Hf_{0.5}Zr_{0.5}O_2$ film and ZrO_2 film. While, the HfO_2 film does not show o(111)/t(101) diffraction peaks when the sample is heated to 1000 K, and the crystal transformation is irreversible. The systematically investigation shows that with Zr content increase, the remanent polarization increase, indicating ferroelectricity with good insulating properties in epitaxial ZrO_2 and HfO_2 films. The high P_r up to 30 $\mu C/cm^2$ in the ZrO_2 film is associated with ferroelectric polarization switching added to resistive switching or other contributions. The endurance indicates

that there is no wake-up effect in films with explored compositions and best ferroelectric endurance is present in $Hf_{0.5}Zr_{0.5}O_2$ film. The endurance is limited by hard breakdown in Zr-rich films, whereas, limited by fatigue and low pristine memory window in Hf-rich films.

5.2 Epitaxial La-doped HfO_2 thin films

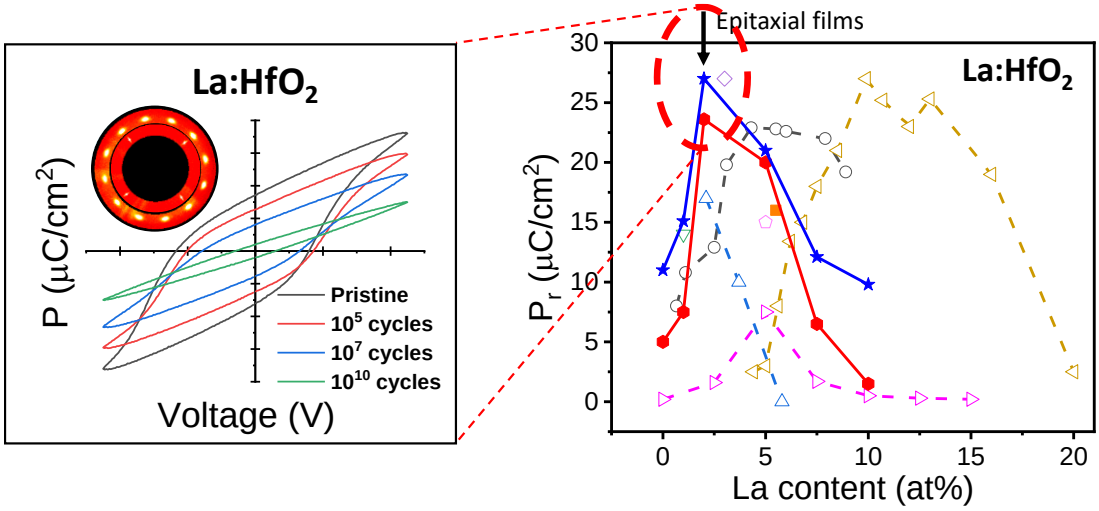

Abstract

La, with large atomic radius, is one of the most promising dopant to achieve high remanent polarization and good ferroelectricity in doped HfO_2 films. Here, we investigated the influence of La content, film thickness, and substrate induced epitaxial stress on the ferroelectricity of La:HfO_2 films. First, the optimized La concentration for stabilizing orthorhombic phase in epitaxial HfO_2 thin films has been determined by grown films on STO and Si substrates. Films with 2-5 at% La doping present more polar orthorhombic phase and indicate a higher remanent polarization above 20 $\mu C/cm^2$. With La content increase, coercive electric field and leakage current decrease, and dielectric permittivity increases. Second, to explore the thickness effect on the ferroelectricity of La doped epitaxial HfO_2 films. 2 at% La doped HfO_2 films with thickness ranging from 4.5 to 17.5 nm were prepared. Films of less than 7 nm thickness show a high remanent polarization of about 30 $\mu C\ cm^{-2}$, slight wake-up, an endurance of at least 10^{10} cycles and a retention of more than 10 years, with the endurance and retention measured at the same poling voltage. La-doped HfO_2 films even as thin as 4.5 nm also show robust ferroelectricity. Third, to further investigate the epitaxial stress effect on the polarization of 2 at% La-doped HfO_2 films, different perovskite substrates were employed to grow films on. Films grown on substrates with large pseudocubic in-plane parameters ($TbScO_3$ and $GdScO_3$) show large values of remanent polarization up to 29 $\mu C/cm^2$, while on substrates with small parameters ($LaAlO_3$) show low remanent polarization of 5.3 $\mu C/cm^2$.

Introduction

Among the different atoms used to stabilize the ferroelectric orthorhombic phase in polycrystalline HfO_2 film, La, with large atomic radius, is one of the most promising dopant to achieve high remanent polarization and good ferroelectricity for industry applications.[44] In this section, we investigated the influence of La content, film thickness, and substrate induced epitaxial stress on the ferroelectricity of La:HfO_2 films. First, the reported dependence of the polarization of La:HfO_2 films on the La content on polycrystalline films is focused to range from 2% to 12%.[58,153–155] Here, we prepared a series of La:HfO_2 films with varied La content (0,1, 2, 5, 7.5, and 10 at%) deposited on (001)-oriented STO and Si substrates. The optimized La content is 2-5 at% with remanent polarization higher than 20 $\mu C/cm^2$. Second, the thickness effect is known to modulate the ferroelectricity of La:HfO_2 films. The reported results of polycrystalline films deposited by atomic layered deposition indicates that when the endurance is up to 10^{10} cycles, the P_r is limited to 13 $\mu C/cm^2$.[35] However, La:HfO_2 films with a very high polarization do not show good endurance due to the endurance-polarization dilemma.[37,38] On the other hand, the ferroelectricity has been reported in La:HfO_2 films with a thickness of 1 μm, but no reports are focused on films with thickness thinner than 10 nm.[153] Based on the optimized La concentration, the 2 at% La:HfO_2 films with thickness ranging from 4.5 to 17.5 nm were prepared. Films with thickness less than 7 nm show a high remanent polarization of about 30 $\mu C\ cm^{-2}$, slight wake-up, endurance of at least 10^{10} cycles and retention of more than 10 years, with the endurance and retention measured at the same poling voltage. La:HfO_2 films even as thin as 4.5 nm also present robust ferroelectricity. Third, different perovskite substrates have been used to modulate the LSMO buffer layer below the epitaxial deposited Zr-doped hafnium films.[157] Nevertheless, the influence of epitaxial stress on the ferroelectricity of hafnium films with different doping chemical is still unknown. We prepared 2 at% La:HfO_2 films on different perovskite substrates, showing remanent polarization up to 29 $\mu C/cm^2$, obtained in a film deposited on $TbScO_3$ substrate.

Sample preparation

La:HfO_2 films and bottom $La_{0.67}Sr_{0.33}MnO_3$ (LSMO) electrodes were grown on STO(001) substrates in a single process by PLD using a KrF excimer laser. $Hf_{1-x}La_xO_{2-\delta}$ (x = 0, 0.01, 0.02, 0.05, 0.075 and 0.1) and $La_{0.67}Sr_{0.33}MnO_3$ sintered pellets of 1 inch diameter were used as targets. The corresponding parameters used to grow La:HfO_2 films (around 8.5 nm) were T_s = 800 °C, PO_2 = 0.1 mbar and 2 Hz. More details of sample preparation can be found in Chapter 3. An equivalent series of La:HfO_2/LSMO bilayers was grown on Si(001) wafers (p-type, resistivity 1-10 Ω·cm) buffered with epitaxial STO films deposited *ex-situ* by molecular beam epitaxy (MBE). Details of MBE deposition of the STO buffers are reported elsewhere.[29,158] The same method has been used to grow 2 at% La:HfO_2 films with thickness ranging from 4.5 to 17.5 nm. Platinum top electrodes of a 14 μm diameter were additionally deposited on the t = 4.5 nm film on Si(001) to reduce the leakage effect on the measurement of polarization loops.

5.2.1 Impact of La concentration on epitaxial hafnium film

The structural characterization of different La content doped HfO_2 films is shown in Figure 5.2.1. The XRD 2θ-χ maps (Figure 5.2.1a) present bright spots around χ=0 ° in all films. The spots around 23° and 47° are related to STO(001) and STO(002) reflections. The spots at 2θ around 28.3° and 34.4° correspond to m(-111) and m(002) phases, with brighten m(-111) reflection when decreasing La content and the m(002) phase is only clearly observed in the film with 10 at% La content. In all films, there is a bright spot around 30°, where the (111) reflection of the orthorhombic (o) phase, the (111) reflection of the cubic (c) phase, and the (101) reflection of the tetragonal (t) phase are located. At here, it is not possible to distinguish which kind of phase is formed. However, in polycrystalline La:HfO_2 films, the o phase stabilizes at moderately lower La content and the c phase tends to form at high La content.[58,74] Therefore, here we mainly consider the possible formation of o and c phase. Figure 5.2.1b shows the XRD θ-2θ scans measured with a point detector. Laue oscillations can be clearly observed around 30°, indicating a good crystallinity in the films. The film thickness is determined from the simulation of the Laue oscillations (not shown). The films are around 8 nm thick, except the 10 at% film which is 10.5 nm thick. The out-of-plane lattice parameter (Figure 5.2.1c) of o/c(111) reflection is around 2.98 Å in the films with content up to 5 at%, and slightly expanded to around 3.0 Å in the 7.5 and 10 at% La doped film, which could signal an increase of

cubic phase in the higher La doped films, as it has been observed in polycrystalline films.[58] The $d_{o/c(111)}$ values of equivalent films deposited on Si substrate have also been summarized. Here we also observed $d_{o/c(111)}$ increases with La content. The relatively smaller $d_{o/c(111)}$ value in films deposited on Si substrate than that on STO substrate is considered an effect of the tensile stress caused by the unmatched thermal expansion of Si while cooling. Si has a low thermal expansion coefficient and this produces a tensile stress on the film when it is cooled after growth at high temperature.[30,31] The 12 peaks of o/c(111) reflection indicates four in-plane orientations and the film epitaxial growth (Figure 5.2.1d).

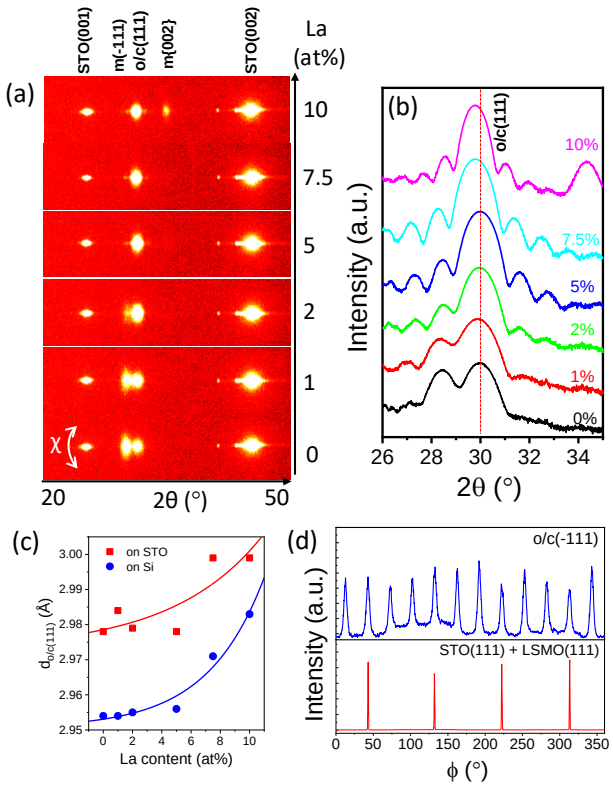

Figure 5.2.1 *(a). XRD 2θ-χ maps (b) and θ-2θ scans (c) of the La:HfO_2 films on STO(001). (e) Out-of-plane lattice parameter associated with the o/c(111) reflection as a function of the La concentration for films on STO(001) (red squares) and Si(001) (blue circles). Lines are guides for the eye. (d) XRD ϕ-scans, measured in the 2 at. % La film on STO(001), around o/c(-111) reflections (top panel) and STO(111)/LSMO(111) reflections..*

The topograph AFM images (Figure 5.2.2) present morphology of terraces and steps, indicating flat surface with low root-mean-square roughness (rms) of around 1.5-2 Å in films with La content lower than 10 at%. A slightly higher roughness is indicated in 10 at% La doped film with rms increase to 3.7 Å.

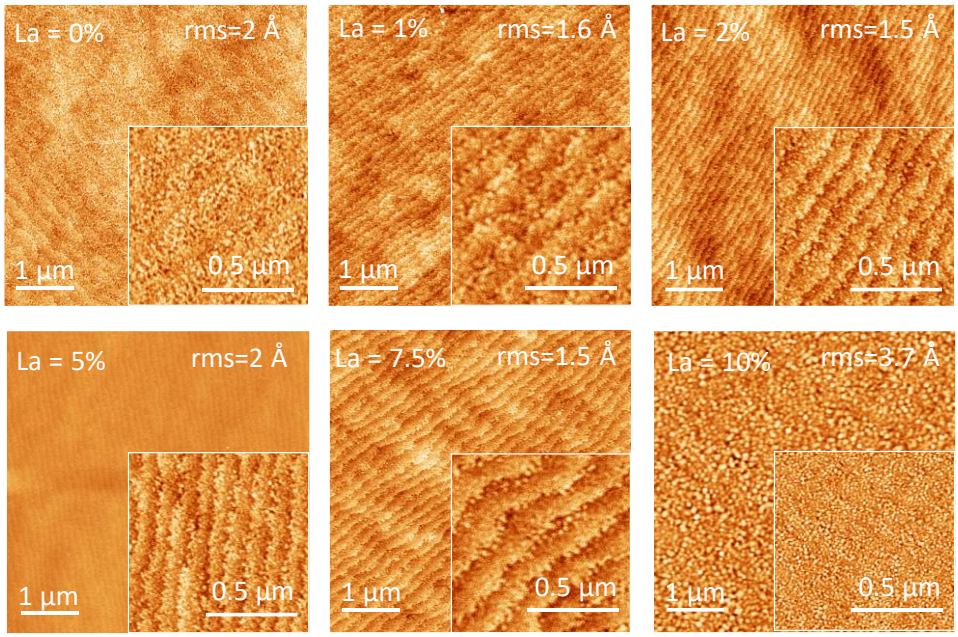

Figure 5.2.2 *Topographic AFM images of the La doped films on STO(001), scanned in 5 µm × 5 µm and 1 µm × 1 µm regions.*

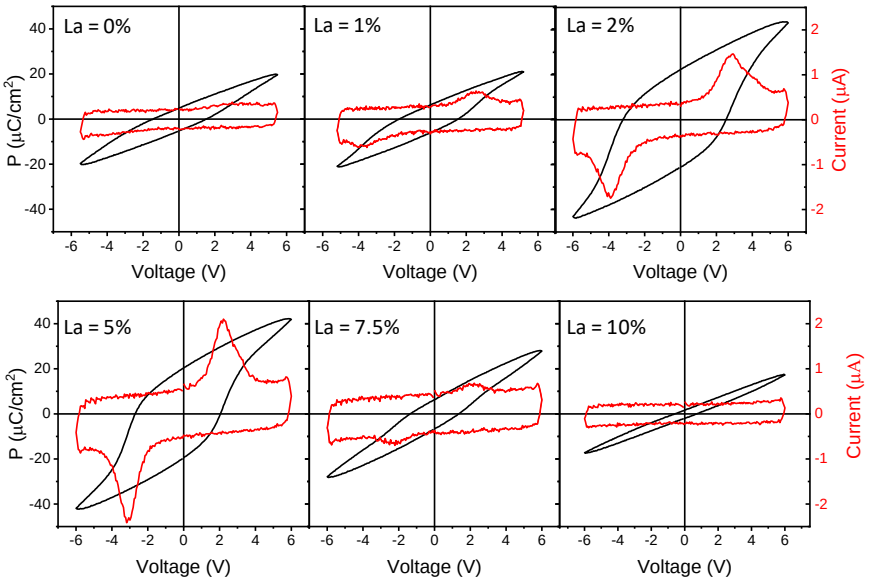

Figure 5.2.3 *Current-voltage curves (red lines) and polarization loops (black lines) of the series of La:HfO_2 films on STO(001). The La concentration is indicated in the label at the top left of each panel.*

The current-voltage curves (red lines) and polarization loops (black lines) of the films on STO(001) measured in the pristine state by the DLCC method is shown in Figure 5.2.3. In the pure HfO_2 film, the switching current is small with low remanent polarization around 5 µC/cm^2. With La content increase, the amplitude of the ferroelectric switching

current and remanent polarization become greater. The highest remanent polarization around 22 μC/cm^2 is obtained in film doped with 2 at% La, and slightly drops to ~ 20 μC/cm^2 in 5 at% La doped films. The polarization decreases in the films with a higher amount of La, being P_r ~ 6.5 μC/cm^2 in the 7.5 at% La film, while the 10 at. % La film does not show ferroelectric switching peaks. The corresponding current-voltage and polarization loops of films on Si was indicated in Figure 5.2.4. A similar dependence on the La concentration can be observed, with P_r above 25 and 20 μC/cm^2 in the 2 and 5 at% La doped films, respectively.

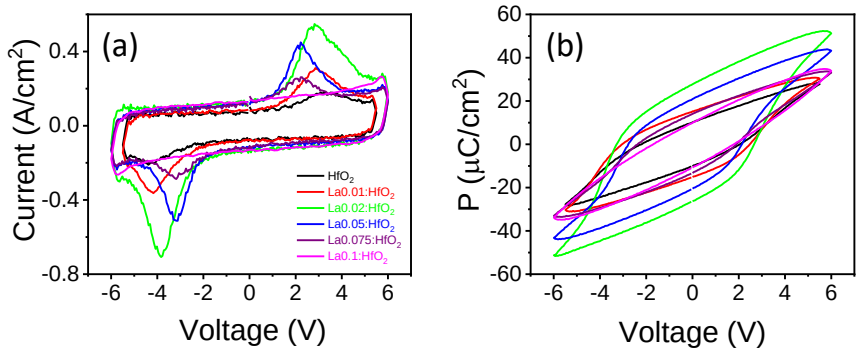

Figure 5.2.4 *Current-voltage curves and polarization loops of films on Si substrate measured by DLCC are in (a) and (b), respectively.*

The dependence of the remanent polarization of the epitaxial films on STO(001) (solid red rhombi) and Si(001) (solid blue diamonds) on the La concentration is shown in Figure 5.2.5. The optimized La concentration is in the range of 2-5 at% for the films deposited on both substrates. Meanwhile, the report by Li et al.[159] for a t = 12 nm epitaxial 5.5 at% La doped film (solid orange square) fits well to our data. The other data reported for polycrystalline films have also been plotted in Figure 5.2.5. It can be seen that the optimized La content reported by Chernikova et al.[58] (open blue triangles) and Schenk et al.[153] (open pink triangles) do not differ greatly from the epitaxial films. However, the data reported by Mart et al.[155] (open gray circles) and particularly by Schroeder et al.[154] (open gold triangles) indicate that a higher La content is needed to get the largest polarization. The reason of this could be La segregation depending on the preparation conditions, or different strain effect under capping layer. Because epitaxial films are closer to intrinsic HfO_2 than polycrystalline films, a concentration of 2-5 at% is estimated to be optimal to stabilize the ferroelectric phase in La-doped HfO_2.

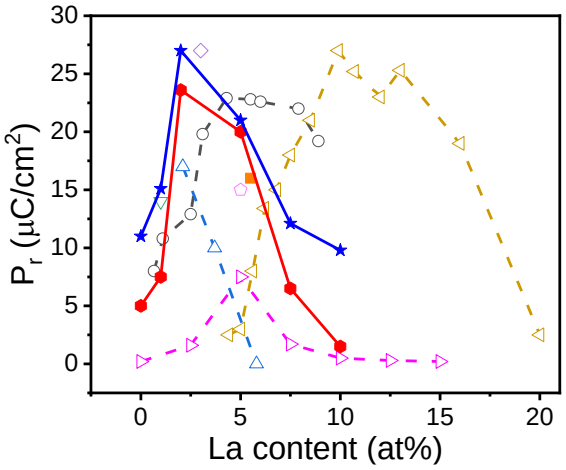

Figure 5.2.5 *Dependence of the remanent polarization with the La concentration of the epitaxial films on STO(001) (solid red diamonds) and Si(001) (solid blue stars). The empty red diamond and empty blue star correspond to 2 at. % t = 6.9 nm epitaxial films grown by using same conditions on STO(001) and Si(001), respectively. The remanent polarization of a t = 12 nm epitaxial film on STO(001) reported by Li et al. is indicated by a solid orange square. Data of series of polycrystalline films with varied La concentration are shown with open gray circles (t = 10 nm), open up blue triangles (t = 10 nm), open pink right triangles (t = 45 nm), and open gold left triangles (t = 10 nm). Other reported data of polycrystalline films with fixed La concentration are indicated by open pink pentagon (t = 45 nm)*[160] *and open violet diamond (t = 50 nm).*[69]

Figure 5.2.6 shows the influence of La concentration on the coercive fields (E_C). The solid symbols indicate the E_C value reported for epitaxial films. Open symbols indicate reported E_C values for polycrystalline films. It can be seen from Figure 5.2.6a that the monotonic decrease of E_C from 4.42 to 2.55 MV/cm with La concentration increase is remarkable. The same dependence is observed in the films on Si(001), with a decrease in E_C from 4.92 to 3.1 MV/cm. And the E_C value of an epitaxial La:HfO_2 film on STO(001) reported by another group (solid right green triangle) fits very well with the E_C-La content dependence of our epitaxial films.[159] The decrease of the E_C of the epitaxial film with La content increase could be due to a greater number of defects that would facilitate domain switching.[154] The epitaxial La-doped HfO_2 films also indicates a larger coercive field than that of polycrystalline films. The E_C values of most polycrystalline films range from 0.5 to 1.7 MV/cm (empty symbols) without a clear dependence on La content. Schroeder et al.[154] noted a slight decrease in E_C with La concentration (for simplicity, we only show two of the reported values). More recently, they have reported $E_C \sim 3$ MV/cm in $t = 10$ nm polycrystalline La:HfO_2 films.[161] The reasons for the smaller E_C in polycrystalline films could be the greater quantity of defects or larger

lateral grain size than that in epitaxial films.[161,162] Furthermore, $E_C \sim t^{-2/3}$ scaling is reported for epitaxial films,[23,65,163] but it has rarely been observed with polycrystalline films. A more recent report shows a strong dependence of the coercive field of polycrystalline HZO and La:HfO_2 (the concentration of La is not indicated) on thickness of the film and the grain size. As indicated in Figure 5.2.6b, the E_C values are very high, and the comparison with equivalent epitaxial HZO[65] and La:HfO_2 films[163] evidences that (1) the polycrystalline films (HZO and La:HfO_2)[161] exhibit $E_C \sim t^{-2/3}$ scaling and have E_C values similar to epitaxial films of the same thickness and (2) E_C values are slightly higher in La:HfO_2 than in films of HZO of the same thickness.

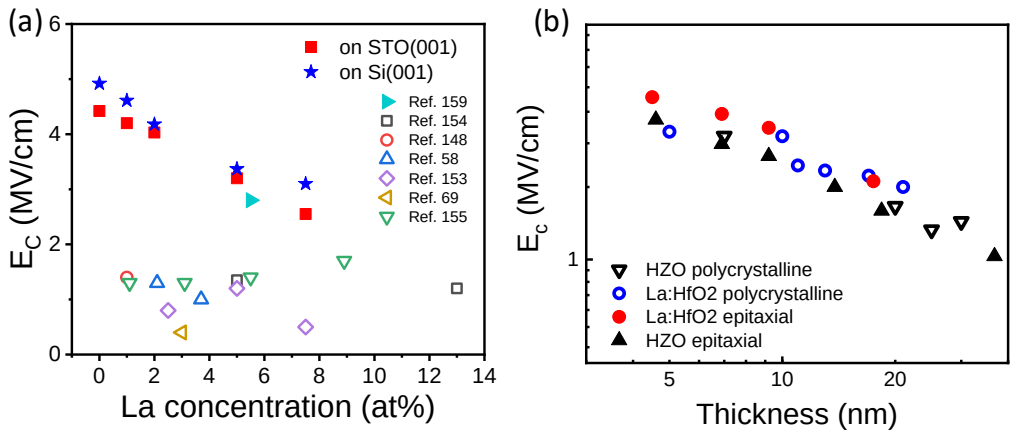

Figure 5.2.6 *(a) Coercive electric field dependence of La concentration for epitaxial films on STO(001) (solid red squares) and Si(001) (solid blue stars). Values were determined from the current peak position on the current-voltage curves measured by DLCC. Open symbols indicate reported E_C values for polycrystalline films. (b) Comparison of E_C values that we report for epitaxial HZO films*[31] *and La:HfO_2 films*[163] *and the ones reported for polycrystalline HZO and La:HfO_2 films by Materano et al.*[161]

The leakage curve of the films on STO(001) and Si(001) are shown in Figure 5.2.7a-b. The pure HfO_2 film (0 at. % La) on STO(001) exhibits leakage current of $\sim 5 \times 10^{-6}$ and $\sim 5 \times 10^{-7}$ A/cm^2 at 2 and 1 V, respectively. In the doped films, leakage decreases down to $\sim 1 \times 10^{-6}$ A/cm^2 (at 2 V) and $\sim 2 \times 10^{-7}$ A/cm^2 (at 1 V) with La concentration >1 at. % (Figure 5.2.7c). The leakage current values are similar to those commonly reported in doped HfO_2 polycrystalline films with similar thickness.[86] The leakage current values of epitaxial La:HfO_2 films on Si(001) (Figure 5.2.7d) show similar dependence to that on STO(001). Leakage current decreases with La concentration increase. However, the leakage current, particularly at high voltage, is greater than that in the equivalent films on

STO(001). Similarly larger leakage current in epitaxial Zr doped HfO_2 films on STO-buffered Si(001) was previously reported.[163,164] The higher leakage of films on Si(001) could be due to differences in the grain boundaries density or in grain boundaries microstructure. When measuring leakage current, a rather long voltage pulse (2s) is applied, under this condition, ionic motion at grain boundary may introduce some contributions.[165,166]

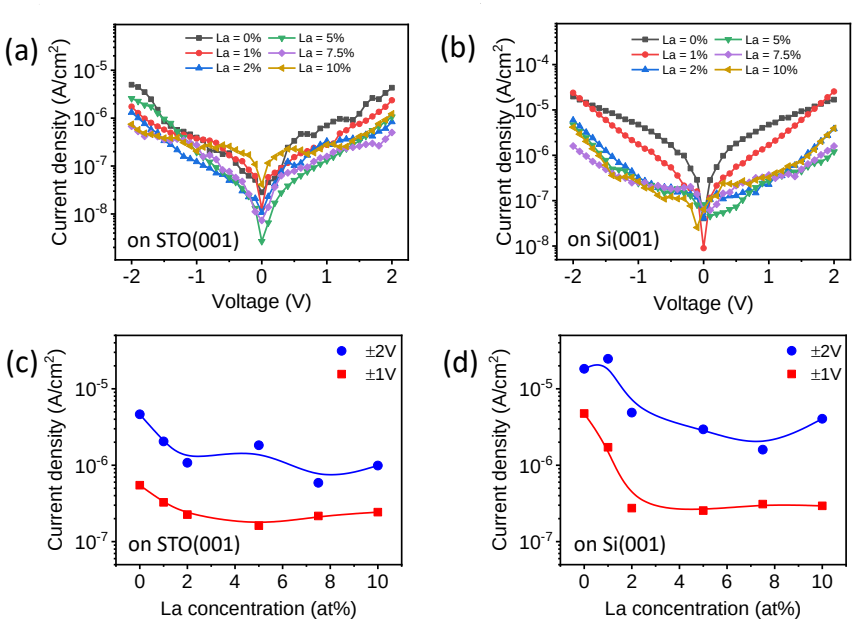

Figure 5.2.7 *Current leakage curves of the films on STO(001) (a) and Si(001) (b). Dependence of the current leakage at 1 V (red squares) and 2 V (blue circles) on the La concentration in films on STO(001) (c) and Si(001) (d). The current leakage values in (b) and (c) are the average values at positive and negative bias.*

The dielectric constant loops of the films on STO(001) and Si(001) are plotted in Figure 5.2.8a and b. In the pure HfO_2 film and 1% La doped HfO_2 film, there is almost no hysteresis. With La content increase, hysteresis becomes evident in films with 2-7.5 at% La doped, and more saturated permittivity loop is observed in 5 at% La films. The reason why permittivity loops with higher La content are more saturated is that coercive field is relatively lower, as indicated in Figure 5.2.6a. Therefore, dielectric loop is more saturated in films with higher La content, although a lower ferroelectric polarization is shown in those films. Further increase La content to 10%, results in narrower hysteresis and lower permittivity. The tendency of the permittivity loop shape on La content is the same in the films deposited on STO(001) and Si(001). There are also large differences in the dielectric constant values of the films. Figure 5.2.8c shows the dependence of the permittivity at

high voltage as a function of La concentration for films on STO(001) (red down triangles) and Si(001) (blue up triangles). The dielectric constant increase with La concentration increase, and in general, the values are higher in the films deposited on Si substrate. It can be seen that the dielectric constant is 21-27 in undoped and 1 at% films, and up to 30-35 in films with La concentration higher than 5 at%. What has been reported in polycrystalline films is that dielectric constant is around 24-29, 24-57, 36, and 19-25 for the orthorhombic, tetragonal, cubic, and monoclinic phases, respectively.[37,167] The relatively low dielectric constants in pure HfO_2 film and 1% La doped HfO_2 film is consistent with the coexisting of monoclinic phase in these films. Meanwhile, the high dielectric constant in films doped with more La also indicates the possibility of more cubic phase formed in these films, which is in agreement with the results reported in polycrystalline.[58,154] The dielectric constant reflects the crystalline phase evolution with La content, which is consistence to the dependence of P_r on the La content. Namely, the optimized La concentration for high polarization is 2-5 at%, and when the La concentration is lower or higher, more monoclinic or cubic phase will decrease the P_r value.

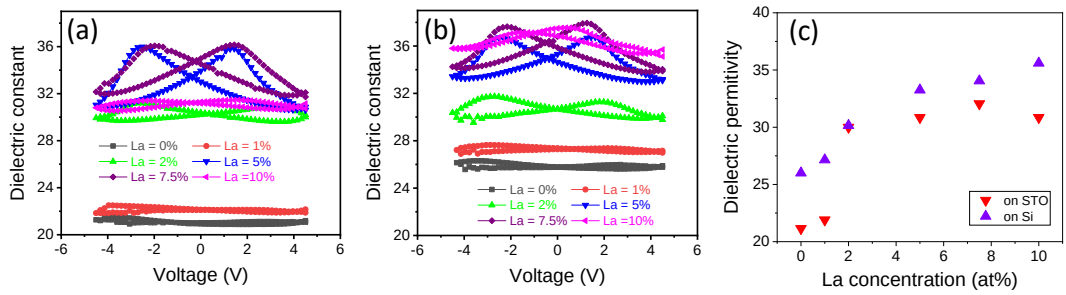

Figure 5.2.8 *Dielectric constant loops of the films on STO(001) (a) and Si(001) (b). (c) Dependence of the dielectric constant at high field (average values at positive and negative bias) on the La concentration of films on STO(001) (red down triangles) and Si(001) (top blue triangles).*

The endurance of 2 and 5 at% La doped HfO_2 film is shown in Figure 5.2.9a. The films on STO and Si were measured under 5V and 4.5V, respectively. It can be seen that wake-up effect exists in both cases, but is limited to first few cycles. After the first ten cycles, the films start to suffer fatigue. The memory window of 2 at% La doped film (black squares) on STO decreases from ~ 25 to 4.6 $\mu C/cm^2$ after 10^9 cycles. Comparatively, higher memory window indicates in 5 at% La doped film (red circles), and it decreases slowly from 31.5 $\mu C/cm^2$ to 25 $\mu C/cm^2$ after 10^7 cycles and then drops to 5 $\mu C/cm^2$ after

10^{10} cycles. The larger P_r and superior endurance under 5V cycling of 5 at% La doped film are a consequence of the lower coercive field, which allows more saturated ferroelectric switching under a relatively lower electric field to avoid dielectric breakdown and severe fatigue. Interestingly, the endurance result is comparable to the best reported value in polycrystalline film,[58] even though a higher voltage is applied, which indicates a lower defects amount in our epitaxial film. On the other hand, the endurance of the samples with the same composition grown on Si are also shown in Figure 5.2.9. It can be observed that dielectric breakdown occurs at 10^8 and 10^9 (empty symbols) for 2% and 5% La doped films, respectively. The faster breakdown is probably related to the higher leakage of films grown on Si compared to those grown on STO. Apart from the endurance, we also measured the retention of the 5 at% La doped film on STO(001) and Si(001) measured at 85 °C after positively or negatively poled at 5V and 4.5V, respectively, as shown in Figure 5.2.9b. Good retention can be achieved in both films, with extrapolated P_r retaining longer than 10 years for both up and down polarization states after being poled at 5 V and 4.5 V, respectively.

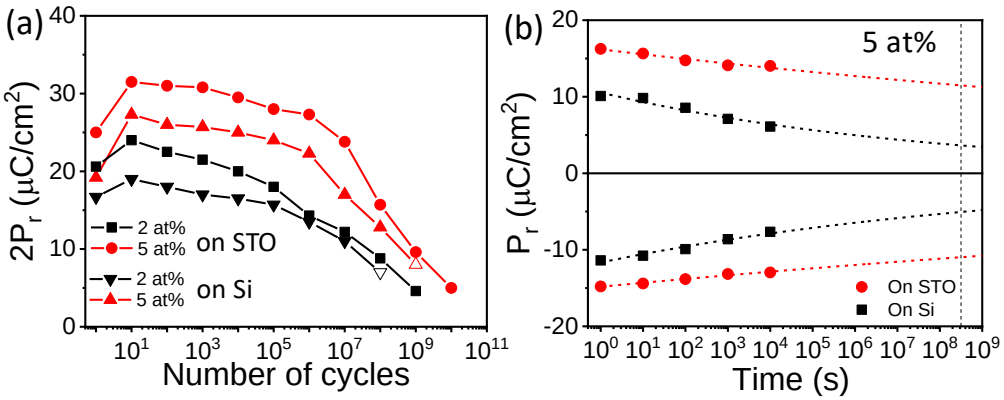

Figure 5.2.9 *(a) Polarization window ($2P_r$) as a function of the number of bipolar cycles of amplitude 5 V of films on STO(001) with La concentration 2 at% (black squares) and 5 at% (red circles), 4.5 V of films on Si(001) with La concentration 2 at% (black down triangles) and 5 at% (red up triangles). (b) Retention of the 5 at% film on STO(001) and Si(001) measured at 85 ℃ after poled positively or negatively at 5V and 4.5V, respectively. Red dashed lines are fits to $P_r = P_0 \cdot t_d^{-n}$ (see ref. [163]). The vertical black dashed line marks a time of 10 years.*

Conclusion

In summary, the impact of La content on the crystalline phase and ferroelectricity has been systematically investigated by growing La doped HfO_2 films on LSMO buffered STO(001) and Si(001). The optimized concentration is 2-5 at%, with greater amount of

orthorhombic phase and high remanent polarization above 20 μC/cm^2. With less doping content, the films have larger amount of monoclinic phase, while the cubic phase appears in films doped with high La content. The coercive field and leakage current of the films on both substrates decrease with the concentration of La. The 5 at% La doped film on STO has high remanent polarization and endurance up to 10^{10} cycles with high extrapolated polarization after 10 years at 85 °C. The equivalent film on Si has higher leakage current and limited endurance to 10^9 cycles, but still with long retention.

5.2.2 Impact of thickness on La doped epitaxial hafnium film

The structural information of 2 at% La doped HfO_2 films with thickness ranging from 4.5 to 17.5 nm are shown in Figure 5.2.10. The XRD 2θ-χ maps (Figure 5.2.10a) present bright spots around χ=0 ° in all films. The spots at 2θ ~23° and ~47° correspond to (001) and (002) reflections of the STO substrate and LSMO electrode. The other spots are related to the reflections from La:HfO_2 films. It can be seen that a bright circular spot at 2θ ~30°, the position of o(111) reflection, presents in all films. An elongated bright spot that corresponds to m(-111) can be observed in the 17.5 nm film. The reflection of m{002} is nearly not visible in all films. The right panel indicates the XRD 2θ-χ maps of the equivalent series of La doped HfO_2 films on Si(001). Similar results reveal the o phase formation in all thickness, but with slightly higher intensity of m{002} reflections. In figure 5.2.10b, θ-2θ scans around the main reflections of the La:HfO_2 film, measured with a point detector, are presented. The o(111) reflection with Laue fringes can be clearly observed in all films on STO and Si substrates, with m(-111) in thicker films (17.5 nm) but not in the thinner ones. Meanwhile, slightly m{002} is present in 9.2 and 17.5 nm films, but nearly not visible in thinner films. The out-of-plane lattice parameter of $d_{o\text{-}(111)}$ is determined from the position of the corresponding diffraction peak in the θ-2θ scans (as shown in Figure 5.2.10c). In the films grown on STO(001), the $d_{o\text{-}(111)}$ value of 4.5 nm film is close to 3 Å and with thickness increase, the $d_{o\text{-}(111)}$ value decreases to less than 2.98 Å in films with thickness more than 10 nm. The films on Si(001) show the similar dependence between $d_{o\text{-}(111)}$ value and thickness, but with smaller lattice parameter in the range of 2.95-2.96 Å. The lower $d_{o\text{-}(111)}$ of the films on Si(001) is due to the low coefficient of thermal expansion of Si(001), which introduces tensile stress in the films when cooling down after growth.[168] The $d_{o\text{-}(111)}$ value of equivalent La:HZO films are also plotted,[164] indicating similar dependence with La:HfO_2 films, but the $d_{o\text{-}(111)}$ parameters of the La: HZO films are slightly smaller. The pole figures around the o(-111) reflections of La:HfO_2 and (111) of STO(Figure 5.2.10d) of the t = 17.5 nm film on STO(001) confirm the epitaxy of the orthorhombic phase. The twelve o(-111) poles indicate the presence of four in-plane crystal variants of o-HfO_2. The epitaxial relationships with the STO substrate are [1-10]o-HfO_2(111)//[1-10]STO(001) and [11-2]o-HfO_2(111)//[1-10]STO(001).

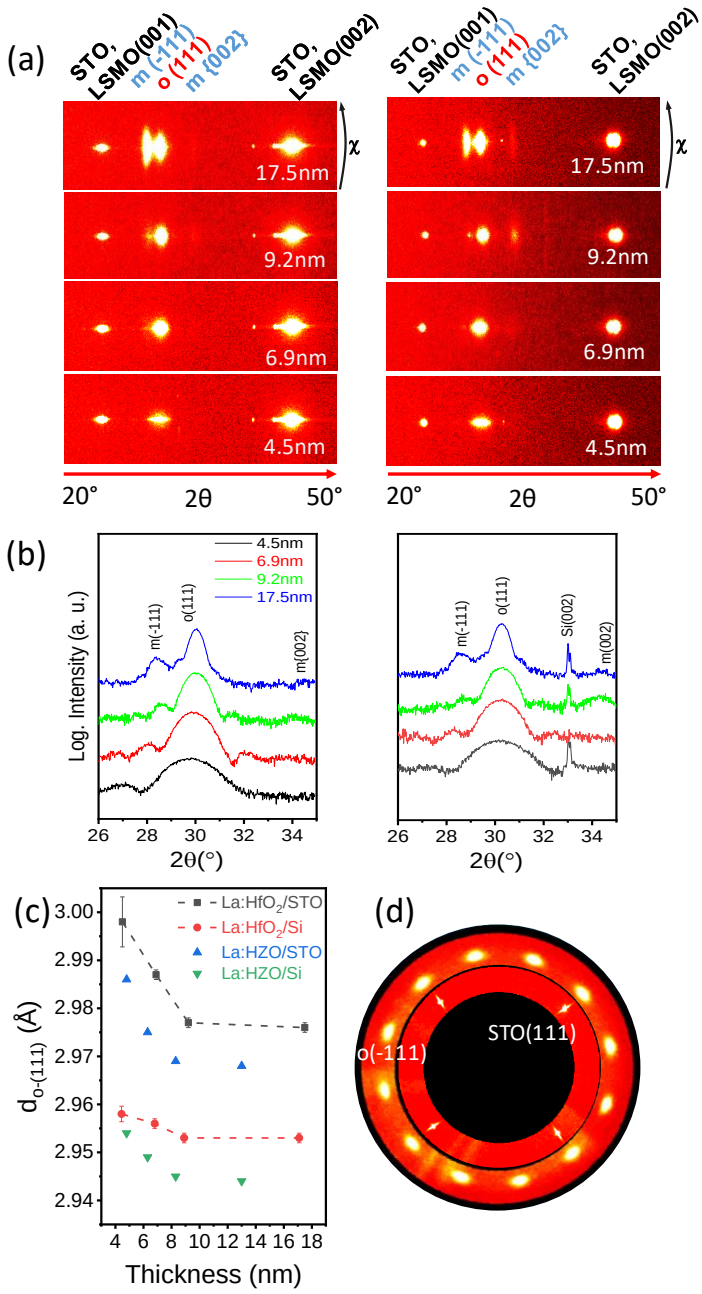

Figure 5.2.10 *XRD measurements of the La:HfO_2 films on STO(001) (left side) and Si(001) (right side): (a) XRD 2θ-χ maps obtained with a 2D detector. The χ range is from -10° to +10°. (b) XRD θ-2θ scans of films on STO(001) (left side) and Si(001) (right side)obtained with a point detector. (c) Out-of-plane lattice parameter determined from the θ-2θ scans. (d) Pole figures around o(-111) and STO(111) reflections of the t = 17.5 nm film on STO(001).*

The AFM topographic images of the La doped HfO_2 films on STO(001) with different thickness are shown in Figure 5.2.11. The formation of terraces and steps can be clearly observed in all films, indicating a flat surface condition. The root mean square roughness of the 5 μm × 5 μm area is less than 2 Å in 4.5 nm, 6.9 nm, and 9.2 nm film, and slightly higher in 17.5 nm film (2.8 Å).

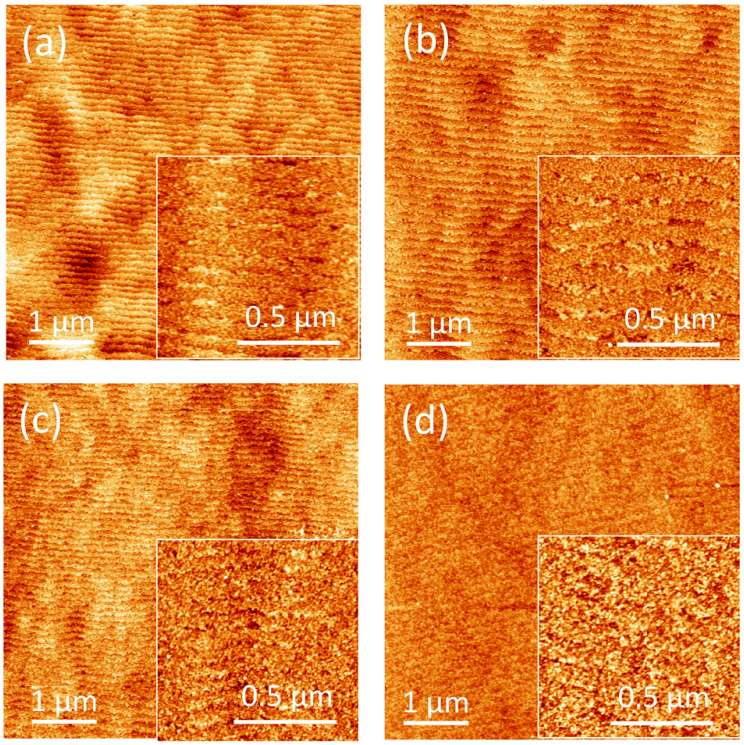

Figure 5.2.11 *Topographic AFM images (5 μm × 5 μm) of La:HfO_2 films on STO(001) with a thickness of (a) 4.5 nm, (b) 6.9 nm, (c) 9.2 nm, and (d) 17.5 nm. Insets: 1 μm × 1 μm topographic images.*

The ferroelectric polarization loops of films deposited on STO(001) and Si(001) are shown in Figure 5.2.12a-b. The loops are measured under the maximum electric field that can be applied to the thin films, and after 10 times cycles to avoid the possible wake-up effect discussed as follows and obtain comparable results. It can be seen that high remanent polarization can be obtained in 4.5 nm and 6.9 nm films with P_r around 26 and 30 μC/cm^2, respectively. With further increase of thickness, the value decreases to around 10 μC/cm^2 in 17.5 nm film. Similarly, in films deposited on Si substrate, the highest remanent polarization is obtained in 6.5 nm film with P_r about 32 μC/cm^2. Note that the round shape of the loops near the maximum applied electric field is a symbol of the influence from leakage current, which can result in a possible overestimation of the remanent polarization within 2 μC/cm^2.[31] The dependence of the P_r on the thickness of the films on STO and Si substrates are plotted in Figure 5.2.12c. Both series exhibit a similar thickness dependence, with the maximum P_r in the 6.9 nm films. And with thickness decrease, the P_r decrease to around 26 μC/cm^2 in 4.5 nm films, and with thickness increase, the P_r decrease to around 10 μC/cm^2 in 17.5 nm films. Compared with the former results in epitaxial HZO and La doped HZO films on Si, here, films thinner

than 5 nm have the highest P_r.[65,164] The dependence of the coercive electric field and film thickness is indicated in Figure 5.2.12d. On both STO(001) and Si(001) substrates, the coercive filed decreases linearly with the increase of the thickness (in the logarithmic scale), with a slop around 0.5. It follows approximately the $E_C \propto t^{-2/3}$ dependence usually observed in high-quality ferroelectric perovskite films[169–171] and epitaxial HfO_2-based films.[65,164]

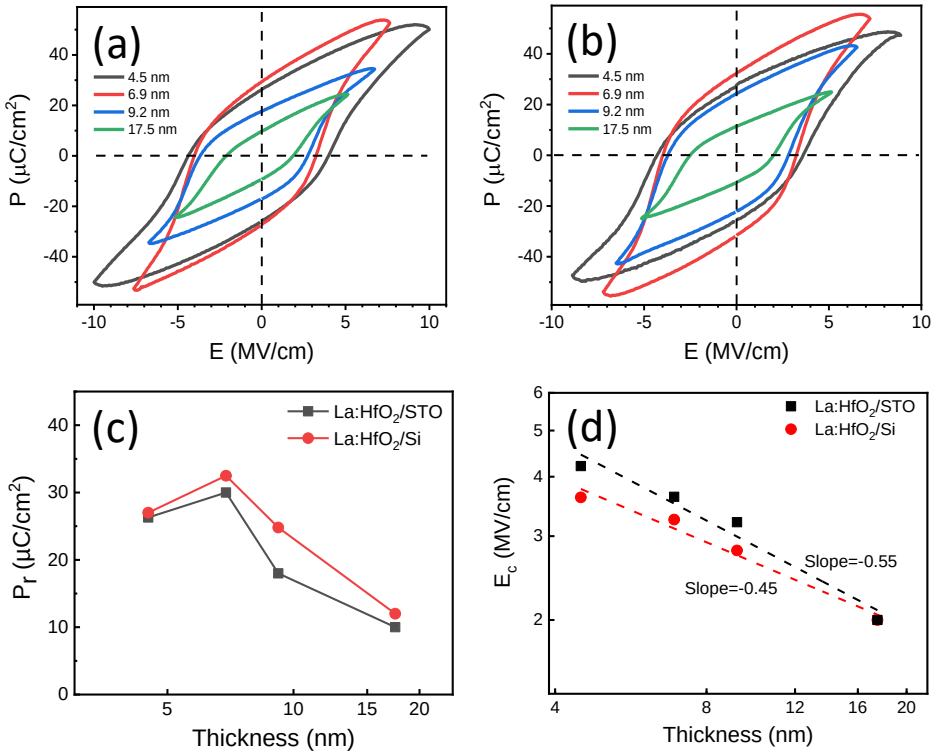

Figure 5.2.12 *Polarization loops of the films on (a) STO(001) and (b) Si(001). Dependence on the thickness of the remanent polarization (c) and the coercive electric field (d) of the films on STO(001) (black squares) and Si(001) (red circles).*

The wake-up effect in La doped HfO_2 films is explored under high electric field (Figure 5.2.13) and lower electric field (Figure 5.2.14). The wake-up effect can be evidenced from double switching peaks in the current-voltage curves, simultaneously, causing a shrinkage of the polarization loop. This phenomenon can be observed in 4.5 nm, 6.9 nm and 9.2 nm films, as indicated in Figure 5.2.13a-c. However, the wake-up effect is nearly limited to the first cycles and the influence on the polarization value is negligible. In thicker films (17.5 nm), there is no visible wake-up effect (Figure 5.2.13d). Comparatively, when applying a lower electric field to cycle films (Figure 5.2.14), a more pronounced wake-up effect can be observed, leading to a longer increase of polarization

after cycling. Generally, the redistribution of oxygen vacancies or phase transition under electric field cycling are proposed as the reason for wake-up effect.[156] In polycrystalline La:HfO_2 films, the wake-up effect is explained by the redistribution of oxygen vacancies induced phase transition (from monoclinic phase to orthorhombic phase).[74] Compared to polycrystalline La:HfO_2 films,[58,74,148] the wake-up effect in epitaxial films is less pronounced. The possible reasons[23] for the negligible wake-up effect in epitaxial films compared to that of polycrystalline films are that (i) more stable electrodes (LSMO and Pt) used against oxidation, (ii) a lower number of defects in optimized epitaxial films, and (iii) a semi-coherent interface between the bottom electrode and the epitaxial HfO_2 film. The dropping of high residual leakage at the maximum applied voltage after cycling also indicates the redistribution of the defects in the film, especially in thinner films (Figure 5.2.13a-b).

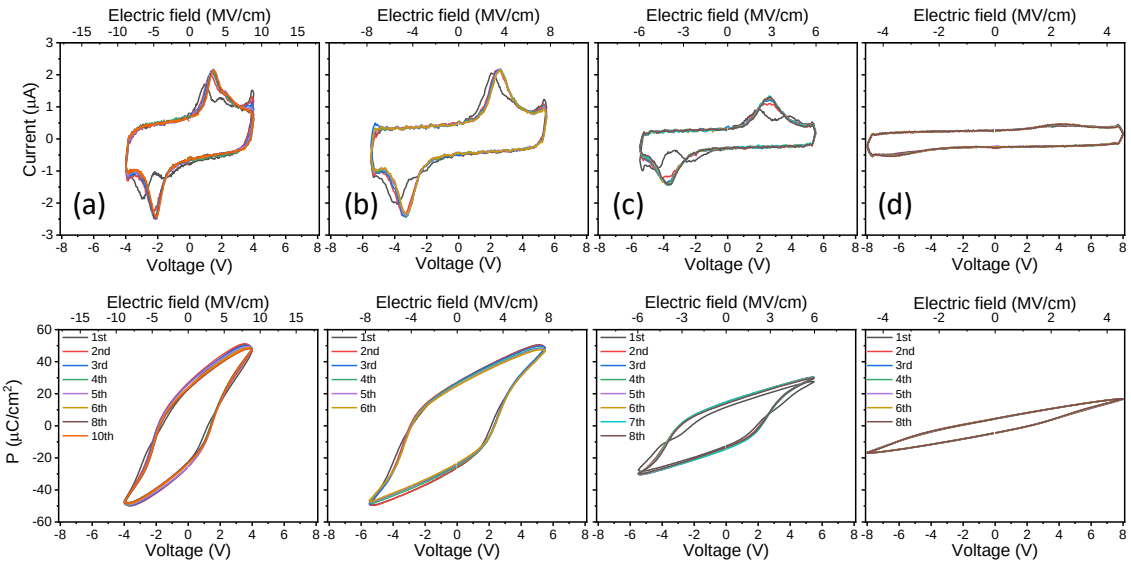

Figure 5.2.13 *Evolution with the number of cycles of current-voltage curves and the corresponding polarization loops of films on STO(001) with a thickness of (a) 4.5 nm, (b) 6.9 nm, (c) 9.2 nm, and (d) 17.5 nm under high voltage.*

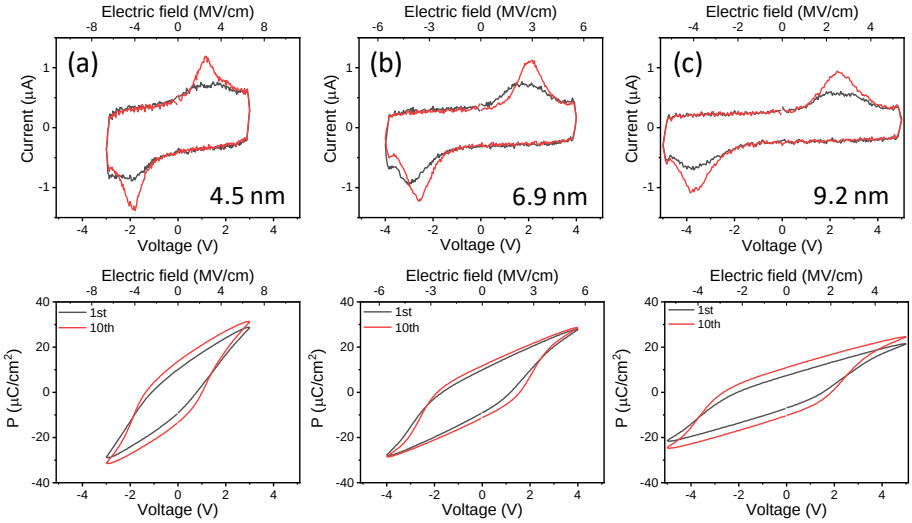

Figure 5.2.14 *Current-voltage curves and polarization-voltage loops in pristine state and after 10 cycles of La:HfO_2 films on STO(001) of thickness (a) 4.5 nm, (b) 6.9 nm, (c) 9.2 nm under lower electric field.*

The leakage current of La:HfO_2 films on STO and Si is shown in Figure 5.2.15a-b. It can be seen that the leakage current of films on STO is in the range of 8×10^{-4} A/cm^2 to 8×10^{-6} A/cm^2 at 2 MV/cm. The highest leakage current is in the 4.5 nm film because the utra-low thickness. And the lowest leakage presents in 17.5 nm film. Interestingly, the 6.9 nm film is also very insulating, with leakage current below 10^{-8} A/cm^2 at low electric field and less than 5×10^{-8} A/cm^2 at 1 MV/cm. Therefore, the 6.9 nm film combines high P_r of about 30 μC/cm^2 and low conductivity. The films on Si substrate shows higher leakage current, with the range of 9×10^{-3} A/cm^2 to 1×10^{-6} A/cm^2 at 2 MV/cm. Figure 5.2.15c-d indicate the dependence of leakage current with the film thickness at 1MV/cm and 2MV/cm. The overall tendency is that the higher leakage is present in the thinner film and the films on STO have lower leakage current. However, there is a local minimum in film with thickness around 7 nm. The reason is that leakage current is expected to decrease with film thickness increase, but on the other hand, the relative amount of monoclinic phase increase with thickness, thus leading to more incoherent grain boundaries between monoclinic phase and orthorhombic phase. And this kind of incoherent grain boundaries are known to act as current paths.[165] The combination of both factors affecting leakage cause the local minimum at a thickness of around 7 nm in the leakage current-thickness graphs. Figure 5.2.15e shows the dielectric loops of the films on STO(001). The loops with thickness lower than 9.2 nm have a well-defined butterfly shape, but with thickness up to 17.5 nm, there is nearly no open shape. The dielectric

constant also has a clear dependence with the film thickness. The dielectric constant is around 30 in 4.5 nm and 6.9 nm films, and it reduces to around 28 in 9.2 nm film and to around 24.5 in 17.5 nm film. The decrease of dielectric constant is in agreement with the observed increase of monoclinic phase in films with thickness increase.

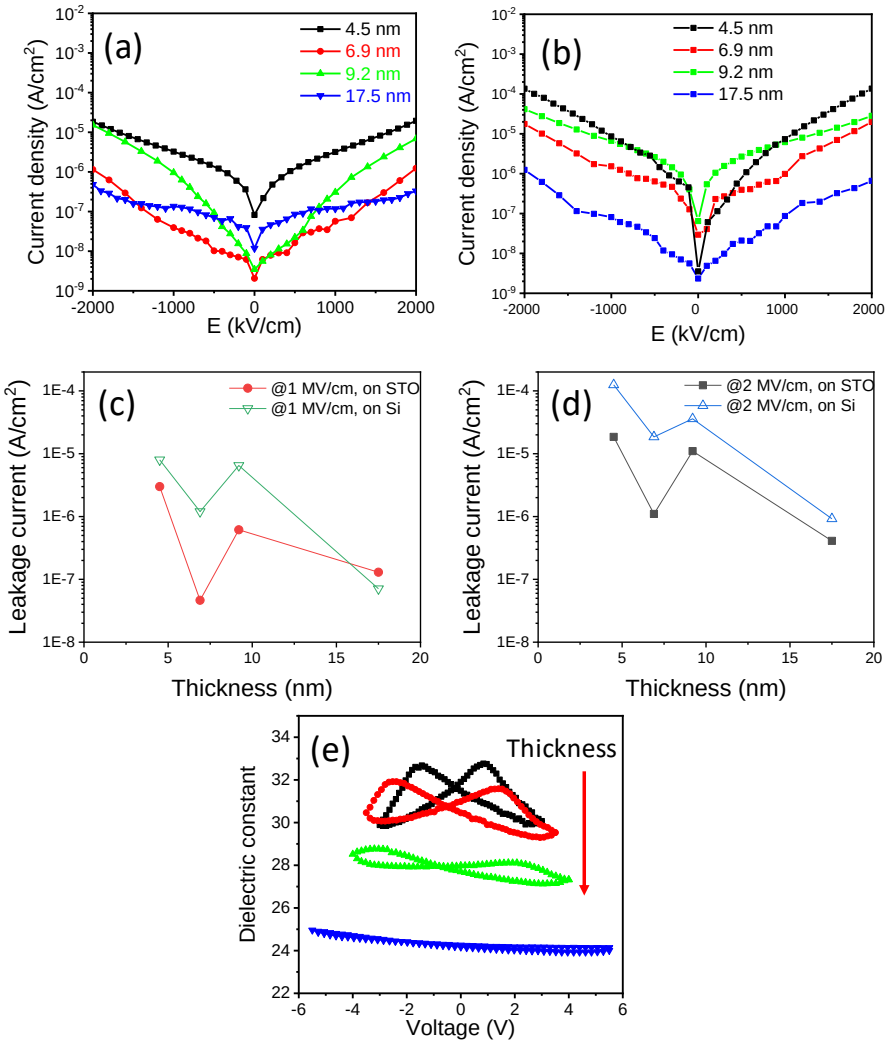

Figure 5.2.15 *Leakage current curves of the films on (a) STO(001) and (b) Si(001). Dependence of the leakage current at (c) 1 MV/cm and (d) 2 MV/cm for films on STO(001) (solid symbols) and Si(001) (empty symbols). (e) Dielectric constant loops of the films on STO(001).*

The endurance of the La:HfO_2 films on STO with different thickness are shown in Figure 5.2.16. In 4.5 nm film (Figure 5.2.16a), the pristine memory window is around 20 μC/cm^2. After 10 cycles, the value increases to 25 μC/cm^2, indicating slightly wake-up effect under electric field of 6.7 MV/cm, as discussed above. Further cycling results in gradually decrease of memory window and after 10^9 cycles, the $2P_r$ decreases to 6 μC/cm^2. A similar behaviour can be observed in 6.9 nm film (Figure 5.2.16b) when cycling under

5.8 MV/cm, with $2P_r$ around 2.8 μC/cm^2 after 10^{10} cycles. When cycling under higher electric field of 6.5 MV/cm and 7.2 MV/cm, highest memory window can be obtained at pristine state in 6.9 nm film, and then the capacitors suffer fatigue. $2P_r$ of 4 μC/cm^2 is left when cycling under 6.5 MV/cm after 10^{10} cycles, but there is a hard breakdown when cycling under 7.2 MV/cm after 10^9 cycles. The endurance of 9.2 nm film is similar to that of thinner films, but the endurance is highly degraded in 17.5 nm film. This is because relatively low memory window in 17.5 nm film. If higher voltage is applied, there is a fast hard breakdown. The ionic conduction path formed at the boundaries between monoclinic and orthorhombic grains, more abundant in thicker films, as shown in XRD characterization, can be a relevant contribution.[165]

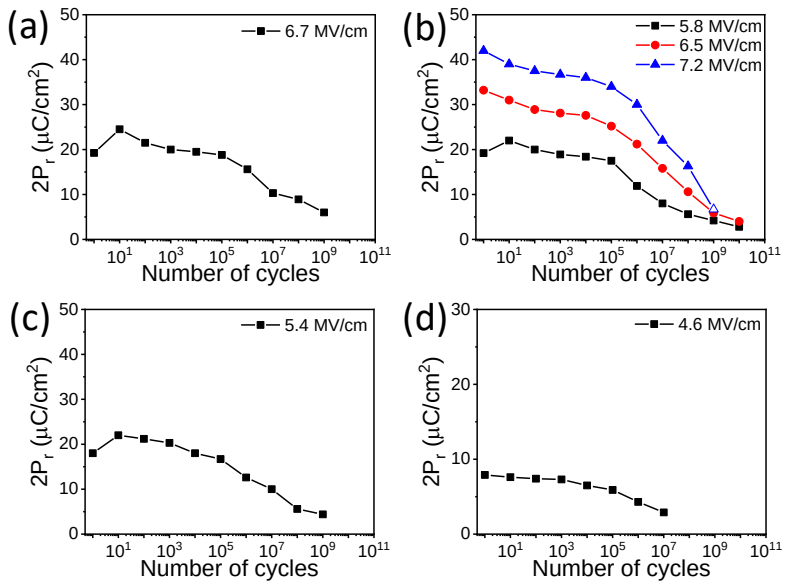

Figure 5.2.16 *Endurance measurements of the films on STO(001) with a thickness of (a) 4.5 nm, (b) 6.9 nm, (c) 9.2 nm, and (d) 17.5 nm. The electric field of the cycles is indicated in the top right of each panel.*

The influence of frequency on the fatigue and endurance has been explored in La:HfO_2 films on STO substrate (Figure 5.2.17). It can be seen that in 4.5 nm film, when cycling at 3V with 10kHz, the endurance is only 10^6 cycles and the capacitor suffers hard breakdown. When increase frequency to 1000kHz, the endurance can reach up to 10^9 cycles. Furthermore, the polarization values have been normalized to the maximum P_r under each frequency, and the result indicates that with frequency increase, a slower fatigue can be obtained in films. Similar results also present in films with other thickness. Starschich *et al.*[90] observed that hard breakdown occurred earlier, as the cycling frequency was lower, and they assumed that this was due to the suppression of generation

of oxygen vacancies at higher frequencies. Besides, a longer pulse also promotes the migration of free carriers towards domain walls, thus inducing a severer pinning effect.[92] On the other hand, there are also some reversal results about the influence of frequency on fatigue. Li *et al.*[159] reported the endurance of La:HfO_2 films, and the loss of polarization was more severe when the electric pulse was shorter. It was explained that the high density of charged domain walls in incompletely switched capacitors could be pinned and then cause fatigue. In the research of polycrystalline La:HfO_2 film,[172] the faster degradation under higher frequency was argued that oxygen vacancies migrated during each cycle from switchable regions to non-switchable regions, creating local fields. The intensity of the local field strength could increase with cycling until the domains of the initially switchable regions would be pinned.

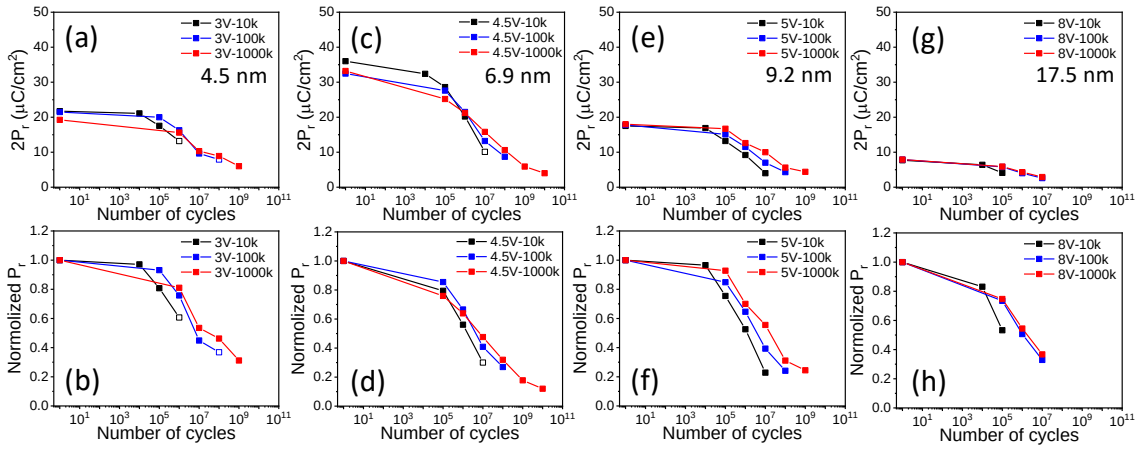

Figure 5.2.17 *Memory window and normalized polarization of La:HfO_2 on STO(001) films as a function of the number of cycles. Capacitors were cycled at a frequency of 10k (black squares), 100k (blue squares) and 1000k (red squares). The film thickness is (a-b) 4.5 nm, (c-d) 6.9 nm, (e-f) 9.2 nm, (g-h) 17.5 nm. The polarization values are normalized to the maximum P_r under each frequency. Open symbols indicate breakdown.*

The retention of the films with different thickness on STO substrate are shown in Figure 5.2.18. The electric fields used for retention measurement are the same as that for endurance measurement. The experimental data are fitted (blue and red dashed lines) by the rational dependence $P_r = P_0 \cdot t^{-n}$ to estimate the remanent polarization after 10 years, where P_0 is initial polarization. The black vertical dash line marks the position of 10 years delay time. It can be seen that all measured films retain a fraction of the initial polarization after extrapolating to 10 years. In 4.5 nm and 17.5 nm films, the retained polarization is around 53% of the initial value. However, in 6.9 nm and 9.2 nm films, the percentage of retained polarization can as high as 69% and 63%, respectively.

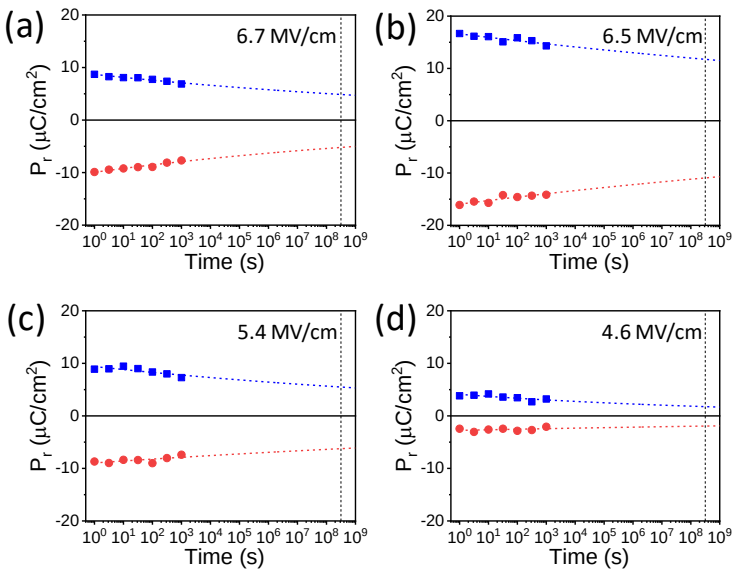

Figure 5.2.18 *Retention measurements of the films on STO(001) with a thickness of (a) 4.5 nm, (b) 6.9 nm, (c) 9.2 nm, and (d) 17.5 nm, and for positive (blue squares) and negative (red circles) poling fields. The electric field of the cycles is indicated in the top right of each panel.*

The wake-up effect of the 6.9 nm film on Si(001) is small and limited to a very few cycles, with P_r increasing from 32.4 to 34.1 μC/cm^2 under cycling field of 4V. Then, the P_r gradually decrease with cycling, being $2P_r$ = 5.2 μC/cm^2 after 5×10^9 cycles without dielectric breakdown. The film also exhibits excellent retention after being poled with the same electric field used to determine the endurance, maintaining 69% of the initial memory window.

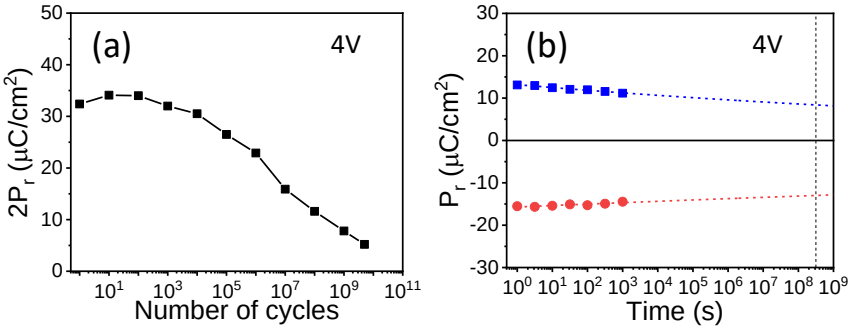

Figure 5.2.19 *Endurance (a) and (b) retention of the 6.9 nm La:HfO_2 film on Si(001).*

Conclusion

In summary, epitaxial 2% La doped HfO_2 films with thickness ranging from 4.5 nm to 17.5 nm were grown on both STO and Si substrates. The films are dominated by 111 oriented orthorhombic phase, with an increased fraction of monoclinic phase in films thicker than 10 nm. Films of less than 7 nm thickness show a high remanent polarization

of about 30 μC/cm^2, slight wake-up, an endurance of at least 10^{10} cycles and a retention of more than 10 years, with the endurance and retention measured at the same poling voltage. La-doped HfO_2 films even as thin as 4.5 nm also show robust ferroelectricity.

5.2.3 Impact of epitaxial stress on La:HfO_2 film

5.2.3.1 Film growth

Epitaxial bilayers of 2 % La:HfO_2 (LHO) films on bottom LSMO bottom electrodes (t = 25 nm) were grown in a single process by PLD (KrF excimer laser). A set of (001)-oriented cubic and (110)-oriented rhombohedral and orthorhombic substrates were used. For the sake of simplicity, a pseudocubic cell is used here for the rhombohedral and orthorhombic substrates, their orientation being (001) in this setting. The lattice (cubic or pseudocubic) parameter of the used substrates is in the a_s = 3.71-4.21 Å range. The La:HfO_2 films were deposited at a substrate temperature of 800 °C under a dynamical oxygen pressure of 0.1 mbar.

5.2.3.2 Structure characterization

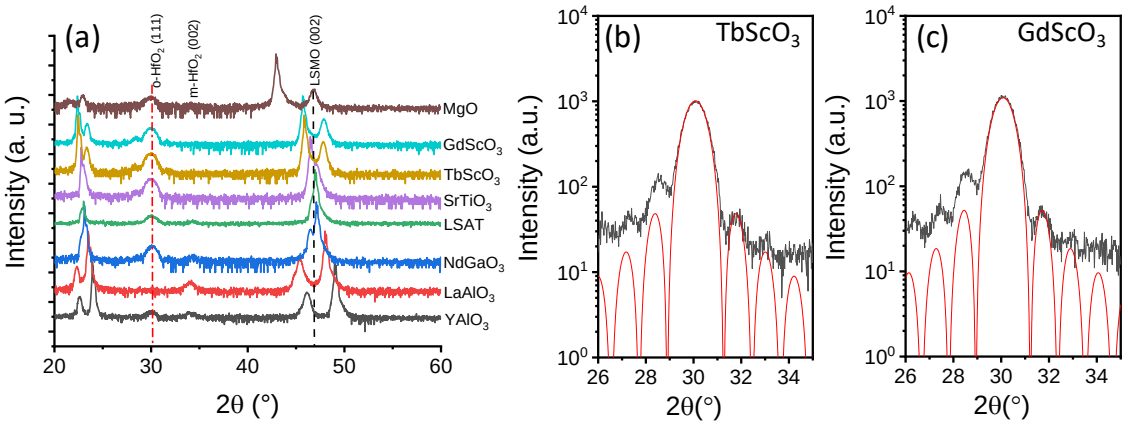

Figure 5.2.20 *(a) XRD θ-2θ symmetric scans of films deposited on different substrates. XRD θ-2θ symmetric scans around the o(111) reflection of the (b) LHO/LSMO/$TbScO_3$ and (c) LHO/LSMO/$GdScO_3$ with longer acquisition time. The red curves are simulated result.*

The XRD θ-2θ symmetric scans of all films are investigated. The red vertical dash line indicates the position of o(111) reflection from La:HfO_2 films and the black dash line marks the position of the (002) reflection in bulk LSMO. It can be seen that the LSMO (002) peak position varies with the applied substrates because the misfit induced between the substrate and LSMO. In contrast, there is no significant variation of the peak position of o(111) reflections. What's interesting is that the intensity of o(111) reflections of La:HfO_2 films depends strongly on the substrates. A very low intensity of o(111) reflections presents in the films deposited on $(LaAlO_3)_{0.3}(Sr_2TaAlO_6)_{0.7}$ (LSAT), $LaAlO_3$(LAO) and $YAlO_3$(YAO). Comparatively, a higher intensity indicates in the films deposited on scandate substrates, like $TbScO_3$ and $GdScO_3$. The film thickness is

determined by Laue simulation around the Laue fringes from the o(111) reflections, as indicated in Figure 5.2.20. The fitted thickness is around 8.8 and 9.1 nm for films deposited on $TbScO_3$ and $GdScO_3$, respectively. The surface condition of all films is revealed by AFM topographic images. It can be seen that the film surface is flat, with root mean square (rms) less than 4 Å, and a morphology of terraces and steps can be appreciated in some of the images. The rms roughness is plotted as a function of the lattice parameter of the substrate, indicating that surface roughness is around 2 Å except for the film on MgO (around 3.2 Å).

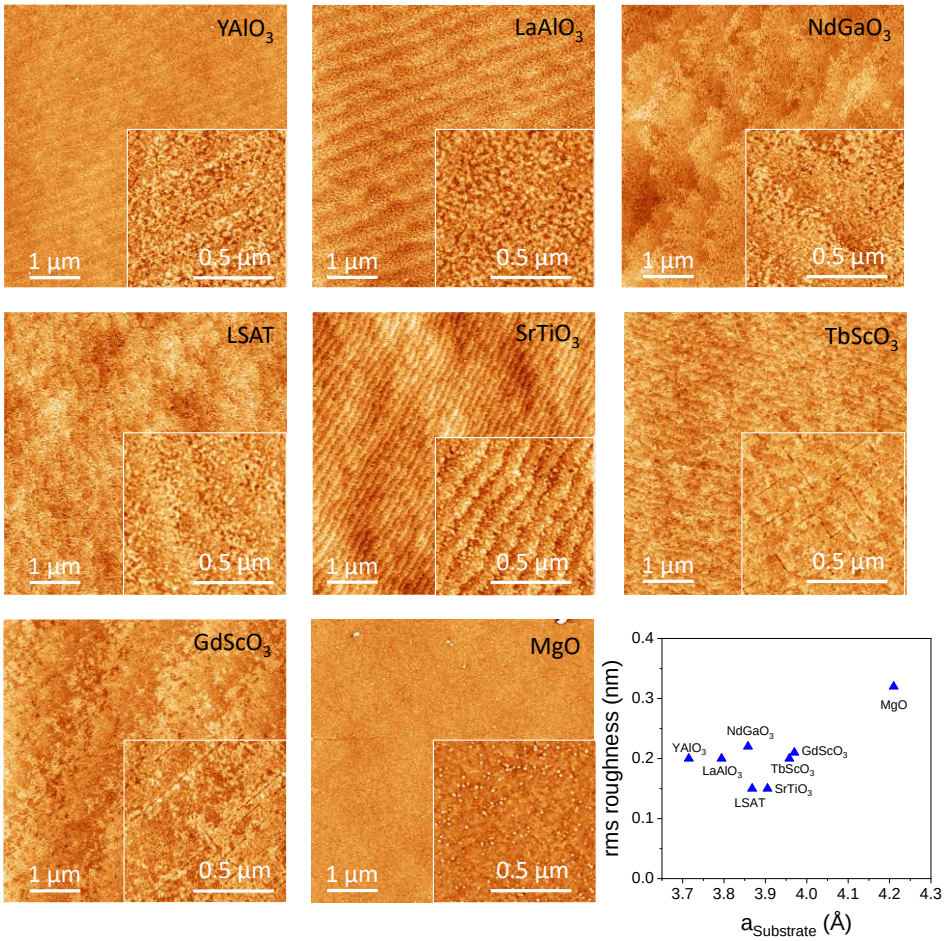

Figure 5.2.21 *Topographic AFM images (5 × 5 µm and 1 × 1 µm in the inset) of LHO films on indicated substrates.*

The XRD 2θ-χ frames of all films, shown in Figure 5.2.22a, further evident the impact of the substrate on the formation of HfO_2 phases. It is noticed that the o(111) is a bright circular spot, whereas the m(002) reflection is generally elongated along χ direction, signalling higher mosaicity. Figure 5.2.22b shows the θ-2θ scans around the o(111) peak position. Quantification of the different phases presence is summarized in Figure 5.2.22c.

The intensity of the orthorhombic peak is plotted as a function of the out-of-plane LSMO lattice parameter (c_{LSMO}). It can be observed that the general trend is that the o(111) peak intensity increases while decreasing the c_{LSMO}. At the same time, less monoclinic phase is formed. The coexistence between monoclinic and orthorhombic phases can be further confirmed by the cross-sectional high-angle annular dark field (HAADF) images collected by STEM images shown in Figure 5.2.22d for the LHO film grown on $SrTiO_3$. First, one can observe that different grains with different contrast exist. The presence of monoclinic and orthorhombic grains is identified and there is only very few monoclinic phase formed in this film, as indicated from the XRD data. In Figure 5.2.22e, a zoom of an orthorhombic grain allows to better visualize its crystalline structure.

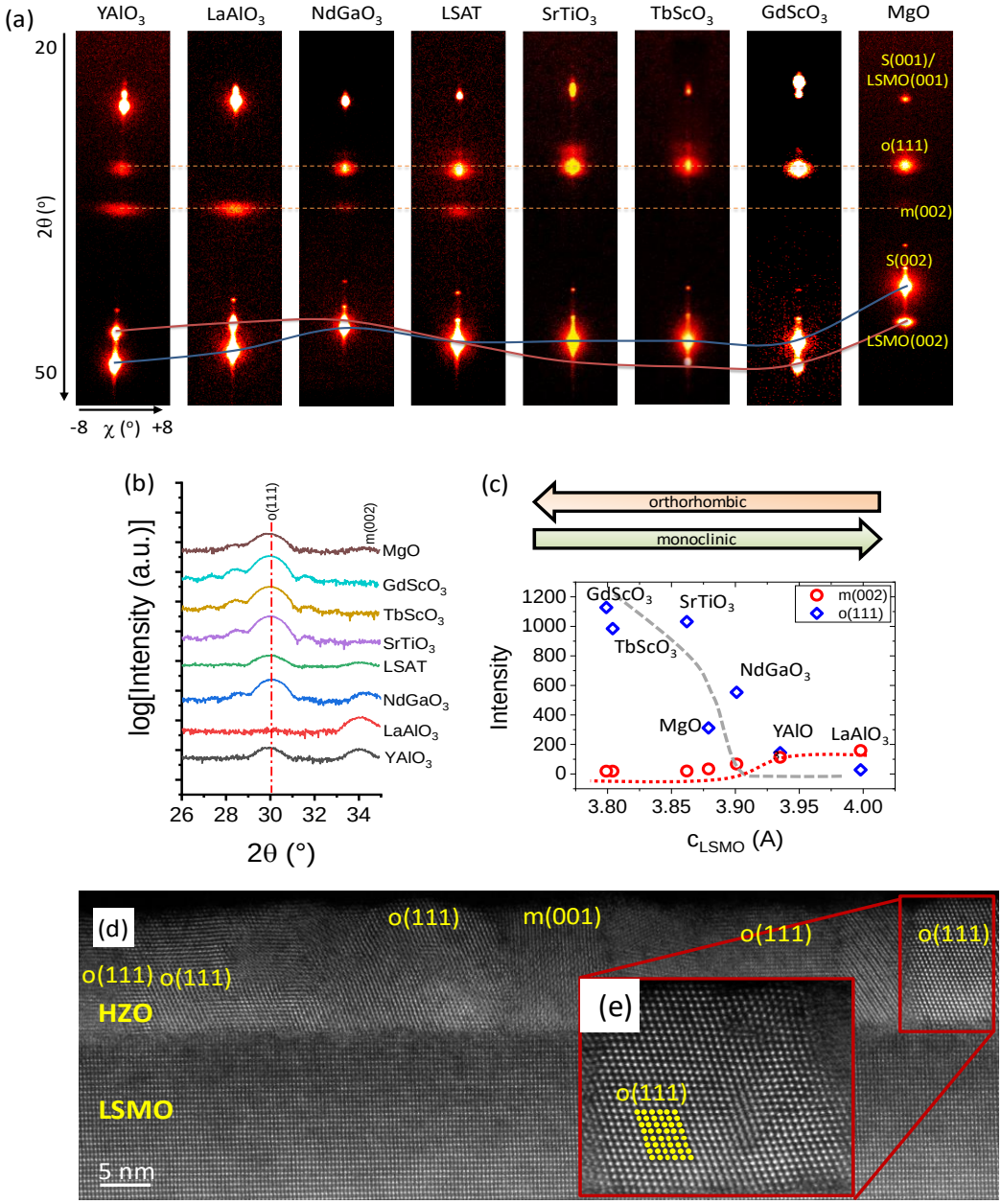

Figure 5.2.22 *(a) XRD 2θ-χ frames of the LHO/LSMO bilayers. The 2θ and χ ranges are integrated from 20 to 50° and from -10 to +10°, respectively. (b) XRD θ-2θ symmetric scans of the LHO/LSMO bilayers. Vertical solid line at 2θ around 30.1° marks the position of the o(111) peak in the films. (c) The extracted phase intensity versus out-of-plane lattice parameter of LSMO. (d) Cross-sectional HAADF STEM images of LHO/LSMO films on $SrTiO_3$ substrate. The images were acquired along the [110] zone axes of the substrates. Bottom insets are magnified images of the regions indicated above. (e) Zoom of an orthorhombic grain in (d).*

5.2.3.3 Electrical characterization

Figure 5.2.23a shows the P-E loops for all the samples. The hysteresis loop can be observed in all films. It can be seen that the relatively larger P_r presents in the films deposited on $TbScO_3$, $GdScO_3$, and $SrTiO_3$ substrates with a value around 29 μC/cm^2, 25 μC/cm^2 and 23 μC/cm^2, respectively. This is consistence with the relatively higher o phase ratio determined in the XRD measurement. Comparatively, a small P_r value around 5.3 μC/cm^2 presents in the films deposited on $YAlO_3$ and $LaAlO_3$ substrate. The I-V loops are included in Figure 5.2.23b. The coercive voltage is very similar in all the films, except that grown on $LaAlO_3$, ascribed to the significant lower amount of orthorhombic phase in this sample.

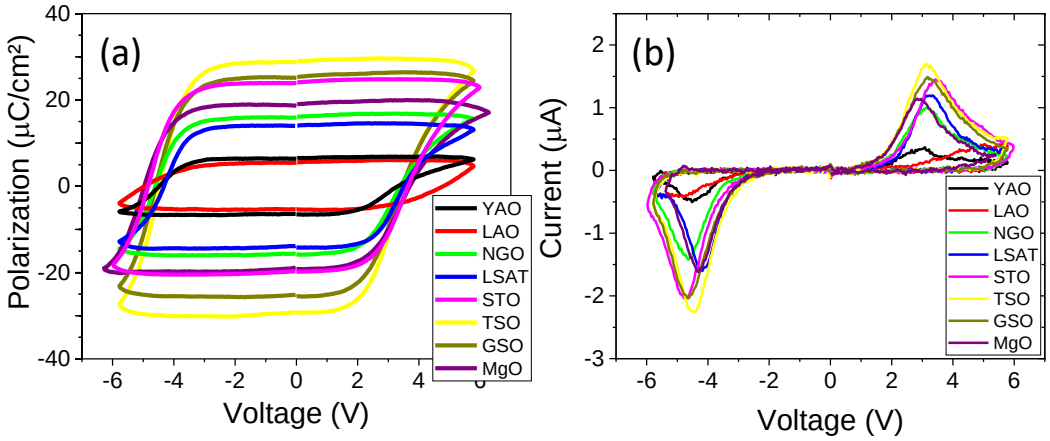

Figure 5.2.23 *(a) Ferroelectric polarization loops of the LHO films and (b) corresponding current-voltage curves.*

Quantified P_r value versus the out-of-plane LSMO lattice parameter, (c_{LSMO}), is shown in Figure 5.2.24a. For comparative, the results obtained in HZO grown on the same substrates (results belonging to the thesis of Dr. Saúl Estandía) are also included. It can be observed that with c_{LSMO} decrease, the P_r increases in both La and Zr doped HfO_2 films, with a larger P_r in La doped HfO_2 films. In Figure 5.2.24b, a clear increase of P_r can be

observed with the increase of the normalized o(111) peak intensity. The orthorhombic diffraction peak intensity is normalized to the maximum value of the La:HfO_2 film on $GdScO_3$ based on the XRD data in Figure 5.2.22. The influence of c_{LSMO} on o(111) out-of-plane lattice parameter, $d_{o(111)}$ value, is not significant (Figure 5.2.24c). The dependence of P_r with $d_{o(111)}$ value is shown in Figure 5.2.24d. It seems that the HZO films with smaller $d_{o(111)}$ value have larger P_r, but this is not obvious in the La doped films. Thus, it exists a clear dependence between the amount of the orthorhombic phase determined by the different used substrates and P_r. Instead, the dependence between P_r and out of plane lattice parameter of orthorhombic (111) seems less significant. On the other hand, the larger P_r in La doped films when using the same substrate also indicates that chemical doping can cooperate with the epitaxial stress imposed by the substrate to improve the remanent polarization value.

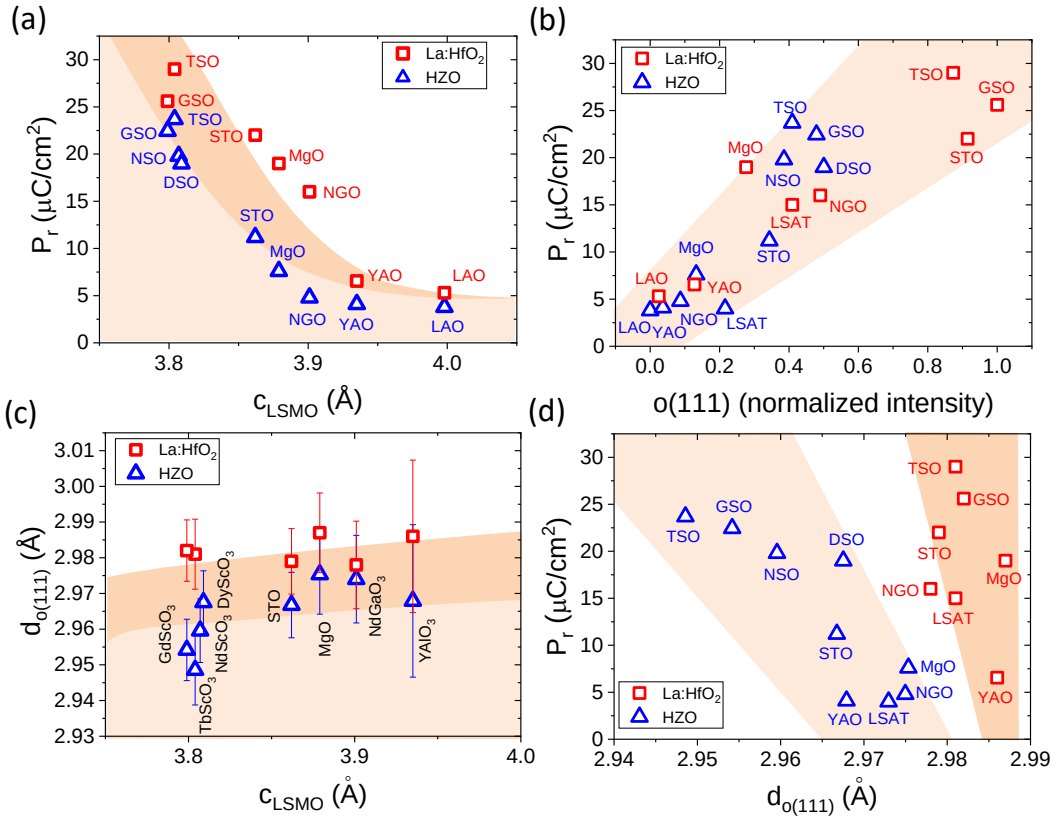

Figure 5.2.24 *(a) Remnant polarization as a function of c_{LSMO}. (b) Remnant polarization as a function of the normalized intensity of the XRD o(111) reflection for the LHO film on $GdScO_3$. (c) $d_{o\text{-}HZO(111)}$ as a function of c_{LSMO}. (d) Remnant polarization as a function of $d_{o\text{-}HZO(111)}$.*

Conclusion

In summary, the use of different substrates for the growth of La:HfO_2 film has been shown to be relevant to determine the amount of the metastable orthorhombic ferroelectric phase. The mismatch between the substrate and the LSMO induced stress is useful to modulate the lattice parameter of deposited LSMO, which is ultimate responsible for the amount of the stabilized orthorhombic phase in the films. We have found that the ferroelectric polarization magnitude is directly connected to the amount of the stabilized orthorhombic phase. In comparison with Zr doped films, films with La stabilize greater amount of orthorhombic phase irrespectively of the used substrate and the highest remanent polarization reaches up to 29 $\mu C/cm^2$ in films grown on $TbScO_3$.

5.3 Epitaxial La-doped $Hf_{0.5}Zr_{0.5}O_2$ and La-doped $(Hf,Zr)O_2$ thin films

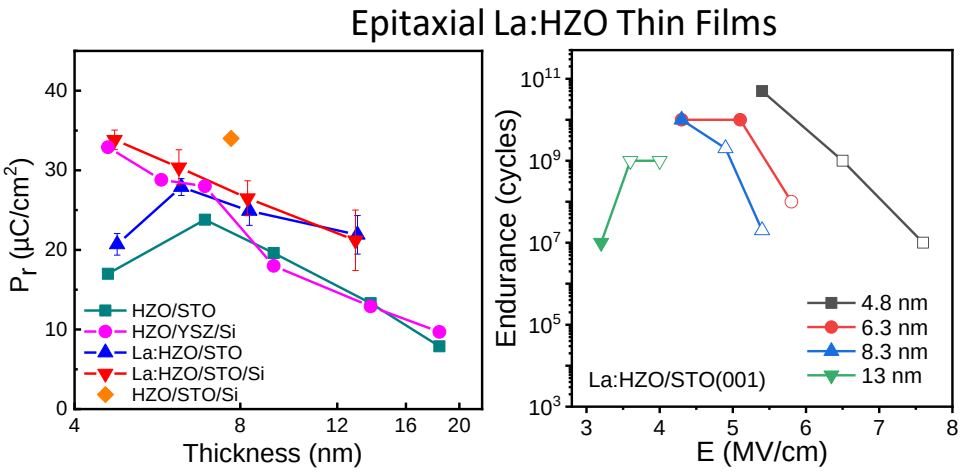

Abstract

Doping ferroelectric $Hf_{0.5}Zr_{0.5}O_2$ with La is a promising route to improve endurance. However, the beneficial effect of La on the endurance of polycrystalline films may accompanied by degradation of the retention. Here, we have investigated whether this endurance-retention dilemma also occurs in epitaxial 1 % La-doped HZO (La:HZO) films. The results indicate that ferroelectric polarization and coercive voltage are greater than that of undoped HZO epitaxial films, and the leakage current is substantially reduced. The wake-up effect, common in polycrystalline La:HZO films, is limited to few cycles in epitaxial films. The films exhibit fatigue, but endurance exceeds 10^{10} cycles, and accompanied by retention of more than 10 years. This demonstrates that there is no intrinsic dilemma between endurance and retention in La-doped HZO films. The final chapter of this section details a comprehensive study of the crystal phases and ferroelectric polarization in the HfO_2-ZrO_2-La_2O_3 ternary system.

Introduction

Doping is a promising method to stabilize the ferroelectric o-phase and optimize the ferroelectricity for HfO_2-based thin film. One of extensively investigated dopant is Zr, since the wide doping window and low crystallization temperature.[147] La is another promising dopant with large atomic radius to achieve high remanent polarization and good ferroelectric properties (low leakage current and long endurance).[74,148] In order to combine the advantages from the two dopants, La has been introduced to improve the ferroelectric properties of HZO film.[96,173–175] However, the beneficial effect of La on the endurance of polycrystalline films may be accompanied by degradation of retention.[96] In first section, we explored the epitaxial 1% La doped HZO film with different thicknesses. The results indicate that La decreases the degradation of polarization with thickness increase. Despite fatigue, endurance in epitaxial La-doped films is more than 10^{10} cycles, and this good property is accompanied by excellent retention of more than 10 years, which proves that there is no endurance-retention dilemma in La-doped epitaxial HZO films.

The improved endurance in La doped HZO film makes HfO_2-ZrO_2-La_2O_3 ternary system interesting for further exploration. In second section, the epitaxial La_y:$Hf_{1-x}Zr_xO_2$ films with x =0, 0.5, 1 and y=0-0.1 are systematically investigated. When increasing the Zr content, a lower La content is more suitable for achieving higher P_r, and the optimized P_r of about 30 μC/cm^2 can be obtained in 2% La:HZO film.

5.3.1 Epitaxial Ferroelectric La-Doped $Hf_{0.5}Zr_{0.5}O_2$ Thin Films

5.3.1.1 Film growth

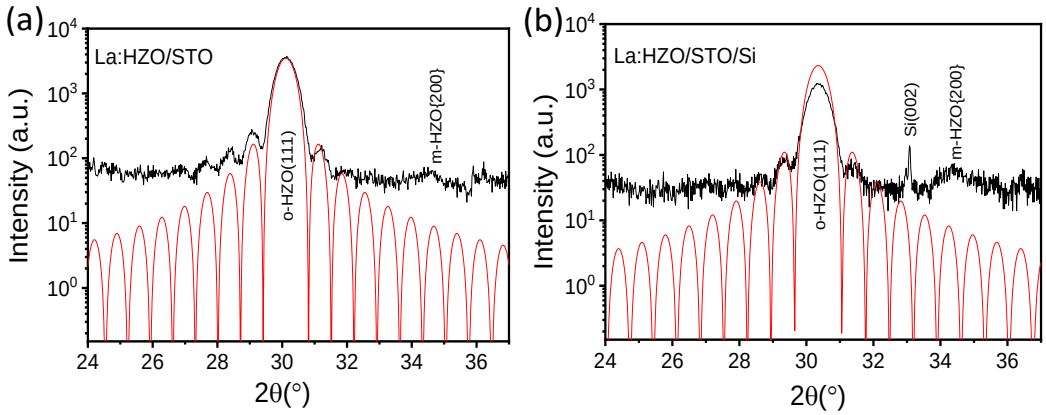

Figure 5.3.1 *XRD θ-2θ scans of t = 13 nm films on (a) LSMO/STO(001) and (b) LSMO/STO/Si(001). Red curves are simulations of Laue oscillations.*

La doped HZO films with composition of $Hf_{0.5}Zr_{0.49}La_{0.01}O_2$ were grown (800°C, 0.1 mbar of O_2) on STO(001) and STO/Si(001) substrates buffered with a $La_{0.67}Sr_{0.33}MnO_3$ electrode with thickness ~25 nm. The film thickness ranges from 4.5 nm to 13 nm, as shown in Figure 5.3.1, by estimating from simulation of Laue oscillations. The fitting curves were simulated considering peak position 2θ = 30.111° and thickness of 130.6 Å (N = 44 and c = 2.968 Å), for the film on STO(001), and 2θ = 30.357° and thickness of 129.5 Å (N = 44 and c = 2.944 Å) for the film on Si(001).

5.3.1.2 Structure characterization

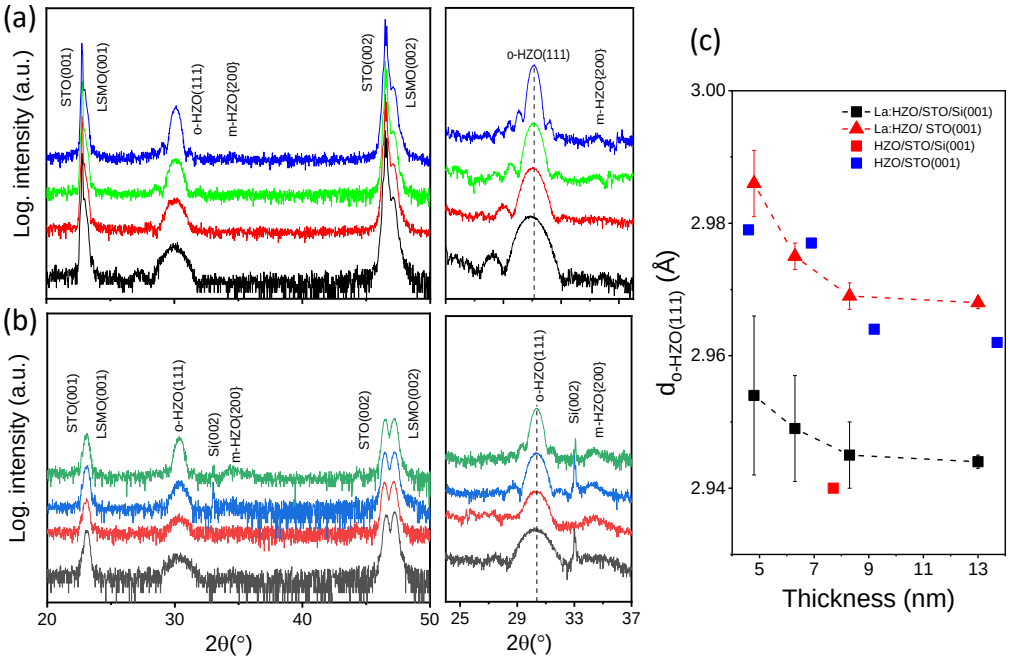

Figure 5.3.2 *XRD θ-2θ scans of La:HZO films on (a) LSMO/STO(001) and (b) LSMO/STO/Si(001). Right panels: scans acquired with a longer time. (c) Out-of-plane o-HZO(111) lattice distance of La:HZO films on LSMO/STO(001) (red triangles) and LSMO/STO/Si(001) (black squares), plotted as a function of thickness. Out-of-plane lattice distance values of epitaxial undoped HZO on LSMO/STO(001) (blue squares) and LSMO/STO/Si(001) (red square) are plotted for comparison.*

The XRD θ-2θ scans of the La:HZO/LSMO/STO(001) and La:HZO/LSMO/STO/Si(001) samples with different thickness are shown in Figure 5.3.2a-b. From bottom to top, the thickness is increasing from 4.5 nm to 13 nm. It can be observed that the reflections around 23° and 47° are related to (001) and (002) peaks of LSMO/STO, and the peaks around 2θ around 30° are corresponding to the position of orthorhombic (111) reflection in epitaxial undoped HZO film.[65] A zoomed region around

111 reflections, with longer acquisition time, are indicated in the right panel of Figure a and b. With thickness increases, the 111 peaks are narrower and the Laue oscillation is more clear. What different between the films on STO and Si is that the reflections around 34°, corresponding to monoclinic HZO{200}, is nearly not visible in films on STO, but more evident in films grown on Si substrates. Furthermore, the out-of-plane (oop) lattice parameter of o-HZO(111), $d_{o\text{-}HZO(111)}$, is determined from the θ-2θ scans in Figure 5.3.2 a and b. The dependence of the $d_{o\text{-}HZO(111)}$ value versus the thickness is plotted in Figure 5.3.2c. It can be seen that no matter on STO or Si substrates, the oop parameter decreases slightly with *t* up to $t \sim 8$ nm, and the value remains constant in the thicker film ($t \sim 13$ nm). Similar dependence (blue squares) was found for undoped HZO films on STO(001).[65] The relatively lower $d_{o\text{-}HZO(111)}$ value in the films on Si is a consequence of the large mismatch of the thermal expansion between the oxides and silicon. The smaller thermal expansion coefficient of Si introduces an in-plane tensile stress to La doped HZO films during cooling, thus causing contraction of the out-of-plane $d_{o\text{-}HZO(111)}$ parameter. The comparison of the $d_{o\text{-}HZO(111)}$ value between the La doped film and the undoped HZO films indicates that a slightly larger d values are in the series of doped films, which is different from the reported slight shrinkage for polycrystalline HZO films doped with similar La content.[96,176]

The XRD 2θ-χ frames and pole figure are shown in Figure 5.3.3. Bright spots from substrates and La:HZO films around $\chi=0$ can be observed. In the films on STO substrate, the o(111) peaks are intense, while the monoclinic reflections are nearly not visible, indicating a very low amount of monoclinic phase in epitaxial La:HZO films, smaller than that in equivalent epitaxial undoped HZO films.[65,157] In polycrystalline films, the La:HZO films also show similar reduction of monoclinic phase ratio.[96,176] In the films deposited on Si substrates, the tracks of monoclinic {002} phase is more evident, especially in the films thicker than 8 nm, with elongated low intensity spots along χ direction. The pole figure (Figure 5.3.3 c-d) presents 12 spots and corresponding integrated peaks from o(-111) reflections, indicating four in-plane crystal variants and the same epitaxial relationship as the films without La.[28,177] In summary, XRD confirms that the orthorhombic phase present in the La-doped HZO films has grown epitaxially but exhibits crystal variants and coexists with a minority monoclinic phase.

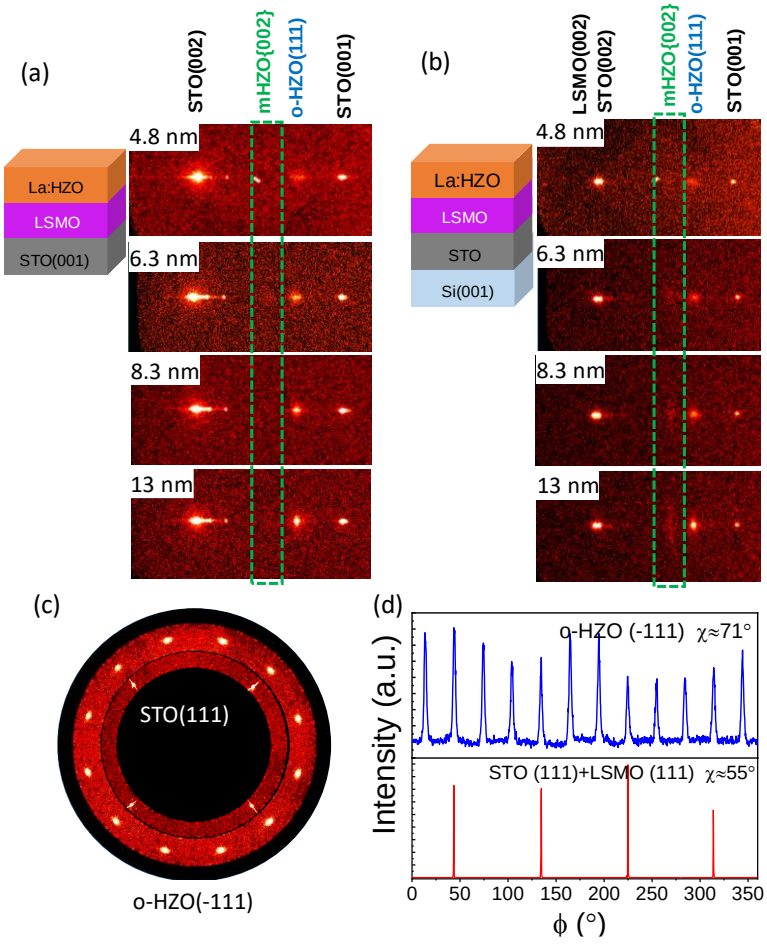

Figure 5.3.3 *XRD 2θ-χ frames of films on (a) LSMO/STO(001) and (b) LSMO/STO/Si(001). The HZO thickness is indicated in the corresponding frame. Dashed green line rectangles mark the position of the m-HZO{002} reflections. XRD pole figures of t = 8.3 nm La:HZO film on STO(001), from (c) o-HZO(-111) and STO(111) reflections. (d) Corresponding ϕ-scans around o-HZO(-111) and STO(111).*

The surface characterization indicates that terrace and step morphology are shown in La:HZO films on STO(001) (Figure 5.3.4a), revealing a very flat surface condition. The root-means-square (rms) roughness is less than 0.2 nm in all films and the line topographic profiles show height variation of less than 1 nm over a distance of 5 μm. Comparatively, terraces are not distinguished in films grown on Si(001) (Figure 5.3.4b), but the rms is around 0.2-0.3 nm and height profiles are within the range of 2 nm along a distance of 5 μm, still indicating a flat surface state.

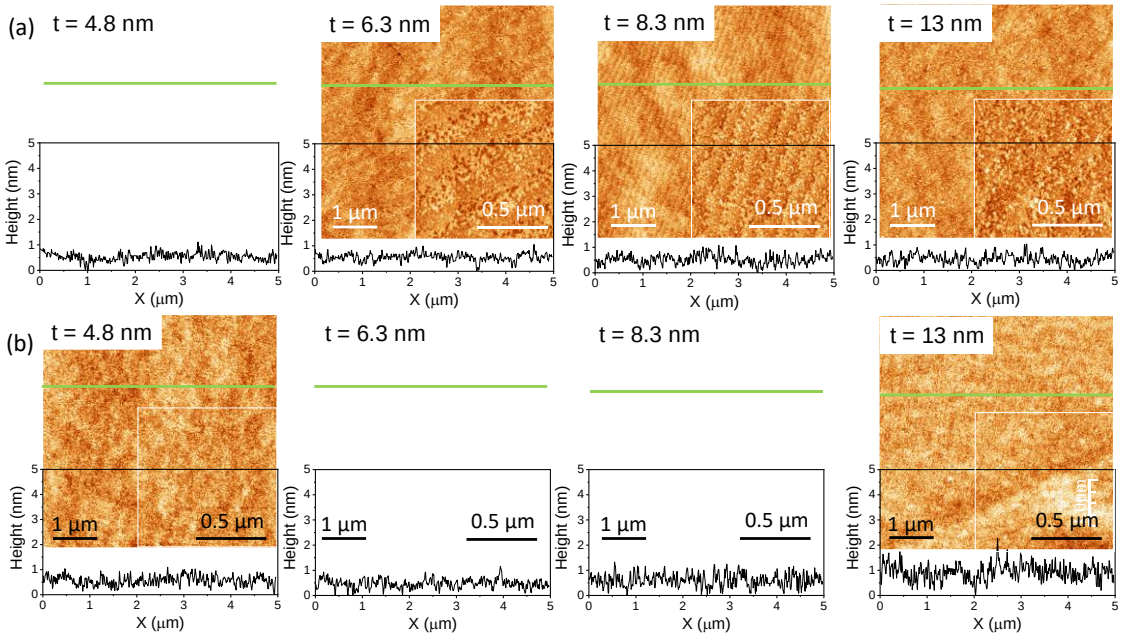

Figure 5.3.4 *Topographic AFM images, 5 μm × 5 μm, of the films on (a) LSMO/STO(001) and (b) LSMO/STO/Si(001). The thickness of the films is indicated at the upper of each image. A height profile along the marked horizontal green lines are shown below each image. The inset in each image is 1 μm × 1 μm scanned area.*

5.3.1.2 Electrical characterization

Figure 5.3.5a and b show the polarization loops of the films on STO(001) and Si(001). Clear hysteresis loops present in all films, indicating ferroelectric properties. The round shape at the maximum applied voltage indicates the influence from the leakage current. The dependence of the remanent polarization and coercive field versus film thickness are shown in Figure 5.3.3c and d. It can be observed that the P_r value of the La:HZO films deposited on STO(001) (blue down triangles) in the 20-30 μC/cm^2 range. P_r is around 20 μC/cm^2 in the 4.8 nm film, increases to ~28 μC/cm^2 in the 6.2 nm film, and for thicker films, reduces with a thickness of up to ~21 μC/cm^2 in the 13 nm film. The undoped HZO films (green squares) have the similar dependence on thickness. But apparently, La-doped films have higher P_r than undoped films, especially in the thicker thickness range. On the other hand, remanent polarization of La:HZO films on Si(001) decreases monotonically with thickness (red up triangles), from larger than 30 μC/cm^2 in 4.8 nm film to 21 μC/cm^2 in 13 nm film. Similar high P_r in thickness less than 10 nm films and reduction tendency was reported for undoped HZO films integrated epitaxially on Si(001) using yttria-stabilized zirconia (YSZ) buffer layers (pink circles). Overall, no matter on STO or Si substrate, the reduction of polarization in thicker thickness range is less for La doped

films than that for undoped ones. The higher remanent polarization in thicker films could be due to the lower amount of monoclinic phase in La-doped HZO films. Undoped HZO films with very large remanent polarization were also integrated epitaxially on STO-buffered Si(001) wafers (orange diamond), but the dependence on thickness was not reported.[29]

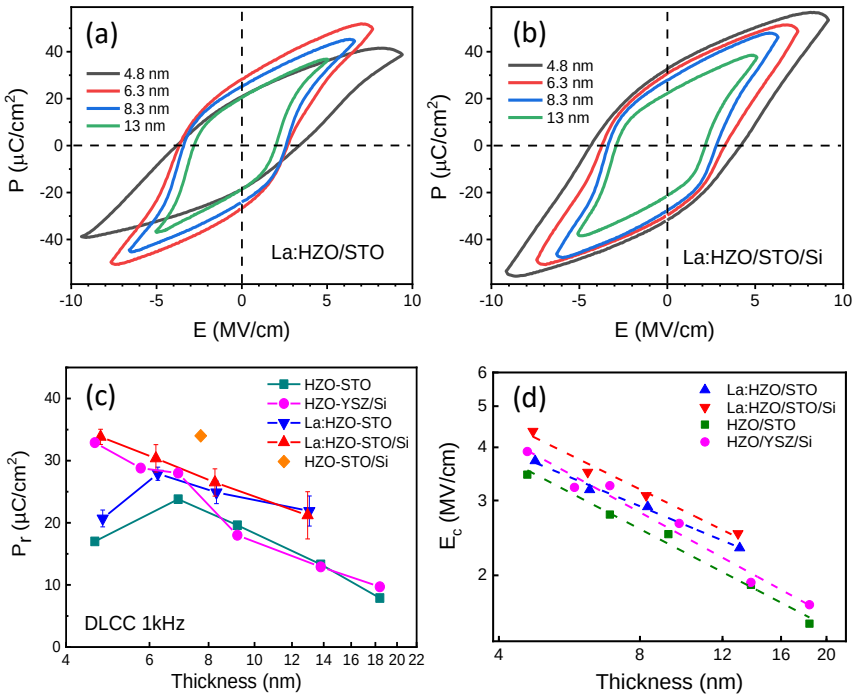

Figure 5.3.5 *Polarization loops of La:HZO films on STO(001) (a) and Si(001) (b). Dependence of remanent polarization (c) and coercive field (d) on thickness for La:HZO films on STO(001) (blue down triangles) and Si(001) (red down triangles). Data reported for epitaxial undoped HZO films on STO(001) (green squares) and YSZ-buffered Si(001) (pink circles) are included. The error bar on remanent polarization corresponds to the standard deviation among around 10 different measured capacitors.*

The dependence between the coercive field and film thickness is plotted in Figure 5.3.5d. As thickness increases from 4.8 nm to 13 nm, E_c decreases from 3.7 to 2.3 MV/cm in films on STO(001) (blue up triangles) and from 4.2 to 2.5 MV/cm in films on Si(001) (red down triangles). It can be seen from the fitting (dash line) that E_c of the films on both substrates depends on thickness, following the $E_c \propto t^{-2/3}$ scaling law. This experience law is common in ferroelectric perovskites, but is rare in polycrystalline ferroelectric HfO_2 based films.[169,178] This rule can also be observed in epitaxial undoped HZO films.[30,65] When compare with the undoped HZO films, the E_c of La doped HZO films is slightly

higher, which is contrary to the reduction of E_c by approximately 30% in polycrystalline HZO films doped with the same 1% mol La.[174,179]

Leakage current curves of La doped HZO films on STO are shown in Figure 5.3.6a. Low leakage current can be obtained in 4.8 nm film, around 10^{-6} A/cm^2 at 1 MV/cm and 10^{-5} A/cm^2 at 2 MV/cm. With thickness increase, leakage current decreases by around on order of magnitude in 13 nm film. Films on Si(001) are slightly more leaky (Figure 5.3.6b), with the leakage current of the thinner film around 3×10^{-6} A/cm^2 at 1 MV/cm and 5×10^{-5} A/cm^2 at 2 MV/cm. Similarly to the films on STO(001), leakage is significantly reduced with thickness. The dependence between the leakage current at 2 MV/cm and film thickness is shown in Figure 5.3.6c. For comparison, the leakage current from equivalent epitaxial undoped HZO films on STO(001) is also included.[65] It is observed that the leakage current of epitaxial La-doped HZO films is considerably reduced, 1-2 orders of magnitude, compared to equivalent undoped HZO films.

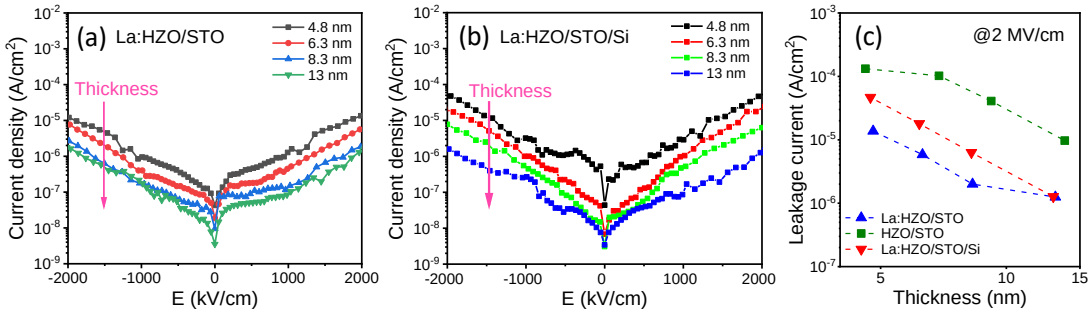

Figure 5.3.6 *Leakage current of La:HZO films on (a) STO(001) and (b) Si(001). (c) Dependence of leakage current on thickness for La:HZO films on STO(001) (blue up triangles) and Si(001) (red down triangles). Reported data for epitaxial undoped HZO films on STO(001) (green squares) are included.*

To check the possible wake-up effect in La doped HZO films, the I-V and P-V loops of each films were measured at pristine, after 10 and 100 cycles under the electric field indicated in Figure 5.3.7. It can be seen that the 4.8 nm film (Figure 5.3.7a-b) shows a double peak in the I-V curve and a pinched polarization loop in the pristine state. The two current peaks get closer to each other after 10 cycles, and merge to one peak after 100 cycles. At the same time, there is no shrinkage in the P-V loop. In 6.3 nm film (Figure 5.3.7c-d), the two current peaks are closer and low amplitude at pristine state, and after 10 cycles, only a smaller secondary peak on the positive side. With more cycles, this peak disappears. The corresponding ferroelectric loops show a significant increase in

polarization with respect to the pristine state. In contrast, no differences in the I-V curves are observed between the pristine state and the 10 times cycled 8.3 nm film. After 100 cycles, there is a diminish of shoulder at the higher voltage side. Consistence with the I-V change, the polarization loops show no significant differences, and there is only a very slight reduction in polarization after 100 cycles. Finally, in the 13 nm film, there is only one single switching peak, decreasing with cycling process. The corresponding polarization loops show a reduction in remanent polarization with cycling. Therefore, the wake-up effect of epitaxial La doped HZO films is highly dependent on film thickness. Similar results can be observed in films grown on Si substrate (Figure 5.3.8). In 4.8 nm and 6.3 nm films, there is an apparent increase of switching current amplitude after 10 cycles. But in thicker films, it is nearly a constant. Compared with undoped epitaxial HZO films, the wake-up effect is more evident in La doped HZO film, but limited to 10 or 100 cycles. On the other hand, in polycrystalline films, the wake-up effect increases strongly compared to undoped films, extending to a larger number of about 10^7 cycles.[174,179,180] Therefore, the strong reduction or suppression of the wake-up effect in epitaxial La:HZO films with respect to polycrystalline La:HZO films is relevant.

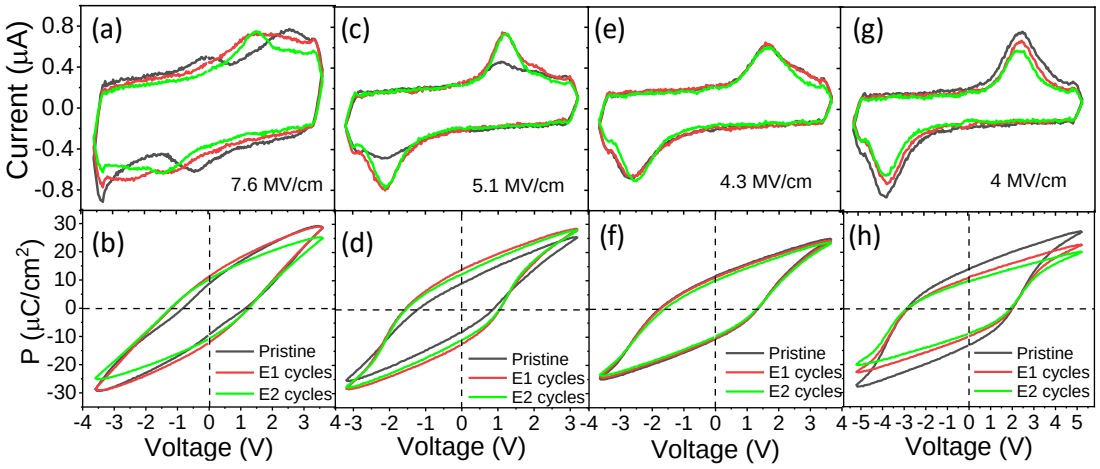

Figure 5.3.7 *(a) Current-voltage (I-V) curves measured in the pristine state and after 10 and 100 cycles and (b) the corresponding polarization-voltage (P-V) loops for the t = 4.8 nm film on STO(001). I-V curves and P-V loops for the t = 6.3, 8.3, and 13 nm films are shown in panels (c,d), (e,f), and (g,h), respectively.*

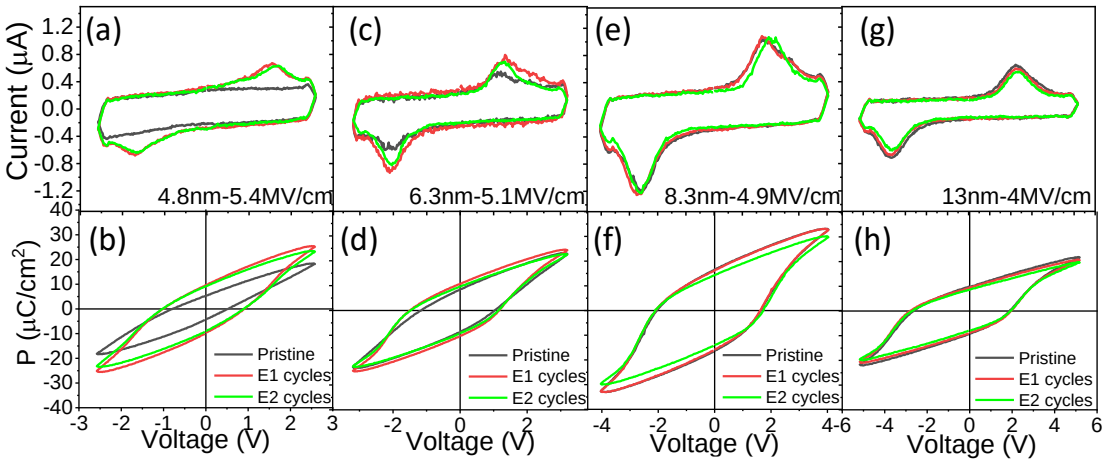

Figure 5.3.8 *(a) Current-voltage (I-V) curves measured in the pristine state and after 10 and 100 cycles and (b) the corresponding polarization-voltage (P-V) loops for the t = 4.8 nm film on Si(001). I-V curves and P-V loops for the t = 6.3, 8.3, and 13 nm films are shown in panels (c,d), (e,f), and (g,h), respectively.*

The endurance of the films on STO are shown in Figure 5.3.9. The capacitors are cycled until hard breakdown (marked by empty symbols) or until a fatigued state with P_r reduced to below 1.5 μC/cm^2. A set of endurance measurements was carried out for each sample by cycling the capacitors with pulses of different amplitudes. The 4.8 nm film is cycled under 6.5 MV/cm, and because the wake-up effect mentioned above, there is a clear increase of the remanent polarization after 10 cycles. Memory window gradually decreases under additional cycling, and dielectric breakdown happens after 10^9 cycles. When applying higher electric field (7.6 MV/cm), the capacitor breaks after 10^7 cycles with retained memory window around 14 μC/cm^2. However, cycling under lower electric field (5.4 MV/cm), there is no hard breakdown. The wake-up effect is elongated to around 100 cycles, with maximum memory window around 11 μC/cm^2, and then $2P_r$ decreases to around 3 μC/cm^2 after 5×10^{10} cycles because of fatigue. The observed wake-up effect is consistent with the results in polycrystalline films with lower amplitude or shorter applied pulse, indicating a possible reason from defects redistribution.[90,181] The change of leakage current with number of cycles is measured under the same electric field for endurance. The leakage current is nearly constant at first 10^4 cycles, but additional cycling increases it sharply under higher electric field (7.6 MV/cm). With electric field decrease, the threshold cycling number increases to 10^6 cycles under 6.5 MV/cm, and there is nearly without increase of leakage current when cycling under lower electric field (5.4 MV/cm). The polarization loops of 6.3 nm film measured at 5.1 MV/cm also indicate wake-up effect at first 10 cycles, with maximum $2P_r$ around 25 μC/cm^2. After additional cycling,

memory window decreases to around 2 μC/cm^2 without breakdown. Enhanced electric field favours higher memory window but leading to breakdown and leakage increase within smaller cycling numbers. On the contrary, the lower electric field (4.3 MV/cm) is beneficial to longer endurance and the limitation of leakage current increase, but decreases the memory window.

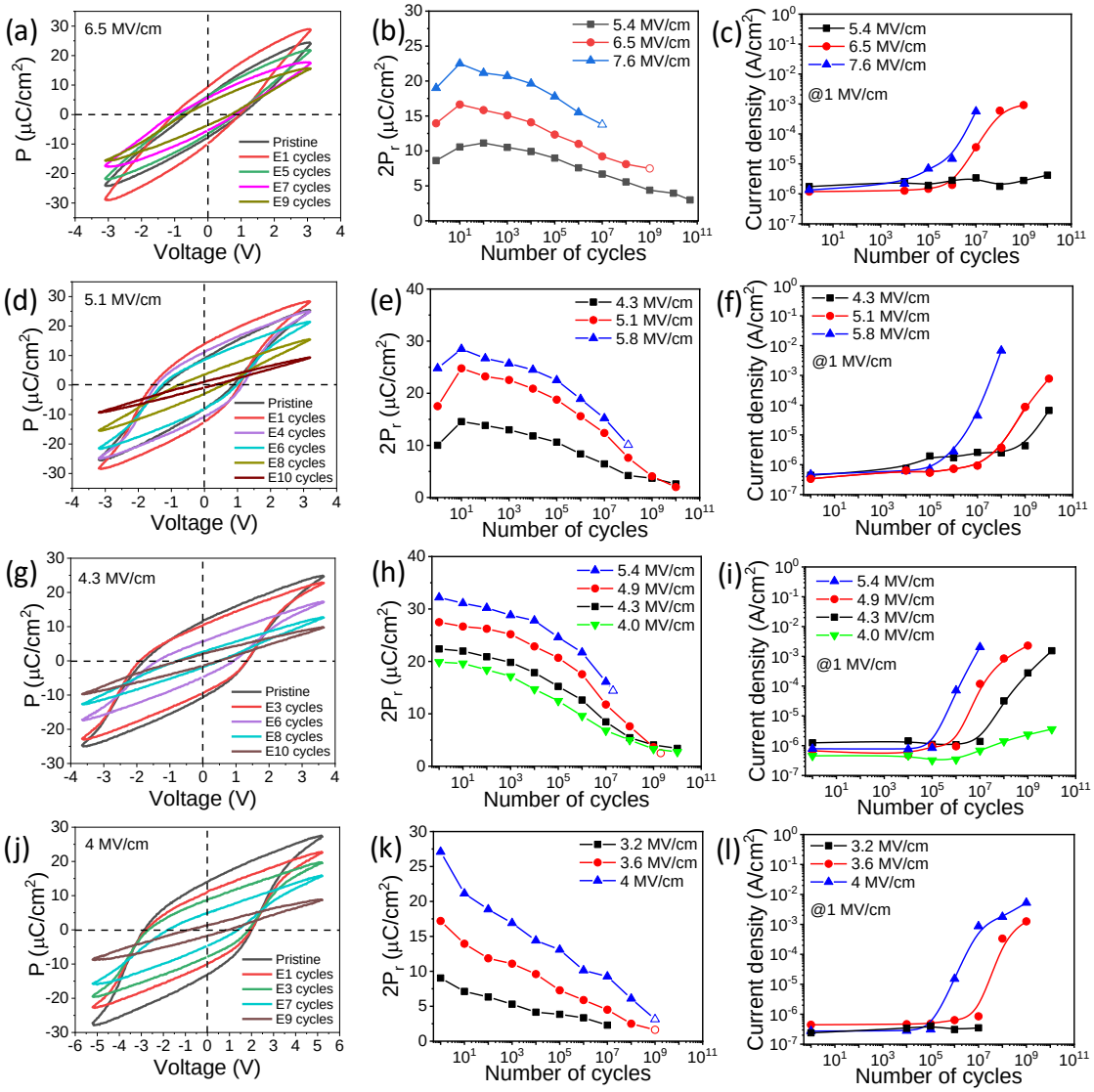

Figure 5.3.9 *(a) Polarization-voltage P-V loops, (b) endurance, and (c) evolution of current leakage with the number of cycles for the t = 4.8 nm film on STO(001). The P-V loops, endurance, and evolution of current leakage with the number of cycles corresponding to the t = 6.3 nm, 8.3 nm, and 13 nm films are shown in panels (d-f), (g-i), and (j-l), respectively. Empty symbols indicate the last measured data point before breakdown.*

Thicker films do not show wake-up effect, and polarization decreases continuously with cycling. In 8.3 nm film, hard breakdown occurs after 2 × 10^7 cycles at 5.4 MV/cm or 2 × 10^9 cycles at 4.9 MV/cm. There is no breakdown under lower electric field of 4.3 or 4.0

MV/cm, but memory window decreases to around 3 μC/cm^2 after 10^{10} cycles because of fatigue. The threshold cycling number for leakage current increases from 10^5 to 10^8 with electric field decrease from 5.4 to 4 MV/cm. In 13 nm film, breakdown happens after 10^9 cycles at 4.0 or 3.6 MV/cm, while for a lower applied field of 3.2 MV/cm, the polarization decreased to $2P_r$ = 2.3 μC/cm^2 after 10^7 cycles. The endurance measurements of the La:HZO films on Si(001) are summarized in Figure 5.3.10. The influence of the switching voltage on endurance follows the observed dependences of the films on STO(001), although the maximum endurance of films on Si is limited to around 10^9 cycles. The limitation of the endurance is also because the fatigue or the high leakage current induced breakdown.

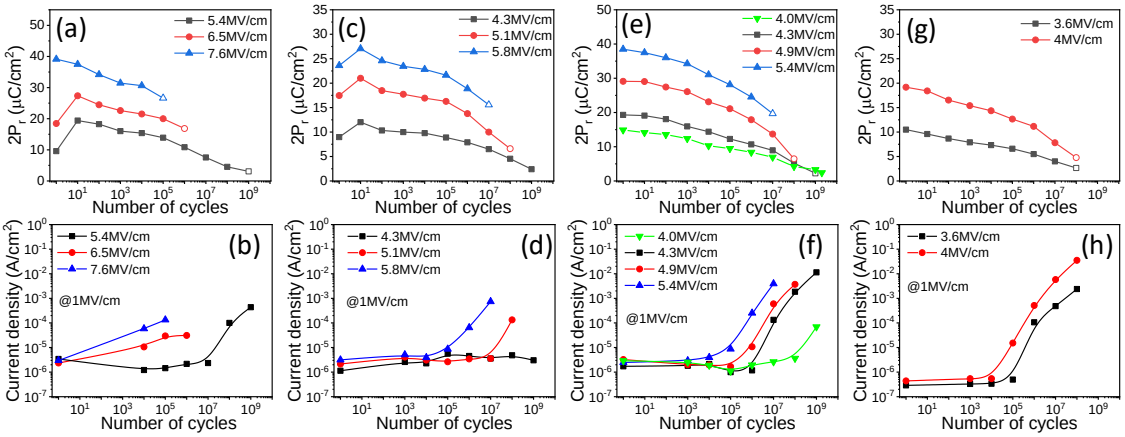

Figure 5.3.10 *(a) Endurance and (b) variation of current leakage measured at 1 MV/cm with the number of cycles for the t = 4.8 nm film on Si(001). The endurance and variation of current leakage with the number of cycles corresponding to the t = 6.3 nm, 8.3 nm, and 13 nm films are shown in panels (c,d), (e,f), and (g,h), respectively.*

The threshold cycles of leakage current versus electric field for different film thickness are shown in Figure 5.3.11a. As can be seen in Figure 5.3.9-5.3.10, the leakage current remains constant for a certain number of cycles but increases sharply by several orders of magnitude after a threshold. With electric field increase, the threshold cycles decreases. And at the same electric field, the higher threshold cycles present in thinner films. The defects generated by cycling probably accumulate at the boundaries between the grains and the crystal variants. The observed threshold in the number of cycles suggests that the new defects only have an impact on the leakage when their density is high enough to allow percolation. The endurance of films on STO(001) with different thickness under varying electric field is shown in Figure 5.3.11. Generally, hard breakdown limits the endurance when applying higher electric field, and thus indicating a relatively low

endurance. Under lower electric field, higher endurance can be achieved in thinner films, but in 13 nm film, the endurance is limited by low memory window. A similar thickness dependence had been observed in polycrystalline HZO films,[182] although breakdown fields in epitaxial films are much higher.

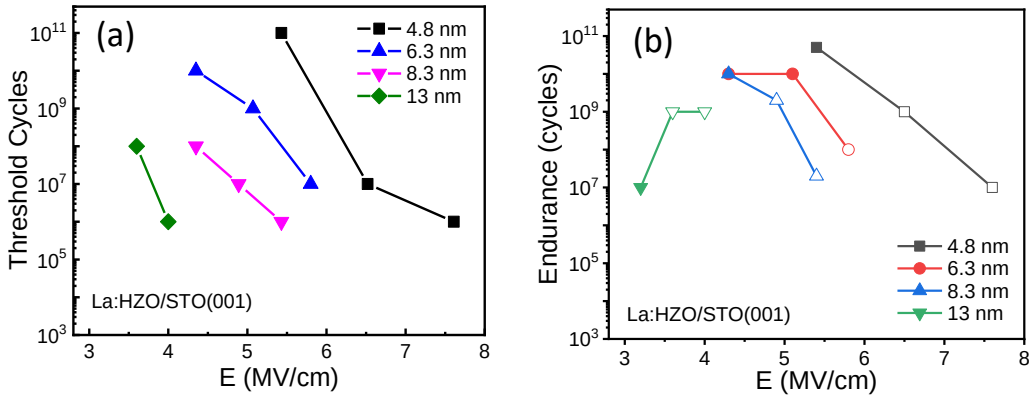

Figure 5.3.11 *(a) Map of the threshold of the number of cycles for an abrupt leakage increase as a function of electric field and thickness of films on STO(001). (b) Map of endurance as a function of electric field and thickness of films on STO(001). Empty symbols indicate breakdown.*

Figure 5.3.12a-d shows the polarization retention of the films on STO(001), measured in the pristine state at room temperature. Retention of the 4.8 nm film is highly dependent on the direction of poling, with the remanent polarization extrapolated to 10 years being 2 μC/cm^2 for positive voltage and larger than 10 μC/cm^2 for negative poling. The asymmetry is less in thicker films, and the extrapolated remanent polarization for both positive and negative poling is high in all films. Data collected at 85 °C in representative 8.3 nm samples on STO and Si are plotted in Figure 5.3.12e-f. Data show that the retention is still high at high temperature with extrapolated polarization at 10 years larger than 5 μC/cm^2. We have quantified retention by fitting the measured data to the $P_r = P_0 t_d^{-k}$ equation (dashed lines in a-d), where t_d refers to the time after poling. The graph of the exponent k against thickness, in Figure 5.3.12g, confirms that the asymmetry is much greater in the 4.8 nm film than in the other films including data measured at 85 °C. The corresponding graph for the films on Si(001) is shown in Figure 5.3.12h. The results confirm the observations on STO: strong asymmetry in the film of thickness less than 5 nm and very long retention in the thicker films for both poling directions. Imprint field, current leakage, and depolarizing field are expected to determine the influence of poling direction and film thickness on retention. Imprint field, critical in the asymmetry, may depend on the presence of the monoclinic phase, more important in thicker films, and also

on the characteristics of the voltage pulses applied (amplitude, time, and polarity).[180] Current leakage decreases monotonically with thickness, which favors a better retention in thicker films. However, the effect of leakage depends on spatial inhomogeneities, mainly because of grain boundaries, and on the possible coexistence of electronic and ionic contributions with different time scales. Finally, thinner films should be more unstable because of the larger depolarization field, although their larger E_c will have the opposite effect. Nevertheless, the excellent properties of the epitaxial La-doped HZO films are achieved with endurance that exceeds 10^{10} cycles, and the films simultaneously exhibit good retention for more than 10 years under the same poling voltage (Figure 5.3.13). A poling voltage of around 3 V can allow the use of the capacitors in a ferroelectric random access memory.

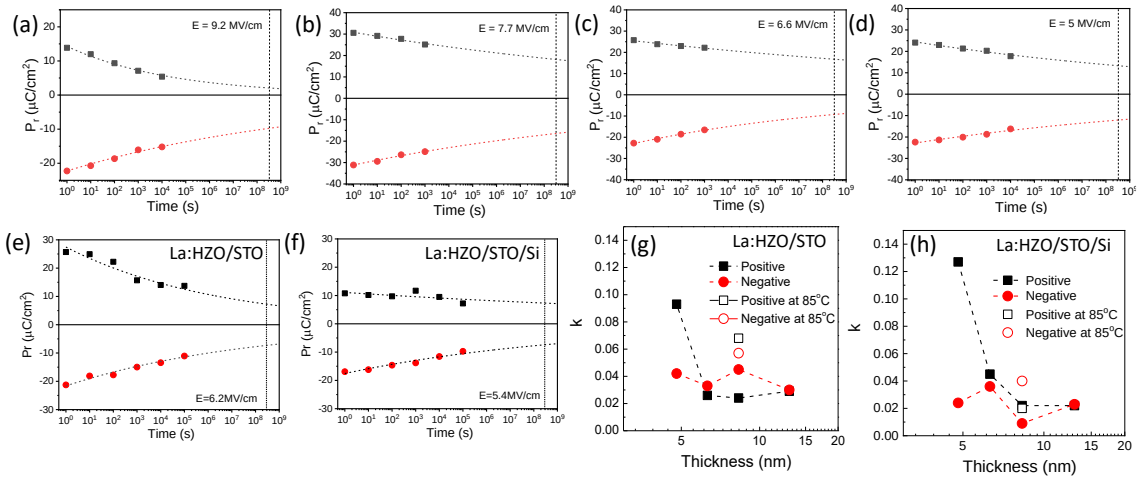

Figure 5.3.12 *Polarization retention at room temperature of (a) t = 4.8 m, (b) t = 6.3 nm, (c) t = 8.3 nm, and (d) t = 13 nm films on STO(001). Polarization retention at 85 °C of films with t = 8.3 nm on (e) STO(001) and (f) Si(001). Lines are fits to the* $P_r = P_0 t_d^{-k}$ *equation for positive and negative poling. The vertical dashed lines mark a time of 10 years. The k parameter plotted for positive and negative poling as a function of thickness for films on (g) STO(001) and (h) Si(001).*

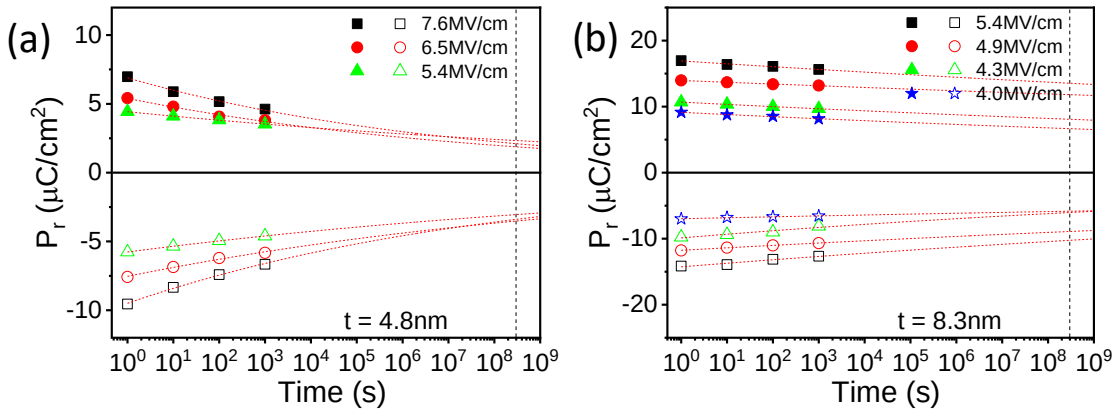

Figure 5.3.13 *Polarization retention of (a) 4.8 nm and (b) 8.3 nm films on STO(001). Lines are fits to $P_r=P_0t_d^{-k}$ equation for positive and negative poling of indicated amplitude of electric field. The vertical dashed lines mark a time of 10 years.*

Conclusion

In summary, the ferroelectric properties (polarization, endurance, and retention) of 1% La doped HZO film deposited on STO(001) and Si(001) with different thickness were systematically investigated. La doping favors the increase of ferroelectric polarization, particularly for films with thickness over 10 nm. Compared to serious drawback in polycrystalline La doped films, it is limited to approximately 100 cycles in epitaxial film and only presents in thinner film. La doping is not benefit to reduce the coercive field, but it significantly reduces the leakage current in the films. Under electric field cycling, the films indicate endurance exceeds 10^{10} cycles, companying fatigue. And the films simultaneously exhibit very high retention more than 10 years. These demonstrate that there is no intrinsic dilemma between endurance and retention in La-doped HZO films.

5.3.2 Epitaxial Ferroelectric La-doped $(Hf,Zr)O_2$ thin films

5.3.2.1 Film growth

Epitaxial $La_y:Hf_{1-x}Zr_xO_2$ films with x=0, 0.5, 1 and y=0~0.1 are were grown on STO(001) substrates buffered with a LSMO electrode with thickness ~25 nm. Detailed deposition conditions are shown in chapter 3. The film thickness is around 7~10 nm, as shown in Figure 5.3.14, by estimating from simulation of Laue oscillations. The film thickness could be alerted by the significant composition difference or density difference of the targets.

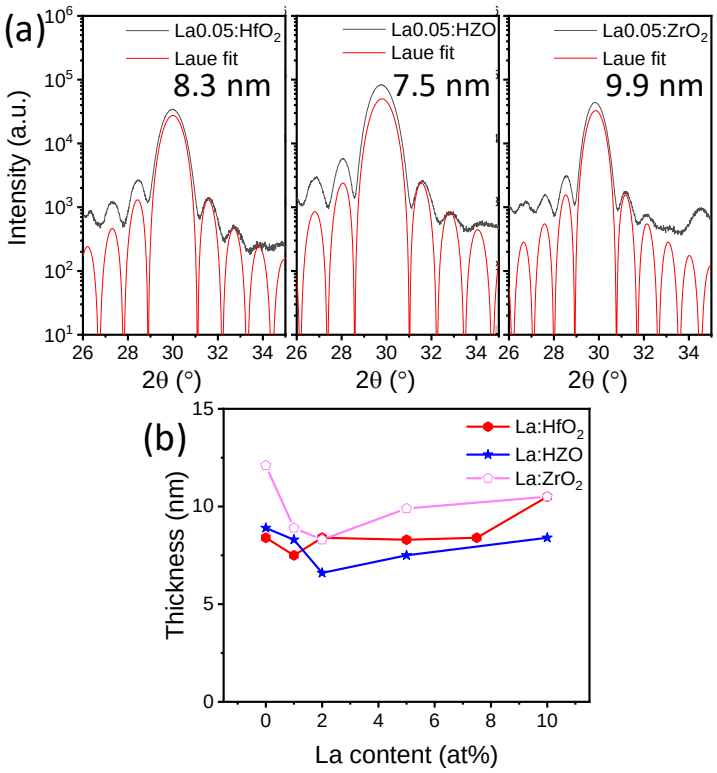

Figure 5.3.14 *(a) Laue simulations of 5% La doped HfO_2, HZO and ZrO_2 thin films. (b) The thickness of films with different compositions.*

5.3.2.2 Structure characterization

The XRD θ-2θ scans of the La doped HfO_2, HZO and ZrO_2 thin films (the heterostructure is sketched at the left) are shown in Figure 5.3.15a-c, respectively. The two highest peaks are related to STO(001) and STO(002) at 2θ ~23° and 2θ ~46°. The corresponding reflections of LSMO are at the right side of the substrate peaks. The reflections related to the thin films are in the 2θ range of 26 - 35°, which is zoomed by high resolution scans and indicated at the right side. The peak around 30° is at the position of the o(111), c(111)

and t(101) reflections of hafnium polymorphs, companied by Laue fringes. It can be seen that with La content increase, there is a clear shift of the peak to a lower 2θ angle. And this kind of shift is much obvious in films with higher Zr content. Apart from the peaks around 30°, some other peaks can also be observed. In figure 5.3.15a, m-(-111) peak at 2θ ~28.4° presents in the undoped and the 1 at% doped HO films. And in 10 at% La doped film, the peak corresponding to m-{200}, o-{200}, t-(002) or c-(200) reflections can be found at 2θ ~34.5°. Comparatively, the peak at 2θ ~28.4° is scarcely observable in La:HZO (Figure 5.3.15b) and La:ZO films (Figure 5.3.15c), whereas, the peak at 2θ ~34.5° is more evident.

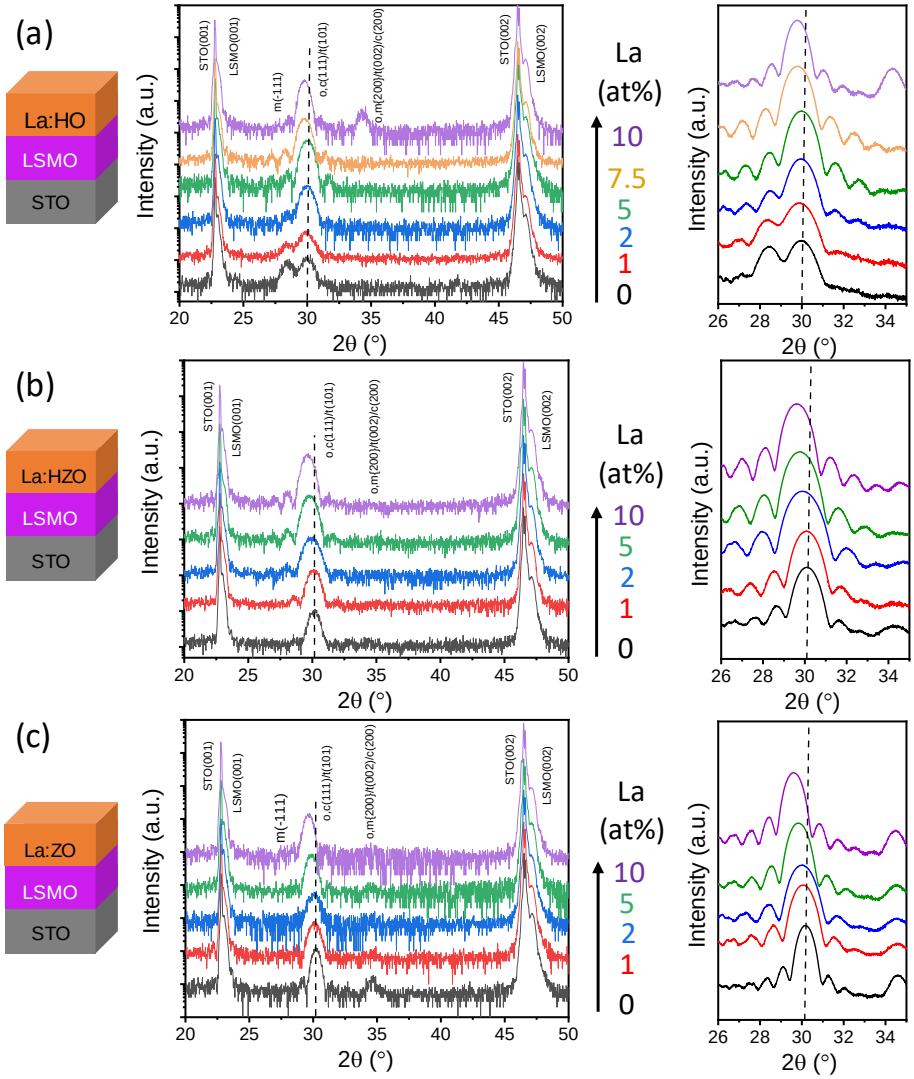

Figure 5.3.15 *Sketches and XRD θ-2θ scans of (a) La:HO films, (b) La:HZO films and (c) La:ZrO_2 films. Vertical dash line marks the position of the o(111)/c(111)/t(101) peak in the 0% La doped film. The La content is indicated at the right side of θ-2θ scans. The high resolution θ-2θ scans of the film peaks are indicated at the right side.*

The out-of-plane lattice parameter (d) of the peaks around 30° is shown in Figure 5.3.16. In La:HO films (Figure 5.3.16a), the d value is around 2.98 Å in the 0 - 5 at% La doped films and increases to ~3.00 Å in the 7.5 - 10 at% La doped films. The expansion of d value in La doped HfO_2 films is associated to the presence of cubic phase.[74] The variation of d value in La:HZO (Figure 5.3.16b) and La:ZO (Figure 5.3.16b) films is similar. With La content increase, the d value increases from around 2.96 Å in the undoped films to around 3.02 Å in the 10 at% La doped films, which is proposed to the presence of cubic or tetragonal phase in polycrystalline films.[96,183]

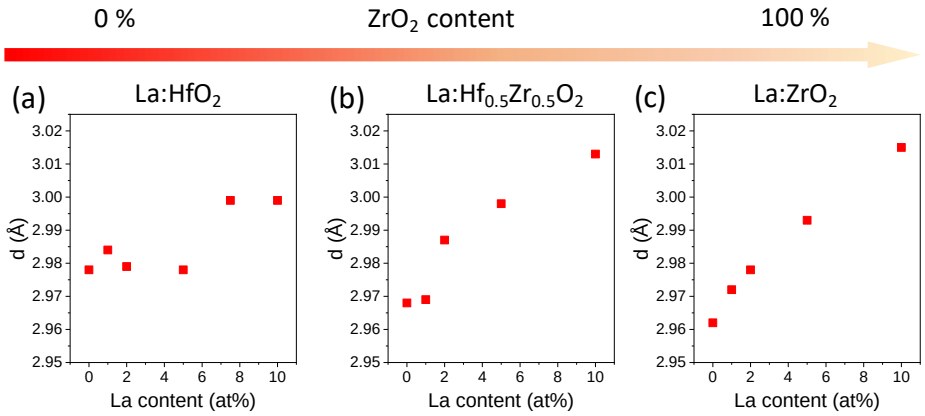

Figure 5.3.16 *The out-of-plane lattice parameter of the peaks around 30° of (a) La:HO, (b) La:HZO and (c) La:ZO films as a function of La content.*

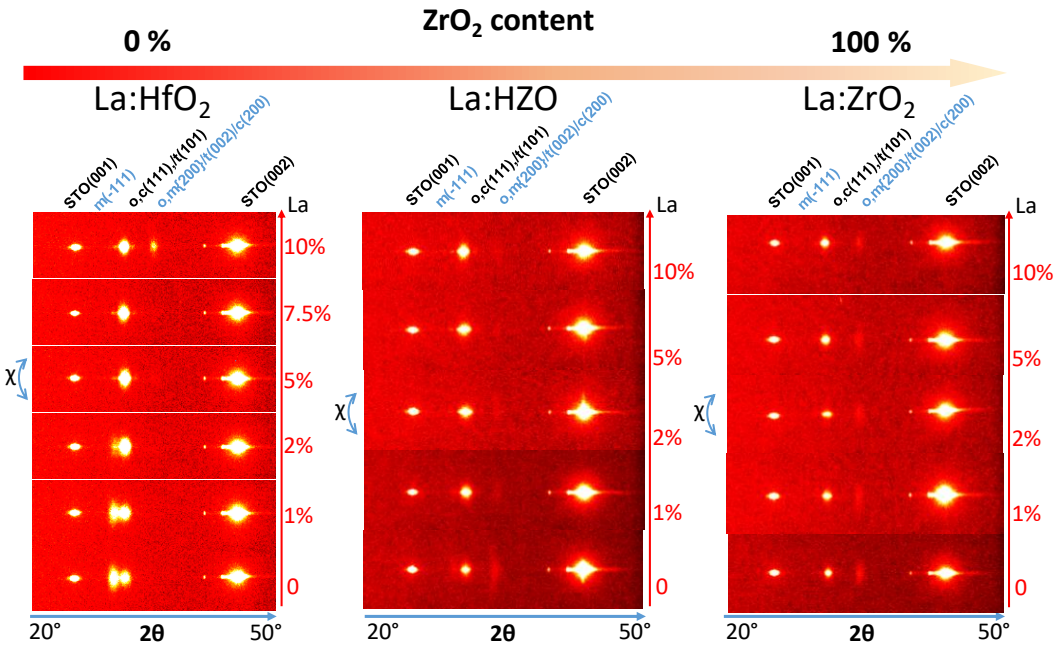

Figure 5.3.17 *The XRD 2θ-χ images of La:HO, La:HZO and La:ZO films with different La content.*

The 2θ-χ maps of La:HO, La:HZO and La:ZO films with different La content are shown in Figure 5.3.17. Bright spots can be found around χ=0, indicating good epitaxial relationship with substrate. Compared with the θ-2θ scans, there is absence of other symmetrical reflections. In summary, La:ZO and La:HZO films have less m(-111) phase, but more m,o-{200}, t-(002) or c-(200) phase than La:HO films, and the (111)-oriented cubic and/or tetragonal phases can be present, particularly in the 10 at% La films.

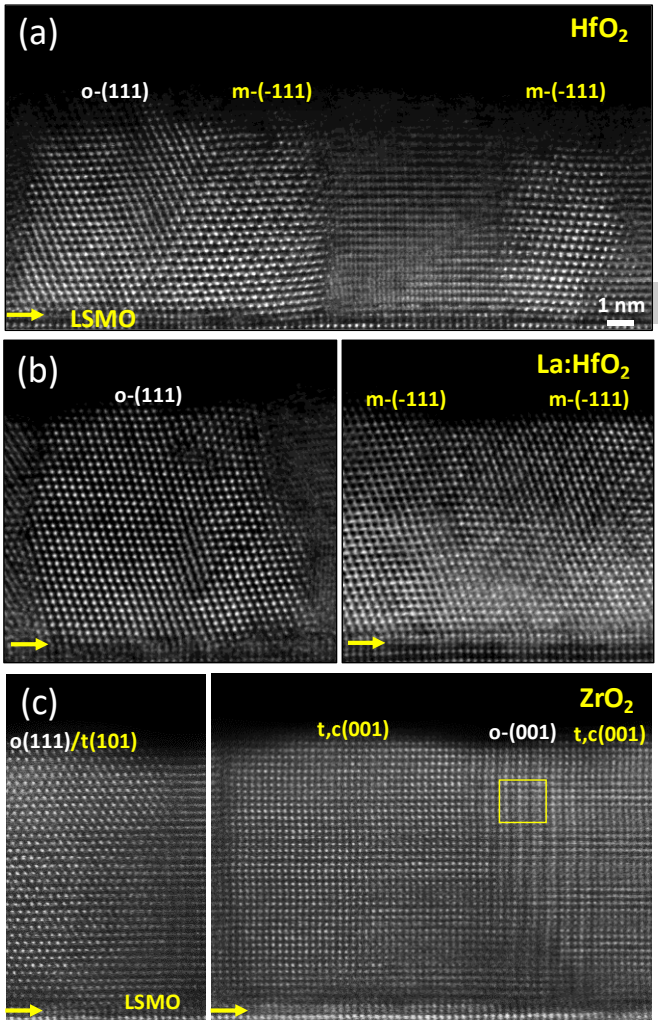

Figure 5.3.18 *The HAADF cross sectional images of (a) La:HO, (b) La:HZO and (c) La:ZO films. The yellow arrows indicate the interface with the bottom LSMO electrode.*

To further identify the phases formed in the films, HAADF cross-sectional images of HO (Figure 5.3.18a), 2 at% La:HO (Figure 5.3.18b) and pure ZO (Figure 5.3.18c) films are collected in an aberration-corrected STEM. From the comparison between the arrangement of the sublattices and the cation model from VESTA, the phase formed in the film can be identified. The phases formed in the HO and 2 at% La:HO films are a

mixture of o(111) and m(-111) crystallites. In Figure 5.3.18c, the yellow rectangular area follows the structure of o phase with orientation of (001). However, the left and right sides of the o-phase likely signal the formation of t/c phase. Therefore, the ZO film (Figure 5.3.18c) is composed of a mixture of i) o(111) and/or t(101), ii) o(001), and iii) t(001) and/or c(001) phases.

5.3.2.2 Electrical characterization

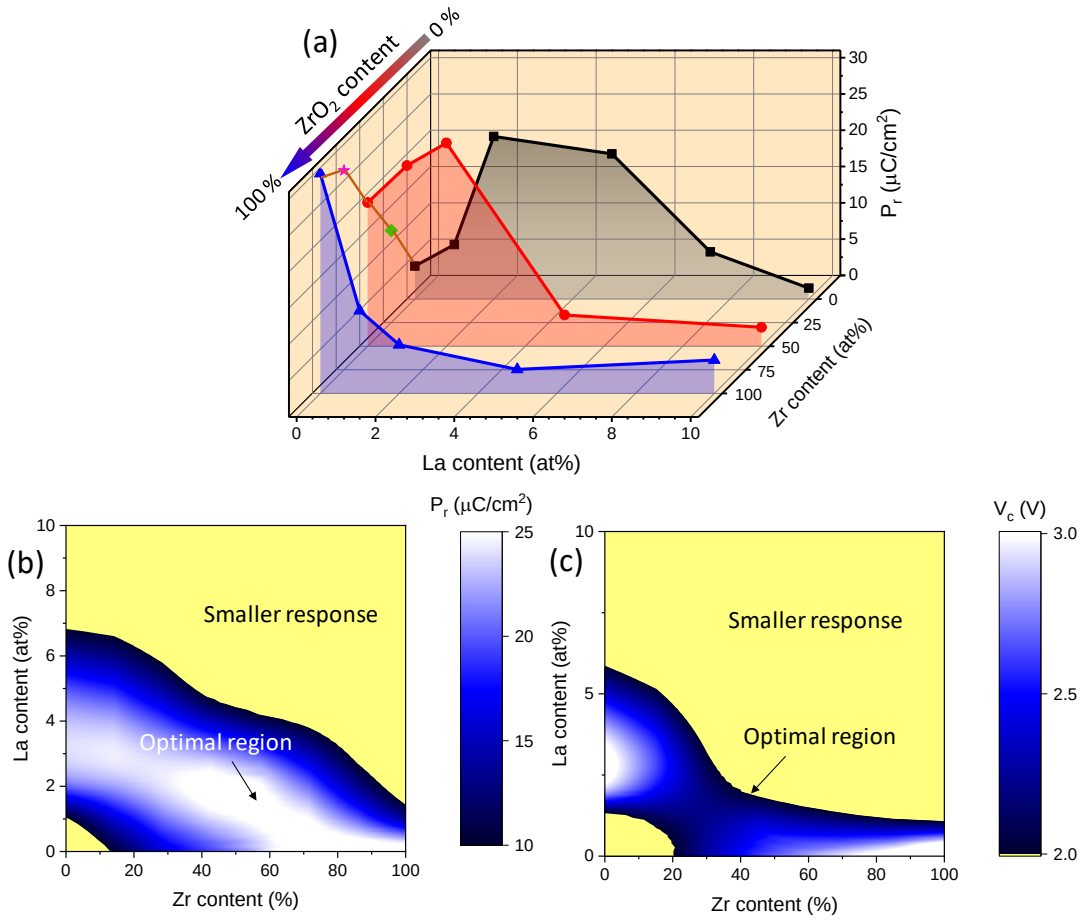

Figure 5.3.19 *(a) Remanent polarization of La:ZO (blue symbols), La:HZO (red symbols) and La:HO (black symbols) as a function of La content, and remanent polarization of 0% La* $Hf_{0.25}Zr_{0.75}O_2$ *(pink star) and* $Hf_{0.75}Zr_{0.25}O_2$ *(green diamond) films. Color maps of (b)* P_r *and (c)* V_c *as a function of Zr and La content.*

Figure 5.3.19a shows the remanent polarization of films with different composition. The P-V loops measured at the maximum voltage before breakdown are shown in appendix 1. It can be seen that the content of La and Zr has a distinct influence on the P_r value of the HfO_2-based thin films. In La:ZO series (blue symbols), the high P_r up to 30 $\mu C/cm^2$ can be obtained in pure ZrO_2 film, but it decreases dramatically with La increase. It has to be

noted that the high P_r in pure ZrO_2 film, as discussed in chapter 5.1, could be companied with ferroelectric polarization switching and resistive switching contributions or other contributions, and thus P_r is overestimated. In La:HZO series (red symbols), the P_r is 20 $\mu C/cm^2$ in HZO film and increases to 28 $\mu C/cm^2$ in 2 at% La doped HZO film. Additional doping to 5 at% results in vanishing of switching current peaks, as indicated in appendix 1. In terms of La:HO series (black symbols), the P_r is very low in pure HfO_2 film and increases to 20-22 $\mu C/cm^2$ in the 2-5 at% La doped HO film. Further increasing La content leads to decreasing of polarization and disappearing in the 10 at% La doped film. The influence of Zr content on the HfO_2-based thin films without La doping is also included in the Figure 5.3.19a. With Zr content decreasing, the polarization gradually reduces. In summary, when increasing the Zr content, a lower La content is more suitable for achieving higher P_r (2-5% in HO, 1-2% in HZO and 0% in ZO). Polarization increases with Zr content in $Hf_{1-x}Zr_xO_2$ films without La doping. Figure 5.3.19b sketches the map of La-Zr content for high ferroelectric polarization (larger than 25 $\mu C/cm^2$, white colored) in HfO_2-ZrO_2-La_2O_3 ternary system. Interestingly, there is also an optimized doping range for relatively lower coercive field of near 2 V (Figure 5.3.19c) with high P_r.

Dielectric constant loop is also effective method to obtain the ferroelectric and crystal phases information. Figure 5.3.20a-c presents the dielectric constant loops of La:ZO, La:HZO and La:HO films, respectively. The extracted dielectric constants at maximum applied voltage with different La content are shown in Figure 5.3.20d. The dielectric permittivity of o, t, c, and m phases of HfO_2 are around 24-29, 24-57, 36, and 19-25,[36,37] respectively, as shown in Figure 5.3.20d for comparison. It can be seen that in La:ZO series (Figure 5.3.20a), the hysteresis is not obvious in pure ZrO_2 film, which is probably related to the high coercive voltage (appendix 1). The permittivity is around 26 in pure ZrO_2 film and increases to 35 in 2 at% La:ZO with slight hysteresis, and then dropping to 25 in 10 at% La doped film. The relative lower permittivity value of ZrO_2 film indicates a higher fraction of o/t phase, and lower fraction of c phase. The value is similar to that reported for undoped ZO polycrystalline films.[184] The high permittivity and low P_r value in 2 at% La:ZO film reveal the increase of t/c phase and decrease of o phase. However, the low permittivity and vanishing of ferroelectric switching in 10 at% La doped ZrO_2 film signal the possible dominated m/t phase and low c phase. The formation of pyrochlore $La_2Zr_2O_7$ phase, with dielectric constant around 23, in highly La doped films could also be responsible for the low permittivity.[185]

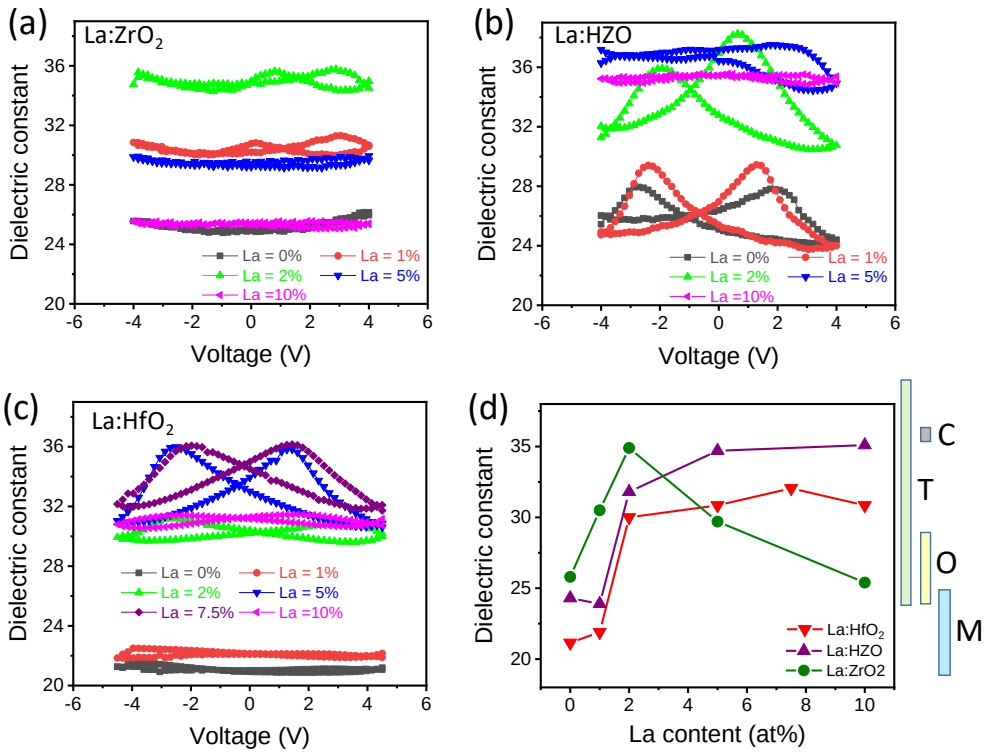

Figure 5.3.20 *Dielectric constant loops for (a) La:ZO, (b) La:HZO, and (c) La:HO films. (d) Dielectric constant as a function of the La content for La:ZO (green circles), La:HZO (purple up triangles), and La:HO (red down triangles). Ranges of values of permittivity expected for monoclinic (M), orthorhombic (O), tetragonal (T) and cubic (C) HfO_2 are indicated at the right.*

In La:HZO series (Figure 5.3.20b), the hysteresis can be clearly observed in undoped, 1 at% and 2 at% La doped films, and is less evident in the 5 at% film and finally not observable in 10 at% doped film. The permittivity is around 24 in the undoped and 1 at% doped films, rises to 32 in the 2 at% La:HZO film, and about 35 in the 5 and 10 at% La:HZO films. Combining the polarization and permittivity value, a phase change tendency can be proposed with La content increase, that mixture of o and m phase, to o phase dominated, to mixture of o and c phase, and finally c phase dominated. In La:HO series (Figure 5.3.20c), the butterfly shape is not observable in HfO_2 and 1 at% doped film, but very evident in the 5 and 7.5 at% La doped films. In terms of the permittivity value, it increases from around 22 in HfO_2 and 1 at% doped film to 30 in the 2 at% doped film, and reaches 31-32 in the 5-10 at% doped films. The variation implies that m phase dominates in the film with La less than 1 at%, and high amount of o phase in 2-5 at% films, but c phase dominates in the film with higher La content.

Conclusion

In summary, the synergic doping effect of La and Zr on the stabilized polymorphs and the ferroelectric properties of epitaxial HfO_2-based thin films is comprehensively explored. In $Hf_{1-x}Zr_xO_2$ films, the decreasing of Zr content favors the formation of m phase. In La:HZO and La:HO films, La favors the formation of o phase in low content, but c phase in highly La doped films. With Zr content decreasing, the optimized La content shifts from 0% for ZrO_2 to 2-5% for HfO_2, and the P_r of about 20-30 $\mu C/cm^2$ can be obtained in the optimized HfO_2-ZrO_2-La_2O_3 ternary system.

Appendix 1

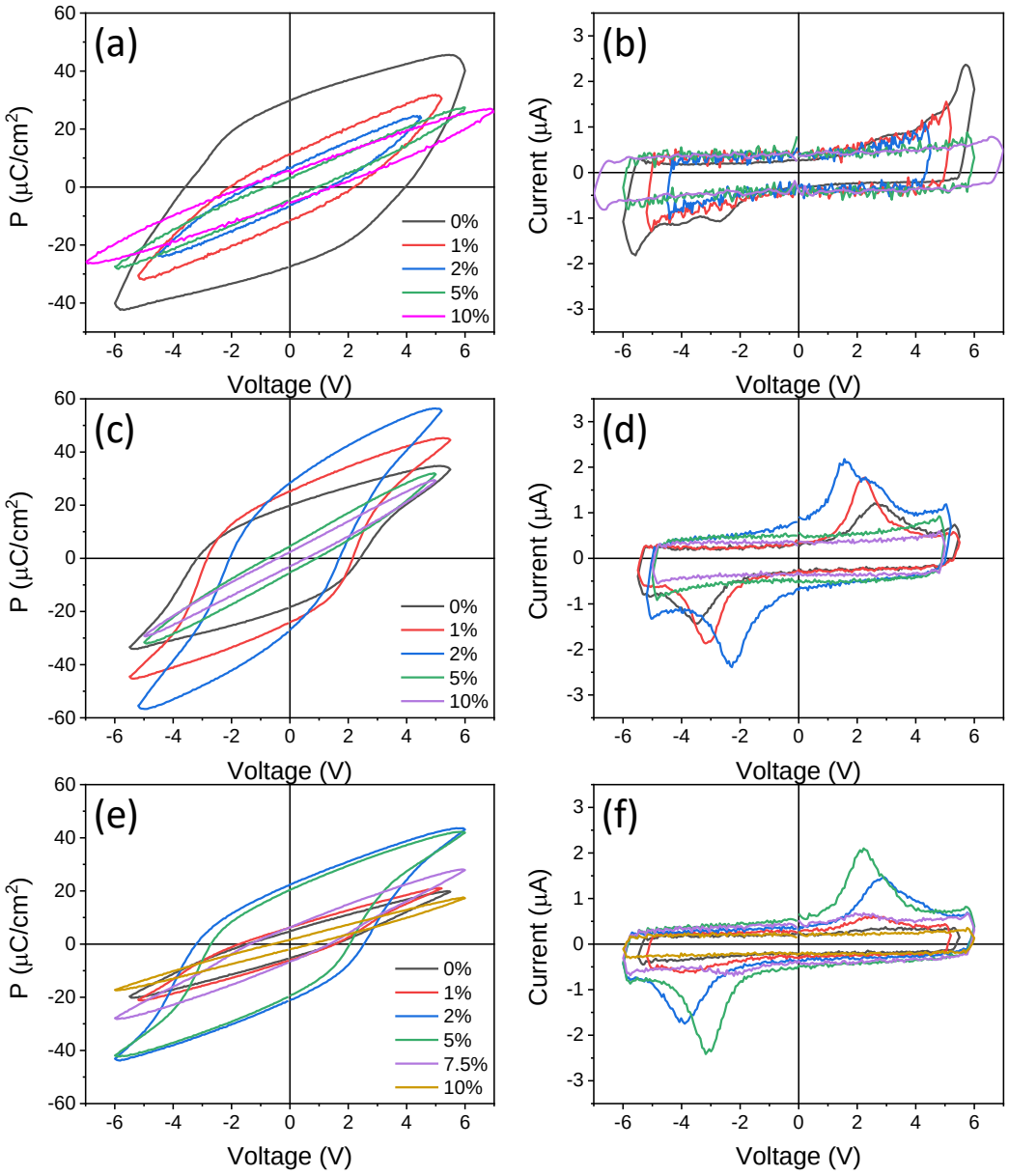

Figure A5.3.1 *The polarization-voltage loops and current-voltage loops of films with different compositions. (a-b) La:ZO, (c-d) La:HZO and (e-f) La:HO.*

Chapter 6. Endurance and switching mechanisms

One of the critical issue of ferroelectric HfO_2-based thin films is the coexistence of non-polar phases (like monoclinic phase) with the ferroelectric ones. This coexistence is detrimental for P_r. However, the influence of paraelectric phase on other ferroelectric properties, such as endurance, and switching dynamics, is still under study. Using different substrates, the relative amount of orthorhombic (ferroelectric) and monoclinic (paraelectric) phases can be controlled. First, the endurance of epitaxial $Hf_{0.5}Zr_{0.5}O_2$ (HZO) films with different orthorhombic/monoclinic ratio is investigated. Epitaxial HZO films almost free of parasitic monoclinic phase suffer severe fatigue. In contrast, fatigue is mitigated in films with greater amount of paraelectric phase. It is argued that the enhancement of endurance in films with coexisting phases results from the suppression of pinned domain propagation at ferroelectric-paraelectric grain boundaries, whereas in pure o-phase film, there is a rapid increase of the size of the pinned domains. Second, a direct comparison of switching dynamics in epitaxial 1%La doped HZO films with pure orthorhombic phase and coexisting orthorhombic/monoclinic phase is conducted. Switching spectroscopy analysis reveals that pure orthorhombic phase films follow the Kolmogorov-Avrami-Ishibashi (KAI) switching model. Instead, the mixed orthorhombic/monoclinic phase films show nucleation limited switching (NLS). Films having larger fraction of non-ferroelectric phase with concomitant larger number of incoherent grain boundaries show 2 orders of magnitude faster switching time. Overall, it is observed that in epitaxial film the presence of non-ferroelectric phase is not necessarily detrimental for endurance and switching speed.

6.1 Effects of crystal phases on endurance

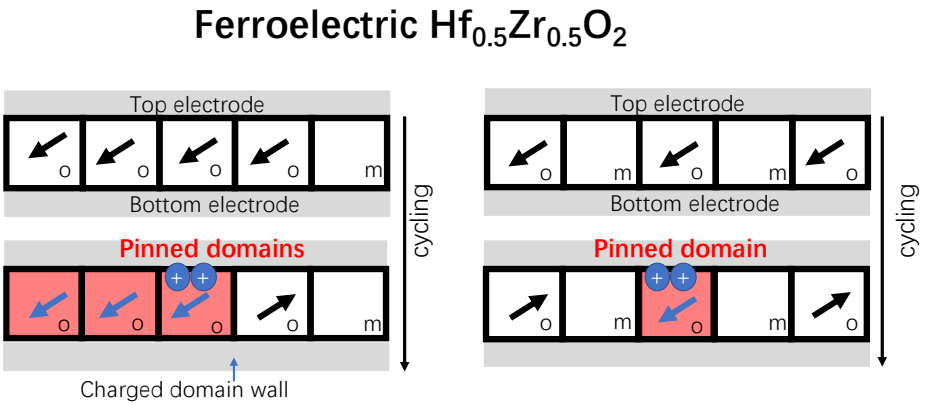

Abstract

Retention and endurance in epitaxial HZO films with different orthorhombic/monoclinic ratio, modulated by epitaxial stress using different substrates, is investigated. Long retention presents in films regardless of the relative amount of parasitic m-phase. However, endurance is highly sensitive to the o/m phase ratio. The films with more ferroelectric o-phase suffers more prominent fatigue, whereas, in the films with more paraelectric m-phase, fatigue is less severe. This suggests that fatigue could be intrinsically severe in ferroelectric hafnia films. Orthorhombic-monoclinic grain boundaries are proposed to reduce propagation of domain pinning, allowing endurance increase.

Introduction

Ferroelectric HfO_2-based thin films have aroused great attention for applications.[8,22,186–188] Besides polarization, retention and endurance are also fundamental properties of ferroelectrics for its use in memories. Retention of ferroelectric HfO_2 capacitors is generally reported to be longer than 10 years,[28,29,189,190] but as mentioned in previous chapter, a possible retention-endurance dilemma exists.[96] Fatigue in ferroelectrics is generally related to the domain pinning or nucleation inhibition during cycling, which is associated to the accumulation of oxygen vacancies and/or injection of charges.[86,96,191–195] Epitaxial HfO_2-based thin films with less defects than polycrystalline films are expected to be less affected by fatigue. However, the reported behaviour is opposite, with epitaxial films showing a significant reduction of polarization under cycling.[28,29,164] Aiming to gain insight into the unexpected increased fatigue of epitaxial films, the endurance of epitaxial HZO films with different orthorhombic/monoclinic ratio, controlled by the use of different substrates,[14] is investigated. Epitaxial HZO films with almost free parasitic monoclinic phase suffer severe fatigue. In contrast, fatigue is mitigated in films with greater amount of paraelectric phase. It is argued that the enhancement of endurance in films with coexisting phases results from the suppression of pinned domain propagation at ferroelectric-paraelectric grain boundaries, whereas in pure o-phase film, there is a rapid increase of the size of the pinned domains.

6.1.1 Structure characterization

Epitaxial HZO films (9.5 nm thick) and LSMO electrodes (25 nm thick) were grown by pulsed laser deposition. A series of HZO/LSMO bilayers were deposited on a set of (001)-oriented cubic or pseudocubic oxide substrates: $SrTiO_3$ (STO), $DyScO_3$ (DSO), $GdScO_3$ (GSO), $TbScO_3$ (TSO), $NdScO_3$ (NSO), MgO, and $((LaAlO_3)_{0.3}(Sr_2TaAlO_6)_{0.7}$ (LSAT). Details on growth conditions of the films are reported elsewhere.[14] The XRD 2θ-χ frames of HZO/LSMO bilayers on MgO, STO, and GSO are shown in Figure 6.1.1a-c. The spots corresponding to reflections of the substrates and the LSMO electrode, as well as to HZO film can be observed. The film on MgO exhibits circular o-HZO(111) reflection and elongated m-HZO(002) spots. In the film deposited on STO substrate, both reflections can still be detected, but intensity for o-HZO(111)-phase increases and for m-HZO(002) phase decreases. The 2θ-χ frame of the film on GSO shows a similar o-HZO(111) bright spot, but there is no monoclinic spot. Thus, there is coexistence of o-phase and m-phase

in the HZO film on STO, and the o/m phase ratio is relatively lower in the film on MgO and much higher in the film on GSO. These results illustrate that substrate selection allows controlling the relative amount of the orthorhombic and monoclinic phases in HZO film.

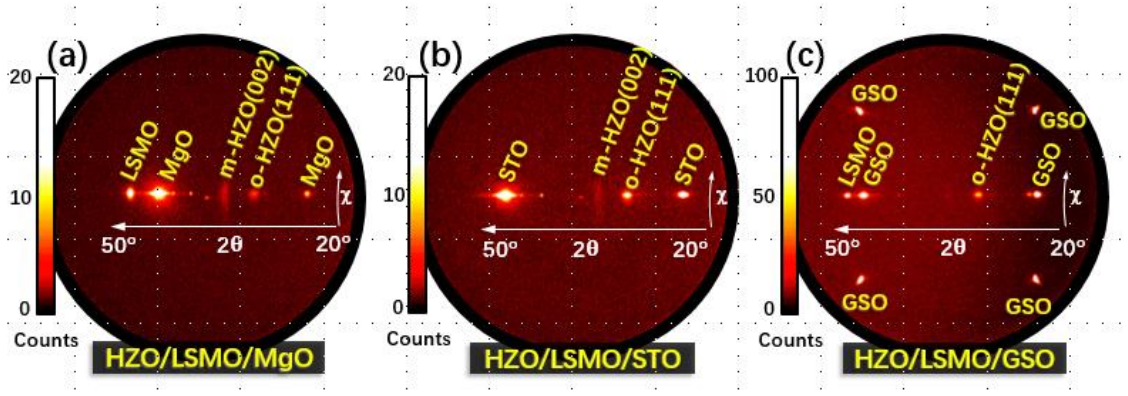

Figure 6.1.1 *XRD 2θ-χ frames of HZO/LSMO bilayers on (a)MgO, (b)STO, and (c)GSO.*

6.1.2 Retention of films with different o/m-phase ratio

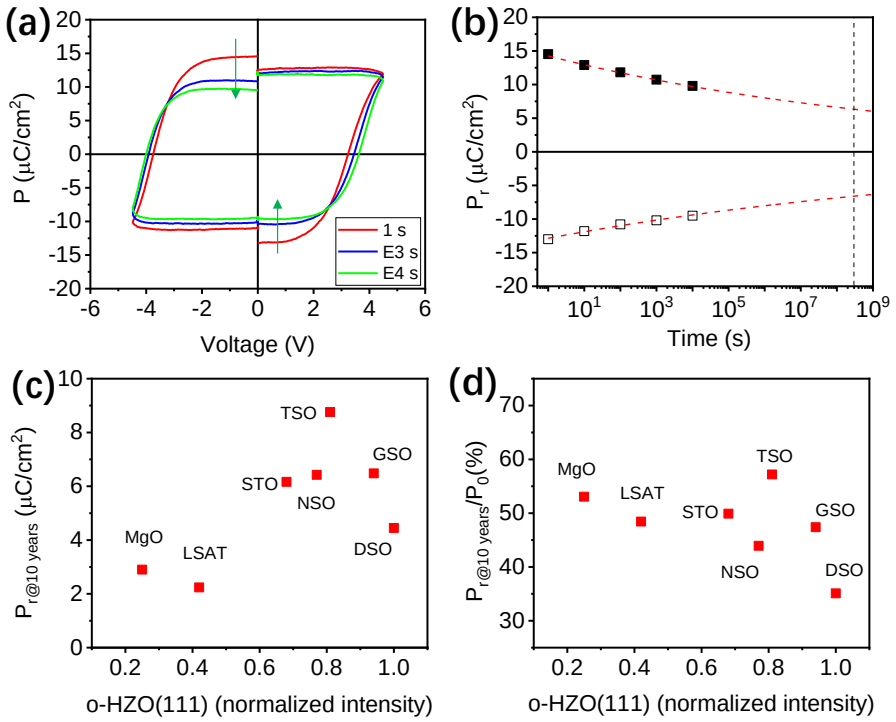

Figure 6.1.2 *(a) Polarization loops of the HZO/LSMO/GSO sample measured after the indicated delay times. (b) Remanent polarization as a function of the time. The red dotted lines are fits to the* $P_r = P_0\, t_d^{-k}$ *dependence. The vertical black dotted line marks 10 years' time. (c) Extrapolated* P_r *and (d) normalized* P_r *after 10 years of all samples, plotted against the normalized intensity of the o-HZO(111) diffraction spot.*

The retention of the HZO film on GSO is shown in Figure 6.1.2a-b. The polarization loops measured from PUND method indicates a clear progressive decrease of the remanent polarization after increase of the delay time from 1s to 10^4s. The dependence of the P_r versus the delay time after applying positive or negative 4.5 V pulses is represented in Figure 6.1.2b. The data show a slow reduction in the polarization with the increase of the delay time. By fitting the data using $P_r = P_0\ t_d^{-k}$ dependence (red dash line),[196] the extrapolation of P_r to 10 years (black vertical dotted line) indicates a value larger than 6 $\mu C/cm^2$. The films on other substrates also show long retention, with an average (positive and negatively poled) remanent polarization in the 2-9 $\mu C/cm^2$ range after extrapolated to 10 years. The raw data of retention measurements are shown in appendix 1. Films with a lower amount of orthorhombic phase (on MgO and LSAT substrates) show a lower extrapolated P_r after 10 years (details of normalized orthorhombic phase intensity are reported elsewhere[14]). However, there is no obvious dependence of P_r after 10 years normalized to P_0 on the amount of orthorhombic phase, with a value around 45% to initial polarization. Thus, all films exhibit a prolonged retention regardless of the relative amount of parasitic m-phase, and the presence of an in-plane bulk depoling field generated by the m-phase[96] does not seem to have important impact on retention.

6.1.3 Endurance of films with different o/m-phase ratio

Figure 6.1.3 presents the current density-voltage (J-V) curves and the corresponding polarization loops of films on GSO (large amount of orthorhombic phase), MgO (low amount of orthorhombic phase), and STO (mixture of orthorhombic and monoclinic phases). The measurements were done in the pristine state (Figure 6.1.3a-b), after 10^4 cycles (Figure 6.1.3c-d) and after 10^7 cycles (Figure 6.1.3e-f) at 4.5 V. It can be seen that in pristine state, apparent ferroelectric switching peaks present in all films, with larger peak area in the films on GSO and STO than on MgO substrate. The higher coercive voltage in negative side indicates an imprint field pointing toward the bottom LSMO electrode. The average coercive and imprint voltages are around 2.7 V and 0.6 V, respectively. The corresponding polarization loops are presented in Figure 6.1.3b. $2P_r$ values are 26.8 $\mu C/cm^2$ (HZO on GSO), 24.6 $\mu C/cm^2$ (HZO on STO), and 12.2 $\mu C/cm^2$ (HZO on MgO). Note that the P_r is measured with the same maximum voltage amplitude of 4.5 V for the endurance tests, which is unsaturated state. Saturated polarization loops measured in pristine state with higher maximum voltage amplitudes are shown in appendix 2. The P_r values in the saturated loops are 25.6 $\mu C/cm^2$ (HZO on GSO), 15.7

μC/cm^2 (HZO on STO), and 9.7 μC/cm^2 (HZO on MgO), which is consistent with the relative amount of the o-phase in the films.[14]

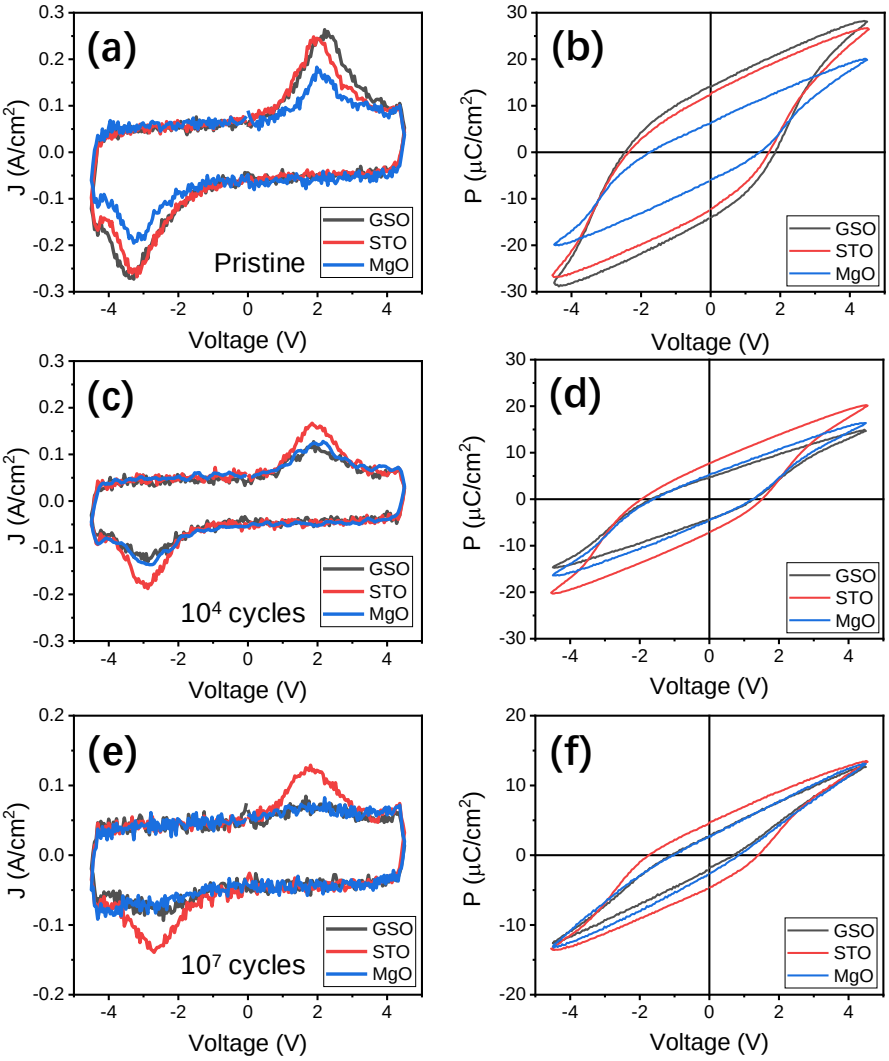

Figure 6.1.3 *(a) J-V curves and (b) corresponding polarization loops of HZO films on GSO, STO and MgO. The measurements were performed in pristine state. (c-d) Equivalent measurements after 10^4 cycles (square pulses of 4.5 V amplitude). (e-f) Equivalent measurements after 10^7 cycles.*

After 10^4 cycles, the ferroelectric switching peaks are still evident in all films, but the area below the current peaks has decreased and it has become similar in the films on GSO and MgO. This indicates fatigue in all three samples, and particularly severe in the film on GSO. Simultaneously, the memory window decreases to 8.9 μC/cm^2 (HZO on GSO), 15.1 μC/cm^2 (HZO on STO), and 9.9 μC/cm^2 (HZO on MgO). Fatigue happens after 10^7 cycles with nearly negligible ferroelectric switching peak in the film on GSO. 2P$_r$ of this film is estimated to be around 5 μC/cm^2, including some contribution (around 2 μC/cm^2)

due to leakage. The fatigue is less severe in the other two samples. $2P_r$ after 10^7 cycles is 8.7 and 6.1 μC/cm^2 in the films on STO and MgO, respectively.

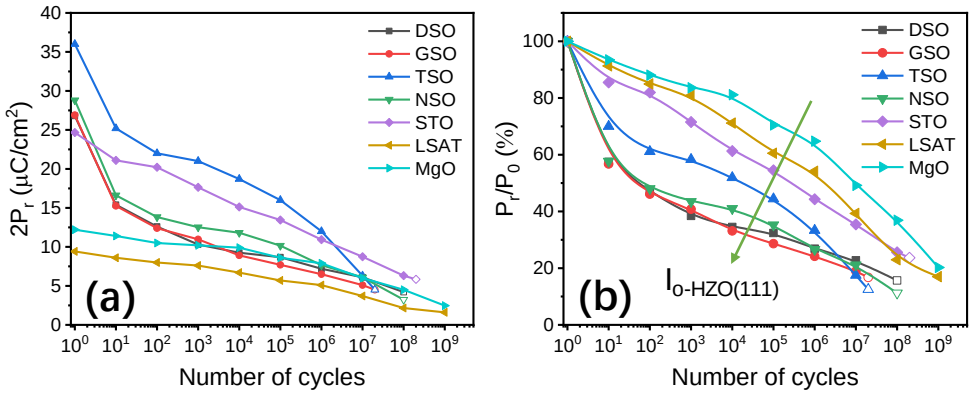

Figure 6.1.4 *Endurance of epitaxial HZO films on different substrates, measured with 4.5 V square pulses. (a) $2P_r$ as a function of number of cycles. (b) Normalized P_r as a function of number of cycles. The open symbols indicate hard breakdown of the capacitor.*

Figure 6.1.4a shows the variation of $2P_r$ of all films with the number of cycles with bipolar amplitude of 4.5 V. The initial memory window changes from 36 μC/cm^2 (TSO) to 24.6 μC/cm^2 (STO) and to 9.5 μC/cm^2 (LSAT), which follows the relative amount of o-phase in the films on each substrate.[14] And there is no wake-up effect in any sample, and fatigue happens from the first cycles. Fatigue is severe in the films on scandate substrates with memory window decreasing to 5.1-6.3 μC/cm^2 after 10^7 cycles. In contrast, the film on STO has $2P_r$ = 8.7 μC/cm^2 after the same number of cycling and the films on MgO and LSAT, which present very low polarization in the initial state, show a slight decrease of $2P_r$ to 6.1 and 3.7 μC/cm^2, respectively. Further cycling leads to hard breakdown in the films on TSO and GSO (2×10^7 cycles), and DSO and NSO (10^8 cycles). The film on STO undergoes breakdown after 2×10^8 cycles, but it still retained $2P_r$ of 5.8 μC/cm^2. In contrast, the films on MgO and LSAT do not exhibit hard breakdown after 10^9 cycles, although $2P_r$ drops to 2.5 and 1.6 μC/cm^2, respectively. Therefore, the endurance of epitaxial HZO is highly dependent on the substrate. To better compare the fatigue in each film, the memory window after different cycling numbers is normalized to the initial value, as shown in Figure 6.1.4b. It can be observed that films with a lower content of o-phase (higher content of m-phase) exhibit slower fatigue and longer endurance. However, the films on scandate substrates, with almost single o-phase, suffer severe fatigue and shorter endurance.

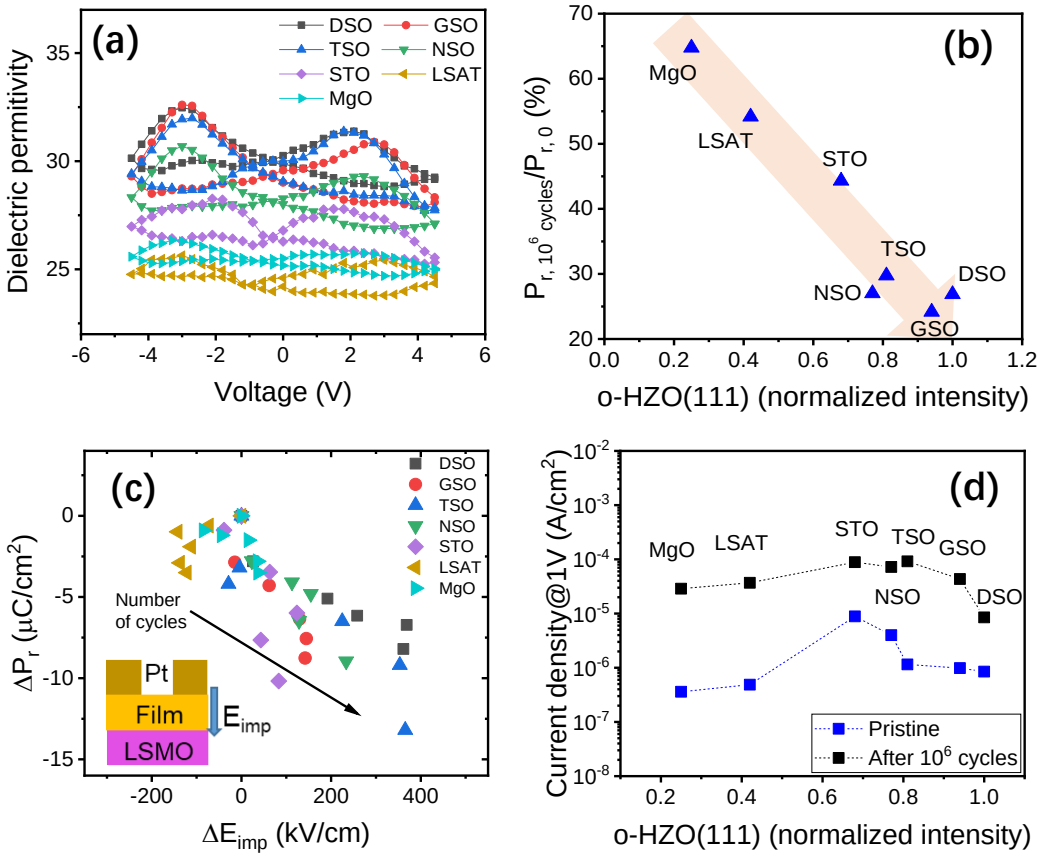

Figure 6.1.5 *(a) Dielectric constant loops of the HZO films with an excitation voltage of 50 mV at 20 kHz. (b) Percentage of P_r after 10^6 cycles, plotted as a function of the intensity of the XRD o-HZO(111) reflection (normalized to the value of the HZO/DSO sample). (c) Loss of remanent polarization with cycling with respect to the value after ten cycles, plotted as a function of the corresponding change in imprint field in the polarization loops. (d) Leakage current in the pristine state and after 10^6 cycles evaluated at 1 V as a function of the normalized intensity of the XRD o-HZO(111) reflection.*

The dielectric constant loops of the films, measured in the pristine state, are shown in Figure 6.1.5a. The films on scandate substrates with almost pure o-phase present a well-defined butterfly shape and permittivity around 30 at saturation. The dielectric constant is smaller in the film on STO with majority of o-phase and minority of m-phase. In the films with high amount of m-phase (MgO and LSAT), the permittivity is further reduced and the butterfly shape is less obvious. Thus, the different relative amount of o and m phases in the films is reflected on their dielectric constant loops. There is also a direct dependence of fatigue on the amount of o-phase (Figure 6.1.5b). The normalized P_r after 10^6 cycles indicates a clear decrease with the normalized intensity of the o-HZO(111) diffraction peak. Therefore, films with more nonpolar m-phase show less fatigue. It is

also found that during capacitor cycling there is a progressive change in the imprint field in each film (Figure 6.1.5c). Imprint is extrapolated from the current-voltage curves, as shown in appendix 3. During the first 10 cycles there is no correlation between fatigue and imprint field, maybe because very small wake-up effects are coexisting. However, after the first ten pulses, there is a correlation between the cumulative loss of polarization (fatigue, $\Delta P_r(\text{cycles}) = (P_r(\text{cycles}) - P_r(10\ \text{cycles}))$) and the change in imprint field (internal field, $\Delta E_{imp}(\text{cycles}) = (E_{imp}(\text{cycles}) - E_{imp}(10\ \text{cycles}))$) among all the films during cycling. This signals that the amount of charged defects or injected charges increases in each film during cycling, and that these charged defects/injected charges are responsible for the fatigue. The magnitudes of polarization loss and change in imprint field are small in the films on MgO and LSAT (large amount of m-phase) and high in the films on scandate substrates (large amount of o-phase). Figure 6.1.5d indicates the leakage current as a function of the relative o-phase intensity at pristine and after 10^6 cycles. It can be observed that in the pristine state, the peak of leakage current is at the film with intermediate o-phase amount, which signals that the incoherent m/o grain boundaries dominate the leakage current. These incoherent m/o grain boundaries are likely to provide film with better charge source, which could compensate the injected carriers and is expected to induce less imprint and slower fatigue. However, after 10^6 cycles, the leakage current is similar in all films irrespectively of the o-phase amount. This means that the leakage current in cycled films is dominated by the new generated defects. Therefore, leakage current and number of defects increase by cycling cannot explain by itself the better endurance for films having high amount of parasitic m-phase. An alternative scenario is proposed below to explain the fatigue phenomenon observed above.

Figure 6.1.6a shows a STEM cross-sectional image of the film on STO. There is a mesh of columnar orthorhombic (ferroelectric) and monoclinic (paraelectric) HZO grains of lateral size of around ten nanometers. Each orthorhombic grain is a single variant, and the incoherent boundaries between o and m grains extend vertically from the bottom to the top of the HZO layer. In this film, and in the films on LSAT and MgO, m and o grains coexist, while the amount of m-phase is very low in the films on the scandate substrates. The HZO films on scandate substrates exhibit also columnar topology, with a single crystal variant in each grain and coherent boundaries between them.[14] The strong dependence of o/m phase ratio on the substrate, and the columnar topology of the grains, can be a relevant factor for the different fatigue of the films.

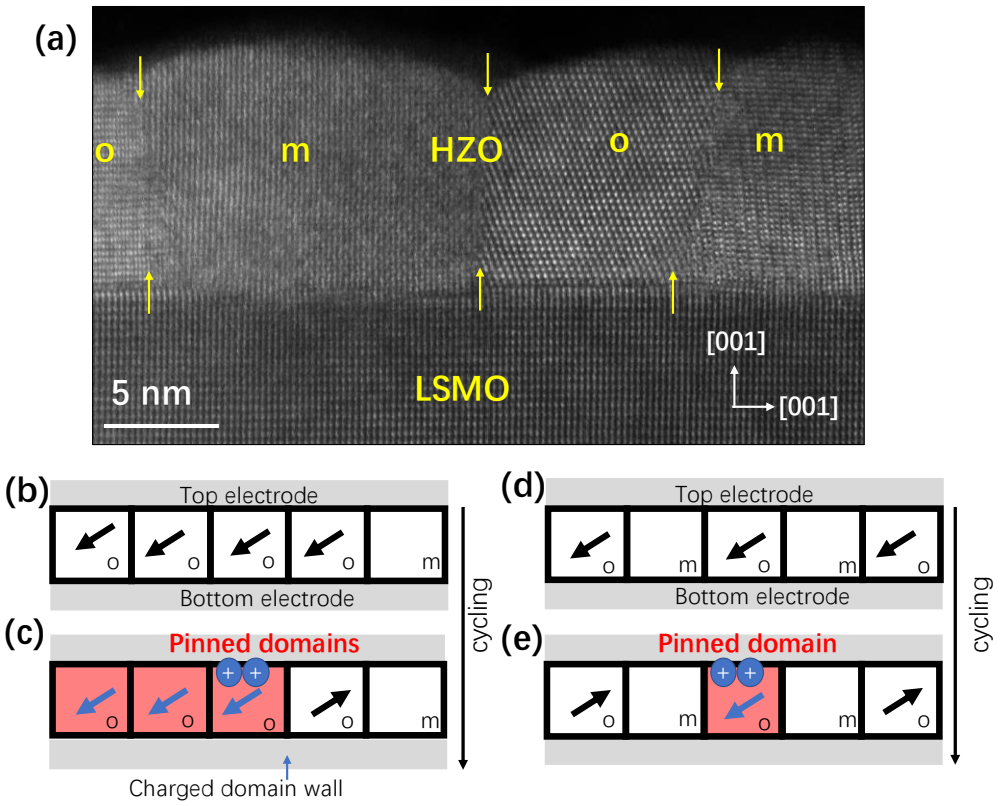

Figure 6.1.6 *(a) Cross-sectional STEM image of the HZO/LSMO/STO(001) sample, showing orthorhombic (o) and monoclinic (m) columnar grains. Grain boundaries are marked by yellow arrows. (b-e) Sketch of the endurance degradation by fatigue in films with small (b-c) and high (d-e) amount of grains of paraelectric m-phase. Oxygen vacancies are represented by blue circles. Blue and black arrows represent pinned and unpinned dipoles, respectively, oriented along [001] in the (111) oriented orthorhombic film.*

Figure 6.1.6b sketches the HZO film with majority o-phase grains, extending from the bottom to the top electrode. Note that only a single crystal variant is sketched at here for the sake of simplicity. Black arrows indicate the direction of the [001]-oriented dipoles (tilted by 57° respect to the out-of-plane direction), after the top electrode is poled positively. Pinning of ferroelectric domains, resulted from charged defects or injected charges, has been proposed to be a main cause of fatigue in HZO films.[86,197,198] In o-phase dominated films, after cycling (Figure 6.1.6c), the charged oxygen vacancies in the interface between the HZO film and top Pt electrode could pin a volume of domains (pinned dipoles are indicated by blue arrows). The pinning and fast propagation of pinned domains in o-phase dominated film will be cyclically repeated in different places of the film, resulting in a severe fatigue during the electrical cycling process. In the sketched case, oxygen vacancies are pinned at the Pt/HZO interface, and the imprint electric field

is also toward LSMO/HZO interface. Therefore, an additional contribution to the E_{imp} toward LSMO is present.

The reason of the fast propagation of pinned domains in o-rich film is that the boundary (signaled by an arrow) with an unpinned region would be charged when the latter switches. Figure 6.1.7 shows a representation of two ferroelectric domains, one of them pinned due to charged oxygen vacancies, within a grain having a single crystal variant. When the adjacent non pinned domain switches, the opposite polarization direction will produce charged domain wall. For the pinned domain, E_x would not affect its polarization state. Instead, for the adjacent unpinned domain with antiparallel polarization direction, the presence of E_x will promote the switching towards the opposite state, resulting in an effective downwards electric field (E_z) which will act as an effective downwards imprint field. Therefore, the adjacent unpinned domain will tend to switch back to the same polarization direction as the pinned domain, as shown in the right side of the sketch. This happens in the film with a large amount of o-phase (Figure 6.1.6c), whereas, the present of nonpolar phase will substantially mitigate this adverse interaction (Figure 6.1.6e).

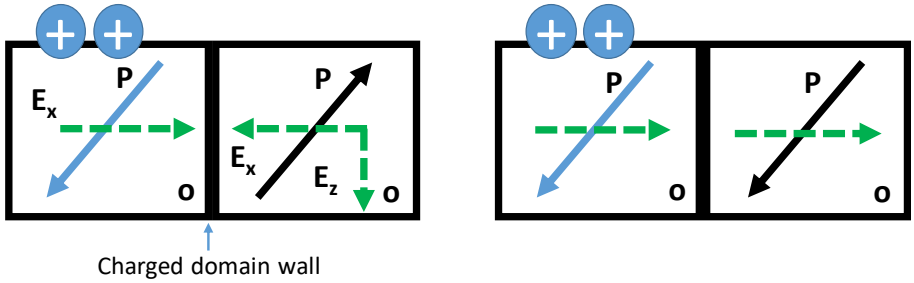

Figure 6.1.7 *Sketch of in-plane electric field induced by charged domain walls resulting in pinning of an adjacent ferroelectric domain.*

In contrast, films with coexisting of o and m grains (Figure 6.1.6d, e) are more stable under electric cycling. When the pinning happens at the interface with electrode (represented by blue circles), the rapid propagation of a pinned domain according to the mechanism proposed above would be limited to the particular grain in which domain pinning begins (red color). Other o-phase grains, separated by m-phase grains, will not be affected and their polarization will be switched (black arrows) when appropriate electric field is applied. In addition, the incoherent grain boundaries[199] between o and m-phases allow conduction of mobile charges, further favoring the screen of the in-plane polarization component. The increase of the imprint field when the films are cycled can

be related to many aspects, including the evolution of the charged domain walls, the balance between generation of charged defect and injected charges, and the uncompensated ferroelectric bound charges. In any case, the imprint and fatigue are lower in the films having higher amount of m-phase, indicating that the coexistence of o with non-ferroelectric m-phase, which a priori appeared to be negative, turns out to be positive to enhance the endurance, one of the main ferroelectric properties.

Conclusion

In summary, retention and fatigue in epitaxial HZO films with different orthorhombic/monoclinic ratio, controlled by using different substrates, is investigated. Long retention presents in films regardless of the relative amount of parasitic m-phase. However, endurance is highly dependent on the o/m phase ratio. Films almost free of parasitic phase, i.e., the closest to single crystalline like films, exhibit strong fatigue. This suggests that fatigue could be intrinsically severe in ferroelectric hafnia. Films with greater amount of parasitic m-phase appreciates slower fatigue and longer endurance. Grain boundaries of o/m phase are proposed to reduce propagation of domain pinning, allowing to increase the endurance.

Appendix 1.

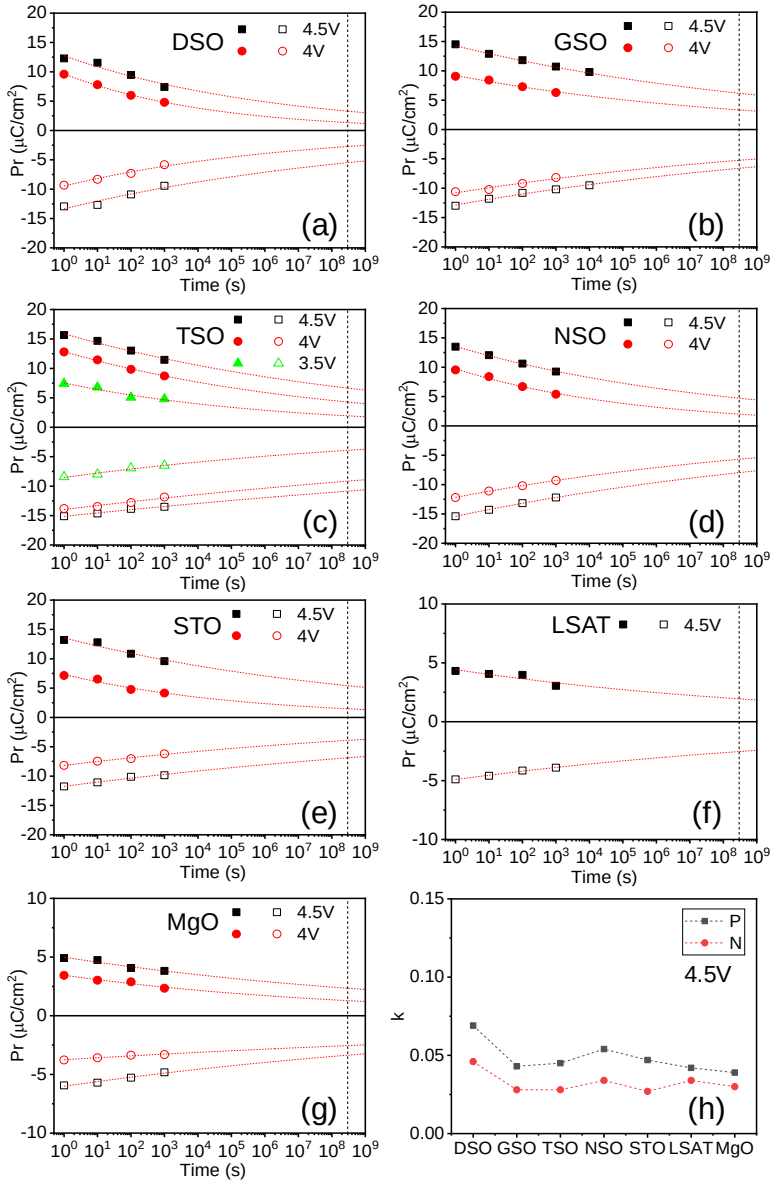

Figure A6.1.1 *Remanent polarization as a function of time of HZO films on (a) DSO, (b) GSO, (c) TSO, (d) NSO, (e) STO, (f) LSAT, (g) MgO substrate. Red dotted lines are fits to the* $P_r = P_0 t_d^{-k}$ *dependence. Vertical black dotted line marks 10 years' time, as indicated, polarization state of all films can be retained more than 10 years. In (h), the k values at 4.5V are summarized and no obvious dependence of the k on the amount of orthorhombic phase.*

Appendix 2.

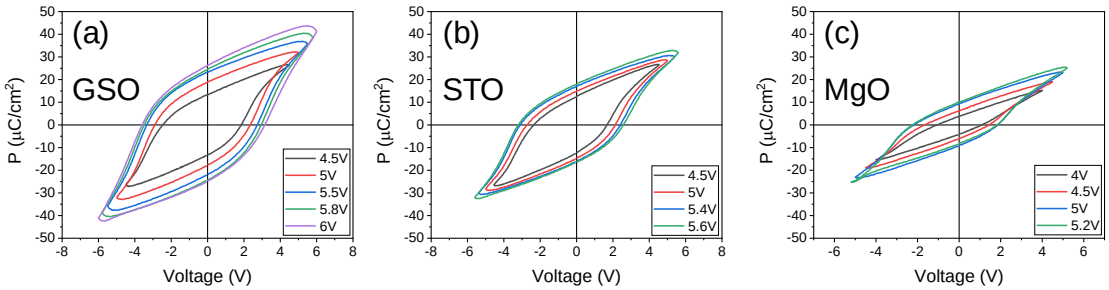

Figure A6.1.2 *The polarization-voltage loops of films on (a) GSO, (b) STO, and (c) MgO substrate after different cycling numbers.*

Appendix 3.

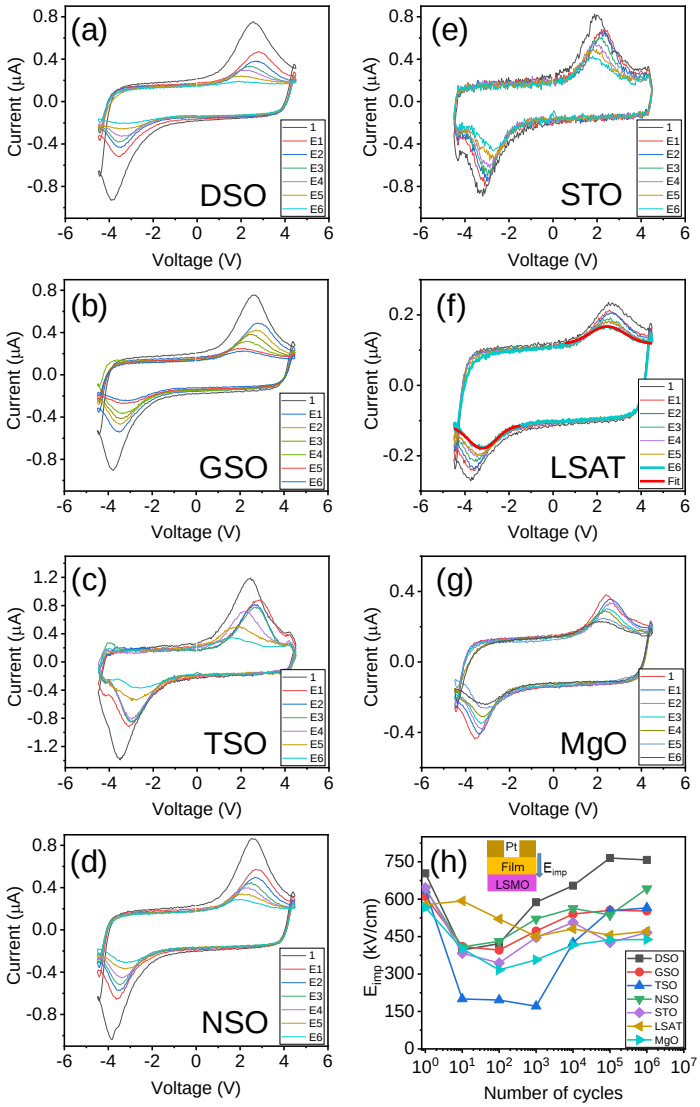

Figure A6.1.3 *The current-voltage loops of films on (a) GSO, (b) DSO, (c) TSO, (d) NSO, (e) STO, (f) LSAT, (g) MgO substrate after different cycling numbers. (h) The imprint field of HZO*

films on different substrates after different cycling numbers. The direction of the imprint is towards bottom LSMO electrode. Imprint is extrapolated from the current-voltage curves. The internal field is determined by $Eimp = |(E_{c+} + E_{c-})|/2$. *Coercive voltage* E_{c+} *and* E_{c-} *are extrapolated from the current-voltage curve by Gauss fit, as indicated in figure f.*

6.2 Effects of crystal phases on switching mechanisms

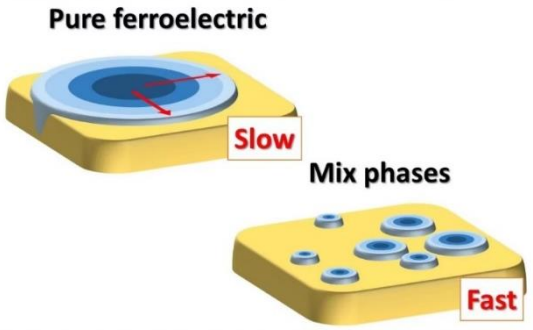

Abstract

Investigation of the switching speed and the switching dynamics mechanism is of the highest relevance for industry applications of HfO_2-based thin films. Results on the switching dynamics spectroscopy of epitaxial ferroelectric 1%La doped $Hf_{0.5}Zr_{0.5}O_2$ films with different orthorhombic/monoclinic phase ratio are explored. In films with pure orthorhombic phase, switching dynamics can be modeled by the Kolmogorov-Avrami-Ishibashi (KAI) mechanism with large characteristic switching time ($\approx 1\ \mu s$), which is shortened in fatigued junctions. However, when the ratio of monoclinic/orthorhombic phase increases, the switching time shorten. A characteristic switching time of 69 ns in pristine state for applied electric field parallel to the imprint enables preliminary neuromorphic-like behavior with fast electric stimulation. Thus, the presence of defects or paraelectric phase is found to improve the switching speed, contrary to what one can expect a priori.

Introduction

Polarization switching dynamics characterization is directly related to the applications and underlying switching mechanisms of HfO_2-based thin films. In polycrystalline films, the switching dynamics follows nucleation limited switching (NLS) model by expansion of the residual (pinned) domains.[200–204] Some reports that the increase of remanent polarization by wake-up or optimized concentration is correlated with an increase of the characteristic switching time.[201,202] While, in contrast, the increase of polarization after high pressure annealing process results in shorter switching time.[203] Besides, the direct comparison between epitaxial and polycrystalline films reveals that epitaxial film has more homogeneous nucleation but with a slower switching time than polycrystalline film.[205] Despite the fact that several works have investigated domain dynamics in ferroelectric hafnium thin films, some of conclusions are contradictory. Thus, further exploration is still needed to fully understand switching dynamics, especially related to the influence of microstructure and defects. In this part, we directly compared the switching dynamics of epitaxial films with well-controlled microstructure, particularly the impact of the paraelectric monoclinic phase. Meanwhile, the potentiation/depression and Spike-Timing-Dependent Plasticity neuromorphic-like behaviour is demonstrated.

Sample preparation

1% La doped $Hf_{0.5}Zr_{0.5}O_2$ films with thickness of 7 nm were deposited on STO and GSO substrates buffered by LSMO bottom electrode to modulate the o/m-phase ratio in the thin films. The mechanism of phase control can be found elsewhere.[14] The films were prepared by PLD with conditions mentioned in Chapter 3. These films have been selected due to their low leakage current, especially necessary to avoid larger extrinsic contribution in the experiment analysed in the present chapter.

6.2.1 Switching dynamics of film with pure o-phase

The XRD 2θ-χ map of the La:HZO film on GSO is shown in Figure 6.2.1a. Apart from the reflections from the GSO substrate and LSMO electrode, there is one clear reflection at $\chi = 0°$ and $2\theta = 30.2°$ corresponds to the o-HZO(111) reflection. And no other phases have been detected, the same as the film reported before.[14,199] Figure 6.2.1b shows the P-V and I-V loop from PUND measurement, the switching current peaks and hysteresis loop confirm the ferroelectric character. The integrated remanent polarization is around 15 $\mu C/cm^2$ and the coercive voltages are 2.6 and -3.1 V, denoting the imprint field towards

LSMO bottom electrode. Figure 6.2.1 c-d shows the change of polarization versus write pulse duration of the film under positive and negative electric field with different amplitude, respectively. The raw data before removing the leakage contribution is shown in appendix 1. It can be observed that the switching starts at around 200 ns (V_w = 4 V) and when decreasing voltage, the onset switching time does not vary but ΔP is reduced. The data are fitted by KAI model (red line), $\Delta P = \Delta Ps * (1 - e^{-(\tau_w/\tau_0)^n})$, where τ_0 is the characteristic switching time, n is the dimensionality exponent and ΔP_s is the saturated switched polarization. At maximum applied voltage (4V), the fitting parameters are τ_0=1.4 μs and n=1.6. With voltage decrease, the n value decrease, but always larger than 1, following KAI model. The obtained n > 1 indicates mixture of 1D and 2D domain wall propagation. For decreasing applied voltage, τ_0 slightly increase, which is a phenomenon commonly reported in other ferroelectric thin films.[206] The switching data of the epitaxial La:HZO films on the GSO substrate can be well described by the KAI model.

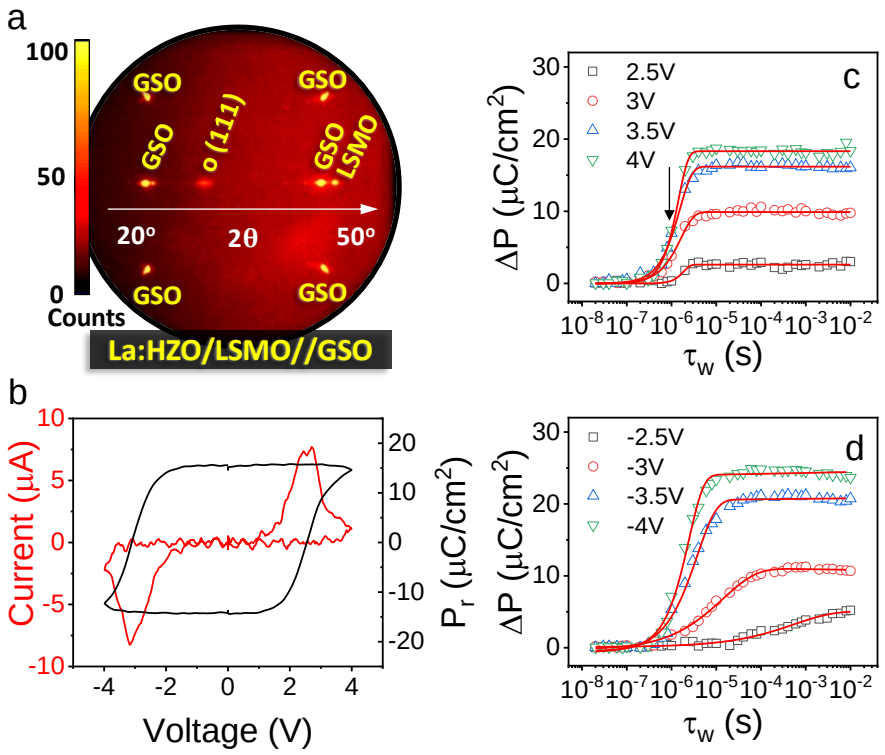

Figure 6.2.1 *(a) XRD 2θ-χ map of the La:HZO film on GSO. (b) Current-voltage loop and corresponding polarization-voltage loop measured at 10 kHz and maximum voltage of 4 V. Dependence of ΔP on τ_w after (c) positive and (d) negative V_w pulses of the indicated amplitude. Red lines are the fitting of the data by the KAI model.*

For the negative part, the τ_0=2.4 μs and n=1 are extracted from the fitting. The reason for the larger τ_0 compared to positive side is the effect form the negative imprint, as mention

in Figure 6.2.1b. In addition, the n value near 1 reflects 1D domain wall propagation dominates. This kind of asymmetric domain wall propagation is attributed asymmetric defect distribution in film along the out-of-plane direction, which is also the origin of the imprint.[207]

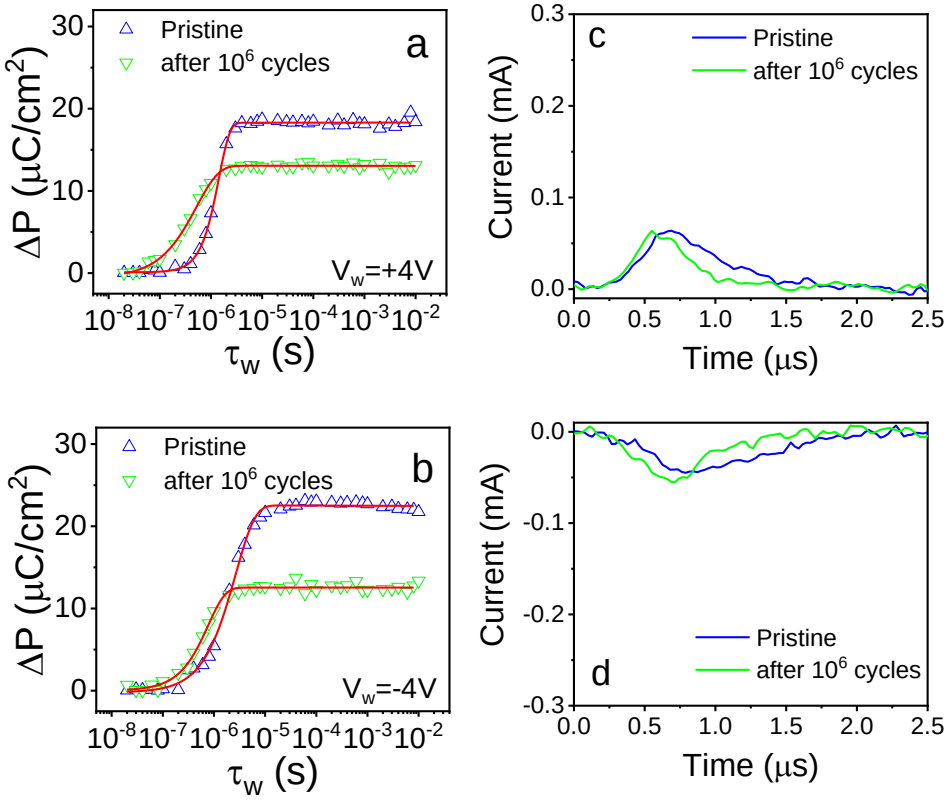

Figure 6.2.2 *ΔP dependence on τ_w for (a) positive and (b) negative V_w pulses in the pristine state and after 10^6 bipolar cycles. Red lines are the fitting of the data by the KAI model. Direct measurement of the ferroelectric switching current before and after cycling for (c) positive and (d) negative reading pulses.*

In Figure 6.2.2a-b, the ΔP versus write pulse duration is shown for a capacitor measured before and after 10^6 cycling at 4 V. It can be seen that after cycling, the polarization value decreases, which is related to fatigue effect. The possible reason is the pinning of ferroelectric domains due to defects redistribution, charge trapping, or transformation of the orthorhombic to monoclinic phase.[86,88] What interesting is that after cycling, τ_0 decreases from 1.4 and 2.5 μs to 0.55 and 0.77 μs for positive and negative polarity, respectively. The n value does not significantly change for negative polarity, but it decreases from 1.6 to 1.1 for positive polarity. Therefore, the formation of pinned domains or non-ferroelectric phases by electric cycling results in a faster switching and an average reduction of the domain growth dimensionality. This conclusion can also be

extracted from the direct measurement of the current switching, as shown in Figure 6.2.2c-d. The shift of the switching current peak position to left side indicates a clear faster switching after cycling treatment.

6.2.2 Switching dynamics of film with coexisting o/m-phase

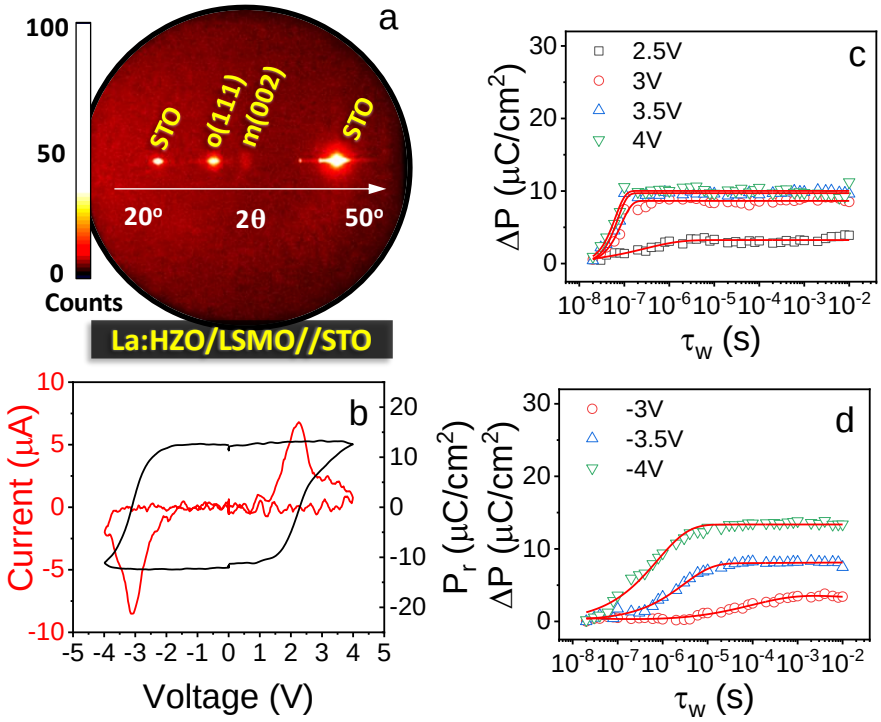

Figure 6.2.3 *(a) XRD 2θ-χ map of the La:HZO film on STO. (b) Current-voltage loop and corresponding polarization-voltage loop measured at 10 kHz and maximum voltage of 4 V. Dependence of ΔP on τ_w after (c) positive and (d) negative V_w pulses of the indicated amplitude. Red lines are the fitting of the data by the KAI model.*

The XRD 2θ-χ map of the La:HZO film on STO is shown in Figure 6.2.3a. In contrast to the map of film on GSO substrate, apart from one clear reflection at χ = 0° and 2θ = 30.2° corresponds to the o-HZO(111) reflection, there is also an additional reflection corresponding to the non-ferroelectric m-phase. This indicates a coexisting of o- and m-phase in the film, which is agreeable to directly identify the role of non-ferroelectric phases in the domain switching dynamics. The ferroelectric characterization (Figure 6.2.3b) indicates a P_r around 12 μC/cm^2 and the coercive voltages are 2.3 and -3.1 V, with a larger imprint compared to the film on GSO. The ΔP dependence on τ_w for different positive and negative voltages are shown in Figure 6.2.3c-d, respectively. It can be observed that some switchable charges can be detected even for a short applied write pulse duration of 50 ns. And a short characteristic switching time of 69 ns is extracted

from fitting, which is limited by the time constant (around 100 ns) of the experimental setup. It has to be noted that because the experimental setup limitation, the KAI model is not suitable for the fitting and the fitting just indicates an exponential dependence. For negative part, τ_0 increases to 820 ns with n = 0.5 for maximum applied voltage. The sharp increase of the switching time compared to positive side is attributed to the imprint, which is against polarization switching.[207] In addition, the n value is smaller than 1 for $V_w < 0$, which indicates that KAI model is not valid in this fitting. Therefore, the fitting using the NLS model for data collected at -4 V is performed (in Figure 6.2.4).

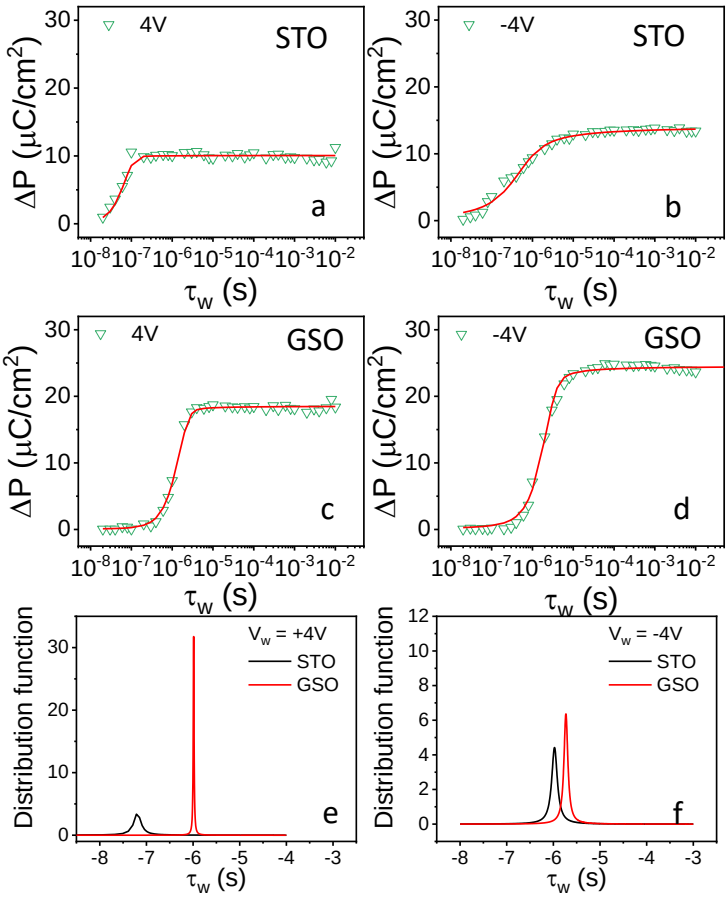

Figure 6.2.4 *Dependence of ΔP on τ_w after (a) positive and (b) negative V_w pulses of the film deposited on STO substrate. Dependence of ΔP on τ_w after (c) positive and (d) negative V_w pulses of the film deposited on GSO substrate. Red lines are the fitting of the data by the NLS model. The distribution function of (e) positive amplitude and (f) negative amplitude for films on STO and GSO are indicated in the figures.*

In the NLS model, ΔP(t) with writing pulse duration is described as this function, $\Delta P(t) = 2P_r \int_{-\infty}^{\infty}[1 - \exp\{-\left(\frac{\tau_w}{\tau_0}\right)^n\}]F(\log\tau_0)\,d(\log\tau_0)$, where τ_0 and n are the characteristic switching time and effective dimension for domain growth, respectively,

and F(log τ_0) is the distribution function of the logarithmic characteristic switching time τ_0 and described as $F(\log \tau_0) = \frac{A}{\pi}\left[\frac{w}{(\log \tau_0 - \log \tau_1)^2 + w^2}\right]$, where A is the normalization constant, w is the half-width at half-maximum, and log τ_1 is the central value of the distribution function. As shown in Figure 6.2.4a-d, the data of film on STO and GSO are properly fitted by NLS model for comparison. The n value is fixed to 2 by assuming 2D growth of domains after nucleation. The data of film on GSO can be fitted by NLS model is due to NLS model is an extended version of the KAI model, when the distribution of switching times is not a delta function.[208] The distribution function (Figure 6.2.4e-f) show narrower distribution functions for the film on GSO than for film on STO, irrespectively of the voltage pulse polarity, which indicates that the switching dynamics is well-described by a single τ_0 and thus by the KAI model. However, the failure of KAI model to describe the switching dynamics of films on STO is observed, indicating NLS model for film with coexistence of orthorhombic and monoclinic phases. And a remarkably fast characteristic switching time of (τ_0 = 69 ns) can be obtained.

In summary, it can be concluded that (i) switching dynamics in agreement with KAI model with n near to 2 is observed for the nominally single orthorhombic phase film, (ii) switching dynamics in agreement with NLS model is observed for the film showing coexisting orthorhombic/monoclinic phases, (iii) faster switching time is observed in films showing larger presence of non-ferroelectric or non-switchable phase induced by a different substrate or by electric field cycling, and (iv) faster switching time is observed if switching is aligned along the imprint direction.

6.2.3 Switching mechanism and neuromorphic-like behaviour

In Figure 6.2.5a-d, the main results and the switching mechanism are summarized. Film on GSO with single orthorhombic phase does not show ferroelectric switching using τ_w of 50 ns, whereas in the film on STO, with coexisting orthorhombic/monoclinic phases, presents clear switching current peak by an amount of near $\Delta P = 4\ \mu C/cm^2$. The observed switching at 50 ns is a benchmark for ferroelectric HfO_2-based thin films, only overpassed by data obtained in ultrafast characterization setups, as summarized in Table 6.2.1. Highly relevant is that with increasing film quality, switching becomes slower. The slow switching in films on GSO is correlated with the less abundant defects, whereas in films on STO, charged defects help on the initiation of the nucleation. The less amount of

defects produces that different nucleation points in the film are equally probable, and thus, switching dynamics with single characteristic time following KAI model.

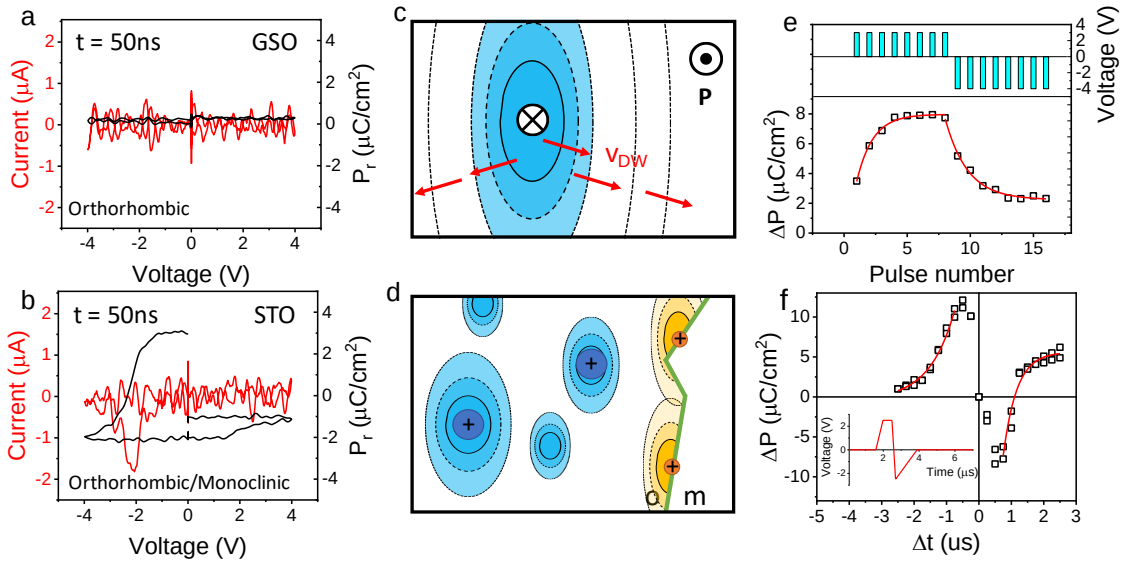

Figure 6.2.5 *I-V and P-V loops showing the polarization switching of (a) single orthorhombic phase and (b) mixed orthorhombic/monoclinic phase films after applying a voltage pulse of τ_w = 50 ns. Top-view sketch for the nucleation and growth process in (c) single orthorhombic phase and (d) mixed orthorhombic/monoclinic phase films. Black outward and inwards arrows account for polarization and red arrows for the domain wall propagation in panel c. (f) Dependence of polarization state in La:HZO film on STO on the applied number of pulses of 50 ns width of opposite polarity (+3/-4 V). (e) Dependence of polarization state in the La:HZO film on STO on the Δt of two consecutive pulse of synaptic-like shape (inset) of 750 ns FWHM and Δt step of 250 ns.*

As sketched in Figure 6.2.5c, the absence of defects favors 2D domain growth with homogenous nucleation, in agreement with the higher n coefficient. However, defects are not inexistent, and they produce non-negligible imprint field, asymmetric domain growth propagation, and n < 2 even for high electric fields. These features are not present in the epitaxial thin films of conventional ferroelectrics, such as PZT[209] or $BiFeO_3$.[210] In addition, τ_0 (larger than 1.4 μs) in single orthorhombic phase films grown on GSO is long compared to conventional ferroelectric oxides with τ_0 below microseconds.[209] The long characteristic time may indicate the participation of ionic motion processes for the domain switching nucleation and expansion,[32,211] as found in other oxides.[212] Note also that τ_0 in pure orthorhombic films is also longer than that found in the epitaxial films grown by post-annealing crystallization.[205] This is related to the higher remanent polarization of the

films reported here, indicating greater presence of orthorhombic phase and thus slower switching.

Table 6.2.1 *Summary of reported results on switching dynamics characteristics in ferroelectric HfO_2 films. Switching time has been extracted from data fitting using the mentioned model if available. Electric field (E). *Similar results in polycrystalline films.*

Composition	Method	Thickness /nm	Voltage /V	Electrode size /um^2	Switching time	Model	Ref.
W/HZO/W	ALD	15	9	7	0.925ns	NLS	[213]
WN/HZO/WN	ALD	15	8.4	80	5.4ns	NLS	[213]
WN/HZO/WN	ALD	15	8.4	400	20ns	NLS	[214]
TiN/$Hf_{0.7}Zr_{0.3}O_2$/TiN	ALD	10	2.5	3600	700ns	IFM	[202]
TiN/Si:HfO_2/TiN	ALD	10	3	7850	500ns	NLS	[201]
TiN/HZO/TiN	ALD	20	4	--	890ns	--	[215]
W/HZO/W	ALD	8	2.5	2826	236ns	NLS	[216]
TiN/La:HfO_2/TiN	ALD	10	4	13750	1500ns	NLS	[200]
Ti/Si:HfO_2/Ti	ALD	10	3	100	1us	NLS	[6]
Pt/HfO_2/TiN	ALD	9	2.25	--	920ns	KAI	[217]
TiN/Si:HfO_2/TiN	ALD	8	3	31400	1000ns	NLS	[204]
TiN/HZO/TiN	ALD	10	3.5	--	66.5ns	IFM	[203]
Pt/HZO/ITO*	PLD and post-annealing	27	9	5800	100ns	KAI (high-E)	[205]
Our work	PLD	7	4	226	69ns	NLS	

The switching sketch of film on STO is shown in Figure 6.2.5d. The film grown on STO is with more defects, and the charged defects are helpful for the nucleation, leading to a faster switching. These defects, probably mainly located at the electrode interfaces (positive blue charges) or at the monoclinic/orthorhombic interfaces (positive orange charges), locally generate different built-in fields, resulting in a distribution of switching times, and thus, NLS model well describes the growth kinetics. In this case, ionic motion can also play a role in the switching process, but the fast switching indicates it is not the dominate effect.

The memristive characteristics of ferroelectric HfO_2-based thin films have been applied to mimic the brain synapse by using voltage pulses with diverse shape and time duration of 1-100 μs.[26,127,130,205] In Figure 6.2.5e-f, the potentiation/depression and STDP neuromorphic-like behavior in the La:HZO/STO film are demonstrated by applying its

fast switching response. The ΔP is measured during application of defined number of positive (+3 V) and negative (−4 V) pulses of 50 ns time width (see top panel of Figure 6.2.5e). The pulse amplitude asymmetry is required to obtain symmetric potentiation/depression curves under imprint influence. Further details of the experiment are provided in chapter 3. A gradual increase and subsequent decrease of the polarization for positive and negative pulse trains can be observed, which results from the continuous switching of polarization using pulse width near the characteristics time. The red line is the fitting of the data by $\Delta P = P_0 + Ae^{-(N_p - N_0)/\tau}$, where P_0 is the initial polarization, N_p is the number of pulses, N_0 is the number of the first pulses, and τ is the exponential coefficient to describe the non-linearity effect.[130] The exponential coefficients extracted from the potentiation/depression curves are 1.2/1.8.

The STDP behavior is performed by using pre- and post-voltage synaptic like pulses (inset of Figure 6.2.5f) of 750 ns full width at half maximum (FWHM) and different delay times (Δt) between them. More details of the experiment are provided in chapter 3. The shape of the curves is not symmetric, and they are shifted along ΔP due to the presence of imprint. The red line is the fitting of the data by asymmetric hebbian learning rule $\Delta P = Ae^{-\Delta t/\tau}$, where A is the scaling factor, Δt is the time interval of the pre- and post-synaptic spikes, and τ is the time constant of a STDP function.[218] The extracted time constant from exponential fits for positive and negative Δt are 800 and 400 ns, which is more than 10 times shorter than former results of HfO_2-based thin films.[127,218] The exploratory characterization shown in Figure 6.2.5e-f demonstrates the potentiality of the system to show synaptic like behaviour, and remarkably in a much shorter time scale.

Conclusion

In summary, the characterization of the switching dynamics in single orthorhombic phase films follows KAI-like domain switching growth even using low voltage pulses. However, switching dynamics in agreement with NLS model is observed for the film showing coexisting orthorhombic/monoclinic phases. In films with the presence of parasitic monoclinic phase or in fatigued films, defects and non-ferroelectric phases help to shorten switching time. Therefore, even limited by the used experimental setup, ferroelectric switching as fast as 50 ns is observed. Fast switching is preferred when the final polarization state is aligned with the imprint field. Potentiation/depression and STDP

preliminary data allow us to demonstrate the potential interest in ferroelectric HfO_2 for fast neuromorphic memory applications.

Appendix 1.

ΔP values obtained before subtracting residual current contribution are shown in Figure A 6.2.1a. Note also that after most of the polarization has been switched, the polarization still increases with τ_w. The data has been fitted with the KAI model including the residual leakage contribution: $\Delta P = \Delta Ps * (1 - e^{-(\tau_w/\tau_0)^n}) + Q * \log(\tau_w)$. Data shown in the main text has been obtained after subtracting the fitted Q*log(τ_w) term, as shown in Figure A 6.2.1b. Note that the increase of residual leakage contribution with log(τ_w) is included in the Q*log(τ_w) term, where Q is a constant that accounts for the residual leakage contribution. Coexisting electronic and ionic leakage mechanisms[126,219–221] are known to be present in hafnium oxide films resulting in resistive switching. This resistive switching contribution results in hysteretic conductivity, as shown in Figure A 6.2.1c (leakage current curve by triangular voltage), which cannot be removed by PUND method. Q*log(τ_w) term is only a phenomenological description that accounts for this residual contribution. It might be also argued that this additional contribution comes from additional ferroelectric switching with different switching dynamics, which is unlikely due to saturation not been identified. In Figure A 6.2.1c, the higher leakage current in STO also indicates more defects in this film.

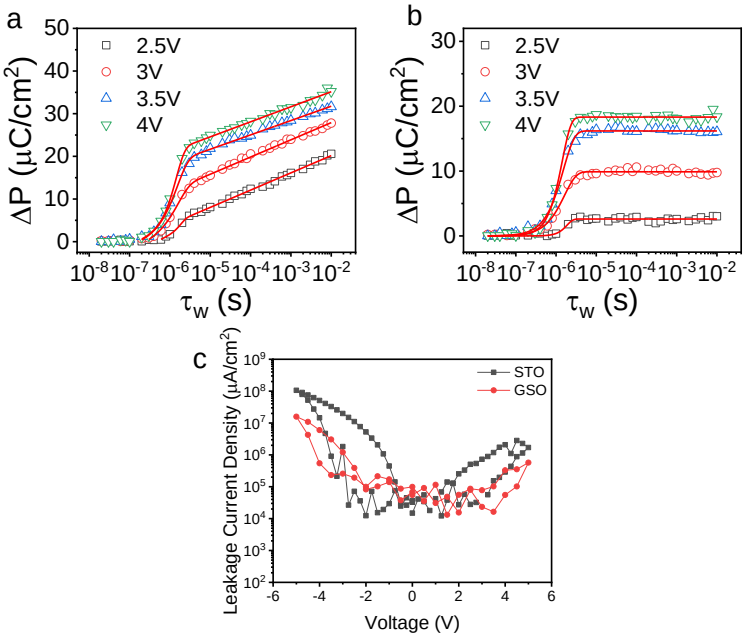

Figure A6.2.1 *Dependence of ΔP on τ_w after positive V_w pulses of indicated amplitude, (a) the raw data, and (b) the data removed the leakage contribution. (c) Leakage current curves of films*

on STO and GSO substrates at pristine state measured using a bipolar triangular voltage pulse from 0 to 5 to -5 to 0 V. Integration time is 2s. Details of the experiment can be found in chapter 3.

Chapter 7. Summary and conclusions

In this thesis, deposition conditions, interfaces and doping effects on epitaxial HfO_2-based thin films have been systematically studied to improve the ferroelectricity. Meanwhile, mechanisms related to ferroelectric properties, endurance and switching dynamics have also been explored.

(i) Three methods have been used to tailor epitaxial of $Hf_{0.5}Zr_{0.5}O_2$ thin films. First, epitaxial HZO films deposited by PLD under optimal mixed Ar/O_2 pressure show low leakage current and high remanent polarization of about 30 $\mu C/cm^2$, which represents a 50% increase with respect to equivalent films grown by conventional PLD. Second, the stabilization of ferroelectric HZO film at lower deposition temperature has been achieved using a seed layer. With seed layer, the ferroelectric o-phase can be stabilized at a temperature as low as 550 °C, with ferroelectric polarization of 14 $\mu C/cm^2$, and with improved endurance in comparison with films deposited at higher temperature. Third, the orthorhombic phase has been stabilized in epitaxial HZO film on LSMO/STO(110) and LSMO/STO(111). The use of STO(110) substrate allows (111) oriented o-phase, free of monoclinic phase and thus with increased ferroelectric polarization up to 30 $\mu C/cm^2$. Besides, the high polarization is accompanied by a long endurance (4×10^{10} cycles) and retention extrapolated to more than 10 years under the same poling voltage. While, the use of STO(111) substrate permits tilted epitaxy of o-phase with three crystal variants at different angles (24°, 66° and 90°) with respect to the plane-normal direction.

(ii) Doping effects of Zr and La elements on the stabilization of polar phase in epitaxial HfO_2-based thin films have been comprehensively investigated. Ferroelectric phase can be epitaxially stabilized in the all $Hf_{1-x}Zr_xO_2$ (x=0, 0.25, 0.5, 0.75, 1) films. The highest P_r of 30 $\mu C/cm^2$ found in the ZrO_2 film is associated with ferroelectric polarization switching and resistive switching. The films do not show wake-up effect in all the explored compositions, and best ferroelectric endurance is present in $Hf_{0.5}Zr_{0.5}O_2$ film. For La doped HfO_2 films, optimized concentration is 2-5 at%. The coercive field and leakage current of films on STO(001) and Si(001) decrease with the concentration of La. Based on the optimized content, the influence of thickness has been investigated in 2% La doped HfO_2 films, and it is found that La-doped HfO_2 films even as thin as 4.5 nm show robust ferroelectricity. Films of less than 7 nm thickness show the highest P_r of about 30 $\mu C/cm^2$, slight wake-up, endurance of at least 10^{10} cycles and retention of more

than 10 years under same voltage. Films on Si(001) exhibit similar properties. Furthermore, different perovskite substrates have been used to control the amount of o-phase in 2 at% La:HfO_2 film. The highest P_r is 29 μC/cm^2 in films grown on $TbScO_3$. Compared with HZO films, the amount of o-phase is greater in La:HfO2 films on the same substrate. Finally, the synergic doping effect of La and Zr on the stabilized polymorphs and ferroelectricity of epitaxial HfO_2-based thin films is comprehensively explored. In La:HZO and La:HO films, La favors the formation of o-phase in low content, but the c-phase appears in highly La doped films. With Zr content decreasing, the optimized La content shifts from 0% for ZrO_2 to 2-5% for HfO_2, and P_r of 20-30 μC/cm^2 can be obtained in the optimized HfO_2-ZrO_2-La_2O_3 ternary system. 1% La doping in HZO film reduces the leakage current and the film exhibits high endurance with limited wake-up effect in films thinner than 10 nm and good retention.

(iii) Endurance and switching mechanisms in HfO_2-based ferroelectric thin films have been explored. Films show long retention regardless of the relative amount of parasitic m-phase. However, endurance is highly dependent on the o/m phase ratio. Films almost free of parasitic phase exhibit strong fatigue. While, films with greater amount of parasitic m-phase appreciates slower fatigue and longer endurance. Grain boundaries of o/m phase are proposed to reduce propagation of domain pinning, allowing to slower fatigue and increase endurance. Besides, the parasitic monoclinic phase also has a dramatically influence on the switching dynamics. In single o-phase film, it follows KAI-like domain switching. However, in the film showing coexisting o/m phases, switching dynamics agrees with nucleation-limited switching model and ferroelectric switching as fast as 50 ns is observed. Fast switching is favored when the final polarization state is aligned along imprint field. Potentiation/depression and STDP behavior demonstrate the potential interest in ferroelectric HfO_2 for fast neuromorphic memory applications.

List of abbreviations and acronyms

Abbreviations

CMOS	complementary metal oxide semiconductor
o-phase	orthorhombic phase
R	rhombohedral phase
t-phase	tetragonal phase
c-phase	cubic phase
m-phase	monoclinic phase
YSZ	yttria-stabilized zirconia
PLD	pulsed laser deposition
LSMO	$La_{0.67}Sr_{0.33}MnO_3$
HZO	$Hf_{0.5}Zr_{0.5}O_2$
STO	$SrTiO_3$
P-E	polarization-electric
PZT	$Pb(Zr,Ti)O_3$
FeRAM	ferroelectric random access memory
1T-1C	one transistor and one capacitor
FeFET	ferroelectric field effect transistor
FTJ	ferroelectric tunnel junction
MOSFET	metal-oxide-semiconductor FET
HZH	HfO_2-ZrO_2-HfO_2
SBT	$SrBi_2Ta_2O_9$
STDP	spike-timing-dependent-plasticity
ALD	atomic layer deposition
GIXRD	grazing incident x-ray diffraction
MW	memory window
YHO	Y-doped HfO_2
ITO	indium tin oxide
TEM	transmission electronic microscopy
XRD	X-ray diffraction
RSM	reciprocal space mapping

AFM	atomic force microscopy
STEM	scanning transmission electron microscopy
DLCC	dynamic leakage current compensation
DHM	dynamic hysteresis measurement
PUND	positive up negative down
LSAT	$(LaAlO_3)_{0.3}(Sr_2TaAlO_6)_{0.7}$
LAO	$LaAlO_3$
YAO	$YAlO_3$
DSO	$DyScO_3$
GSO	$GdScO_3$
TSO	$TbScO_3$
NSO	$NdScO_3$
LHO	$La:HfO_2$
HAADF	high-angle annular dark field
I-V	current-voltage
P-V	polarization-voltage loops
J-V	current density-voltage curves
NLS	nucleation limited switching
KAI	Kolmogorov-Avrami-Ishibashi mechanism
FWHM	full width at half maximum

Acronyms

E_c	coercive field
P_r	remanent polarization
G	Gibb's free energy
r	grains radius
σ	surface energy
T_c	curie temperature
C	capacitance
ε_r	dielectric permittivity
P_{Ar}	Ar pressure
P_{O2}	O_2 pressure
d	out-of-plane lattice parameter

E_{imp}	imprint field
E_{c+} and E_{c-}	coercive field
τ_0	characteristic switching time
T_s	substrate temperature
t	thickness
P_0	initial polarization
N_p	number of pulses
Δt	time difference
ΔP	polarization change
V_w	write voltage

List of publications and communications

1. **Song, T.**; Sánchez, F.; Fina, I. Impact of Non-Ferroelectric Phases on Switching Dynamics in Epitaxial Ferroelectric $Hf_{0.5}Zr_{0.5}O_2$ Films. ***APL Mater***. **2022**, *10*, 031108.

2. **Song, T.**; Estandía, S.; Tan, H.; Dix, N.; Gàzquez, J.; Fina, I.; Sánchez, F. Positive Effect of Parasitic Monoclinic Phase of $Hf_{0.5}Zr_{0.5}O_2$ on Ferroelectric Endurance. ***Adv. Electron. Mater.*** **2022**, *8* (1), 2100420.

3. **Song, T.**; Tan, H.; Estandía, S.; Gàzquez, J.; Gich, M.; Dix, N.; Fina, I.; Sánchez, F. Improved Polarization and Endurance in Ferroelectric $Hf_{0.5}Zr_{0.5}O_2$ Films on $SrTiO_3$ (110). ***Nanoscale*** **2022**, *14* (6), 2337-2343.

4. **Song, T.**; Solanas, R.; Qian, M.; Fina, I.; Sánchez, F. Large Enhancement of Ferroelectric Polarization in $Hf_{0.5}Zr_{0.5}O_2$ Films by Low Plasma Energy Pulsed Laser Deposition. ***J. Mater. Chem. C*** **2022**, *10* (3), 1084-1089.

5. **Song, T.**; Tan, H.; Dix, N.; Moalla, R.; Lyu, J.; Saint-Girons, G.; Bachelet, R.; Sánchez, F.; Fina, I. Stabilization of the Ferroelectric Phase in Epitaxial $Hf_{1-x}Zr_xO_2$ Enabling Coexistence of Ferroelectric and Enhanced Piezoelectric Properties. ***ACS Appl. Electron. Mater***. **2021**, *3* (5), 2106-2113.

6. **Song, T.**; Bachelet, R.; Saint-Girons, G.; Dix, N.; Fina, I.; Sánchez, F. Thickness Effect on the Ferroelectric Properties of La-Doped HfO_2 Epitaxial Films down to 4.5 nm. ***J. Mater. Chem. C*** **2021**, *1* (207890), 3777.

7. **Song, T.**; Tan, H.; Bachelet, R.; Saint-Girons, G.; Fina, I.; Sánchez, F. Impact of La Concentration on Ferroelectricity of La-Doped HfO_2 Epitaxial Thin Films. ***ACS Appl. Electron. Mater.*** **2021**, *3* (11), 4809-4816.

8. **Song, T.**; Bachelet, R.; Saint-Girons, G.; Solanas, R.; Fina, I.; Sánchez, F. Epitaxial Ferroelectric La-Doped $Hf_{0.5}Zr_{0.5}O_2$ Thin Films. ***ACS Appl. Electron. Mater***. **2020**, *2* (10), 3221-3232.

9. **Song, T.**; Estandía, S.; Dix, N.; Gàzquez, J.; Gich, M.; Fina, I.; Sánchez, F. Ferroelectric $Hf_{0.5}Zr_{0.5}O_2$ films on $SrTiO_3$ (111). ***J. Mater. Chem. C*** **2022**, 10, 8407-8413.

10. **Song, T.**; Tan, H.; Robert, A.; Estandía, S.; Gàzquez, J.; Sánchez, F.; Fina, I. Synergetic contributions of chemical doping and epitaxial stress to polarization in ferroelectric HfO_2 films. ***submitted***.

11. **Song, T.**; Estandía, S.; Fina, I.; Sánchez, F. Ferroelectric (Hf, Zr, La)O_2 films. ***Submitted.***

2022.06.27-07.1

ISAF-PFM-ECAPD 2022

Oral: Ferroelectric La-Doped HfO_2 Epitaxial Thin Films

2022.05.30-06.03

E-MRS Spring Meeting

Oral: Ferroelectric Switching Dynamics and Multi-State Memory Performance in Epitaxial $Hf_{0.5}Zr_{0.5}O_2$ Films

2021.09.20-09.23

E-MRS Fall Meeting

Oral: Ferroelectric Properties Dependence on Thickness in Epitaxial La-Doped HfO_2 Films

2021.05.17-05.21

ISAF-ISIF-PFM2021

Poster: Enhanced Ferroelectric Properties of Epitaxial La-doped $Hf_{0.5}Zr_{0.5}O_2$Thin Films

2021.04.11-04.13

Materials Challenges for Memory

Poster: Epitaxial La-Doped $Hf_{0.5}Zr_{0.5}O_2$Thin Films with Enhanced Ferroelectric Properties

2020.08.30-09.03

CMD 2020 GEFES mini-colloquium

Poster: Epitaxial Ferroelectric La-doped $Hf_{0.5}Zr_{0.5}O_2$ Thin Films

2020.12.12

QUOROM 2

Poster: Enhanced Properties of La-Doped Epitaxial $Hf_{0.5}Zr_{0.5}O_2$ Thin Films

References

1 T. S. Böscke, J. Müller, D. Bräuhaus, U. Schröder and U. Böttger, *Appl. Phys. Lett.*, 2011, **99**, 102903.

2 M. H. Park, Y. H. Lee, H. J. Kim, Y. J. Kim, T. Moon, K. Do Kim, J. Müller, A. Kersch, U. Schroeder, T. Mikolajick and C. S. Hwang, *Adv. Mater.*, 2015, **27**, 1811–1831.

3 J. H. Choi, Y. Mao and J. P. Chang, *Mater. Sci. Eng. R Reports*, 2011, **72**, 97–136.

4 S. S. Cheema, D. Kwon, N. Shanker, R. dos Reis, S. L. Hsu, J. Xiao, H. Zhang, R. Wagner, A. Datar, M. R. McCarter, C. R. Serrao, A. K. Yadav, G. Karbasian, C. H. Hsu, A. J. Tan, L. C. Wang, V. Thakare, X. Zhang, A. Mehta, E. Karapetrova, R. V. Chopdekar, P. Shafer, E. Arenholz, C. Hu, R. Proksch, R. Ramesh, J. Ciston and S. Salahuddin, *Nature*, 2020, **580**, 478–482.

5 S. S. Cheema, N. Shanker, L. Wang, C.-H. Hsu, S. Hsu, Y. Liao, M. San Jose, J. Gomez, W. Chakraborty, W. Li, J. Bae, S. K. Volkman, D. Kwon, Y. Rho, G. Pinelli, R. Rastogi, D. Pipitone, C. Stull, M. Cook, B. Tyrrell, V. A. Stoica, Z. Zhang, J. W. Freeland, C. J. Tassone, A. Mehta, G. Saheli, D. Thompson, D. I. Suh, W.-T. Koo, K.-J. Nam, D. J. Jung, W.-B. Song, C.-H. Lin, S. Nam, J. Heo, N. Parihar, C. P. Grigoropoulos, P. Shafer, P. Fay, R. Ramesh, S. Mahapatra, J. Ciston, S. Datta, M. Mohamed, C. Hu and S. Salahuddin, *Nature*, 2022, **604**, 65–71.

6 U. Schroeder, S. Mueller, J. Mueller, E. Yurchuk, D. Martin, C. Adelmann, T. Schloesser, R. van Bentum and T. Mikolajick, *ECS J. Solid State Sci. Technol.*, 2013, **2**, N69–N72.

7 J. Muller, T. S. Boscke, S. Muller, E. Yurchuk, P. Polakowski, J. Paul, D. Martin, T. Schenk, K. Khullar, A. Kersch, W. Weinreich, S. Riedel, K. Seidel, A. Kumar, T. M. Arruda, S. V. Kalinin, T. Schlosser, R. Boschke, R. Van Bentum, U. Schroder and T. Mikolajick, *Tech. Dig. - Int. Electron Devices Meet. IEDM*, 2013, 280–283.

8 M.-K. Kim, I.-J. Kim and J.-S. Lee, *Sci. Adv.*, 2021, **7**, eabe1341.

9 M. H. Park, D. Kwon, U. Schroeder and T. Mikolajick, *MRS Bull.*, 2021, **46**, 1–9.

10 Y. Wei, P. Nukala, M. Salverda, S. Matzen, H. J. Zhao, J. Momand, A. S. Everhardt, G. Agnus, G. R. Blake, P. Lecoeur, B. J. Kooi, J. Íñiguez, B. Dkhil and B. Noheda, *Nat. Mater.*, 2018, **17**, 1095–1100.

11 O. Ohtaka, H. Fukui, T. Kunisada, T. Fujisawa, K. Funakoshi, W. Utsumi, T. Irifune, K. Kuroda and T. Kikegawa, *J. Am. Ceram. Soc.*, 2004, **84**, 1369–1373.

12 D. H. Lee, Y. Lee, K. Yang, J. Y. Park, S. H. Kim, P. R. S. Reddy, M. Materano, H. Mulaosmanovic, T. Mikolajick, J. L. Jones, U. Schroeder and M. H. Park, *Appl. Phys. Rev.*, 2021, **8**, 021312.

13 S. J. Kim, J. Mohan, J. S. Lee, H. S. Kim, J. Lee, C. D. Young, L. Colombo, S. R. Summerfelt, T. San and J. Kim, *ACS Appl. Mater. Interfaces*, 2019, **11**, 5208–5214.

14 S. Estandía, N. Dix, J. Gazquez, I. Fina, J. Lyu, M. F. Chisholm, J. Fontcuberta and F. Sánchez, *ACS Appl. Electron. Mater.*, 2019, **1**, 1449–1457.

15 M. H. Park, Y. H. Lee, H. J. Kim, Y. J. Kim, T. Moon, K. Do Kim, S. D. Hyun, T. Mikolajick, U. Schroeder and C. S. Hwang, *Nanoscale*, 2018, **10**, 716–725.

16 M. H. Park, Y. H. Lee, T. Mikolajick, U. Schroeder and C. S. Hwang, *Adv. Electron. Mater.*, 2019, **5**, 1800522.

17 M. H. Park, Y. H. Lee and C. S. Hwang, *Nanoscale*, 2019, **11**, 19477–19487.

18 M. Materano, T. Mittmann, P. D. Lomenzo, C. Zhou, J. L. Jones, M. Falkowski, A. Kersch, T. Mikolajick and U. Schroeder, *ACS Appl. Electron. Mater.*, 2020, **2**, 3618–3626.

19 X. Xu, F. Huang, Y. Qi, S. Singh, K. M. Rabe, D. Obeysekera, J. Yang, M. Chu and S. Cheong, *Nat. Mater.*, 2021, **20**, 826–832.

20 M. Materano, P. D. Lomenzo, A. Kersch, M. H. Park, T. Mikolajick and U. Schroeder, *Inorg. Chem. Front.*, 2021, **8**, 2650–2672.

21 U. Schroeder, C. Hwang and H. Funakubo, 2019, 570.

22 T. Schenk, M. Pešić, S. Slesazeck, U. Schroeder and T. Mikolajick, *Reports Prog. Phys.*, 2020, **83**, 086501.

23 I. Fina and F. Sánchez, *ACS Appl. Electron. Mater.*, 2021, **3**, 1530–1549.

24 J. Cao, S. Shi, Y. Zhu and J. Chen, *Phys. status solidi – Rapid Res. Lett.*, 2021, **15**, 2100025.

25 T. Shimizu, K. Katayama, T. Kiguchi, A. Akama, T. J. Konno and H. Funakubo, *Appl. Phys. Lett.*, 2015, **107**, 032910.

26 H. Y. Yoong, H. Wu, J. Zhao, H. Wang, R. Guo, J. Xiao, B. Zhang, P. Yang, S. J. Pennycook, N. Deng, X. Yan and J. Chen, *Adv. Funct. Mater.*, 2018, **28**, 1–10.

27 Y. Wei, P. Nukala, M. Salverda, S. Matzen, H. J. Zhao, J. Momand, A. S. Everhardt, G. Agnus, G. R. Blake, P. Lecoeur, B. J. Kooi, J. Íñiguez, B. Dkhil and B. Noheda, *Nat. Mater.*, 2018, **17**, 1095–1100.

28 J. Lyu, I. Fina, R. Solanas, J. Fontcuberta and F. Sánchez, *Appl. Phys. Lett.*, 2018, **113**, 082902.

29 J. Lyu, I. Fina, R. Bachelet, G. Saint-Girons, S. Estandía, J. Gázquez, J. Fontcuberta and F. Sánchez, *Appl. Phys. Lett.*, 2019, **114**, 222901.

30 J. Lyu, T. Song, I. Fina and F. Sánchez, *Nanoscale*, 2020, **12**, 11280–11287.

31 J. Lyu, I. Fina, J. Fontcuberta and F. Sánchez, *ACS Appl. Mater. Interfaces*, 2019, **11**, 6224–6229.

32 P. Nukala, M. Ahmadi, Y. Wei, S. de Graaf, E. Stylianidis, T. Chakrabortty, S. Matzen, H. W. Zandbergen, A. Björling, D. Mannix, D. Carbone, B. Kooi and B. Noheda, *Science (80-.).*, 2021, **372**, 630–635.

33 J. Valasek, *Phys. Rev.*, 1921, **17**, 475–481.

34 E. Bersch, S. Rangan, R. A. Bartynski, E. Garfunkel and E. Vescovo, *Phys. Rev. B*, 2008, **78**, 085114.

35 X. Sang, E. D. Grimley, T. Schenk, U. Schroeder and J. M. LeBeau, *Appl. Phys.*

Lett., 2015, **106**, 162905.

36 M. H. Park, T. Schenk, C. M. Fancher, E. D. Grimley, C. Zhou, C. Richter, J. M. LeBeau, J. L. Jones, T. Mikolajick and U. Schroeder, *J. Mater. Chem. C*, 2017, **5**, 4677–4690.

37 R. Materlik, C. Künneth and A. Kersch, *J. Appl. Phys.*, 2015, **117**, 134109.

38 R. Batra, T. D. Huan, G. A. Rossetti and R. Ramprasad, *Chem. Mater.*, 2017, **29**, 9102–9109.

39 R. Batra, T. D. Huan, J. L. Jones, G. Rossetti and R. Ramprasad, *J. Phys. Chem. C*, 2017, **121**, 4139–4145.

40 T. Shimizu, K. Katayama, T. Kiguchi, A. Akama, T. J. Konno, O. Sakata and H. Funakubo, *Sci. Rep.*, 2016, **6**, 32931.

41 T. Li, M. Ye, Z. Sun, N. Zhang, W. Zhang, S. Inguva, C. Xie, L. Chen, Y. Wang, S. Ke and H. Huang, *ACS Appl. Mater. Interfaces*, 2019, **11**, 4139–4144.

42 J. Müller, T. S. Böscke, U. Schröder, S. Mueller, D. Bräuhaus, U. Böttger, L. Frey and T. Mikolajick, *Nano Lett.*, 2012, **12**, 4318–4323.

43 M. H. Park, H. J. Kim, Y. J. Kim, Y. H. Lee, T. Moon, K. Do Kim, S. D. Hyun, F. Fengler, U. Schroeder and C. S. Hwang, *ACS Appl. Mater. Interfaces*, 2016, 8, 15466–15475.

44 S. Starschich and U. Boettger, *J. Mater. Chem. C*, 2017, **5**, 333–338.

45 Y. Qi, S. Singh, C. Lau, F.-T. Huang, X. Xu, F. J. Walker, C. H. Ahn, S.-W. Cheong and K. M. Rabe, *Phys. Rev. Lett.*, 2020, **125**, 257603.

46 Y. C. Zhou, Y. K. Zhang, Q. Yang, J. Jiang, P. Fan, M. Liao and Y. C. Zhou, *Comput. Mater. Sci.*, 2019, **167**, 143–150.

47 T. Mittmann, M. Materano, P. D. Lomenzo, M. H. Park, I. Stolichnov, M. Cavalieri, C. Zhou, C. C. Chung, J. L. Jones, T. Szyjka, M. Müller, A. Kersch, T. Mikolajick and U. Schroeder, *Adv. Mater. Interfaces*, 2019, **6**, 2–10.

48 M. H. Park, D. H. Lee, K. Yang, J.-Y. Park, G. T. Yu, H. W. Park, M. Materano, T. Mittmann, P. D. Lomenzo, T. Mikolajick, U. Schroeder and C. S. Hwang, *J. Mater. Chem. C*, 2020, **8**, 10526–10550.

49 T. Mittmann, M. Michailow, P. D. Lomenzo, J. Gärtner, M. Falkowski, A. Kersch, T. Mikolajick and U. Schroeder, *Nanoscale*, 2021, **13**, 912–921.

50 A. Pal, V. K. Narasimhan, S. Weeks, K. Littau, D. Pramanik and T. Chiang, *Appl. Phys. Lett.*, 2017, **110**, 022903.

51 M. H. Park, H. J. Kim, Y. J. Kim, Y. H. Lee, T. Moon, K. Do Kim, S. D. Hyun and C. S. Hwang, *Appl. Phys. Lett.*, 2015, **107**, 192907.

52 M. H. Park, Y. H. Lee, H. J. Kim, T. Schenk, W. Lee, K. Do Kim, F. P. G. G. Fengler, T. Mikolajick, U. Schroeder and C. S. Hwang, *Nanoscale*, 2017, **9**, 9973–9986.

53 P. Nukala, Y. Wei, V. de Haas, Q. Guo, J. Antoja-Lleonart and B. Noheda, *Ferroelectrics*, 2020, **569**, 148–163.

54 B. Prasad, V. Thakare, A. Kalitsov, Z. Zhang, B. Terris and R. Ramesh, *Adv. Electron. Mater.*, 2021, **7**, 2001074.

55 S. Y. Wu, *IEEE Trans. Electron Devices*, 1974, **21**, 499–504.

56 L. Chen, T.-Y. Wang, Y.-W. Dai, M.-Y. Cha, H. Zhu, Q.-Q. Sun, S.-J. Ding, P. Zhou, L. Chua and D. W. Zhang, *Nanoscale*, 2018, **10**, 15826–15833.

57 A. Chernikova, M. Kozodaev, A. Markeev, D. Negrov, M. Spiridonov, S. Zarubin, O. Bak, P. Buragohain, H. Lu, E. Suvorova, A. Gruverman and A. Zenkevich, *ACS Appl. Mater. Interfaces*, 2016, **8**, 7232–7237.

58 A. G. Chernikova, D. S. Kuzmichev, D. V. Negrov, M. G. Kozodaev, S. N. Polyakov and A. M. Markeev, *Appl. Phys. Lett.*, 2016, **108**, 242905.

59 S. D. Hyun, H. W. Park, Y. J. Kim, M. H. Park, Y. H. Lee, H. J. Kim, Y. J. Kwon, T. Moon, K. Do Kim, Y. Bin Lee, B. S. Kim and C. S. Hwang, *ACS Appl. Mater. Interfaces*, 2018, **10**, 35374–35384.

60 M. Hoffmann, F. P. G. Fengler, M. Herzig, T. Mittmann, B. Max, U. Schroeder, R. Negrea, P. Lucian, S. Slesazeck and T. Mikolajick, *Nature*, 2019, **565**, 464–467.

61 A. G. Chernikova, M. G. Kozodaev, R. R. Khakimov, S. N. Polyakov and A. M. Markeev, *Appl. Phys. Lett.*, 2020, **117**, 192902.

62 S. Starschich, T. Schenk, U. Schroeder and U. Boettger, *Appl. Phys. Lett.*, 2017, **110**, 182905.

63 S. Starschich, D. Griesche, T. Schneller, R. Waser and U. Böttger, *Appl. Phys. Lett.*, 2014, **104**, 202903.

64 S. Starschich and U. Böttger, *J. Appl. Phys.*, 2018, **123**, 044101.

65 J. Lyu, I. Fina, R. Solanas, J. Fontcuberta and F. Sánchez, *ACS Appl. Electron. Mater.*, 2019, **1**, 220–228.

66 U. Schroeder, M. Materano, T. Mittmann, P. D. Lomenzo, T. Mikolajick and A. Toriumi, *Jpn. J. Appl. Phys.*, 2019, **58**, SL0801.

67 T. Shimizu, T. Yokouchi, T. Shiraishi, T. Oikawa, P. S. S. R. Krishnan and H. Funakubo, *Jpn. J. Appl. Phys.*, 2014, **53**, 09PA04.

68 Y. B. Y. H. Lee, H. J. Kim, T. Moon, K. Do Kim, S. D. Hyun, H. W. Park, Y. B. Y. H. Lee, M. H. Park and C. S. Hwang, *Nanotechnology*, 2017, **28**, 305703.

69 Z. Quan, M. Wang, X. Zhang, H. Liu, W. Zhang and X. Xu, *AIP Adv.*, 2020, **10**, 085024.

70 S. Starschich, D. Griesche, T. Schneller and U. Böttger, *ECS J. Solid State Sci. Technol.*, 2015, **4**, P419–P423.

71 H. Chen, X. Zhou, L. Tang, Y. Chen, H. Luo, X. Yuan, C. R. Bowen and D. Zhang, *Appl. Phys. Rev.*, 2022, **9**, 011307.

72 M. H. Park, H. J. Kim, Y. J. Kim, Y. H. Lee, T. Moon, K. Do Kim, S. D. Hyun, F. Fengler, U. Schroeder and C. S. Hwang, *ACS Appl. Mater. Interfaces*, 2016, **8**, 15466–15475.

73 L. Zhao, J. Liu and Y. Zhao, *Appl. Phys. Lett.*, 2021, **119**, 172903.

74 U. Schroeder, C. Richter, M. H. Park, T. Schenk, M. Pešić, M. Hoffmann, F. P. G. G. Fengler, D. Pohl, B. Rellinghaus, C. Zhou, C.-C. C. Chung, J. L. Jones and T. Mikolajick, *Inorg. Chem.*, 2018, **57**, 2752–2765.

75 M. Hyuk Park, H. Joon Kim, Y. Jin Kim, W. Lee, T. Moon and C. Seong Hwang, *Appl. Phys. Lett.*, 2013, **102**, 242905.

76 M. H. Park, H. J. Kim, Y. J. Kim, W. Lee, T. Moon, K. Do Kim and C. S. Hwang, *Appl. Phys. Lett.*, 2014, **105**, 072902.

77 H. J. Kim, M. H. Park, Y. J. Kim, Y. H. Lee, W. Jeon, T. Gwon, T. Moon, K. Do Kim and C. S. Hwang, *Appl. Phys. Lett.*, 2014, **105**, 192903.

78 R. Batra, H. D. Tran and R. Ramprasad, *Appl. Phys. Lett.*, 2016, **108**, 172902.

79 A. N. Morozovska, M. D. Glinchuk and E. A. Eliseev, *Phys. Rev. B*, 2007, **76**, 14102.

80 M. J. Polking, J. J. Urban, D. J. Milliron, H. Zheng, E. Chan, M. A. Caldwell, S. Raoux, C. F. Kisielowski, J. W. Ager, R. Ramesh and A. P. Alivisatos, *Nano Lett.*, 2011, **11**, 1147–1152.

81 Z. Gao, Y. Luo, S. Lyu, Y. Cheng, Y. Zheng, Q. Zhong, W. Zhang and H. Lyu, *IEEE Electron Device Lett.*, 2021, **42**, 1303–1306.

82 T. Schenk, N. Godard, A. Mahjoub, S. Girod, A. Matavz, V. Bobnar, E. Defay and S. Glinsek, *Phys. status solidi – Rapid Res. Lett.*, 2020, **14**, 1900626.

83 P. Polakowski and J. Müller, *Appl. Phys. Lett.*, 2015, **106**, 232905.

84 P. D. Lomenzo, Q. Takmeel, C. Zhou, C. M. Fancher, E. Lambers, N. G. Rudawski, J. L. Jones, S. Moghaddam and T. Nishida, *J. Appl. Phys.*, 2015, **117**, 134105.

85 H. J. Kim, M. H. Park, Y. J. Kim, Y. H. Lee, T. Moon, K. Do Kim, S. D. Hyun and C. S. Hwang, *Nanoscale*, 2016, **8**, 1383–1389.

86 M. Pešić, F. P. G. Fengler, L. Larcher, A. Padovani, T. Schenk, E. D. Grimley, X. Sang, J. M. LeBeau, S. Slesazeck, U. Schroeder and T. Mikolajick, *Adv. Funct. Mater.*, 2016, **26**, 4601–4612.

87 M. Pešić, M. Hoffmann, C. Richter, T. Mikolajick and U. Schroeder, *Adv. Funct. Mater.*, 2016, **26**, 7486–7494.

88 E. D. Grimley, T. Schenk, X. Sang, M. Pešić, U. Schroeder, T. Mikolajick and J. M. LeBeau, *Adv. Electron. Mater.*, 2016, **2**, 1600173.

89 Y. Cheng, Z. Gao, K. H. Ye, H. W. Park, Y. Zheng, Y. Zheng, J. Gao, M. H. Park, J.-H. Choi, K.-H. Xue, C. S. Hwang and H. Lyu, *Nat. Commun.*, 2022, **13**, 645.

90 S. Starschich, S. Menzel and U. Böttger, *J. Appl. Phys.*, 2017, **121**, 154102.

91 D. Zhou, J. Xu, Q. Li, Y. Guan, F. Cao, X. Dong, J. Müller, T. Schenk and U. Schröder, *Appl. Phys. Lett.*, **103**, 192904.

92 F. Huang, X. Chen, X. Liang, J. Qin, Y. Zhang, T. Huang, Z. Wang, B. Peng, P. Zhou, H. Lu, L. Zhang, L. Deng, M. Liu, Q. Liu, H. Tian and L. Bi, *Phys. Chem.*

Chem. Phys., 2017, **19**, 3486–3497.

93 T. Schenk, U. Schroeder, M. Pešić, M. Popovici, Y. V. Pershin and T. Mikolajick, *ACS Appl. Mater. Interfaces*, 2014, **6**, 19744–19751.

94 P. Buragohain, A. Erickson, P. Kariuki, T. Mittmann, C. Richter, P. D. Lomenzo, H. Lu, T. Schenk, T. Mikolajick, U. Schroeder and A. Gruverman, *ACS Appl. Mater. Interfaces*, 2019, **11**, 35115–35121.

95 K. Takada, S. Takarae, K. Shimamoto, N. Fujimura and T. Yoshimura, *Adv. Electron. Mater.*, 2021, **7**, 2100151.

96 F. Mehmood, M. Hoffmann, P. D. Lomenzo, C. Richter, M. Materano, T. Mikolajick and U. Schroeder, *Adv. Mater. Interfaces*, 2019, **6**, 1–10.

97 B. Y. Kim, H. W. Park, S. D. Hyun, Y. Bin Lee, S. H. Lee, M. Oh, S. K. Ryoo, I. S. Lee, S. Byun, D. Shim, D. Cho, M. H. Park and C. S. Hwang, *Adv. Electron. Mater.*, 2021, 2100042.

98 K. Katayama, T. Shimizu, O. Sakata, T. Shiraishi, S. Nakamura, T. Kiguchi, A. Akama, T. J. Konno, H. Uchida and H. Funakubo, *Appl. Phys. Lett.*, 2016, **109**, 112901.

99 T. Mimura, T. Shimizu, Y. Katsuya, O. Sakata and H. Funakubo, *Jpn. J. Appl. Phys.*, 2020, **59**, SGGB04.

100 K. Katayama, T. Shimizu, O. Sakata, T. Shiraishi, S. Nakamura, T. Kiguchi, A. Akama, T. J. Konno, H. Uchida and H. Funakubo, *J. Appl. Phys.*, 2016, **119**, 134101.

101 T. Mimura, K. Katayama, T. Shimizu, H. Uchida, T. Kiguchi, A. Akama, T. J. Konno, O. Sakata and H. Funakubo, *Appl. Phys. Lett.*, 2016, **109**, 052903.

102 R. Shimura, T. Mimura, T. Shimizu, Y. Tanaka, Y. Inoue and H. Funakubo, *J. Ceram. Soc. Japan*, 2020, **128**, 539–543.

103 T. Mimura, T. Shimizu, H. Uchida, O. Sakata and H. Funakubo, *Appl. Phys. Lett.*, 2018, **113**, 102901.

104 K. Amanuma, T. Mori, T. Hase, T. Sakuma, A. Ochi and Y. Miyasaka, *Jpn. J. Appl. Phys.*, 1993, **32**, 4150–4153.

105 N. A. Pertsev, J. Rodríguez Contreras, V. G. Kukhar, B. Hermanns, H. Kohlstedt and R. Waser, *Appl. Phys. Lett.*, 2003, **83**, 3356–3358.

106 T. Shimizu, T. Mimura, T. Kiguchi, T. Shiraishi, T. Konno, Y. Katsuya, O. Sakata and H. Funakubo, *Appl. Phys. Lett.*, 2018, **113**, 212901.

107 T. Suzuki, T. Shimizu, T. Mimura, H. Uchida and H. Funakubo, *Jpn. J. Appl. Phys.*, 2018, **57**, 11UF15.

108 T. Mimura, T. Shimizu, H. Uchida and H. Funakubo, *Appl. Phys. Lett.*, 2020, **116**, 062901.

109 T. Li, N. Zhang, Z. Sun, C. Xie, M. Ye, S. Mazumdar, L. Shu, Y. Wang, D. Wang, L. Chen, S. Ke and H. Huang, *J. Mater. Chem. C*, 2018, **6**, 9224–9231.

110 S. Liu and B. M. Hanrahan, *Phys. Rev. Mater.*, 2019, **3**, 054404.

111 T. KIGUCHI, S. NAKAMURA, A. AKAMA, T. SHIRAISHI and T. J. KONNO, *J. Ceram. Soc. Japan*, 2016, **124**, 689–693.

112 T. Mimura, T. Shimizu, T. Kiguchi, A. Akama, T. J. Konno, Y. Katsuya, O. Sakata and H. Funakubo, *Jpn. J. Appl. Phys.*, 2019, **58**, 0–5.

113 Z. Zhang, S. Hsu, V. A. Stoica, H. Paik, E. Parsonnet, A. Qualls, J. Wang, L. Xie, M. Kumari, S. Das, Z. Leng, M. McBriarty, R. Proksch, A. Gruverman, D. G. Schlom, L. Chen, S. Salahuddin, L. W. Martin and R. Ramesh, *Adv. Mater.*, 2021, **33**, 2006089.

114 T. Shimizu, Y. Tashiro, T. Mimura, T. Kiguchi, T. Shiraishi, T. J. Konnno, O. Sakata and H. Funakubo, *Phys. status solidi – Rapid Res. Lett.*, 2021, **15**, 2000589.

115 T. Shiraishi, S. Choi, T. Kiguchi, T. Shimizu, H. Uchida, H. Funakubo and T. J. Konno, *Jpn. J. Appl. Phys.*, 2018, **57**, 11UF02.

116 S. Choi, T. Shiraishi, T. Kiguchi, T. Shimizu, H. Funakubo and T. J. Konno, *Appl. Phys. Lett.*, 2018, **113**, 262903.

117 J. Lyu, I. Fina and F. Sánchez, *Appl. Phys. Lett.*, 2020, **117**, 072901.

118 S. Estandía, N. Dix, M. F. Chisholm, I. Fina and F. Sánchez, *Cryst. Growth Des.*, 2020, **20**, 3801–3806.

119 S. Estandía, J. Gàzquez, M. Varela, N. Dix, M. Qian, R. Solanas, I. Fina and F. Sánchez, *J. Mater. Chem. C*, 2021, **9**, 3486–3492.

120 S. Estandía, T. Cao, R. Mishra, I. Fina, F. Sánchez and J. Gazquez, *Phys. Rev. Mater.*, 2021, **5**, 074410.

121 Y. Zhang, Q. Yang, L. Tao, E. Y. Tsymbal and V. Alexandrov, *Phys. Rev. Appl.*, 2020, **14**, 1.

122 K. Lee, T. Y. Lee, S. M. Yang, D. H. Lee, J. Park and S. C. Chae, *Appl. Phys. Lett.*, 2018, **112**, 202901.

123 J. W. Adkins, I. Fina, F. Sánchez, S. R. Bakaul and J. T. Abiade, *Appl. Phys. Lett.*, 2020, **117**, 142902.

124 P. Nukala, J. Antoja-Lleonart, Y. Wei, L. Yedra, B. Dkhil and B. Noheda, *ACS Appl. Electron. Mater.*, 2019, **1**, 2585–2593.

125 L. Pintilie, I. Pasuk, R. Negrea, L. D. Filip and I. Pintilie, *J. Appl. Phys.*, 2012, **112**, 64116.

126 I. Fina, L. Fàbrega, E. Langenberg, X. Martí, F. Sánchez, M. Varela and J. Fontcuberta, *J. Appl. Phys.*, 2011, **109**, 074105.

127 B. Max, M. Hoffmann, H. Mulaosmanovic, S. Slesazeck and T. Mikolajick, *ACS Appl. Electron. Mater.*, 2020, **2**, 4023–4033.

128 S. Oh, T. Kim, M. Kwak, J. Song, J. Woo, S. Jeon, I. K. Yoo and H. Hwang, *IEEE Electron Device Lett.*, 2017, **38**, 732–735.

129 S. Saïghi, C. G. Mayr, T. Serrano-Gotarredona, H. Schmidt, G. Lecerf, J. Tomas, J. Grollier, S. Boyn, A. F. Vincent, D. Querlioz, S. La Barbera, F. Alibart, D. Vuillaume, O. Bichler, C. Gamrat and B. Linares-Barranco, *Front. Neurosci.*, 2015,

9, 1–16.

130 M. Cervo Sulzbach, H. Tan, S. Estandía, J. Gàzquez, F. Sánchez, I. Fina and J. Fontcuberta, *ACS Appl. Electron. Mater.*, 2021, **3**, 3657–3666.

131 A. Pal, V. K. Narasimhan, S. Weeks, K. Littau, D. Pramanik and T. Chiang, *Appl. Phys. Lett.*, 2017, **110**, 022903.

132 Y. H. Lee, H. J. Kim, T. Moon, K. Do Kim, S. D. Hyun, H. W. Park, Y. Bin Lee, M. H. Park and C. S. Hwang, *Nanotechnology*, 2017, **28**, 305703.

133 J. Gonzalo, J. Siegel, A. Perea, D. Puerto, V. Resta, M. Galvan-Sosa and C. N. Afonso, *Phys. Rev. B*, 2007, **76**, 035435.

134 B. Shin and M. J. Aziz, *Phys. Rev. B*, 2007, **76**, 085431.

135 P. R. Willmott, R. Herger, C. M. Schlepütz, D. Martoccia and B. D. Patterson, *Phys. Rev. Lett.*, 2006, **96**, 176102.

136 C. S. Ma, S. K. Hau, K. H. Wong, P. W. Chan and C. L. Choy, *Appl. Phys. Lett.*, 1996, **69**, 2030–2032.

137 T. Scharf and H. U. Krebs, *Appl. Phys. A Mater. Sci. Process.*, 2002, **75**, 551–554.

138 T. Suzuki, T. Shimizu, T. Mimura, H. Uchida and H. Funakubo, *Jpn. J. Appl. Phys.*, 2018, **57**, 11UF15.

139 M. Materano, P. D. Lomenzo, A. Kersch, M. H. Park, T. Mikolajick and U. Schroeder, *Inorg. Chem. Front.*, 2021, **8**, 2650–2672.

140 T. D. Huan, V. Sharma, G. A. Rossetti and R. Ramprasad, *Phys. Rev. B*, 2014, **90**, 064111.

141 F. Delodovici, P. Barone and S. Picozzi, *Phys. Rev. Mater.*, 2021, **5**, 064405.

142 T. Onaya, T. Nabatame, N. Sawamoto, A. Ohi, N. Ikeda, T. Chikyow and A. Ogura, *Appl. Phys. Express*, 2017, **10**, 081501.

143 T. Onaya, T. Nabatame, N. Sawamoto, A. Ohi, N. Ikeda, T. Nagata and A. Ogura, *APL Mater.*, 2019, **7**, 061107.

144 W. Xiao, C. Liu, Y. Peng, S. Zheng, Q. Feng, C. Zhang, J. Zhang, Y. Hao, M. Liao and Y. Zhou, *IEEE Electron Device Lett.*, 2019, **40**, 714–717.

145 D. J. Kim, J. Y. Jo, Y. S. Kim, Y. J. Chang, J. S. Lee, J.-G. Yoon, T. K. Song and T. W. Noh, *Phys. Rev. Lett.*, 2005, **95**, 237602.

146 L. L. Tao, T. R. Paudel, A. A. Kovalev and E. Y. Tsymbal, *Phys. Rev. B*, 2017, **95**, 245141.

147 J. Müller, T. S. Böscke, D. Bräuhaus, U. Schröder, U. Böttger, J. Sundqvist, P. Kücher, T. Mikolajick and L. Frey, *Appl. Phys. Lett.*, 2011, **99**, 112901.

148 M. G. Kozodaev, A. G. Chernikova, E. V. Korostylev, M. H. Park, U. Schroeder, C. S. Hwang and A. M. Markeev, *Appl. Phys. Lett.*, 2017, **111**, 132903.

149 T. Schenk, A. Anspoks, I. Jonane, R. Ignatans, B. S. Johnson, J. L. Jones, M. Tallarida, C. Marini, L. Simonelli, P. Hönicke, C. Richter, T. Mikolajick and U. Schroeder, *Acta Mater.*, 2019, **180**, 158–169.

150 M. H. Park, C.-C. Chung, T. Schenk, C. Richter, M. Hoffmann, S. Wirth, J. L. Jones, T. Mikolajick and U. Schroeder, *Adv. Electron. Mater.*, 2018, **4**, 1700489.

151 T. Y. Hsu, C. L. Kuo, B. T. Lin, J. Shieh and M. J. Chen, *Smart Mater. Struct.*, 2019, **28**, 0–8.

152 S. González-Casal, I. Fina, F. Sánchez and J. Fontcuberta, *ACS Appl. Electron. Mater.*, 2019, **1**, 1937–1944.

153 T. Schenk, N. Godard, A. Mahjoub, S. Girod, A. Matavz, V. Bobnar, E. Defay and S. Glinsek, *Phys. status solidi – Rapid Res. Lett.*, 2020, **14**, 1900626.

154 U. Schroeder, C. Richter, M. H. Park, T. Schenk, M. Pešić, M. Hoffmann, F. P. G. Fengler, D. Pohl, B. Rellinghaus, C. Zhou, C.-C. Chung, J. L. Jones and T. Mikolajick, *Inorg. Chem.*, 2018, **57**, 2752–2765.

155 C. Mart, K. Kühnel, T. Kämpfe, S. Zybell and W. Weinreich, *Appl. Phys. Lett.*, 2019, **114**, 102903.

156 M. H. Park, Y. H. Lee, T. Mikolajick, U. Schroeder and C. S. Hwang, *MRS Commun.*, 2018, **8**, 795–808.

157 S. Estandía, N. Dix, J. Gazquez, I. Fina, J. Lyu, M. F. Chisholm, J. Fontcuberta and F. Sánchez, *ACS Appl. Electron. Mater.*, 2019, **1**, 1449–1457.

158 G. Saint-Girons, R. Bachelet, R. Moalla, B. Meunier, L. Louahadj, B. Canut, A. Carretero-Genevrier, J. Gazquez, P. Regreny, C. Botella, J. Penuelas, M. G. Silly, F. Sirotti and G. Grenet, *Chem. Mater.*, 2016, **28**, 5347–5355.

159 X. Li, C. Li, Z. Xu, Y. Li, Y. Yang, H. Hu, Z. Jiang, J. Wang, J. Ren, C. Zheng, C. Lu and Z. Wen, *Phys. status solidi – Rapid Res. Lett.*, 2021, **15**, 2000481.

160 T. Schenk, A. Bencan, G. Drazic, O. Condurache, N. Valle, B. El Adib, N. Aruchamy, T. Granzow, E. Defay and S. Glinsek, *Appl. Phys. Lett.*, 2021, **118**, 162902.

161 M. Materano, P. D. Lomenzo, H. Mulaosmanovic, M. Hoffmann, A. Toriumi, T. Mikolajick and U. Schroeder, *Appl. Phys. Lett.*, 2020, **117**, 262904.

162 V. M. Fridkin and S. Ducharme, *Phys. Solid State*, 2001, **43**, 1320–1324.

163 T. Song, R. Bachelet, G. Saint-Girons, N. Dix, I. Fina and F. Sánchez, *J. Mater. Chem. C*, 2021, **1**, 3777.

164 T. Song, R. Bachelet, G. Saint-Girons, R. Solanas, I. Fina and F. Sánchez, *ACS Appl. Electron. Mater.*, 2020, **2**, 3221–3232.

165 M. C. Sulzbach, S. Estandía, X. Long, J. Lyu, N. Dix, J. Gàzquez, M. F. Chisholm, F. Sánchez, I. Fina and J. Fontcuberta, *Adv. Electron. Mater.*, 2020, **6**, 1900852.

166 M. Lanza, *Materials (Basel).*, 2014, **7**, 2155–2182.

167 M. H. Park, T. Schenk, C. M. Fancher, E. D. Grimley, C. Zhou, C. Richter, J. M. LeBeau, J. L. Jones, T. Mikolajick and U. Schroeder, *J. Mater. Chem. C*, 2017, **5**, 4677–4690.

168 R. Moalla, B. Vilquin, G. Saint-Girons, G. Sebald, N. Baboux and R. Bachelet, *CrystEngComm*, 2016, **18**, 1887–1891.

169 M. Dawber, P. Chandra, P. B. Littlewood and J. F. Scott, *J. Phys. Condens. Matter*, 2003, **15**, L393–L398.

170 H. N. Lee, S. M. Nakhmanson, M. F. Chisholm, H. M. Christen, K. M. Rabe and D. Vanderbilt, *Phys. Rev. Lett.*, 2007, **98**, 217602.

171 M. Scigaj, N. Dix, I. Fina, R. Bachelet, B. Warot-Fonrose, J. Fontcuberta and F. Sánchez, *Appl. Phys. Lett.*, 2013, **102**, 112905.

172 S. Li, D. Zhou, Z. Shi, M. Hoffmann, T. Mikolajick and U. Schroeder, *Adv. Electron. Mater.*, 2020, **6**, 2000264.

173 M. G. Kozodaev, A. G. Chernikova, E. V. Korostylev, M. H. Park, R. R. Khakimov, C. S. Hwang and A. M. Markeev, *J. Appl. Phys.*, 2019, **125**, 034101.

174 A. G. Chernikova, M. G. Kozodaev, D. V. Negrov, E. V. Korostylev, M. H. Park, U. Schroeder, C. S. Hwang and A. M. Markeev, *ACS Appl. Mater. Interfaces*, 2018, **10**, 2701–2708.

175 F. Mehmood, T. Mikolajick and U. Schroeder, *Phys. status solidi*, 2020, **217**, 2000281.

176 A. G. Chernikova, M. G. Kozodaev, D. V. Negrov, E. V. Korostylev, M. H. Park, U. Schroeder, C. S. Hwang and A. M. Markeev, *ACS Appl. Mater. Interfaces*, 2018, **10**, 2701–2708.

177 S. Estandía, N. Dix, M. F. Chisholm, I. Fina and F. Sánchez, *Cryst. Growth Des.*, 2020, **20**, 3801–3806.

178 S. Migita, H. Ota, H. Yamada, K. Shibuya, A. Sawa and A. Toriumi, *Jpn. J. Appl. Phys.*, 2018, **57**, 04FB01.

179 M. G. Kozodaev, A. G. Chernikova, E. V. Korostylev, M. H. Park, R. R. Khakimov, C. S. Hwang and A. M. Markeev, *J. Appl. Phys.*, 2019, **125**, 034101.

180 F. Mehmood, M. Hoffmann, P. D. Lomenzo, C. Richter, M. Materano, T. Mikolajick and U. Schroeder, *Adv. Mater. Interfaces*, 2019, **6**, 1901180.

181 S. Starschich, S. Menzel and U. Böttger, *Appl. Phys. Lett.*, 2016, **108**, 032903.

182 G. Walters, A. Shekhawat, N. G. Rudawski, S. Moghaddam and T. Nishida, *Appl. Phys. Lett.*, 2018, **112**, 192901.

183 F. Mehmood, T. Mikolajick and U. Schroeder, *Appl. Phys. Lett.*, 2020, **117**, 092902.

184 Z. Wang, A. A. Gaskell, M. Dopita, D. Kriegner, N. Tasneem, J. Mack, N. Mukherjee, Z. Karim and A. I. Khan, *Appl. Phys. Lett.*, 2018, **112**, 222902.

185 X. Cheng, Z. Qi, T. Li, G. Zhang, C. Li, H. Zhou, Y. Wang and M. Yin, *Phys. status solidi*, 2012, **249**, 854–857.

186 T. Mikolajick, S. Slesazeck, M. H. Park and U. Schroeder, *MRS Bull.*, 2018, **43**, 340–346.

187 T. Mikolajick, U. Schroeder and S. Slesazeck, *IEEE Trans. Electron Devices*, 2020, **67**, 1434–1443.

188 J. Y. Park, K. Yang, D. H. Lee, S. H. Kim, Y. Lee, P. R. S. Reddy, J. L. Jones and M. H. Park, *J. Appl. Phys.*, 2020, **128**, 240904.

189 K. Florent, S. Lavizzari, L. Di Piazza, M. Popovici, J. Duan, G. Groeseneken and J. Van Houdt, *IEEE Trans. Electron Devices*, 2017, **64**, 4091–4098.

190 N. Gong and T. Ma, *IEEE Electron Device Lett.*, 2016, **37**, 1123–1126.

191 X. J. Lou, *J. Appl. Phys.*, 2009, **105**, 024101.

192 S. M. Yang, T. H. Kim, J.-G. Yoon and T. W. Noh, *Adv. Funct. Mater.*, 2012, **22**, 2310–2317.

193 U. Böttger and R. Waser, *J. Appl. Phys.*, 2017, **122**, 024105.

194 M. Dawber, K. M. Rabe and J. F. Scott, *Rev. Mod. Phys.*, 2005, **77**, 1083–1130.

195 A. K. Tagantsev, I. Stolichnov, E. L. Colla and N. Setter, *J. Appl. Phys.*, 2001, **90**, 1387–1402.

196 J. Y. Jo, D. J. Kim, Y. S. Kim, S.-B. Choe, T. K. Song, J.-G. Yoon and T. W. Noh, *Phys. Rev. Lett.*, 2006, **97**, 247602.

197 F. P. G. G. Fengler, M. Hoffmann, S. Slesazeck, T. Mikolajick and U. Schroeder, *J. Appl. Phys.*, 2018, **123**, 204101.

198 D. R. Islamov, V. A. Gritsenko, T. V. Perevalov, V. A. Pustovarov, O. M. Orlov, A. G. Chernikova, A. M. Markeev, S. Slesazeck, U. Schroeder, T. Mikolajick and G. Y. Krasnikov, *Acta Mater.*, 2019, **166**, 47–55.

199 M. C. Sulzbach, S. Estandía, X. Long, J. Lyu, N. Dix, J. Gàzquez, M. F. Chisholm, F. Sánchez, I. Fina and J. Fontcuberta, *Adv. Electron. Mater.*, 2020, **6**, 0–9.

200 P. Buragohain, C. Richter, T. Schenk, H. Lu, T. Mikolajick, U. Schroeder and A. Gruverman, *Appl. Phys. Lett.*, 2018, **112**, 222901.

201 T. Y. Lee, K. Lee, H. H. Lim, M. S. Song, S. M. Yang, H. K. Yoo, D. I. Suh, Z. Zhu, A. Yoon, M. R. Macdonald, X. Lei, H. Y. Jeong, D. Lee, K. Park, J. Park and S. C. Chae, *ACS Appl. Mater. Interfaces*, 2019, **11**, 3142–3149.

202 Y. Li, J. Li, R. Liang, R. Zhao, B. Xiong, H. Liu, H. Tian, Y. Yang and T.-L. Ren, *Appl. Phys. Lett.*, 2019, **114**, 142902.

203 B. Buyantogtokh, V. Gaddam and S. Jeon, *J. Appl. Phys.*, 2021, **129**, 244106.

204 K. Lee, K. Park, H.-J. Lee, M. S. Song, K. C. Lee, J. Namkung, J. H. Lee, J. Park and S. C. Chae, *Sci. Rep.*, 2021, **11**, 6290.

205 P. Buragohain, A. Erickson, T. Mimura, T. Shimizu, H. Funakubo and A. Gruverman, *Adv. Funct. Mater.*, 2022, **32**, 2108876.

206 Y. W. So, D. J. Kim, T. W. Noh, J.-G. Yoon and T. K. Song, *Appl. Phys. Lett.*, 2005, **86**, 092905.

207 T. H. Kim, S. H. Baek, S. M. Yang, Y. S. Kim, B. C. Jeon, D. Lee, J.-S. Chung, C. B. Eom, J.-G. Yoon and T. W. Noh, *Appl. Phys. Lett.*, 2011, **99**, 12905.

208 J. Y. Jo, H. S. Han, J.-G. Yoon, T. K. Song, S.-H. Kim and T. W. Noh, *Phys. Rev. Lett.*, 2007, **99**, 267602.

209 W. Li and M. Alexe, *Appl. Phys. Lett.*, 2007, **91**, 262903.

210 D. Pantel, Y.-H. Chu, L. W. Martin, R. Ramesh, D. Hesse and M. Alexe, *J. Appl. Phys.*, 2010, **107**, 084111.

211 M. D. Glinchuk, A. N. Morozovska, A. Lukowiak, W. Stręk, M. V. Silibin, D. V. Karpinsky, Y. Kim and S. V. Kalinin, *J. Alloys Compd.*, 2020, **830**, 153628.

212 S. Santucci, H. Zhang, S. Sanna, N. Pryds and V. Esposito, *J. Mater. Chem. A*, 2020, **8**, 14023–14030.

213 X. Lyu, M. Si, P. R. Shrestha, K. P. Cheung and P. D. Ye, *Tech. Dig. - Int. Electron Devices Meet. IEDM*, 2019, **2019-Decem**, 342–345.

214 M. Si, X. Lyu, P. R. Shrestha, X. Sun, H. Wang, K. P. Cheung and P. D. Ye, *Appl. Phys. Lett.*, 2019, **115**, 072107.

215 H. Liu, T. Lu, Y. Li, Z. Ju, R. Zhao, J. Li, M. Shao, H. Zhang, R. Liang, X. R. Wang, R. Guo, J. Chen, Y. Yang and T. Ren, *Adv. Sci.*, 2020, **7**, 2001266.

216 C. Alessandri, P. Pandey, A. Abusleme and A. Seabaugh, *IEEE Electron Device Lett.*, 2018, **39**, 1780–1783.

217 S.-N. Choi, S.-E. Moon and S.-M. Yoon, *Ceram. Int.*, 2019, **45**, 22642–22648.

218 H. Y. Yoong, H. Wu, J. Zhao, H. Wang, R. Guo, J. Xiao, B. Zhang, P. Yang, S. J. Pennycook, N. Deng, X. Yan and J. Chen, *Adv. Funct. Mater.*, 2018, **28**, 1806037.

219 G. Bersuker, D. C. Gilmer, D. Veksler, P. Kirsch, L. Vandelli, A. Padovani, L. Larcher, K. McKenna, A. Shluger, V. Iglesias, M. Porti and M. Nafría, *J. Appl. Phys.*, 2011, **110**, 124518.

220 M. Lanza, G. Bersuker, M. Porti, E. Miranda, M. Nafría and X. Aymerich, *Appl. Phys. Lett.*, 2012, **101**, 193502.

221 S. Dueñas, H. Castán, O. G. Ossorio and H. García, *Microelectron. Eng.*, 2019, **216**, 111032.